UNIVERSITY OF CALIFORNIA

Santa Barbara

From Nano to Micro: Versatile Strategies for Near-Infrared Light-controlled Nitric Oxide Delivery and Their Therapeutic Applications

A dissertation submitted in partial satisfaction of the

requirements for the degree Doctor of Philosophy

in Chemistry

by

Po-Ju Huang

Committee in charge:

Professor Peter C. Ford, Chair

Professor Galen Stucky

Professor Javier Read de Alaniz

Professor Trevor Hayton

December 2017

The dissertation of Po-Ju Huang is approved.

_____

Javier Read de Alaniz

_____

Trevor Hayton

_____

Galen Stucky

_____

Peter C. Ford, Committee Chair

November 2017

From Nano to Micro: Versatile Strategies for Near-Infrared Light-controlled Nitric Oxide Delivery and Their Therapeutic Applications

by

Po-Ju Huang

ACKNOWLEDGEMENTS

First of all, I would like to thank my committee: Prof. Ford, Prof. Stucky, Prof. Hayton and Prof. Read for giving me valuable advice to my research, especially my advisor Prof. Ford. He gave me a lot of opportunities to expand my personal and research skills such as proposal writing, photochemistry, nanotechnology, robotic application in materials science and bioengineering. I believe, without these experiences, I may not be able to get the job offer from Agilent with an advanced level position.

Secondly, I would like to thank former and current Ford group members for making work in lab fun during my 5 years. Thanks to Dr. Peter Burks for the training in quantum dots synthesis, Dr. John Garcia for the laser training, Dr. Agustin Pierri for the training in photoCORMs synthesis, Dr. Meredith Crisalli for the NOA training, Dr. Anthony Demartino for the initial training in CrONO project, Dr. Chris Bernt for discussing ideas, Dr. Megan Chui for ICP analysis and Dr. Maykon Lima for sharing all his knowledge and skills in chemistry. Additionally, thanks to Zhi and Jacob for helping me maintain our lab and let me have more time to focus on my research.

Thirdly, I would like to thank my collaborators: Aaron, Michael, Dean and Erin for biological studies; Yuji for providing NIR sensitive photoNORM; Dr. Emory Chan for supporting us to use his robot; Dr. Binghui Wu for all technical support and idea sharing; Dr. Xiaojing Zhao for TEM analysis.

Finally, I would like to thank Marco for his help. He and my wife take care of me when I was in hospital. To my parents and my wife, I deeply appreciate all your support. Without you, I wouldn’t be able to overcome all challenges I had. Thank you and love you.

VITA OF Po-Ju Huang

November 2017

EDUCATION

Bachelor of Science, Major in Chemistry, National Chung Cheng University, Taiwan, June 2006

Master of Science, Major in Materials Science and Engineering, National Chiao Tung University, Taiwan, July 2008

Doctor of Philosophy, Major in Inorganic Chemistry, University of California-Santa Barbara, USA, December 2017 (expected)

PROFESSIONAL EMPLOYMENT

2004-2006: Undergraduate Student Researcher (total synthesis), Department of Chemistry and Biochemistry, National Chung Cheng University, Taiwan

2006-2007: Teaching Assistant, Department of Materials Science and Engineering, National Chiao Tung University, Taiwan

2006-2008: Internship (organic semiconductor), Industrial Technology Research Institute, Taiwan

2009-2010: Assistant Researcher (polymer mechanics/chemistry/physics and project management), Plastics Industry Development Center, Taiwan

2010-2010: Research Assistant (chemical vapor deposition), Industrial Technology Research Institute, Taiwan

2016-2017: Affiliate (robotic application), Lawrence Berkeley National Laboratory, USA

2013-2017: Teaching Assistant/Graduate Student Researcher (photochemical NO targeted delivery), Department of Chemistry & Biochemistry, University of California-Santa Barbara, USA

FELLOWSHIPS/SCHOLARSHIPS

2015-2016 B.R. Baker Memorial Fellowship, Department of Chemistry & Biochemistry, University of California, Santa Barbara

2014-2015 Jarrod Davidson Memorial Scholarship, Department of Chemistry & Biochemistry, University of California, Santa Barbara

2014-2015 Partnership in International Research and Education in Electron Chemistry and Catalysis at Interfaces (PIRE-ECCI) Fellowship, NSF-sponsored program

PUBLICATIONS

1. " Compositions and Methods for Delivering Nitric Oxide to Cells" Michael Evans, Po-Ju Huang, Peter C. Ford* and Samir Mitragotri*, *Provisional Patent* (2017-249)

2. " Dinuclear PhotoCORMs: Dioxygen-Assisted Carbon Monoxide Uncaging from Long-Wavelength-Absorbing Metal–Metal-Bonded Carbonyl Complexes " Zhi Li, Agustin E. Pierri, Po-Ju Huang, Guang Wu, Alexei V. Iretskiia, and Peter C. Ford*, *Inorg. Chem*., **2017**, 56, 6094–6104

3. "A photoCORM nanocarrier for CO release using NIR light" Agustin E. Pierri, Po-Ju Huang, John V. Garcia, James G. Stanfill, Megan Chui, Guang Wu, Nanfeng Zheng * and Peter C. Ford *, *Chem. Commun.*, **2015**, 51, 2072-2075

4. "Tunable Novel Cyclopentadithiophene-Based Copolymers Containing Various Numbers of Bithiazole and Thienyl Units for Organic Photovoltaic Cell Applications" Kuang-Chieh Li, Jen-Hsien Huang, Ying-Chan Hsu, Po-Ju Huang, Chih-Wei Chu, Jiann-T'suen Lin, Kuo-Chuan Ho, Kung-Hwa Wei, and Hong-Cheu Lin *, *Macromolecules* **2009**, 42, 3681-3693

ABSTRACT

From Nano to Micro: Versatile Strategies for Near-Infrared Light-controlled Nitric Oxide Delivery and Their Therapeutic Applications

by

Po-Ju Huang

Nitric oxide (NO) has attracted considerable attention due to its promising applications in cancer treatment. The therapeutic effect of NO pro-drugs greatly depends on the concentration, duration and the specific site of NO delivered. Photochemical delivery can control the timing, dosage and location of NO release by administering the intensity and location of light irradiation. However, there are key challenges associated with using such photo-activated NO releasing molecules ("photoNORMs"). One is to activate these precursors with tissue penetrating near infrared (NIR) light, while another is to deliver these precursors directly to inflammatory sites, including tumors. Here, we describe two different NIR light-activated NO releasing composites with nano and micron size, and demonstrate their delivery strategies to cancer cells and tumor spheroids by using cell penetrating peptides (CPPs) and macrophages mediation respectively.

For the nano-delivery, we developed new nano-carriers with graphene quantum dots (GQDs) as photo-active cores, lipophilic domains and a surface modified with cell-penetrating peptides. The lipophilic domains in the CPP-nano-carriers can be loaded with

hydrophobic photoNORMs. Such CPPs can overcome the barrier of cellular membranes and efficiently deliver our nano-carriers inside the cell. Moreover, GQD is able to absorb 794 nm photon and transfer energy to trigger NO release from the NO precursors in lipophilic domains. We showed NO photo-release in HeLa cancer cells under 794 nm laser irradiation can be visualized by using a fluorescent NO probe dye (DAF-FM-2DA).

For the micro-delivery, we applied bone marrow macrophages (BMMs) as "Trojan horses" to deliver biocompatible polymer micro-particles incorporating photoNORMs and upconversion nanoparticles (UCNPs) to breast cancer spheroids. Both components are activated by tissue penetrating NIR light allowing for simultaneous therapeutic NO delivery and photoluminescence (PL) imaging capabilities with a single NIR laser source. By varying light source intensity, we were able to garner control over NO release rates reducing hypoxia inducible factor 1 alpha (HIF-1α) levels with low doses of NO while demonstrating direct cytoxicity to spheroids with high doses of NO.

Table of Contents

Chapter I. Introduction

A. Nitric Oxide

Nitric oxide (NO), one of small molecule bioregulators (SMBs), is endogenously generated from L-arginine via the enzyme nitric oxide synthase (NOS) in mammalian physiology[1] and plays pivotal roles in diverse biological processes such as vasodilation,[1] platelet aggregation and adhesion,[1] the immune response to infection,[2,3] wound repair,[4] cancer biology and pathology[5]. Due to its integral role in human physiology, many disease states have been attributed to deficiencies in NO biosynthesis.[6] Therefore, developing strategies for conveying NO to specific disease sites hold promise to many biomedical applications such as cardiovascular regulation,[7–9] antimicrobial therapies[2,10,11] and tumoricidal treatments[12,13]. However, depending on oxygen concentration and distance from vessel, NO has short extravascular half-life which is in a range of 0.09 to over 2 second,[14] and, its intravascular half-life is down to 2 ms.[15]

Therefore, in order to achieve controlled NO delivery, different types of NO donors have already been investigated and synthesized. These include organic nitrates[16], nitrites[16], metal–NO complexes[17–25], chromium dinitrito (CrONO)[26–33], nitrosamines[16], N-diazeniumdiolates (NONOates)[34–38], and S-nitrosothiols (RSNOs)[39–46]. In the Ford group, we are focusing on light sensitive metal-NO complexes and CrONO derivatives for photochemical NO delivery.

B. Photo-triggered NO Delivery

In addition to reactivity and delivered sites of NO, precise dosage-control for NO delivery is another critical factor to influence the efficacy of such photochemical NO therapy.[47,48] For example, at nanomolar concentrations, NO is a vasodilator[49] and is cytoprotective[50], while at micromolar concentrations, NO can suppress tumor growth[5] and is a radiation sensitizer when administered in tandem with γ-radiation.[51] Photochemical delivery can control the timing, dosage and location of NO release by administering the intensity and location of light irradiation. However, there are several key challenges associated with this approach in biological systems. One is the need to trigger NO release from photo-activated NO releasing moieties ("photoNORMs") using tissue-penetrating wavelengths (ideally NIR light),[48] and the second is to develop targeting strategies for delivery to specific sites in vitro or in vivo.

Most photoNORMs such as Ru-NO complexes require UV or visible light at wavelengths that do not deeply penetrate tissue to uncage NO.[24,25] However, the optimal wavelength for light transmission through tissue is approximately 700 nm to 900 nm (the therapeutic window)[52,53] where water, tissue and blood have low absorbance. Some research groups have worked on the synthesis of NIR light sensitive photoNORMs to address this issue.[54,55] Others have already applied different types of NIR photosensitizers to indirectly trigger NO release via energy transfer between NO donors and the sensitizers in hybrid composites. Ford et al. have already utilized up-converting nanoparticles (UCNPs) as antennas to photosensitize the release of NO[23,56] and of carbon monoxide (CO)[57] from various precursors. The earlier proof-of-concept studies with UCNPs[23,56,58] utilized Yb:Er- or Yb:Tm-doped $NaYF_4$ nanocrystals as photosensitizers with 980 nm irradiation. However,

water has significant absorption after 900 nm wavelength. Therefore, Nd:Yb:Er- and Nd:Yb:Tm-doped nanocrystals[59–62] or 100 % Er doped $NaErF_4$ nanomaterials[63] to serve as photosensitizers that operate with the 800 nm excitation have been considered to avoid overheating effect, since they should lead to less collateral damage to tissue.

In addition to UCNPs, hollow gold nanoparticles (HGNs) and carbon dots (CDs) as 800 nm photosensitizers were used in the photo-triggered NO delivery. Ford and his co-workers reported the first example of utilizing gold nanoparticle platforms for NO delivery with NIR external stimuli.[64] The plasmonic HGNs can locally generate high temperature upon irradiation with biocompatible near infrared light (~800 nm) to further thermally decompose thiolated cupferron attached on the surface of HGNs to release NO.

For CDs applications in NO photo-release, carbon nanomaterials are effective two-photon absorbers that have been utilized in NIR photo-delivery for NO release based on their high two-photon cross-sectiones.65 Additionally, CDs have also been used as NIR photosensitizers to uncage carbon monoxide (CO)66, another SMB, and NO67 from their nano-composites via photocatalyic and photothermal decomposition, respectively.

C. NIR Photosensitizers

C-1. Lanthanide-doped Upconversion Nanoparticles (UCNPs)

Upconversion is a nonlinear optical process which converts absorbed two or multi-photons at long wavelength to emit a single photon at shorter wavelength. Lanthanide-doped nanomaterials have long lifetimes of excited states and a ladder-like energy levels system to achieve such optical property.[68] These so-called upconverting nanoparticles (UCNPs) usually consist of a crystalline host with lanthanide ions as dopants.[69] The partly filled 4f orbital of lanthanide ions ($Ln^{3+)}$ has 4f - 4f electronic transitions that primarily contribute the unique photophysical properties and luminescence spectra are further influenced by the inorganic host material, the organic ligands, and surface quenching effects.[70]

Typically, host materials are fluoride composites such as $NaYF_4$ or $NaGdF_4$.[71] Ln^{3+} cations are substitutionally doped into these host composites to replace the trivalent cations. Electric dipole transitions in the anisotropic crystal field surrounding a dopant site are forbidden and strictly prohibited only in a spherically symmetric environment.[70] Therefore, host materials such as hexagonal β phase of $NaYF_4$ and $NaGdF_4$ can have emission an order of magnitude greater than cubic α phase of NaYF4 owing to less symmetric lanthanide dopant sites in hexagonal structure.[72,73]

Additionally, lanthanide dopants in UCNPs can serve as either photon absorbers or photon emitters by accepting energy from another species via energy transfer (ET). Therefore, varying the composition of lanthanide ions in such heterostructures can greatly influence their excitation and emission wavelengths as well as upconverting efficiency.[70] For general upconversion mechanism, Yb^{3+} and Nd^{3+} as NIR photon absorbers can be

excited at 980 nm and 800 nm respectively, and transfer energy to the emitters such as Tm^{3+}, Er^{3+} and Ho^{3+} to correspondingly generate blue, orange and green emission if considering a single doping system.[74] However, Almutairi and her co-workers recently show Er^{3+} ion possesses interesting energy levels that can absorb 800 nm and 980 nm photons, and have downshifted emission at 1550 nm as well as upconversion emission at 540 nm and 650 nm.[63] Therefore, in this case, Er^{3+} can not only serve as a NIR photon absorber but also act as an upconversion emitter. Particularly, they reported 100 % Er doped core-shell nanoparticles ($NaErF_4$@$NaLuF_4$) have upconversion emission intensity higher than the 5-50% Er doped core-shell nanoparticles. However, unshelled 100 % Er doped core nanoparticles have totally opposite results. So, the reason is that high dopant concentrations of UCNPs have predominant quenching process due to the energy migration to surface not the cross-relaxation between dopants. Thus, inert epitaxial shell growth on the surface of highly doping core UCNPs can prevent surface quenching to afford higher emission intensity. This research works will inspire scientists to work on heavily lanthanide-doping UCNPs for high upconversion efficiency.

C-2. Carbon Dots (CDs)

Fluorescent carbon dots (CDs) were first discovered in 2004 as impurities of single-walled carbon nanotube.[75] Based on preparation method and solid morphology, carbon dots can be classified into three categories[76,77]: carbon quantum dots (CQDs), graphene quantum dots (GQDs) and polymer dots (PDs). CQDs are graphite or graphite-like nanoparticles while GQDs are graphene nano-fragments. PDs are made not only by several organic molecules with some functional groups such as thiol, hydroxy, carboxylic acid and amine but also synthetic or natural polymers under hydrothermal process.[78–82]

Typically, GQDs have dimensions in the size range from 3 nm to 20 nm diameter that cause excitonic quantum confinement effect.[83] Such carbon nanomaterials have been prepared by top-down fragmentation such as Hummers' oxidation,[84] electrochemical exfoliation,[85–87] ultrasonic exfoliation[88,89] and solvothermal cutting[90–92] of graphene sheets or graphite materials. Because of their superiority in chemical inertness, biocompatibility,[93] low toxicity,[94] high fluorescent quantum yield (QY_f) up to 65%)[95] and high two-photon absorption cross sections (up to 48000 Göppert-Mayer (GM) units)[96,97], GQDs have potential applications in bioimaging, biosensor and biomolecule/drug delivery. Moreover, through surface passivation and modification, GQDs can either have enhanced photoluminescence property[95] or exhibit photothermal effect[67].

D. Versatile Strategies for Targeted NO Delivery

The long-term goal of photochemical NO delivery is to develop versatile strategies to address the challenges described in Section B: application of appropriate wavelength to have deeper tissue penetration[52,98] and avoid over-heating effect[60] as well as development of methods for precise delivery[47]. Therefore, we are applying NIR sensitive photoNORMs and composites containing NIR photosensitizers and NO donors for NIR light triggered NO release. Additionally, two different targeted delivery strategies are designed and developed for precise NO therapeutics: macrophage-mediated micro-delivery and peptide-modified nano-delivery.

For macrophage-mediated micro-delivery described in Chapter III, we applied polymer microemulsion technique to encapsulate a 794 nm sensitive manganese nitrosyl complex as a photoNORM[54] and Nd^{3+} doped upconverting nanoparticles (Nd-UCNPs) as bioimaging agent[59–62] into biocompatible poly(lactide-co-glycolide) (PLGA) spherical microparticles with ca. 1 micron size.[99–101] Both components can be activated by tissue penetrating NIR light allowing for simultaneous therapeutic NO delivery and photoluminescence (PL) imaging capabilities with a single NIR laser source. Since tumors can send out signals to immune system and recruit monocytes/macrophages to comprise upto 50-70% tumor mass based on wound healing process,[102] the microparticles engulfed by macrophages can be delivered into tumors and release NO upon NIR laser irradiation.

For peptide-modified nano-delivery, we utilized GQDs as a 794 nm light responsive photosensitizer to photothermally trigger NO release[67] from a new chromium (III) dinitrito complex (CrONO). GQDs with carboxylic acid can be covalently bonded with oleylamine to

generate hydrophobic oleyl GQDs via amide coupling and further assemble with biotinylated amphiphilic polyethylene glycol (PEG) lipids via entanglement of long aliphatic chains and van der Waals force to afford 55 nm (avg.) nano-carriers containing lipophilic domains. Hydrophobic CrONO can infuse into these domains[58] and the surface of nano-carriers can be modified with biotinylated cell penetrating peptides (CPPs) via biotin-streptavidin-biotin assembly to enhance penetrating ability to cancer cells.[103]

Through these proof-of-concept investigations, we want to demonstrate NO can be carried into tumor and cancer cells by using designed carriers with different size and versatile delivery strategies. Moreover, we are able to tune the intensity of light to control specific concentration of NO release inside tumors for diverse therapeutic purposes.

E. Reference

(1) Walford, G.; Loscalzo, J. Nitric Oxide in Vascular Biology. *J. Thromb. Haemost.* **2003**, *1* (10), 2112–2118.

(2) Fang, F. C. Perspectives Series: Host/Pathogen Interactions. Mechanisms of Nitric Oxide-Related Antimicrobial Activity. *J. Clin. Invest.* **1997**, *99* (12), 2818–2825.

(3) Bogdan, C. Nitric Oxide and the Immune Response. *Nat. Immunol.* **2001**, *2* (10), 907–916.

(4) Luo, J.; Chen, A. F. Nitric Oxide: A Newly Discovered Function on Wound Healing. *Acta Pharmacol. Sin.* **2005**, *26* (3), 259–264.

(5) Mocellin, S.; Bronte, V.; Nitti, D. Nitric Oxide, a Double Edged Sword in Cancer Biology: Searching for Therapeutic Opportunities. *Med. Res. Rev.* **2007**, *27* (3), 317–352.

(6) Radi, R.; Denicola, A.; Alvarez, B.; Ferrer-Sueta, G.; Rubbo, H. Chapter 4 - The Biological Chemistry of Peroxynitrite. In *Nitric Oxide*; Ignarro, L. J., Ed.; Academic Press: San Diego, 2000; pp 57–82.

(7) Cannon, R. O. Role of Nitric Oxide in Cardiovascular Disease: Focus on the Endothelium. *Clin. Chem.* **1998**, *44* (8), 1809–1819.

(8) Lundberg, J. O.; Gladwin, M. T.; Weitzberg, E. Strategies to Increase Nitric Oxide Signalling in Cardiovascular Disease. *Nat. Rev. Drug Discov.* **2015**, *14* (9), 623–641.

(9) Yetik-Anacak, G.; Catravas, J. D. Nitric Oxide and the Endothelium: History and Impact on Cardiovascular Disease. *Vascul. Pharmacol.* **2006**, *45* (5), 268–276.

(10) Lee, W. H.; Ren, H.; Wu, J.; Novak, O.; Brown, R. B.; Xi, C.; Meyerhoff, M. E. Electrochemically Modulated Nitric Oxide Release From Flexible Silicone Rubber Patch:

Antimicrobial Activity For Potential Wound Healing Applications. *ACS Biomater. Sci. Eng.* **2016**, *2* (9), 1432–1435.

(11) Mihu, M. R.; Cabral, V.; Pattabhi, R.; Tar, M. T.; Davies, K. P.; Friedman, A. J.; Martinez, L. R.; Nosanchuk, J. D. Sustained Nitric Oxide-Releasing Nanoparticles Interfere with Methicillin-Resistant Staphylococcus Aureus Adhesion and Biofilm Formation in a Rat Central Venous Catheter Model. *Antimicrob. Agents Chemother.* **2017**, *61* (1), e02020-16.

(12) Tannous, M.; Labbe, N.; Redmond, R. W.; Mutus, B. A Photo-Activated, Protein-Based, NO/H2O2 Generating System with Tumoricidal Activity Composed of the Nitric Oxide Derivative of Apo-Metallothionein (Thionein-NO) and Glucose Oxidase. *J. Photochem. Photobiol. B* **1997**, *41* (3), 249–254.

(13) Vicetti Miguel, R. D.; Cherpes, T. L.; Watson, L. J.; McKenna, K. C. CTL Induction of Tumoricidal Nitric Oxide Production by Intratumoral Macrophages Is Critical for Tumor Elimination. *J. Immunol. Baltim. Md 1950* **2010**, *185* (11), 6706–6718.

(14) Thomas, D. D.; Liu, X.; Kantrow, S. P.; Lancaster, J. R. The Biological Lifetime of Nitric Oxide: Implications for the Perivascular Dynamics of NO and O2. *Proc. Natl. Acad. Sci.* **2001**, *98* (1), 355–360.

(15) Lancaster, J. R. Simulation of the Diffusion and Reaction of Endogenously Produced Nitric Oxide. *Proc. Natl. Acad. Sci. U. S. A.* **1994**, *91* (17), 8137–8141.

(16) Wang, P. G.; Xian, M.; Tang, X.; Wu, X.; Wen, Z.; Cai, T.; Janczuk, A. J. Nitric Oxide Donors: Chemical Activities and Biological Applications. *Chem. Rev.* **2002**, *102* (4), 1091–1134.

(17) Hitomi, Y.; Iwamoto, Y.; Kodera, M. Electronic Tuning of Nitric Oxide Release from Manganese Nitrosyl Complexes by Visible Light Irradiation: Enhancement of Nitric

Oxide Release Efficiency by the Nitro-Substituted Quinoline Ligand. *Dalton Trans.* **2013**, *43* (5), 2161–2167.

(18) Ramos, L. C. B.; Marchesi, M. S. P.; Callejon, D.; Baruffi, M. D.; Lunardi, C. N.; Slep, L. D.; Bendhack, L. M.; da Silva, R. S. Enhanced Antitumor Activity against Melanoma Cancer Cells by Nitric Oxide Release and Photosensitized Generation of Singlet Oxygen from Ruthenium Complexes. *Eur. J. Inorg. Chem.* **2016**, *2016* (22), 3592–3597.

(19) Pereira, A. de C.; Araújo, A. V.; Paulo, M.; Andrade, F. A. de; Silva, B. R.; Vercesi, J. A.; da Silva, R. S.; Bendhack, L. M. Hypotensive Effect and Vascular Relaxation in Different Arteries Induced by the Nitric Oxide Donor RuBPY. *Nitric Oxide* **2017**, *62*, 11–16.

(20) Cacita, N.; Possato, B.; da Silva, C. F. N.; Paulo, M.; Formiga, A. L. B.; Bendhack, L. M.; Nikolaou, S. Investigation of a Novel Trinuclear μ-Oxo Ruthenium Complex as a Potential Nitric Oxide Releaser for Biological Purposes. *Inorganica Chim. Acta* **2015**, *429*, 114–121.

(21) Liu, J.; Duan, Q.; Wang, J.; Song, Z.; Qiao, X.; Wang, H. Photocontrolled Nitric Oxide Release from Two Nitrosylruthenium Isomer Complexes and Their Potential Biomedical Applications. *J. Biomed. Opt.* **2015**, *20* (1), 015004–015004.

(22) Santana, A. P. M.; Tavares, B. M.; Lucetti, L. T.; Gouveia Jr., F. S.; Ribeiro, R. A.; Soares, P. M. G.; Sousa, E. H. S.; Lopes, L. G. F.; Medeiros, J.-V. R.; Souza, M. H. L. P. The Nitric Oxide Donor Cis-[Ru(bpy)2(SO3)NO](PF6) Increases Gastric Mucosa Protection in Mice – Involvement of the Soluble Guanylate Cyclase/KATP Pathway. *Nitric Oxide* **2015**, *45*, 35–42.

(23) Garcia, J. V.; Yang, J.; Shen, D.; Yao, C.; Li, X.; Wang, R.; Stucky, G. D.; Zhao, D.; Ford, P. C.; Zhang, F. NIR-Triggered Release of Caged Nitric Oxide Using Upconverting Nanostructured Materials. *Small* **2012**, *8* (24), 3800–3805.

(24) Works, C. F.; Jocher, C. J.; Bart, G. D.; Bu, X.; Ford, P. C. Photochemical Nitric Oxide Precursors: Synthesis, Photochemistry, and Ligand Substitution Kinetics of Ruthenium Salen Nitrosyl and Ruthenium Salophen Nitrosyl Complexes1. *Inorg. Chem.* **2002**, *41* (14), 3728–3739.

(25) Works, C. F.; Ford, P. C. Photoreactivity of the Ruthenium Nitrosyl Complex, Ru(salen)(Cl)(NO). Solvent Effects on the Back Reaction of NO with the Lewis Acid RuIII(salen)(Cl)1. *J. Am. Chem. Soc.* **2000**, *122* (31), 7592–7593.

(26) Mase, J. D.; Razgoniaev, A. O.; Tschirhart, M. K.; Ostrowski, A. D. Light-Controlled Release of Nitric Oxide from Solid Polymer Composite Materials Using Visible and near Infra-Red Light. *Photochem. Photobiol. Sci.* **2015**, *14* (4), 775–785.

(27) DeRosa, F.; Bu, X.; Ford, P. C. Chromium(III) Complexes for Photochemical Nitric Oxide Generation from Coordinated Nitrite: Synthesis and Photochemistry of Macrocyclic Complexes with Pendant Chromophores, Trans-[Cr(L)(ONO)2]BF4. *Inorg. Chem.* **2005**, *44* (12), 4157–4165.

(28) Ostrowski, A. D.; Lin, B. F.; Tirrell, M. V.; Ford, P. C. Liposome Encapsulation of a Photochemical NO Precursor for Controlled Nitric Oxide Release and Simultaneous Fluorescence Imaging. *Mol. Pharm.* **2012**, *9* (10), 2950–2955.

(29) Ostrowski, A. D.; Deakin, S. J.; Azhar, B.; Miller, T. W.; Franco, N.; Cherney, M. M.; Lee, A. J.; Burstyn, J. N.; Fukuto, J. M.; Megson, I. L.; Ford, P. C. Nitric Oxide Photogeneration from Trans-Cr(cyclam)(ONO)2+ in a Reducing Environment. Activation of

Soluble Guanylyl Cyclase and Arterial Vasorelaxation. *J. Med. Chem.* **2010**, *53* (2), 715–722.

(30) Ostrowski, A. D.; Absalonson, R. O.; Leo, M. A. D.; Wu, G.; Pavlovich, J. G.; Adamson, J.; Azhar, B.; Iretskii, A. V.; Megson, I. L.; Ford, P. C. Photochemistry of Trans-Cr(cyclam)(ONO)2+, a Nitric Oxide Precursor. *Inorg. Chem.* **2011**, *50* (10), 4453–4462.

(31) DeLeo, M. A.; Ford, P. C. Photoreactions of Coordinated Nitrite Ion. Reversible Nitric Oxide Labilization from the chromium(III) Complex [Trans-Cr(cyclam)(ONO)2]+. *Coord. Chem. Rev.* **2000**, *208* (1), 47–59.

(32) De Leo, M.; Ford, P. C. Reversible Photolabilization of NO from Chromium(III)-Coordinated Nitrite. A New Strategy for Nitric Oxide Delivery. *J. Am. Chem. Soc.* **1999**, *121* (9), 1980–1981.

(33) De Leo, M. A.; Bu, X.; Bentow, J.; Ford, P. C. The Synthesis, Characterization and Structures of the chromium(III) Dinitrito Complexes: Trans-[Cr(L)(ONO)2]+ (L=1,4,8,11-Tetraazacyclotetradecane or 5,7,7,12,14,14-Hexamethyl-1,4,8,11-Tetraazacyclotetradecane). *Inorganica Chim. Acta* **2000**, *300–302*, 944–950.

(34) Soto, R. J.; Yang, L.; Schoenfisch, M. H. Functionalized Mesoporous Silica via an Aminosilane Surfactant Ion Exchange Reaction: Controlled Scaffold Design and Nitric Oxide Release. *ACS Appl. Mater. Interfaces* **2016**, *8* (3), 2220–2231.

(35) Choi, H. W.; Kim, J.; Kim, J.; Kim, Y.; Song, H. B.; Kim, J. H.; Kim, K.; Kim, W. J. Light-Induced Acid Generation on a Gatekeeper for Smart Nitric Oxide Delivery. *ACS Nano* **2016**, *10* (4), 4199–4208.

(36) Ko, H. M.; Joo, S. H.; Jo, J. H.; Park, W. S.; Jung, W. Y.; Shin, J. H.; Ahn, H. J. Liver-Wrapping, Nitric Oxide-Releasing Nanofiber Downregulates Cleaved Caspase-3 and

Bax Expression on Rat Hepatic Ischemia-Reperfusion Injury. *Transplant. Proc.* **2017**, *49* (5), 1170–1174.

(37) Lu, Y.; Slomberg, D. L.; Schoenfisch, M. H. Nitric Oxide-Releasing Chitosan Oligosaccharides as Antibacterial Agents. *Biomaterials* **2014**, *35* (5), 1716–1724.

(38) Reighard, K. P.; Ehre, C.; Rushton, Z. L.; Ahonen, M. J. R.; Hill, D. B.; Schoenfisch, M. H. Role of Nitric Oxide-Releasing Chitosan Oligosaccharides on Mucus Viscoelasticity. *ACS Biomater. Sci. Eng.* **2017**, *3* (6), 1017–1026.

(39) Goudie, M. J.; Brainard, B. M.; Schmiedt, C. W.; Handa, H. Characterization and in Vivo Performance of Nitric Oxide-Releasing Extracorporeal Circuits in a Feline Model of Thrombogenicity. *J. Biomed. Mater. Res. A* **2017**, *105* (2), 539–546.

(40) Xu, L.-C.; Wo, Y.; Meyerhoff, M. E.; Siedlecki, C. A. Inhibition of Bacterial Adhesion and Biofilm Formation by Dual Functional Textured and Nitric Oxide Releasing Surfaces. *Acta Biomater.* **2017**, *51*, 53–65.

(41) Neufeld, M. J.; Lutzke, A.; Tapia, J. B.; Reynolds, M. M. Metal–Organic Framework/Chitosan Hybrid Materials Promote Nitric Oxide Release from S-Nitrosoglutathione in Aqueous Solution. *ACS Appl. Mater. Interfaces* **2017**, *9* (6), 5139–5148.

(42) Lutzke, A.; Neufeld, B. H.; Neufeld, M. J.; Reynolds, M. M. Nitric Oxide Release from a Biodegradable Cysteine-Based Polyphosphazene. *J. Mater. Chem. B* **2016**, *4* (11), 1987–1998.

(43) Pelegrino, M. T.; Silva, L. C.; Watashi, C. M.; Haddad, P. S.; Rodrigues, T.; Seabra, A. B. Nitric Oxide-Releasing Nanoparticles: Synthesis, Characterization, and Cytotoxicity to Tumorigenic Cells. *J. Nanoparticle Res.* **2017**, *19* (2), 57.

(44) Wo, Y.; Brisbois, E. J.; Wu, J.; Li, Z.; Major, T. C.; Mohammed, A.; Wang, X.; Colletta, A.; Bull, J. L.; Matzger, A. J.; Xi, C.; Bartlett, R. H.; Meyerhoff, M. E. Reduction of Thrombosis and Bacterial Infection via Controlled Nitric Oxide (NO) Release from S-Nitroso-N-Acetylpenicillamine (SNAP) Impregnated CarboSil Intravascular Catheters. *ACS Biomater. Sci. Eng.* **2017**, *3* (3), 349–359.

(45) Lourenço, S. D. M.; de Oliveira, M. G. Topical Photochemical Nitric Oxide Release from Porous Poly(vinyl Alcohol) Membrane for Visible Light Modulation of Dermal Vasodilation. *J. Photochem. Photobiol. Chem.* **2017**, *346*, 548–558.

(46) Pant, J.; Goudie, M. J.; Hopkins, S. P.; Brisbois, E. J.; Handa, H. Tunable Nitric Oxide Release from S-Nitroso-N-Acetylpenicillamine via Catalytic Copper Nanoparticles for Biomedical Applications. *ACS Appl. Mater. Interfaces* **2017**, *9* (18), 15254–15264.

(47) Ford, P. C. Photochemical Delivery of Nitric Oxide. *Nitric Oxide* **2013**, *34*, 56–64.

(48) Ford, P. C. Polychromophoric Metal Complexes for Generating the Bioregulatory Agent Nitric Oxide by Single- and Two-Photon Excitation. *Acc. Chem. Res.* **2008**, *41* (2), 190–200.

(49) Krasuski, R. A.; Warner, J. J.; Wang, A.; Harrison, J. K.; Tapson, V. F.; Bashore, T. M. Inhaled Nitric Oxide Selectively Dilates Pulmonary Vasculature in Adult Patients with Pulmonary Hypertension, Irrespective of Etiology. *J. Am. Coll. Cardiol.* **2000**, *36* (7), 2204–2211.

(50) Wink, D. A.; Mitchell, J. B. Chemical Biology of Nitric Oxide: Insights into Regulatory, Cytotoxic, and Cytoprotective Mechanisms of Nitric Oxide. *Free Radic. Biol. Med.* **1998**, *25* (4–5), 434–456.

(51) Bourassa, J.; DeGraff, W.; Kudo, S.; Wink, D. A.; Mitchell, J. B.; Ford, P. C. Photochemistry of Roussin's Red Salt, Na2[Fe2S2(NO)4], and of Roussin's Black Salt,

NH4[Fe4S3(NO)7]. In Situ Nitric Oxide Generation To Sensitize γ-Radiation Induced Cell Death1. *J. Am. Chem. Soc.* **1997**, *119* (12), 2853–2860.

(52) König, K. Multiphoton Microscopy in Life Sciences. *J. Microsc.* **2000**, *200* (2), 83–104.

(53) Jacques, S. L. Optical Properties of Biological Tissues: A Review. *Phys. Med. Biol.* **2013**, *58* (11), R37.

(54) Hitomi, Y.; Iwamoto, Y.; Kodera, M. Electronic Tuning of Nitric Oxide Release from Manganese Nitrosyl Complexes by Visible Light Irradiation: Enhancement of Nitric Oxide Release Efficiency by the Nitro-Substituted Quinoline Ligand. *Dalton Trans.* **2013**, *43* (5), 2161–2167.

(55) Eroy-Reveles, A. A.; Leung, Y.; Beavers, C. M.; Olmstead, M. M.; Mascharak, P. K. Near-Infrared Light Activated Release of Nitric Oxide from Designed Photoactive Manganese Nitrosyls: Strategy, Design, and Potential as NO Donors. *J. Am. Chem. Soc.* **2008**, *130* (13), 4447–4458.

(56) Burks, P. T.; Garcia, J. V.; GonzalezIrias, R.; Tillman, J. T.; Niu, M.; Mikhailovsky, A. A.; Zhang, J.; Zhang, F.; Ford, P. C. Nitric Oxide Releasing Materials Triggered by Near-Infrared Excitation Through Tissue Filters. *J. Am. Chem. Soc.* **2013**, *135* (48), 18145–18152.

(57) Pierri, A. E.; Huang, P.-J.; Garcia, J. V.; Stanfill, J. G.; Chui, M.; Wu, G.; Zheng, N.; Ford, P. C. A photoCORM Nanocarrier for CO Release Using NIR Light. *Chem. Commun.* **2015**, *51* (11), 2072–2075.

(58) Pierri, A. E.; Huang, P.-J.; Garcia, J. V.; Stanfill, J. G.; Chui, M.; Wu, G.; Zheng, N.; Ford, P. C. A photoCORM Nanocarrier for CO Release Using NIR Light. *Chem. Commun.* **2015**, *51* (11), 2072–2075.

(59) Xie, X.; Gao, N.; Deng, R.; Sun, Q.; Xu, Q.-H.; Liu, X. Mechanistic Investigation of Photon Upconversion in Nd3+-Sensitized Core–Shell Nanoparticles. *J. Am. Chem. Soc.* **2013**, *135* (34), 12608–12611.

(60) Wang, Y.-F.; Liu, G.-Y.; Sun, L.-D.; Xiao, J.-W.; Zhou, J.-C.; Yan, C.-H. Nd3+-Sensitized Upconversion Nanophosphors: Efficient In Vivo Bioimaging Probes with Minimized Heating Effect. *ACS Nano* **2013**, *7* (8), 7200–7206.

(61) Zhao, Y.; Zhan, Q.; Liu, J.; He, S. Optically Investigating Nd3+-Yb3+ Cascade Sensitized Upconversion Nanoparticles for High Resolution, Rapid Scanning, Deep and Damage-Free Bio-Imaging. *Biomed. Opt. Express* **2015**, *6* (3), 838–848.

(62) Bednarkiewicz, A.; Wawrzynczyk, D.; Nyk, M.; Strek, W. Synthesis and Spectral Properties of Colloidal Nd3+ Doped NaYF4 Nanocrystals. *Opt. Mater.* **2011**, *33* (10), 1481–1486.

(63) Johnson, N. J. J.; He, S.; Diao, S.; Chan, E. M.; Dai, H.; Almutairi, A. Direct Evidence for Coupled Surface and Concentration Quenching Dynamics in Lanthanide-Doped Nanocrystals. *J. Am. Chem. Soc.* **2017**, *139* (8), 3275–3282.

(64) Levy, E. S.; Morales, D. P.; Garcia, J. V.; Reich, N. O.; Ford, P. C. Near-IR Mediated Intracellular Uncaging of NO from Cell Targeted Hollow Gold Nanoparticles. *Chem. Commun.* **2015**, *51* (100), 17692–17695.

(65) Fowley, C.; McHale, A. P.; McCaughan, B.; Fraix, A.; Sortino, S.; Callan, J. F. Carbon Quantum dot–NO Photoreleaser Nanohybrids for Two-Photon Phototherapy of Hypoxic Tumors. *Chem. Commun.* **2014**, *51* (1), 81–84.

(66) He, Q.; Kiesewetter, D. O.; Qu, Y.; Fu, X.; Fan, J.; Huang, P.; Liu, Y.; Zhu, G.; Liu, Y.; Qian, Z.; Chen, X. NIR-Responsive On-Demand Release of CO from Metal Carbonyl-Caged Graphene Oxide Nanomedicine. *Adv. Mater.* **2015**, *27* (42), 6741–6746.

(67) Guo, M.; Xiang, H.-J.; Wang, Y.; Zhang, Q.-L.; An, L.; Yang, S.-P.; Ma, Y.; Wang, Y.; Liu, J.-G. Ruthenium Nitrosyl Functionalized Graphene Quantum Dots as an Efficient Nanoplatform for NIR-Light-Controlled and Mitochondria-Targeted Delivery of Nitric Oxide Combined with Photothermal Therapy. *Chem. Commun.* **2017**, *53* (22), 3253–3256.

(68) Haase, M.; Schäfer, H. Upconverting Nanoparticles. *Angew. Chem. Int. Ed.* **2011**, *50* (26), 5808–5829.

(69) Chen, G.; Qiu, H.; Prasad, P. N.; Chen, X. Upconversion Nanoparticles: Design, Nanochemistry, and Applications in Theranostics. *Chem. Rev.* **2014**, *114* (10), 5161–5214.

(70) M. Chan, E. Combinatorial Approaches for Developing Upconverting Nanomaterials: High-Throughput Screening, Modeling, and Applications. *Chem. Soc. Rev.* **2015**, *44* (6), 1653–1679.

(71) Heer, S.; Kömpe, K.; Güdel, H.-U.; Haase, M. Highly Efficient Multicolour Upconversion Emission in Transparent Colloids of Lanthanide-Doped NaYF4 Nanocrystals. *Adv. Mater.* **2004**, *16* (23–24), 2102–2105.

(72) Wang, F.; Han, Y.; Lim, C. S.; Lu, Y.; Wang, J.; Xu, J.; Chen, H.; Zhang, C.; Hong, M.; Liu, X. Simultaneous Phase and Size Control of Upconversion Nanocrystals through Lanthanide Doping. *Nature* **2010**, *463* (7284), 1061–1065.

(73) Yi, G. S.; Chow, G. M. Synthesis of Hexagonal-Phase NaYF4:Yb,Er and NaYF4:Yb,Tm Nanocrystals with Efficient Up-Conversion Fluorescence. *Adv. Funct. Mater.* **2006**, *16* (18), 2324–2329.

(74) Li, X.; Zhang, F.; Zhao, D. Lab on Upconversion Nanoparticles: Optical Properties and Applications Engineering via Designed Nanostructure. *Chem. Soc. Rev.* **2015**, *44* (6), 1346–1378.

(75) Xu, X.; Ray, R.; Gu, Y.; Ploehn, H. J.; Gearheart, L.; Raker, K.; Scrivens, W. A. Electrophoretic Analysis and Purification of Fluorescent Single-Walled Carbon Nanotube Fragments. *J. Am. Chem. Soc.* **2004**, *126* (40), 12736–12737.

(76) Zhu, S.; Song, Y.; Zhao, X.; Shao, J.; Zhang, J.; Yang, B. The Photoluminescence Mechanism in Carbon Dots (Graphene Quantum Dots, Carbon Nanodots, and Polymer Dots): Current State and Future Perspective. *Nano Res.* **2015**, *8* (2), 355–381.

(77) Shamsipur, M.; Barati, A.; Karami, S. Long-Wavelength, Multicolor, and White-Light Emitting Carbon-Based Dots: Achievements Made, Challenges Remaining, and Applications. *Carbon* **2017**, *124* (Supplement C), 429–472.

(78) Liu, H.; Ye, T.; Mao, C. Fluorescent Carbon Nanoparticles Derived from Candle Soot. *Angew. Chem. Int. Ed.* **2007**, *46* (34), 6473–6475.

(79) Souza, D. R. da S.; Mesquita, J. P. de; Lago, R. M.; Caminhas, L. D.; Pereira, F. V. Cellulose Nanocrystals: A Versatile Precursor for the Preparation of Different Carbon Structures and Luminescent Carbon Dots. *Ind. Crops Prod.* **2016**, *93*, 121–128.

(80) Briscoe, J.; Marinovic, A.; Sevilla, M.; Dunn, S.; Titirici, M. Biomass-Derived Carbon Quantum Dot Sensitizers for Solid-State Nanostructured Solar Cells. *Angew. Chem. Int. Ed.* **2015**, *54* (15), 4463–4468.

(81) Peng, H.; Li, Y.; Jiang, C.; Luo, C.; Qi, R.; Huang, R.; Duan, C.-G.; Travas-Sejdic, J. Tuning the Properties of Luminescent Nitrogen-Doped Carbon Dots by Reaction Precursors. *Carbon* **2016**, *100*, 386–394.

(82) Jiang, K.; Sun, S.; Zhang, L.; Lu, Y.; Wu, A.; Cai, C.; Lin, H. Red, Green, and Blue Luminescence by Carbon Dots: Full-Color Emission Tuning and Multicolor Cellular Imaging. *Angew. Chem. Int. Ed.* **2015**, *54* (18), 5360–5363.

(83) Bacon, M.; Bradley, S. J.; Nann, T. Graphene Quantum Dots. *Part. Part. Syst. Charact.* **2014**, *31* (4), 415–428.

(84) Sun, Y.; Wang, S.; Li, C.; Luo, P.; Tao, L.; Wei, Y.; Shi, G. Large Scale Preparation of Graphene Quantum Dots from Graphite with Tunable Fluorescence Properties. *Phys. Chem. Chem. Phys.* **2013**, *15* (24), 9907–9913.

(85) Ming, H.; Ma, Z.; Liu, Y.; Pan, K.; Yu, H.; Wang, F.; Kang, Z. Large Scale Electrochemical Synthesis of High Quality Carbon Nanodots and Their Photocatalytic Property. *Dalton Trans.* **2012**, *41* (31), 9526–9531.

(86) Lu, J.; Yang, J.; Wang, J.; Lim, A.; Wang, S.; Loh, K. P. One-Pot Synthesis of Fluorescent Carbon Nanoribbons, Nanoparticles, and Graphene by the Exfoliation of Graphite in Ionic Liquids. *ACS Nano* **2009**, *3* (8), 2367–2375.

(87) Lee, S.-H.; Seo, S.-D.; Jin, Y.-H.; Shim, H.-W.; Kim, D.-W. A Graphite Foil Electrode Covered with Electrochemically Exfoliated Graphene Nanosheets. *Electrochem. Commun.* **2010**, *12* (10), 1419–1422.

(88) Liu, F.; Jang, M.-H.; Ha, H. D.; Kim, J.-H.; Cho, Y.-H.; Seo, T. S. Facile Synthetic Method for Pristine Graphene Quantum Dots and Graphene Oxide Quantum Dots: Origin of Blue and Green Luminescence. *Adv. Mater.* **2013**, *25* (27), 3657–3662.

(89) Jang, M.-H.; Ha, H. D.; Lee, E.-S.; Liu, F.; Kim, Y.-H.; Seo, T. S.; Cho, Y.-H. Is the Chain of Oxidation and Reduction Process Reversible in Luminescent Graphene Quantum Dots? *Small* **2015**, *11* (31), 3773–3781.

(90) Pan, D.; Guo, L.; Zhang, J.; Xi, C.; Xue, Q.; Huang, H.; Li, J.; Zhang, Z.; Yu, W.; Chen, Z.; Li, Z.; Wu, M. Cutting sp2clusters in Graphene Sheets into Colloidal Graphene Quantum Dots with Strong Green Fluorescence. *J. Mater. Chem.* **2012**, *22* (8), 3314–3318.

(91) Pan, D.; Zhang, J.; Li, Z.; Wu, M. Hydrothermal Route for Cutting Graphene Sheets into Blue-Luminescent Graphene Quantum Dots. *Adv. Mater.* **2010**, *22* (6), 734–738.

(92) Kwon, W.; Kim, Y.-H.; Lee, C.-L.; Lee, M.; Choi, H. C.; Lee, T.-W.; Rhee, S.-W. Electroluminescence from Graphene Quantum Dots Prepared by Amidative Cutting of Tattered Graphite. *Nano Lett.* **2014**, *14* (3), 1306–1311.

(93) Nurunnabi, M.; Khatun, Z.; Nafiujjaman, M.; Lee, D.; Lee, Y. Surface Coating of Graphene Quantum Dots Using Mussel-Inspired Polydopamine for Biomedical Optical Imaging. *ACS Appl. Mater. Interfaces* **2013**, *5* (16), 8246–8253.

(94) Zhao, Y.; Liu, Q.; Shakoor, S.; Gong, J. R.; Wang, D. Transgenerational Safety of Nitrogen-Doped Graphene Quantum Dots and the Underlying Cellular Mechanism in Caenorhabditis Elegans. *Toxicol. Res.* **2015**, *4* (2), 270–280.

(95) Feng, L.; Tang, X.-Y.; Zhong, Y.-X.; Liu, Y.-W.; Song, X.-H.; Deng, S.-L.; Xie, S.-Y.; Yan, J.-W.; Zheng, L.-S. Ultra-Bright Alkylated Graphene Quantum Dots. *Nanoscale* **2014**, *6* (21), 12635–12643.

(96) Kuo, W.-S.; Chang, C.-Y.; Chen, H.-H.; Hsu, C.-L. L.; Wang, J.-Y.; Kao, H.-F.; Chou, L. C.-S.; Chen, Y.-C.; Chen, S.-J.; Chang, W.-T.; Tseng, S.-W.; Wu, P.-C.; Pu, Y.-C. Two-Photon Photoexcited Photodynamic Therapy and Contrast Agent with Antimicrobial Graphene Quantum Dots. *ACS Appl. Mater. Interfaces* **2016**, *8* (44), 30467–30474.

(97) Liu, Q.; Guo, B.; Rao, Z.; Zhang, B.; Gong, J. R. Strong Two-Photon-Induced Fluorescence from Photostable, Biocompatible Nitrogen-Doped Graphene Quantum Dots for Cellular and Deep-Tissue Imaging. *Nano Lett.* **2013**, *13* (6), 2436–2441.

(98) Weissleder, R. A Clearer Vision for in Vivo Imaging. *Nat. Biotechnol.* **2001**, *19* (4), 316–317.

(99) Park, T. G.; Yong Lee, H.; Sung Nam, Y. A New Preparation Method for Protein Loaded Poly(d,l-Lactic-Co-Glycolic Acid) Microspheres and Protein Release Mechanism Study. *J. Controlled Release* **1998**, *55* (2–3), 181–191.

(100) Zambaux, M. F.; Bonneaux, F.; Gref, R.; Maincent, P.; Dellacherie, E.; Alonso, M. J.; Labrude, P.; Vigneron, C. Influence of Experimental Parameters on the Characteristics of Poly(lactic Acid) Nanoparticles Prepared by a Double Emulsion Method. *J. Controlled Release* **1998**, *50* (1–3), 31–40.

(101) Champion, J. A.; Katare, Y. K.; Mitragotri, S. Particle Shape: A New Design Parameter for Micro- and Nanoscale Drug Delivery Carriers. *J. Controlled Release* **2007**, *121* (1–2), 3–9.

(102) Choi, M.-R.; Stanton-Maxey, K. J.; Stanley, J. K.; Levin, C. S.; Bardhan, R.; Akin, D.; Badve, S.; Sturgis, J.; Robinson, J. P.; Bashir, R.; Halas, N. J.; Clare, S. E. A Cellular Trojan Horse for Delivery of Therapeutic Nanoparticles into Tumors. *Nano Lett.* **2007**, *7* (12), 3759–3765.

(103) Braun, G. B.; Friman, T.; Pang, H.-B.; Pallaoro, A.; de Mendoza, T. H.; Willmore, A.-M. A.; Kotamraju, V. R.; Mann, A. P.; She, Z.-G.; Sugahara, K. N.; Reich, N. O.; Teesalu, T.; Ruoslahti, E. Etchable Plasmonic Nanoparticle Probes to Image and Quantify Cellular Internalization. *Nat. Mater.* **2014**, *13* (9), 904–911.

Chapter II. The Synthesis

A. Materials

Section C&D: Benzylideneacetone (98%) was purchased from Alfa Aesar. Ethylenediamine (anhydrous) was purchased from TCI. Potassium carbonate (anhydrous) was purchased Fisher Scientific. Sodium borohydride, 1-(triphenylphosphoranylidene)-2-propanone, 3-nitrobenzaldehyde, chromium(III) chloride tetrahydrofuran complex (1:3), sodium nitrite and sodium tetraphenylborate were purchased from Sigma-Aldrich. Sodium tetrafluoroborate (technical grade) was purchased from Baker&Adamson.

Section E: Sodium tetraphenylborate, sodium trifluoroacetate, sodium oleate, ammonium fluoride, lanthanide chlorides (99.9+%), oleic acid (OA) (90%), 1-octadecene (ODE) (90%) were purchased from Sigma-Aldrich.

Section G: Poly(vinyl) alcohol (PVA, Mw: 13000-23000), 4-morpholineethanesulfonic acid (MES, low moisture content, 99+%), immunoglobulin G (IgG from mouse serum), N-(3-dimethylaminopropyl)-N′-ethylcarbodiimide hydrochloride (EDC•HCl, commercial grade), sodium hydroxide (NaOH, ACS reagent grade) were purchased from Sigma-Aldrich. Poly(lactic-co-glycolic acid) (5050 DLG 8A, acid terminated) was purchased from Lakeshore Biomaterials. N-hydroxysuccinimide (NHS) was purchased from Pierce.

Section H: Potassium permanganate (reagent grade) was purchased from Baker&Adamson, reagent). Phosphorus pentoxide was purchased from Fisher Scientific. Sulfuric acid, hydrochloric acid, dimethylformamide, hydrogen peroxide were purchased

from EMD. Graphite nanoparticles and graphene nanopowder (1-5nm) were purchased from SkySpring Nanomaterials.

B. Analytical Instrumentation

Absorbance spectra were taken on a Shimadzu UV-2401PC. Infrared spectra were taken using a Mattson Research Series FTIR. Fluorescence spectra were measured on a PTI fluorimeter equipped with a Hammamatsu R928P PMT. Nitric oxide was measured using a General Electric Sievers Nitric Oxide Analyzer NOA 280i. Samples were photolyzed with a 3 watt 798 nm SheauPac fiber coupled laser module (actual excitation wavelength: 794 nm) or a 451 nm royal blue LED. NMR spectra were obtained on Varian 400 MHz or 500 MHz spectrometers. ESI-MS spectra were taken on a QTOF2 mass spectrometer (Waters Corporation). XRD spectra were obtained on a Bruker AXS D8 Discover GADDS X-Ray diffractometer (XRD). TEM images were obtained on a FEI Titan 300 kV FEG Transmission electron microscope. SEM images were obtained on a FEI Nova Nano 650 FEG scanning electron microscope. AFM images were obtained on an Agilent 5500 atomic force microscope (Agilent Technologies) in tapping mode. X-ray photoelectron spectroscopy (XPS) was performed on a Quantum 2000 spectrometer, and the Al-Kα line was used as the excitation source.

C. Tetraaza-macrocyclic Ligands

C -1. Ligand Design and Synthesis

The advantage of photo-triggered drug delivery is that biological active component can be released upon light exposure to achieve precisely-controlling the dosage, location and timing of drug release in targeted sites.[1] However, if these photosensitive pro-drugs leak out from their carriers during the transportation in the blood circulatory system and diffuse into skin tissues and eyes, it may cause patients who expose to ambient light to have side effect due to unexpected release of photosensitive drugs. Therefore, in order to address potential drug leakage from the polymeric carriers we developed, a hydrophobic ligand 5,12-dimethyl-7,14-diphenyl-1,4,8,11-tetraazacyclotetradecane (PetA, **3**), was synthesized by a modification of a published procedure.[2] Compared to 1,4,8,11-tetraazacyclotetradecane (cyclam)[3] and 5,5,7,12,12,14-hexamethyl-1,4,8,11-tetraazacyclotetradecane (TetA)[4–6], the PetA ligand has intrinsically higher hydrophobicity due to introduction of two phenyl rings on the macrocyclic structure. (**Figure II-C-1**) The brief synthetic procedure of PetA analogue involves the reaction of the E form of a α-β unsaturated ketone such as benzylideneacetone with ethylenediamine to form a 14-member ring tetraaza-macrocyclic ligand with two diimine groups. (**Scheme II-C-1**) This unreduced ligand (PetA-diene) is moisture sensitive due to ring strain in its macrocyclic structure and would irreversibly decompose into two fragments with more stable π-conjugated structure via retro-Michael reaction.[7] (**Scheme II-C-2**) However, once these two diimines are reduced with sodium tetrahydroborate ($NaBH_4$) to generate tetraazacyclotetradecane, the PetA ligand becomes stable toward hydrolysis.

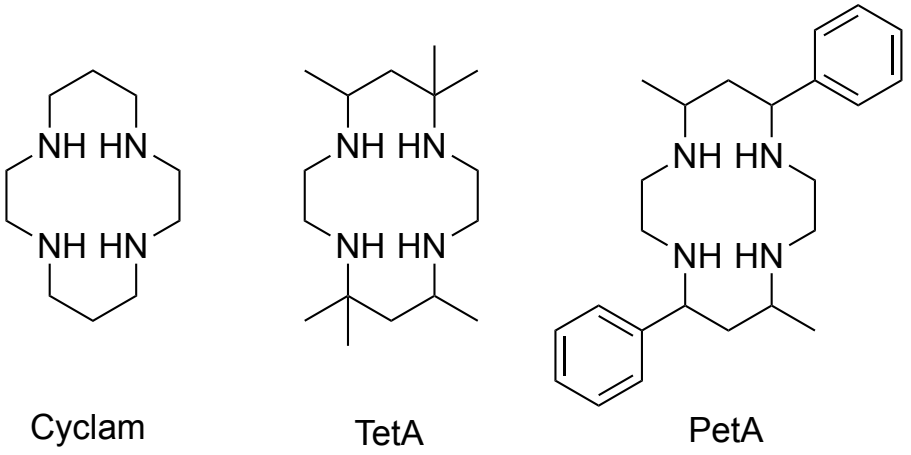

Figure II-C-1. Three different 14-member ring tetraazamacrocyclic ligands.

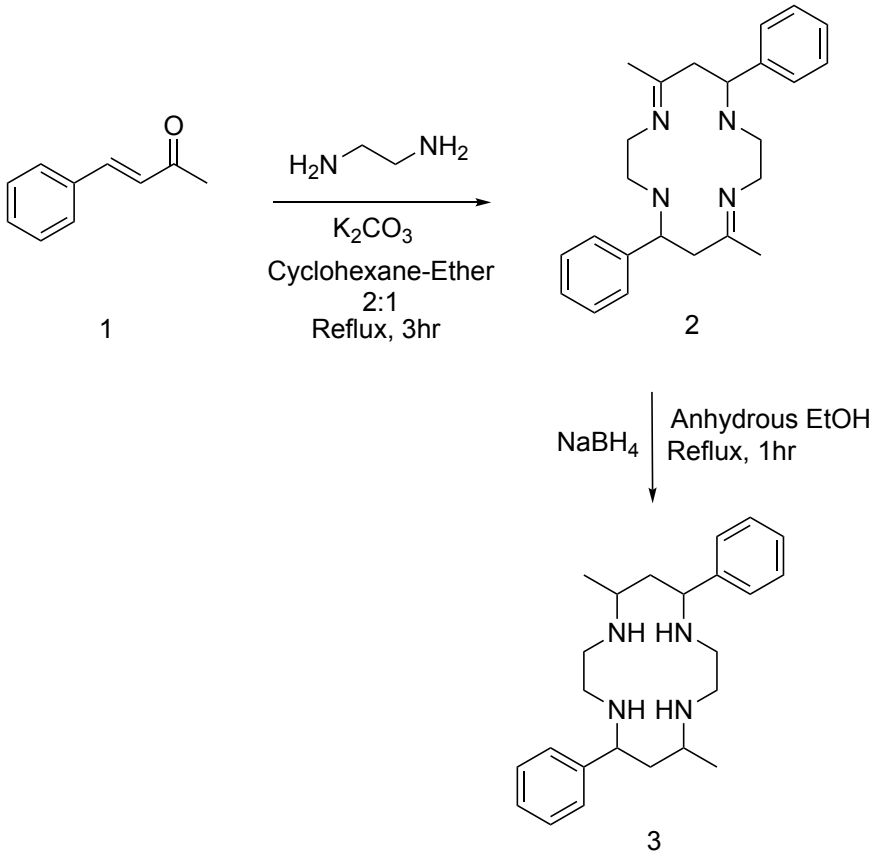

Scheme II-C-1. The synthetic pathway of PetA ligand (**3**).

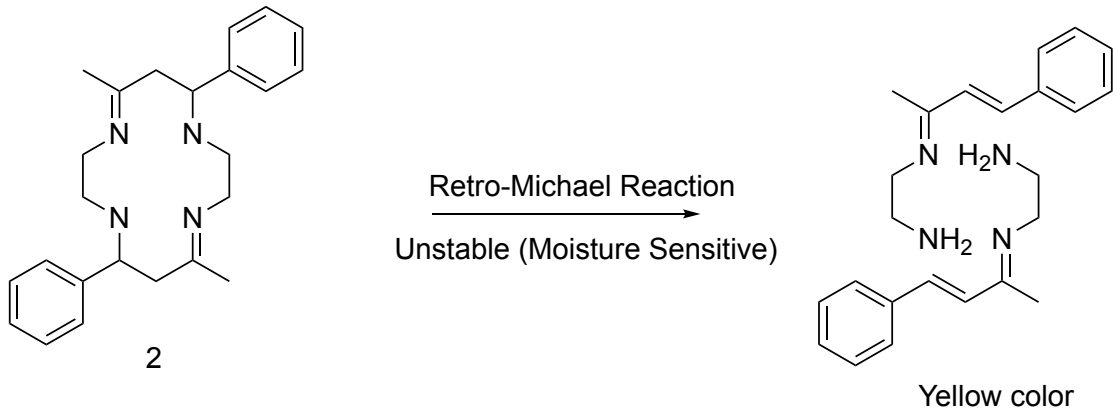

Scheme II-C-2. The decomposition of PetA-diene (**2**).

Moreover, in order to increase the variability of the products from the coupling reactions for PetA, different functional groups such as hydroxyl (-OH) and amine (-NH_2) can be introduced to its phenyl ring via general synthetic strategies for various (E)-4-(substituted phenyl) but-3-en-2-one.[8] (**Scheme II-C-3**) However, commercial aminobenzaldehydes are too expensive to be applied in large-scale synthesis. Hence, a nitro group was used as a precursor of amine functional group and the (E)-4-(3-nitrophenyl) but-3-en-2-one (**1"**) was prepared by Wittig reaction. (**Scheme II-C-4**) The 5,12-dimethyl-7,14-bis(3-nitrophenyl)-1,4,8,11-tetraazacyclotetradecane (NitroPetA, **3"**) was synthesized by following the procedure similar to that used for the PetA synthesis. (**Scheme II-C-5**) However, the NitroPetA-diene ligand (**2"**) is very unstable compared to PetA-diene (**2**), and it even decomposes in deuterium chloroform ($CDCl_3$) in 3 min. The possible reason for the decomposition is that the nitro groups on the phenyl rings as electron-withdrawing groups can stabilize π electrons on the π-conjugated system of decomposed fragments. Therefore, if some electron-donating groups such as hydroxyl (-OH) and amine (-NH_2) are used instead of nitro group (-NO_2), it would greatly enhance the stability of the PetA-diene analogues and increase the production yield. According to the crystal structure of NitroPetA (**Figure II-C-**

2), it has a symmetrical structure with R, R, S, S configuration as same as PetA ligand.[9,10] Additionally, the circular dichroism spectrum shows this molecule has no chirality. (**Figure II-C-3**)

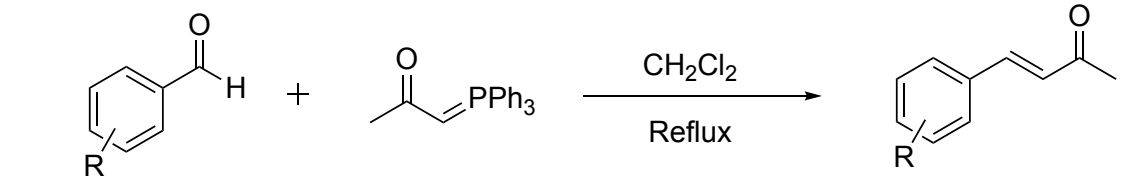

R= -OH, -NH_2, -NO_2 …et al.

Scheme II-C-3. The general synthetic strategy for (E)-4-(substituted phenyl)but-3-en-2-one.

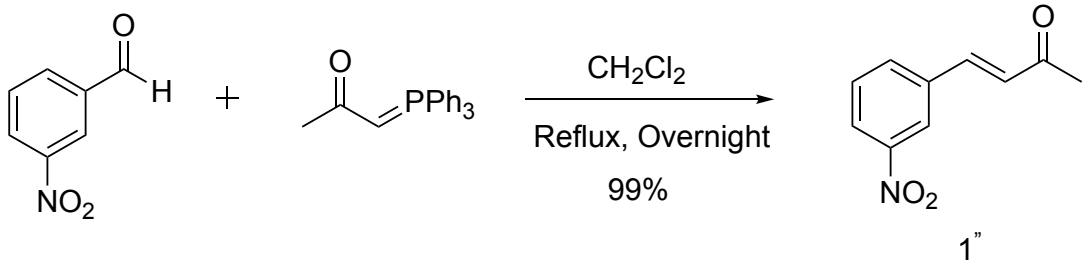

Scheme II-C-4. The synthetic pathway of (E)-4-(3-nitrophenyl) but-3-en-2-one (**1"**).

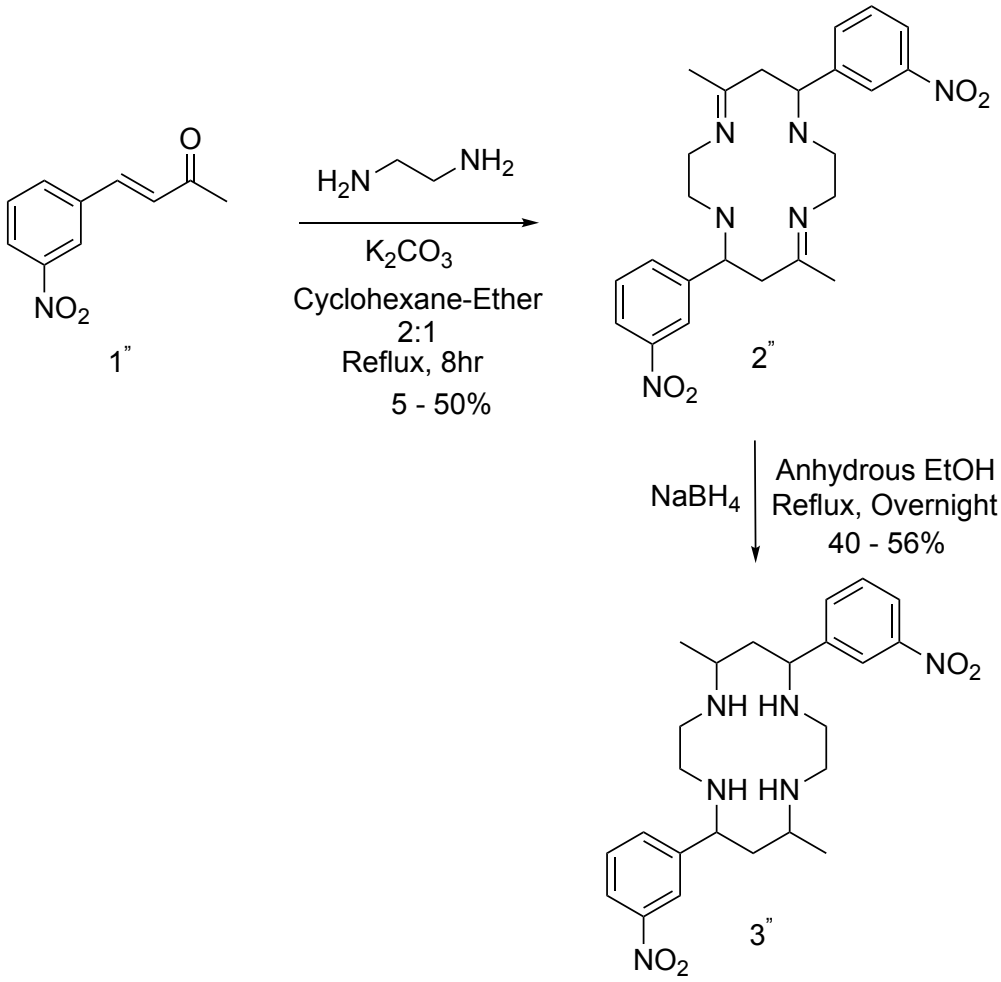

Scheme II-C-5. The synthetic pathway of NitroPetA ligand (**3"**).

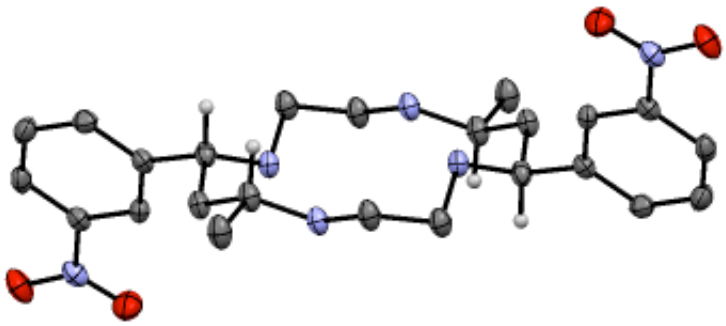

Figure II-C-2. The crystal structure of NitroPetA ligand (**3"**)

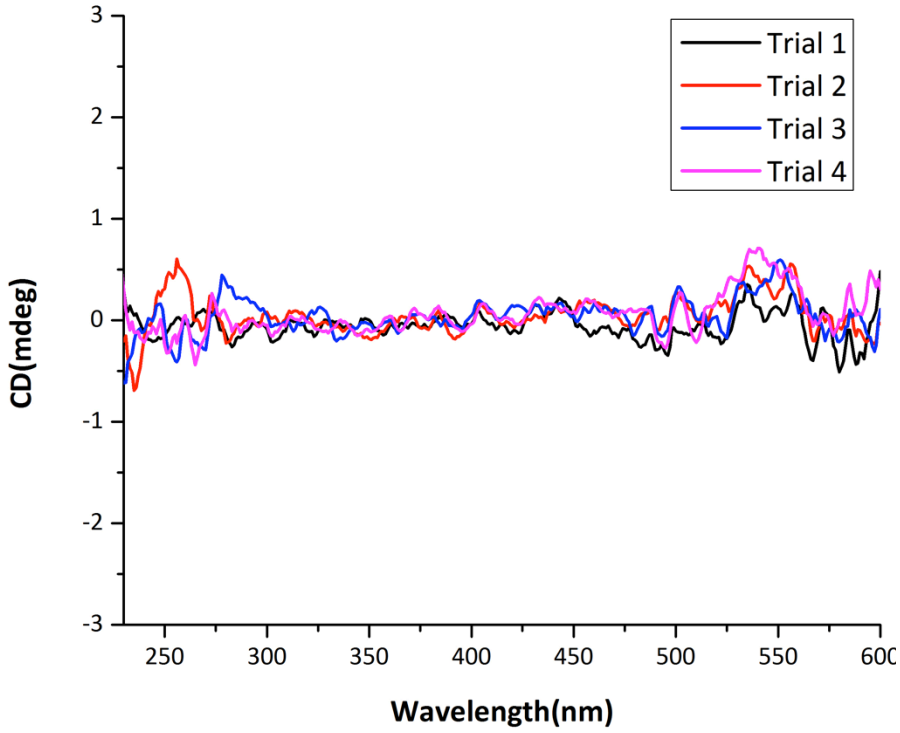

Figure II-C-3. The circular dichroism spectra of NitroPetA (3") ligand in dichloromethane.

C-2. Synthetic Procedure

PetA-diene (2): 5,12-Dimethy-7,14 diphenyl-l,4,8,11 tetraazacyclotetradeca-4,11-diene (PetA-diene) was synthesized by a procedure modified from that reported by Lloyd.[1] Benzyladineacetone (5 g, 1 equiv.) was dissolved in 3:1 anhydrous cyclohexane: anhydrous ethyl ether (50 mL) over anhydrous potassium carbonate (3.43 g, 0.72 equiv.) and the resulting solution was heated to 80 ^{o}C under argon atmosphere. Anhydrous ethylenediamine (2.27 mL, 1 equiv.,) was added dropwise to this solution. After 2.5 h the solution was filtered through a medium sintered glass frit to remove all solids. The pale yellow filtrate

was reduced to dryness by rotary evaporation to afford a yellow residue. Cool ethyl ether (10 mL) was mixed with the residue to form a white solid suspension. The white powder was collected by filtration and washed with ethyl ether (3 x 5 mL). The yellow filtrate was collected, dried by rotary evaporation and re-suspended in 5 mL cool ether to obtain more white solid. All white powder was dried under vacuum for at least 24 h. Yield: 5.28 g (82%). ESI-MS (m/z): 376. Melting point: 133-135 ^{o}C.

PetA Ligand (3): Reduction of PetA-diene afforded 5,12-dimethyl-7,14-diphenyl-1,4,8,11-tetraaza-cyclotetradecane (PetA). A sample of PetA-diene (400 mg, 1 equiv.) was added to 20 mL of 200 proof ethanol at room temperature and solid $NaBH_4$ (94 mg, 2.33 equiv.) was then added to the solution. The reaction was heated at 50 ^{0}C for 2 h. The solution was then filtered to remove the solid sodium borate. The filtrate was reduced to dryness by rotary evaporation to afford a white paste. This paste was subsequently suspended in water and then extracted into chloroform. The chloroform solution was dried with $MgSO_4$, filtered and reduced to dryness by rotary evaporation to afford a white solid. This solid was resuspended in diethyl ether, filtered and washed with diethyl ether (3 x 3 mL) to afford a fluffy white powder. Yield: 331 mg (77%). ESI-MS (m/z): 380. Anal. Calcd for $C_{24}H_{36}N_4$: C, 75.74; H, 9.53; N, 14.72. Found: C, 75.70; H, 9.54; N, 14.60.

(E)-4-(3-nitrophenyl)but-3-en-2-one (1"): 3-Nitrobenzaldehyde (3.02 g, 20 mmol) and 1-(triphenylphosphoranylidene)-2-propanone (7.00 g, 22 mmol) were dissolved in 20 mL dichloromethane (DCM), and the solution was refluxed under argon atmosphere overnight. After refluxing, the solution was dried by rotary evaporation. Silica gel column purification

was performed with hexane : DCM = 15:5 (v/v) eluent to afford a yellow powder (3.82 g, 100%) after removing the solvent by rotary evaporation.

NitroPetA-diene (2"): potassium carbonate (1.16 g, 8.37 mmol) was added into a 90 mL mixture of anhydrous cyclohexane : anhydrous diethyl ether = 2 :1. (E)-4-(3-nitrophenyl)but-3-en-2-one (**1"**, 2.00 g, 10.46 mmol) was then added, and the solution was heated under reflux under argon atmosphere. Once all the yellow powder fully dissolved, anhydrous ethylenediamine (0.73 mL, 10.98 mmol) was slowly injected into the solution. The solution was refluxed with stirring for 8 h and then filtrated to remove the solid potassium carbonate to obtain a light yellow filtrate. The filtrate was dried by rotary evaporation and vacuum to afford viscous yellow liquid. 5 mL cool diethyl ether was added to the yellow liquid to precipitate out and collect white powder. The residue ether mixture was dried by rotary evaporation and vacuum again, and 3 mL cool ether was added to collect more white powder. The white powder is crude NitroPetA-diene (0.41 g, 16.8%) and has to totally be dried by vacuum for 1 day before using.

NitroPetA Ligand (3"): Anhydrous NitroPetA-diene (0.524 g, 1.124 mmol) was dissolved into anhydrous ethanol dried by Molecular Sieve 3A from 200 proof ethanol, and sodium borohydride (0.34 g, 8.992 mmol) was immediately added to the ethanol solution. Until bubbling gradually ceased, the solution was heated up to 80 ^{0}C overnight to complete the reaction and then dried by rotary evaporation to afford crude white powder. The crude white powder was mixed with DCM and filtrated out insoluble impurities to collect filtrate. The filtrate was dried by rotary evaporation and washed with cool diethyl ether to obtain pure white powder (yield: 0.246 g, 46.6%).

D. Trans-Chromium(III) Dinitrito Complexes (CrONO)

D-1. Discussion for CrONO Synthesis

CrONO analogues have a high quantum yield for NO release in visible region and can be synthesized from *trans*-[Cr(L)Cl_2]Cl.[11] Generally, the *trans*-[Cr(L)Cl_2]Cl can be prepared by chromium insertion into tetraaza-macrocyclic ligands such as cyclam[12,13], TetA[14], PetA[7], NitroPetA and tetraphenylporphyrin (TPP)[15–18] in dimethylformamide (DMF) under reflux. However, this procedure can also produce *cis*-[Cr(L)Cl_2]Cl which does not give the *trans*-chromium dintrito complexes needed for the photochemical experiments.[19] (**Scheme II-D-6**) PetA ligand has two phenyl rings can create steric hindrance favors formation of *trans*-[Cr(PetA)$(Cl)_2$]$^+$ (Yield: 70%) over *cis*-[Cr(PetA)$(Cl)_2$]$^+$ (Yield: 10%). (**Figure II-D-4**) The pink color of *cis* form complex can be separated from the *cis/trans* mixture by flash column chromatography with normal phase silica gel and dichloromethane (DCM) serve as an eluent. Moreover, the *cis* form can be converted to the *trans* form in DCM under reflux and argon atmosphere.

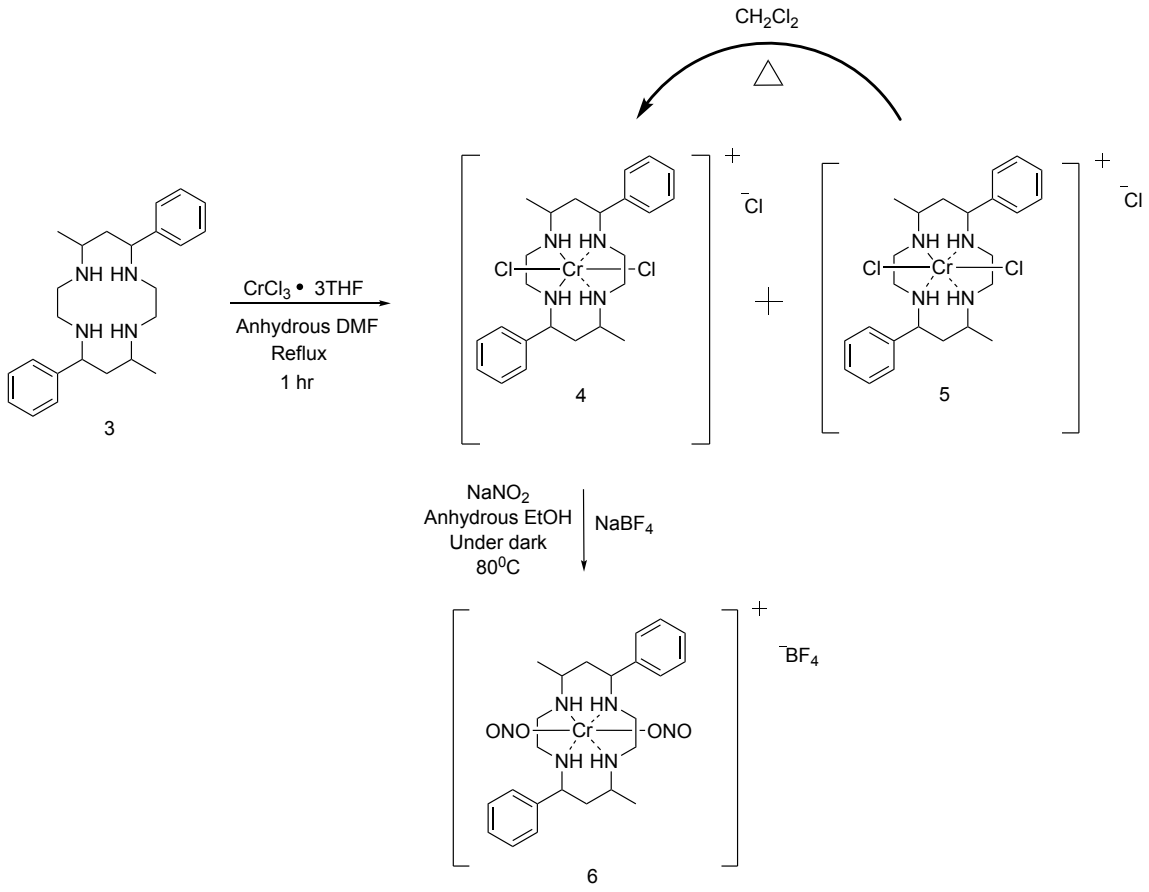

Scheme II-D-6. The synthetic pathway of *trans*-[Cr(PetA)$(ONO)_2$]BF_4 (**6**).

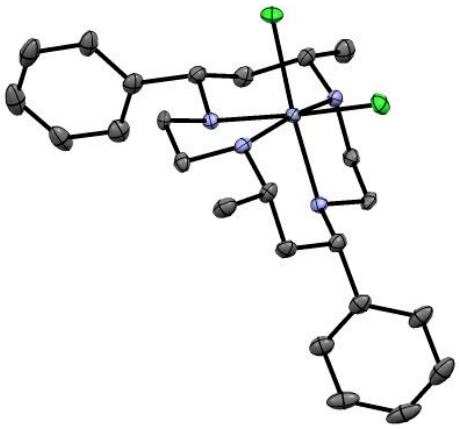

Figure II-D-4. The crystal structure of *cis*-[Cr(PetA)$(Cl)_2$]Cl (**5**)

Figure II-D-5 shows the crystal structure of *trans*-[Cr(PetA)$(Cl)_2$]Cl (**4**). The green spot in the figure is chloride and can be replaced by nitrite under dark to from *trans*-[Cr(PetA)$(ONO)_2$]BF_4 salt. (**Figure II-D-6**)

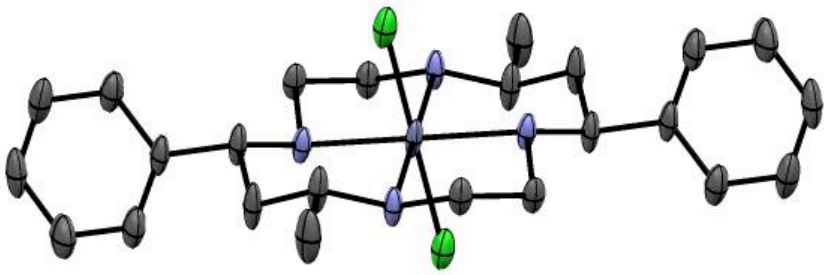

Figure II-D-5. The crystal structure of *trans*-[PetACrCl_2]Cl (**4**)

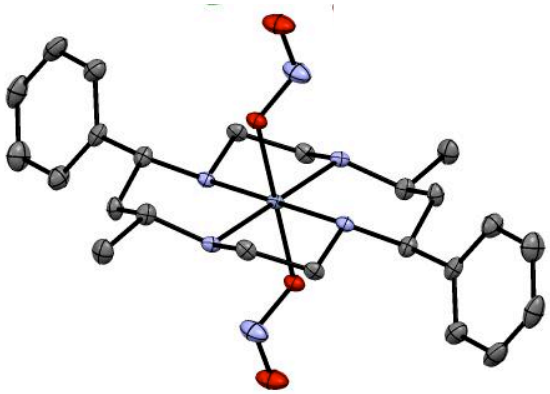

Figure II-D-6. The crystal structure of *trans*-[Cr(PetA)$(ONO)_2$]BF_4 (**6**)

The primary amine group was introduced to PetA analogue for the purpose of coupling with carboxyl group on targets. As described in the Section II-C, commercial aminobenzaldehydes are so expensive that (4-aminobenzaldehyde: $75 USD/250 mg; 2-aminobenzaldehyde: $185.5 USD/g) that it was deemed necessary to use a different synthetic strategy. Therefore, NitroPetA (**3"**) was synthesized, reacted with chromium(III) chloride tetrahydrofuran complex (1:3) to generate *trans*-[Cr(NitroPetA)$(Cl)_2$]Cl (**4"**) and reduced to *trans*-[Cr(AminoPetA)$(Cl)_2$]Cl (**5"**) under 30 psi H_2 with Pd/C as a hydrogenation catalyst. (**Scheme II-D-7**) Figure II-D-7 shows *trans*-[Cr(NitroPetA)$(Cl)_2$]Cl (**4"**) has the same configuration as *trans*-[PetACrCl_2]Cl (**4**) and the nitro groups on the phenyl rings are successfully reduced to primary amine groups without affecting its configuration. (**Figure II-D-8**) For *trans*-[Cr(AminoPetA)$(ONO)_2$]Cl (**6"**) synthesis, *trans*-[Cr(AminoPetA)$(Cl)_2$]Cl (**5"**) was dissolved into 200 proof ethanol and then mixed with excess amount of sodium nitrite. The solution was refluxed in the dark and under an argon atmosphere for 2 h. (**Scheme II-D-8**) The crude solution was dried by rotary evaporation and dissolved into DCM for ESI-MS experiment. (**Figure II-D-9**) Based on the mass spectrum, the molecular ion peak shows 554 m/z consistent with that expected for *trans*-[Cr(AminoPetA)$(ONO)_2]^+$. However, the pure compound can't be successfully obtained by following the same procedure as the preparation of PetACrONO due to its high solubility in water.

Here, I would like to share a possible purification method to obtain pure *trans*-$[Cr(AminoPetA)(ONO)_2]^+$. The purification procedure may involve drying the post-reaction solution by rotary evaporation and follow by extracting the solid with acetonitrile (or DCM) to remove excess sodium nitrite and collecting the orange filtrate. Before removing excess sodium nitrite, the process can't have water involved. The volume of filtrate is reduced to 3-5 mL after which was added 1-2 mL 18 MΩ pure water (make sure pH of water is over 7). A saturated sodium tetraphenylborate solution in acetonitrile is slowly added to the mixture to give the expected 1:1 molar ration to the crude AminoPetACrONO used. House vacuum overnight is used to slowly evaporate the acetonitrile to give an orange solid that could be suspended in water collected by filtration. This could be recrystalized from DCM against diethyl ether.

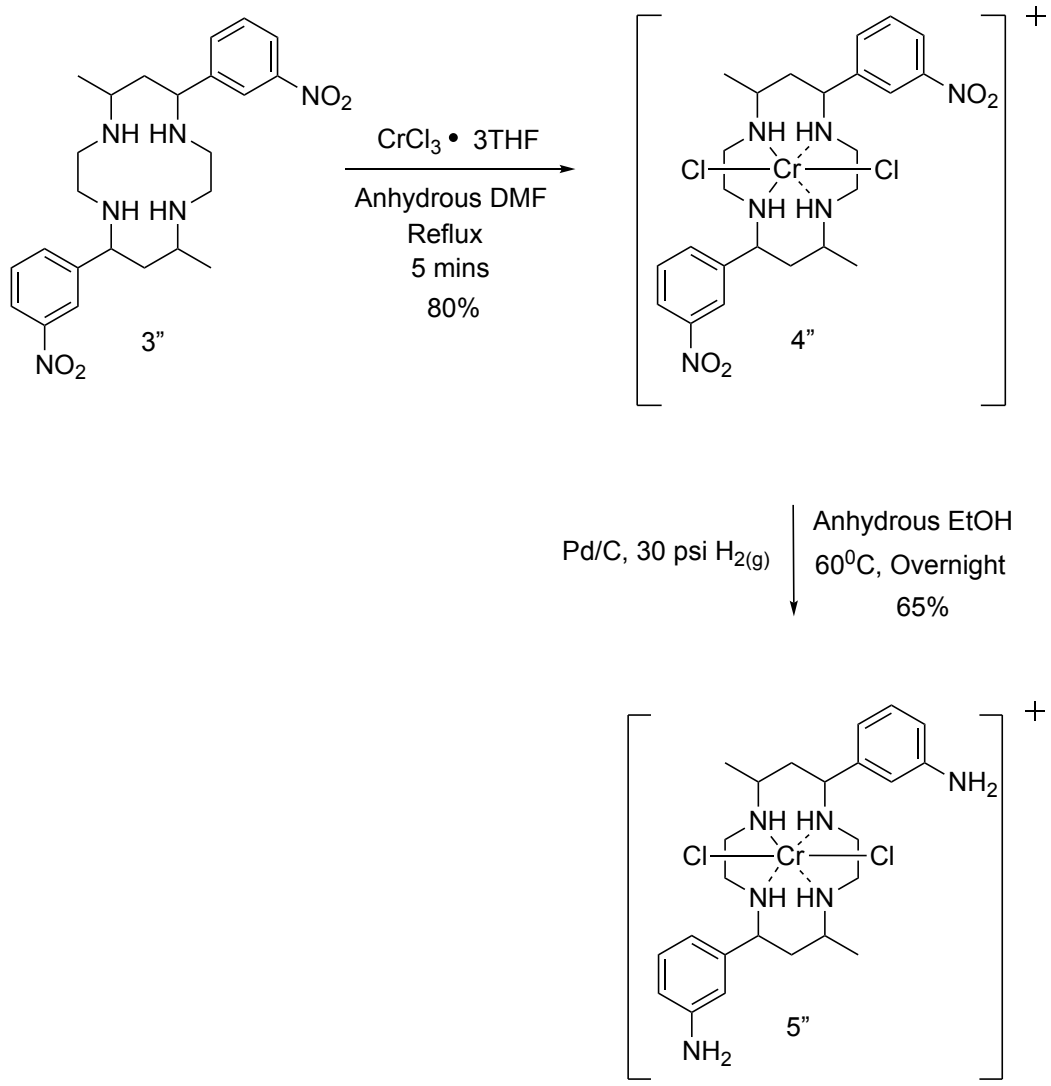

Scheme II-D-7. The synthetic pathway to *trans*-[Cr(AminoPetA)$(Cl)_2$]Cl (**5”**).

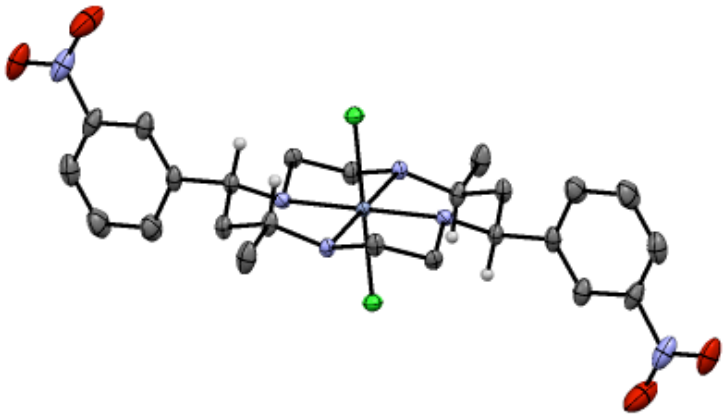

Figure II-D-7. The crystal structure of *trans*-[Cr(NitroPetA)$(Cl)_2$]Cl (**4”**)

Figure II-D-8. The crystal structure of *trans*-[Cr(AminoPetA)$(Cl)_2$]BF_4 (**5”**)

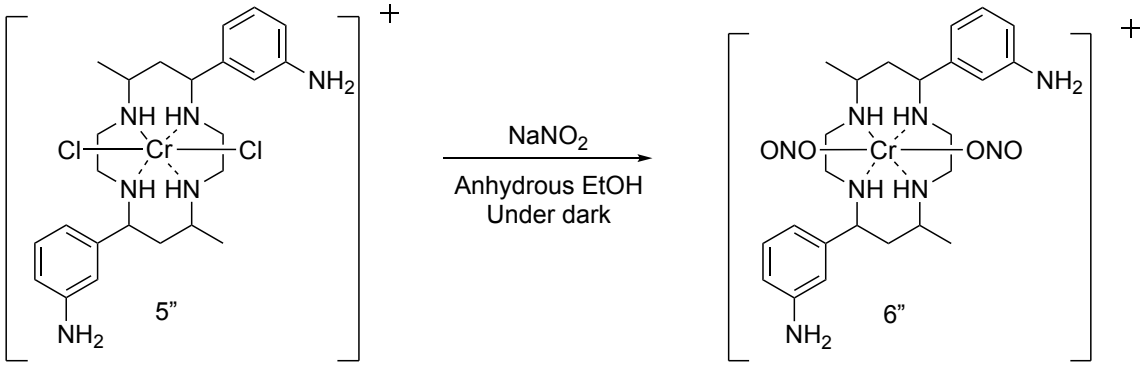

Scheme II-D-8. The synthetic pathway to *trans*-$[Cr(AminoPetA)(ONO)_2]^+$ (**6”**).

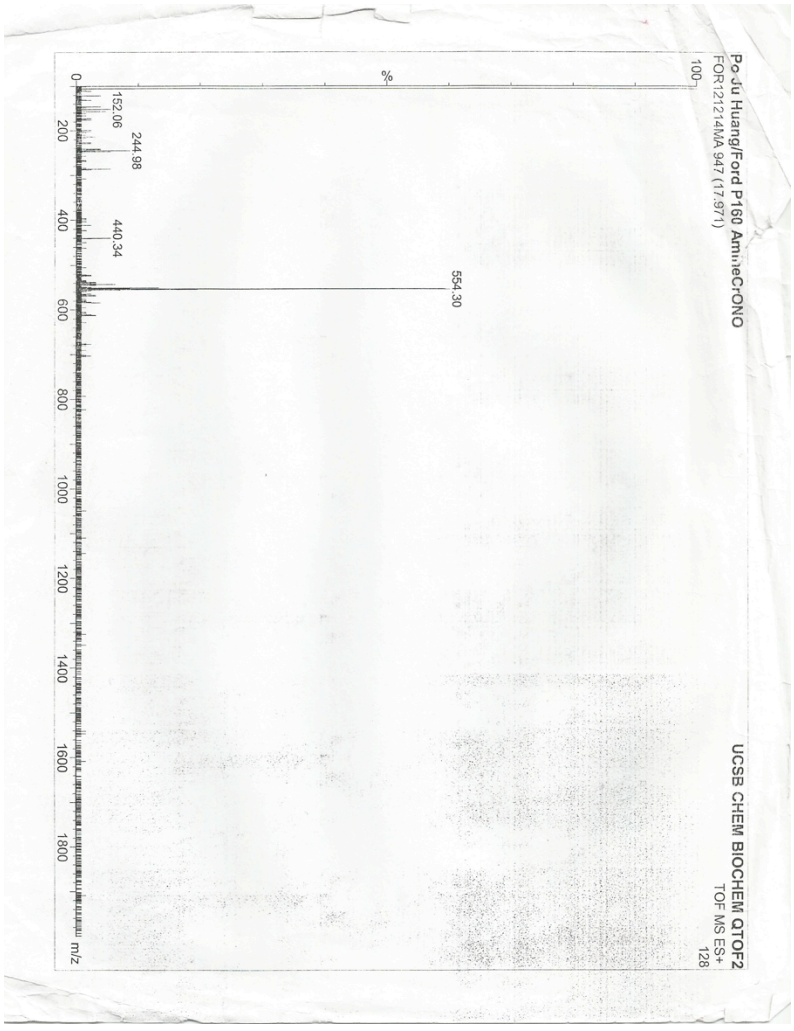

Figure II-D-9. The ESI-MS spectrum of crude *trans*-$[Cr(AminoPetA)(ONO)_2]^+$

D-2. Synthetic Procedure

trans-[Cr(PetA)Cl$_2$]Cl: *trans*-[dichoro(5,12-dimethyl-7,14-diphenyl-1,4,8,11-tetraazacyclo-tetradecane)chromium(III)] chloride was synthesized by a procedure modified from that reported by DeRosa et al.[2] The ligand PetA (150 mg, 1 equiv.) was dissolved in anhydrous dimethylformamide (30 mL) at 150 ^{o}C. $CrCl_3(THF)_3$ (149.2 mg, 1 equiv.) was added into the PetA solution under Argon purge. The solution was refluxed for 1 h and monitored by UV-vis spectroscopy. After cooling, the solution was dried by rotary evaporation and purified by silica gel column chromatography. The eluent DCM was used to wash out unreacted PetA and impurities, and the PetA chromium chloride was flushed out by methanol (MeOH). The methanol solution was dried by rotary evaporation, and a purple powder was obtained. Crude yield: 149 mg (70% yield). The powder was then dissolved in a minimal amount of MeOH and crystalized by vapor diffusion of diethyl ether to produce deep purple crystals. Crystallization yield: 120 mg (63%). ESI-MS (m/z): 502.18 (M+). Uv-Vis (ε in $M^{-1}cm^{-1}$) in methanol solution: 243 nm (2543) 389 nm (43), 439 nm (sh, 20), 562 nm (18). Anal. Calcd for $C_{24}H_{36}Cl_3CrN_4$: C, 53.49; H, 6.73; N, 10.40. Found: C, 51.07; H, 6.66; N, 9.87.

trans-[Cr(PetA)(ONO)$_2$]BF$_4$: *trans*-[(5,12-dimethyl-7,14-diphenyl-1,4,8,11-tetraazacyclotetradecane)dinitritochromium(III)] tetrafluoroborate was synthesized by a procedure modified from that described by Ostrowski et al for the cyclam analog.[3] Sodium nitrite (1373 mg, 20 equiv.) was dissolved in anhydrous ethanol (30 mL). The resulting solution was transferred via cannula into a round bottom flask containing *trans*-[Cr(PetA)Cl$_2$]Cl (539 mg, 1 equiv.) under subdued light. This solution was then refluxed in

the dark at 80 ^{o}C for 2 h. The reaction was removed from heat and filtered hot to afford a deep orange filtrate, which was passed through a 0.22 μm filter and reduced to dryness under vacuum. The resulting orange residue was redissolved in a minimal amount of hot 1:1 EtOH:H_2O (5 mL) and added dropwise to a warm 1:1 EtOH:H_2O solution (3 mL) of sodium tetrafluoroborate (105 mg, 1 equiv.). The solution was cooled overnight in a freezer and then filtered to give an orange powder (724 mg, 82% yield). Crystals were obtained slow vapor diffusion of ether into a concentated 9:1 DCM:MeOH to yield small, cubic orange crystals from which an X-ray crystal structure was obtained. ESI-MS (m/z): 524.22 (M+). UV-vis spectrum (ε in $M^{-1}cm^{-1}$) in isobutyronitrile (iBN) solution: 257 nm (3008), 337 nm (276), 491 nm (51). Anal. Calcd for $C_{24}H_{36}BCrF_4N_6O_4$: C, 47.15; H, 5.94; N, 13.75. Found: C, 47.30; H, 6.08; N, 11.60.

trans-[Cr(PetA)(ONO)$_2$]BPh$_4$: *Trans*-[(5,12-dimethyl-7,14-diphenyl-1,4,8,11-tetra-aza-cyclotetradecane)dinitritochromium(III)] tetraphenylborate was synthesized by a procedure modified from that described by Ostrowski et al.[3] Sodium nitrite (1444 mg, 20 equiv.) was dissolved in a 1:1 mixture of EtOH:H_2O (30 mL). The resulting solution was cannula transferred into a round bottom containing *trans*-[Cr(PetA)Cl_2]Cl (564 mg, 1 equiv.) under subdued light. This solution was then refluxed in the dark at 80 ^{o}C for 2 h. The reaction was removed from heat and filtered hot to afford a deep orange filtrate, which was passed through a 0.22 μm filter and reduced to dryness under vacuum. The resulting orange residue was redissolved in a minimal amount of hot 1:1 EtOH:H_2O (5 mL) and added drop-wise to a warm solution (3 mL) of sodium tetraphenylborate (358 mg, 1 equiv.). The solution was cooled overnight in a freezer and then filtered to give an orange powder (724 mg, 82% yield). ESI-MS (m/z): 524.22 (M+). UV-vis spectrum ε ($M^{-1}cm^{-1}$) in DCM solution: 247 nm

(2775), 339 nm (107), 493 nm (24). Anal. Calcd for $C_{49}H_{59}BCrN_6O_4$: C, 68.53; H, 6.92; N, 9.79. Found: C, 68.57; H, 6.95; N, 9.70.

trans-[Cr(NitroPetA)(Cl)$_2$]Cl: NitroPetA (83.5 mg, 0.1776 mmol) was dissolved into 80 ^{0}C 10 mL anhydrous dimethylformamide and heated to 152 ^{0}C under argon atmosphere. 66.5 mg purple chromium(III) chloride tetrahydrofuran complex (1:3) was added into the solution and stirred for 3 min. The brownish purple solution was naturally cooled down to room temperature, dried by rotary evaporation and washed with 1 mL cool ethanol to afford crude purple powder (0.112 g, 55%). The purple crystal was obtained by a vapor diffusion of diethyl ether to methanol solution of crude purple compound.

trans-[Cr(AminoPetA)(Cl)$_2$]Cl: trans-[Cr(NitroPetA)(Cl)$_2$]Cl (0.7 g, 1.18 mmol) and Pd/C (20 mg) were added into 10 mL anhydrous ethanol, and heated up to 50 ^{0}C with stirring. The reaction was performed under 30 psi hydrogen atmosphere overnight. The Pd/C was filtrated out and the magenta filtrate was collected and dried by rotary evaporator to obtain magenta powder (0.435 g, 65%). Magenta crystals were obtained by vapor diffusion of diethyl ether into an acetonitrile solution of the as-synthesized compound.

D-3. Photochemistry of *trans*-$[Cr(PetA)(ONO)_2]^+$

It has been shown that the chromium (III) dinitrito complex (CrONO) undergoes reversible photo-induced cleavage of the CrO-NO bond to release NO instead of Cr-ONO bond due to the high oxygen affinity of chromium.[11,14,20] The centrosymmetric CrONO derivatives usually have Laporte forbidden d-d absorption bands between 450 and 500 nm and their extinction coefficients at that range are very small (~ 40-55 M^{-1} cm^{-1}). However, the quantum yield for NO photo-release (Φ_{NO}) is significant high up to ~30% at visible range. The absorption spectrum of *trans*-$PetACrONO^+$ also has the same features as most of CrONO analogues. Figure II-D-10 shows the ligand field band of *trans*-$[Cr(PetA)(ONO)_2]BF_4$ is at 491 nm with very low extinction coefficient (51 M^{-1} cm^{-1} in acetonitile). The spectrum also displays a n-π^* intraligand band at 337 nm (276 M^{-1} cm^{-1} in acetonitile) and an intense π-π^* band of the phenyl ring (3008 M^{-1} cm^{-1} in acetonitile).(**Table II-D-1**)[20]

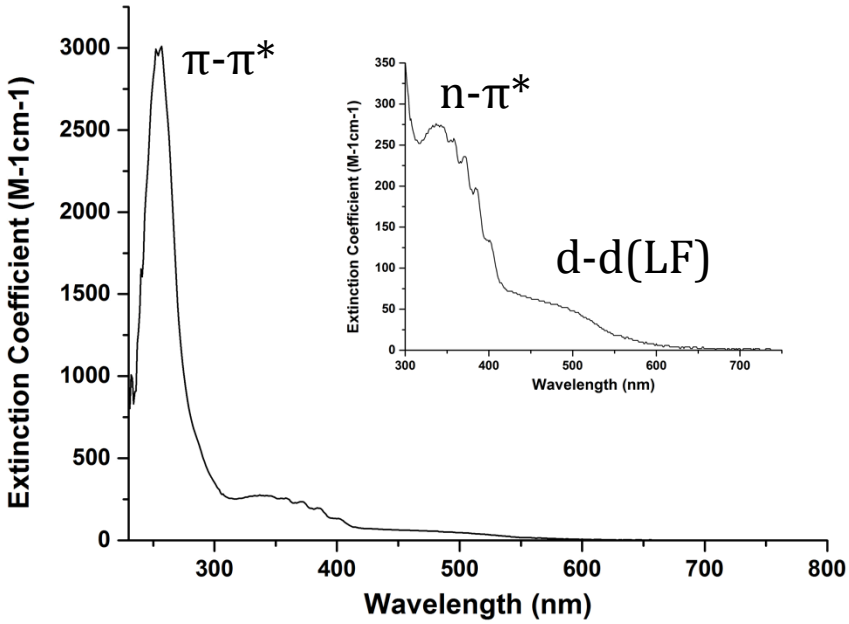

Figure II-D-10. Electronic absorption spectrum of *trans*-$[Cr(PetA)(ONO)_2]BF_4$ in acetonitrile.

Wavelength	ε in M^{-1} cm^{-1}	Peak Assignment
257 nm	3008	π-π*
337 nm	276	n-π*
491 nm	51	d-d (LF)

Table II-D-1. The peak assignment for electronic absorption spectrum of trans-$[Cr(PetA)(ONO)_2]BF_4$ in acetonitrile.

The quantum yield study of light-triggered NO release was performed by following a published procedure. (**Figure II-D-11**)[11] The light resource is 451 nm LED with 18 mW

power. A solution of *trans*-[Cr(PetA)$(ONO)_2$]BF_4 (0.5 mM) in isobutyronitrile was prepared and a 2.5 mL volume of the solution was added into the photolysis Y cell. During the photolysis experiment, the solution was purged with medical grade air to transport the NO generated to the Sievers Nitric Oxide Analyzer (NOA). Figure II-D-12 shows NO release as indicated by signals from a solution of 0.5 mM *trans*-[Cr(PetA)$(ONO)_2$]BF_4 in isobutyronitrile. Different irradiation times (1, 2, 2.5 and 3 sec) were applied in this study. The quantum yield of NO release can be obtained by plotting the NO produced versus the light absorbed; the slope (0.318) is the quantum yield for NO release $\Phi_{(NO)}$ for *trans*-[Cr(PetA)$(ONO)_2$]BF_4. (**Figure II-D-13**)

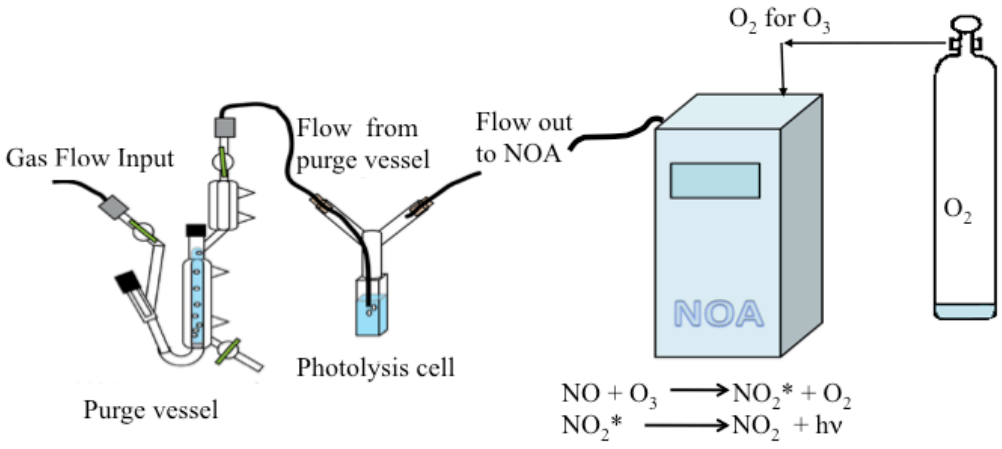

Figure II-D-11. Apparatus for measuring NO release quantum yields in solution where the purging gas (Medical-grade air) passes first through a solvent purge vessel to reduce evaporative losses then through the photolysis "Y" cell. NO released from the photolysis cell is transferred to the Sievers Nitric Oxide Analyzer (NOA, GE model NOA-280i), where it is detected via a very sensitive, calibrated, chemiluminescence technique.

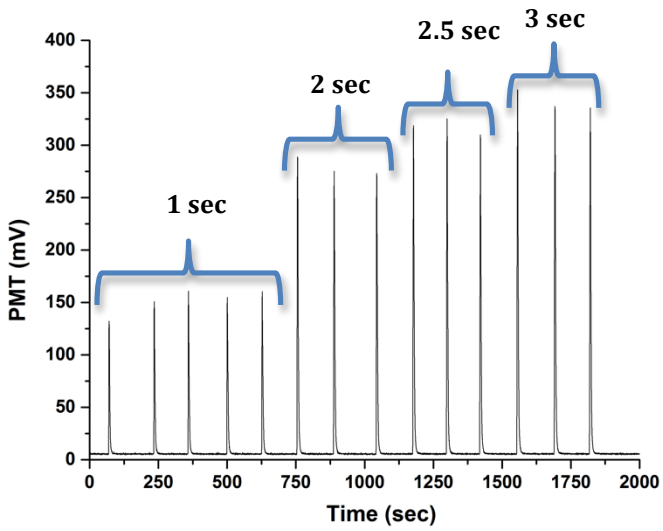

Figure II-D-12. NOA signals from the 451 nm LED photolysis of *trans*-[Cr(PetA)(ONO)$_2$]BF$_4$ in isobutyronitrile at 18 mW power with different irradiation time (1, 2, 2.5 and 3 sec).

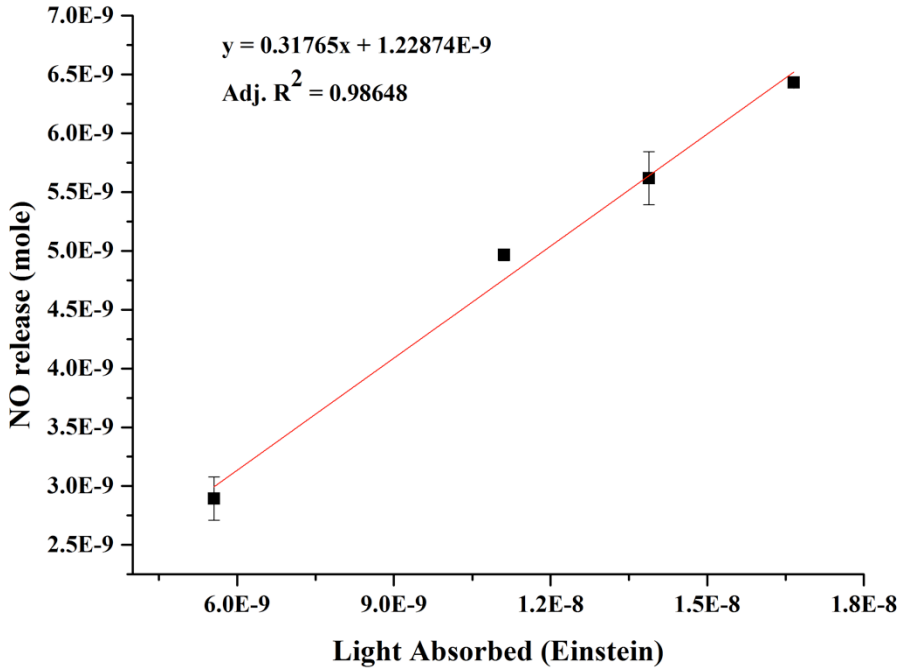

Figure II-D-13. Plot of NO produced versus light absorbed for the 451 nm photolysis (18mW) of *trans*-[Cr(PetA)(ONO)$_2$]BF$_4$ in isobutyronitrile under medical grade air purge. The slope (0.318) is the quantum yield for NO release $\Phi_{(NO)}$.

E. Upconverting Nanoparticles (UCNPs)

E -1. Discussion for UCNPs Synthesis

The 800 nm absorbing Tm-UCNPs and Er-UCNPs were high quality core/shell upconverting nanoparticles (Figure II-E-1 & Figure II-E-2) synthesized using the robotic Workstation for Automated Nanocrystal Discovery and Analysis (WANDA) of the Molecular Foundry at the Lawrence Berkeley National Laboratory.[21–23] The host material for the 10 nm cores was $NaYF_4$ with 20% Gd^{3+} to give hexagonal structures to give higher upconversion efficiency and were also doped with the lanthanide ions Yb^{3+} (30%) and Nd^{3+} (1.0%)..[24,25] The XRD spectra of both types of UCNPs showed hexagonal patterns. (Figure II-E-3). Additionally, emitter dopant in the Tm-UCNPs was Tm^{3+} (0.5%) and in the Er-UCNPs was Er^{3+} (0.5%). The 2 nm thick shells were $NaGdF_4$ doped with Nd (20%) for both UCNPs. The shell minimizes surface quenching effects and improves the luminescence efficienies. The Nd^{3+} dopant in these $NaYF_4$:Yb/Gd/Nd/Tm(30/20/1/0.5%)@$NaGdF_4$:Nd(20%) and $NaYF_4$:Yb/Gd/Nd/Er(30/20/1/0.5%)@$NaGdF_4$:Nd(20%) core-shell nanoparticles has an absorption band at ca. 800 nm allowing these UCNPs to be excited at wavelengths (ca. 775-825 nm, better absorption between 785-800 nm) where the absorption of water is minimal.[26] Energy transfer from the excited Nd^{3+} to Yb^{3+} in the core[27] is followed by energy migration from Yb^{3+} to Tm^{3+} or Er^{3+}, respectively, from which various photoluminescence (PL) bands in the UV and visible range are observed. The PL spectra of these Nd doped UCNPs are shown in Figure II-E-4.

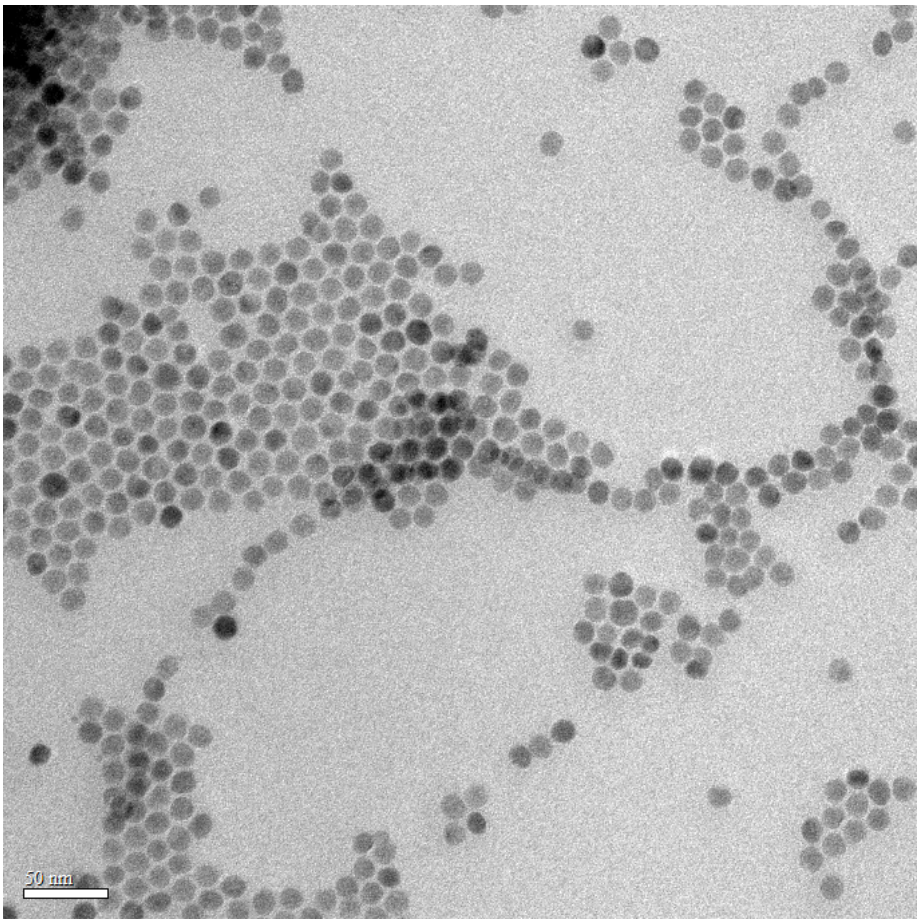

Figure II-E-1. TEM image of $NaYF_4$:Yb/Gd/Nd/Tm(30/20/1/0.5%)@$NaGdF_4$:Nd(20%) core-shell nanoparticles.

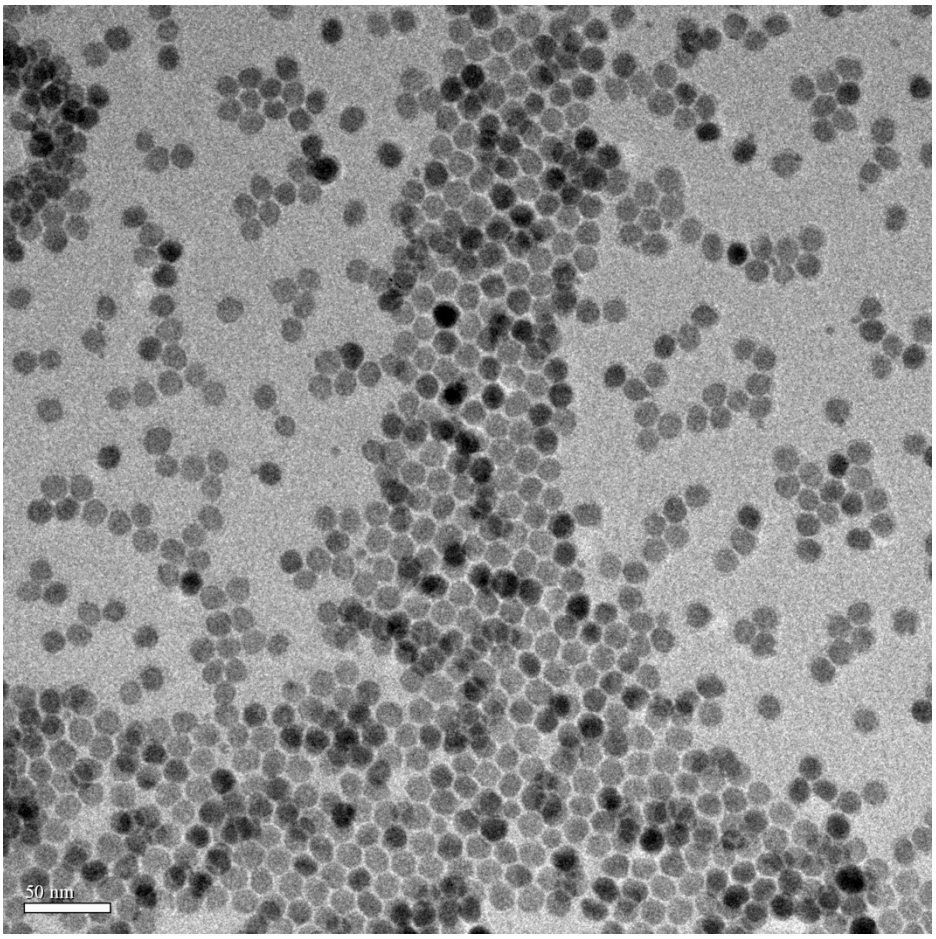

Figure II-E-2. TEM image of $NaYF_4$:Yb/Gd/Nd/Er(30/20/1/0.5%)@$NaGdF_4$:Nd(20%) core-shell nanoparticles.

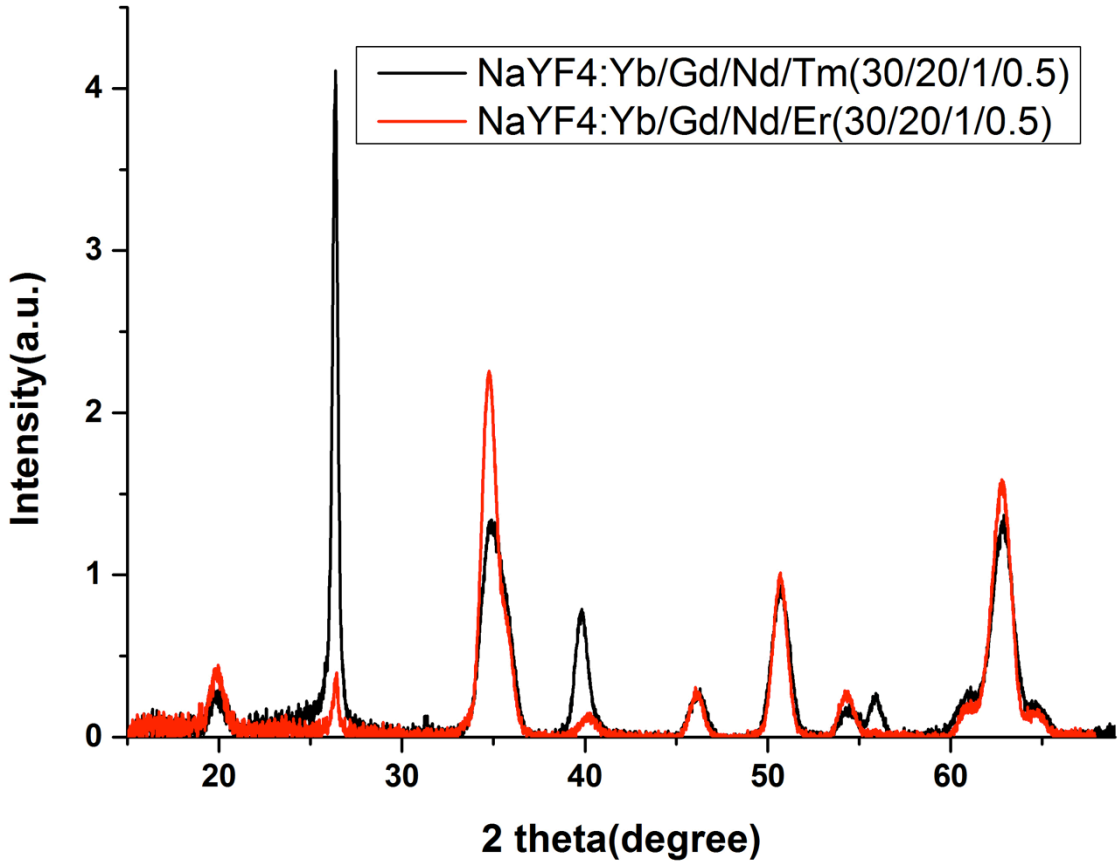

Figure II-E-3. The XRD patterns for two cores $NaYF_4$:Yb/Gd/Nd/Tm(30/20/1/0.5%) and $NaYF_4$:Yb/Gd/Nd/Er(30/20/1/0.5%).

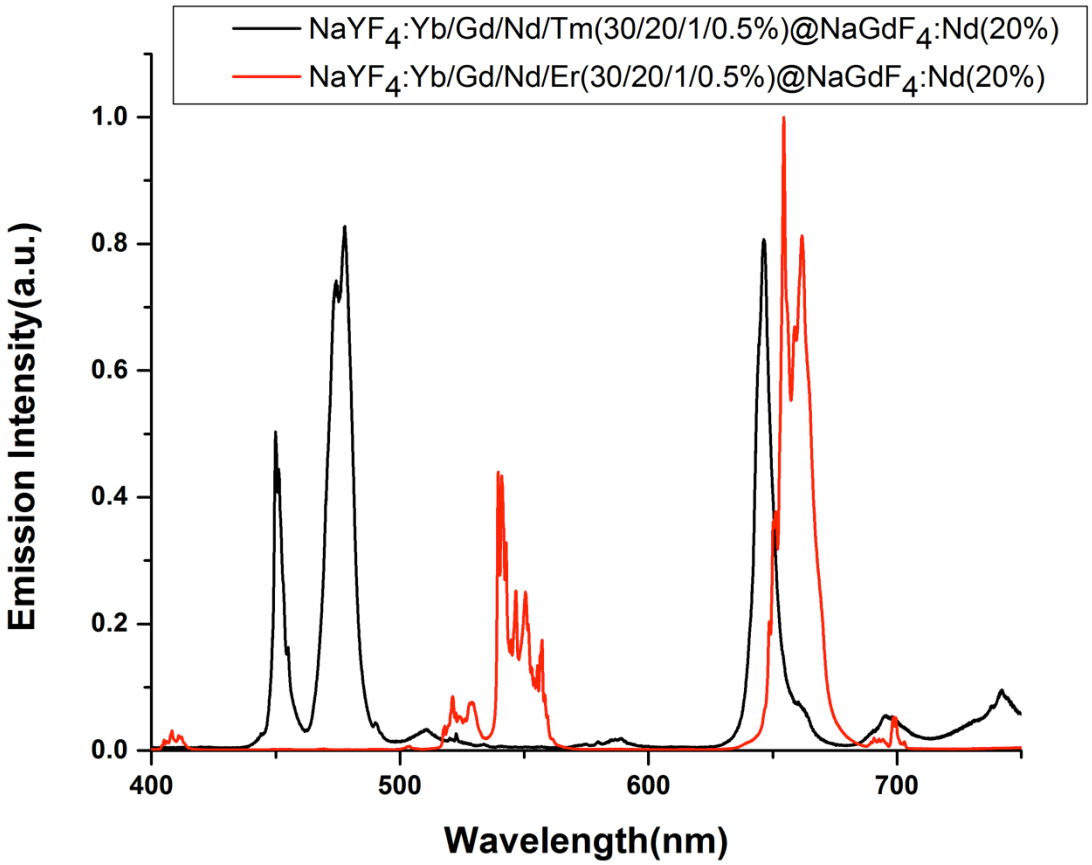

Figure II-E-4. The solid-state up-conversion photoluminescence spectra for core-shell Tm-UCNPs and Er-UCNPs under excitation by an 800 nm continuous-wave (CW) laser.

E -2. Synthetic Procedure

The composition of UCNPs was modified from the literature.[21–23] The robot known as WANDA in Molecular Foundry was applied to prepare these nanoparticles. All solutions used in the WANDA glovebox were deaerated. Oleic acid (OA) and 1-octadecene (ODE) were heated to 100 ^{0}C (no more than 110 ^{0}C) separately in three-necked round bottles under vacuum and then purged with nitrogen (N_2) for deaeration. The deaerating cycle should be performed at 100^{0}C for at least three times. The final pressure and temperature in the glassware should be around 160 mTorr and room temperature respectively before putting into a glove box. For the stock solution, YCl_3 (2.43 mmol), $YbCl_3$ (1.50 mmol), $NdCl_3$ (0.05 mmol), $TmCl_3$ (0.025 mmol), $GdCl_3$ (1.0 mmol), OA (26.834 g) and ODE (15.73 g) were mixed in a round bottle and deaerated by following the previous procedure. Then, the mixture was heated to 190 ^{0}C under N_2 atmosphere to make sure all salts dissolved. The homogenous stock solution was cooled down to 100 ^{0}C and evacuated to 160 mTorr. After cooling down to room temperature, the degassed solution was transferred into the WANDA glovebox. For the core synthesis, sodium oleate (1.25 mmol), NH_4F (20.00 mmol), stock solution (4.384 g, 10% of the stock), OA (0.569 g) and ODE (3.5 g) were added into 20 mL glass vial and heated to 315 ^{0}C with 30 ^{0}C/min heating ramp rate and 500.0 rpm stirring rate for 40 min. For particle purification, the core solution was transferred to a centrifuge tube and ethanol was added to form white colloidal solution. The white precipitate was obtained after centrifugation to remove excess OA and ODE, and washed with ethanol for two more times. The cores sample was weighed after vacuum drying.

In order to increase UC luminescence efficiency, $NaGdF_4$ shell doped with 20% Nd was grown on the surface of UCNP cores. The Gd/Nd shell stock solution ($GdCl_3$: 3.20 mmol,

$NdCl_3$: 0.80 mmol, OA: 7.1539 g, ODE: 9.4664 g) and 0.2 M NaTFA solution (sodium trifluoroacetate: 1.0095 g, OA: 9.0592 g, ODE: 21.3050 g) were prepared and degassed by following previous procedure. 6 mL ODE and 4 mL OA were added into dried UCNP cores and heated to 275 ^{0}C in the WANDA glovebox. The automated protocol alternated between injections of a 0.2 M NaTFA solution and a Gd/Nd stock solution in a 2:1 mole ratio of sodium to gadolinium precursor. One injection was performed every 15 min for a total of 12 injections (6 injections for each precursor). After the last injection, the reaction was heated at 275 °C for an additional 30 min and then cooled down by N_2 flow. The core/shell UCNPs was purified by following the same procedure of UCNPs cores.

F. [Mn(dpaq$^{NO}{}_2$)(NO)]BPh$_4$

These procedures were carried out under reduced lighting. The [Mn(dpaq$^{NO}{}_2$)(NO)]ClO_4 salt was provided by Professor Hitomi.[28] This perchlorate salt (119.3 mg?, 0.195 mmol) was dissolved in 3 mL solution of 1:1 acetonitrile/deionized (DI) water that was then added to a 2 mL volume of acetonitrile in which was dissolved $NaBPh_4$ (66.7 mg, 0.195 mmol). The resulting mixture was sonicated for 3 min after which most of the solvent was removed under reduced pressure. The resulting hydrophobic black solid was suspended in aqueous solution then collected by filtration, washed with DI water and dried under vacuum. The solid was then dissolved in DCM and recrystallized by vapor diffusion of ether to produce crystalline black needles of [Mn(dpaq$^{NO}{}_2$)(NO)]BPh_4.

G. IgG-modified micro-carriers

The procedure of polymer micro-emulsion was modified from the literature.[29–31] Acid-terminated PLGA (100 mg) and ~80 μL of a solution of Nd-UCNPs in hexane (~10 mg UCNPs) were added into 500 μL DCM, and sonicated for 45 min at room temperature. A 14 mg sample of **I** was dissolved in a mixture of ACN (150 μL) and DCM (400 μL) to form a dark purple solution that was then transferred into the PLGA solution, and the mixture was sonicated until homogenous. If the volume of as-prepared solution was lower than 1.1 mL, more DCM was added. The polymer solution was slowly added into 200 mL of 1 wt% polyvinyl alcohol (PVA) aqueous solution contained in a 250 mL half-spherical container while the ultrasonic homogenizer was turned to 350 watts for 30 s. A dark brown colloidal solution formed immediately. The flask containing the colloidal suspension was fully covered with aluminum foil and stirred overnight to evaporate the volatile organic solvents. The milky solution was centrifuged to collect a solid, which was washed with 18 megohm pure water to remove the PVA. Following particle purification, the brown pellet was re-suspended in 45 mL pure water and then the 1-micron particles were separated by different centrifuge speed (4000 rpm to remove particles < 500 nm and 300 rpm to remove particles size > 3 μm). The resulting micro-particles were dried under vacuum and re-suspended in 0.1 M pH 5.5 MES buffer solution with the concentration of 1 mg/mL. 1-ethyl-3-(3-dimethylaminopropyl)carbodiimide hydrochloride (EDC•HCl) (70.94 μmole/1 mg particles) and N-hydroxysuccinimide (NHS) (106.87 μmole/1 mg particles) were added into the colloidal 2-(N-morpholino)ethanesulfonic acid (MES) solution which was then sonicated at room temperature for 30 min. Subsequently, 10 μL IgG solution (11.21 mg/mL) per 1 mg micro-particles was added and the mixture stirred overnight. The IgG modified particles

were collected by centrifugation and washed with 18 megohm pure water for at least three times. IgG concentration was determined with a micro bicinchoninic acid (BCA) assay according to the manufacturer's instructions. After incubation, particles were removed from solution with centrifugation to avoid light scattering during absorbance measurements.

Initially, a beaker was utilized during the emulsion process, however; better yields were obtained using a half-spherical glass flash, since there are no corners in the latter and the sonic energy is distributed equally preventing settling and allowing more of the PLGA to form particles of the correct size.

H. Carbon Dots (CDs)

There are two comprehensive preparation strategies for carbon dots (CDs): bottom-up techniques[32–37] and top-down techniques[38–42]. Generally, the bottom-up technique is to graphitize carbohydrates or organic carbon sources under high temperature and pressure while the top-down technique is to break down and exfoliate bulk graphite via electrochemical exfoliation[43–51], Hummers' method[52,53] or solvothermal decomposition[42,54–57]. In most cases, the latter methods can generate carbon quantum dots (CQDs) and graphene quantum dots (GQDs). Here, two top-down methods for GQDs preparation were described.

H-1-1. Electrochemical Exfoliation

The method of electrochemical exfoliation is modified from the previous literature procedure.[46] A bulk graphite serves as an anode electrode while a platinum net acts as a cathode electrode. The electrolysis was performed in a 0.1M $(NH_4)_2SO_4$ aqueous solution with 10 V DC power supply for one h. The graphite electrode was gradually exfoliated and broken down into small pieces of graphite in the beaker. (**Figure II-H-1**) This preparation also generated a lot of carbon particles suspended in the electrolyte. There is no evidence to prove if they are graphene-like but the TEM image indicates the distribution of particle size is between 1.0 and 4.0 nm. (**Figure II-H-2** & **Figure II-H-3**) Therefore, I prefer to call them carbon quantum dots (CQDs). The procedure of purification is that the electrolyte excluding massive graphite fragments was decanted into 50 mL centrifuge tubes and then centrifuged under 5000 rpm for 20 min. The black precipitate was obtained and resuspended into 18 megaohm (MΩ) pure water under sonication for 30 min. The black suspension was

centrifuged under 5000 rpm for 20 min to obtain purified black precipitate. The black solid was dried under vacuum and then suspended in 25 mL DMF with 4 h sonication. The DMF solution was kept in a hood overnight to precipitate most of the aggregates. The top dispersion solution was used for the characterization of optical property and morphology.

The UV-vis absorption spectrum shows the same features reported in literature.[58] (**Figure II-H-4**) Additionally, under 335 nm and 365 nm excitation, the photoluminescence (PL) spectrum shows the as-prepared CQDs to have a blue emission that matches the published data.[51] (**Figure II-H-5**) The process of electrochemical exfoliation generally doesn't introduce many hydrophilic and electron-withdrawing functional groups such as carboxylic acids and amines on the surface of CQDs. This kind of pristine CQDs usually has blue emission and don't suspend in pure water very well. Additionally, they can't be straightforwardly bonded with other targets that possess common functional groups such as carboxylic acids and amines for further application in photosensitizer. Deng et al. utilized Billups-Birch reduction to modify pristine graphitic carbon particles with a long chain n-alkyl carboxylic acid[58], which can covalently bond with primary amine functionalized compounds via amide coupling. Unfortunately, Dr. Deng's student, Xue-Huan Song, and I can't repeat their synthetic method. Additionally, the yield of electrochemical preparation for CQDs is quite low in our case even though the preparation procedure is relatively simple compared with other published methods.[33,42,59]

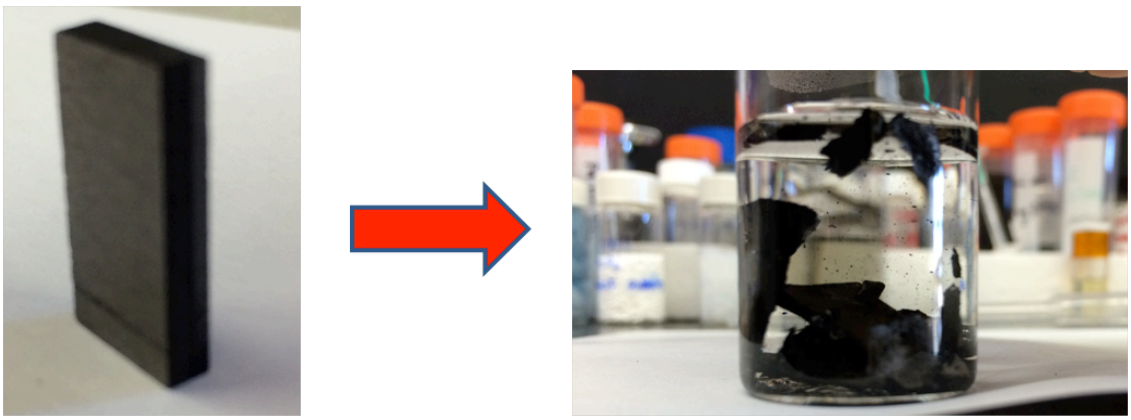

Figure II-H-1. A bulk graphite under electrolysis in 0.1 M $(NH_4)_2SO_4$(aq) to generate exfoliated graphite.

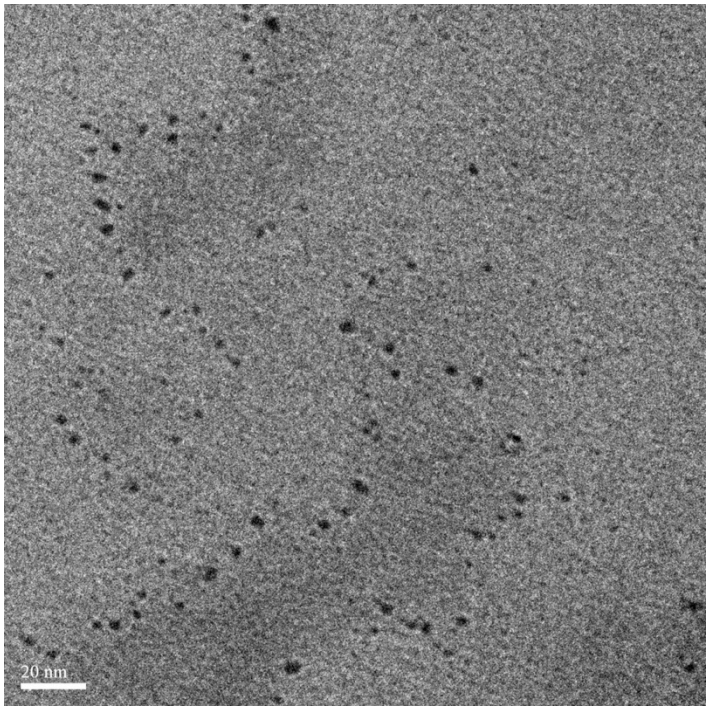

Figure II-H-2. The TEM image of purified carbon quantum dots.

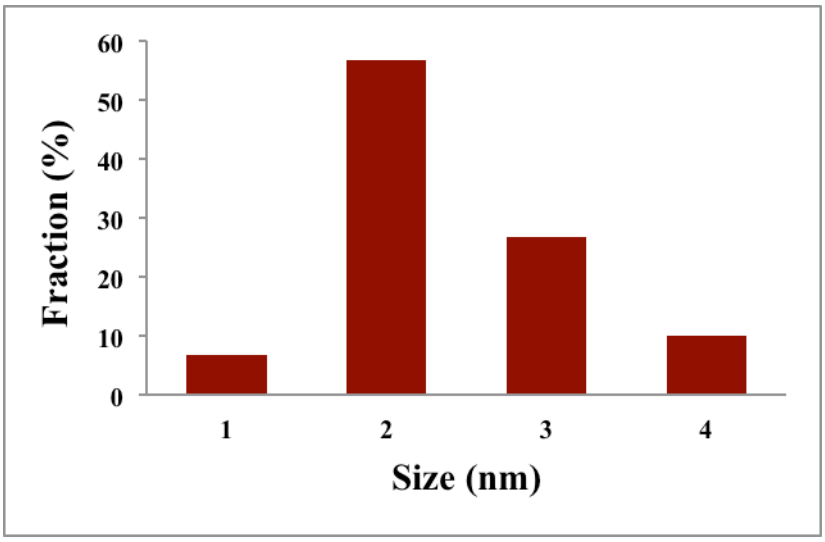

Figure II-H-3. The size distribution of purified carbon quantum dots (number of particles >30).

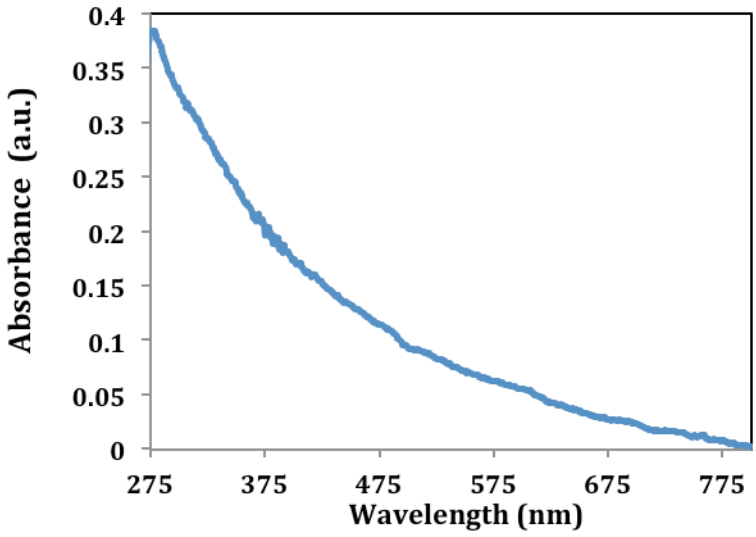

Figure II-H-4. The absorption spectrum of carbon quantum dots in DMF.

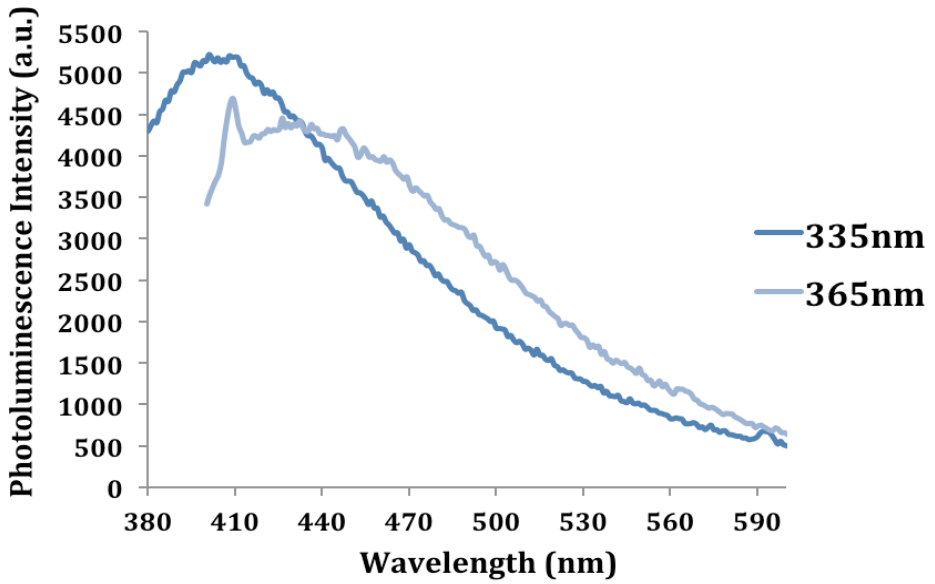

Figure II-H-5. The emission spectrum of carbon quantum dots in DMF with different excitation wavelength (335 nm and 365 nm).

H-1-2. Possible Improvement

To the best of my knowledge, electrochemical exfoliation is the most easy and feasible method to prepare high-quantity CQDs. Therefore, in order to improve this top-down strategy, I would like to provide a modified procedure for further study.

At the beginning of this project, the graphite ingot block was used for electrolysis and the yield of CQDs production is very low due to low surface area to interact with electrolyte via an intercalation mechanism. Therefore, the shape of graphite electrode is one of important factor to increase the production yield and commercial graphite rod would be a good candidate with higher surface area.[60] Moreover, an acidic electrolyte solution would be possible to introduce carboxyl function group on the surface of CQDs for amide coupling with targets.[61–63] After washing out all electrolyte, long sonication in organic solvent such as

DMF or ethanol may exfoliate and break down more graphene nanosheet or graphite particles to further increase the preparation yield.[64,65]

H-2. Hummers' Oxidation/ Solvothermal Decomposition

Hummers' oxidation is a general method to produce graphene/graphene oxide sheets from graphite.[52] Through this oxidation process, graphene oxide sheets have significant defects and can be broken down into small fragments via solvothermal decomposition.[42,56] Gong et al. reported a method to synthesize nitrogen doped graphene quantum dots (N-GQDs) with high two-photon cross section (48000 Göppert-Mayer units).[42] However, the synthetic condition can't be repeated and the yield of N-GQDs production is too low to be applied in our photo-triggered drug delivery system. The possible reason could be that the graphite powder (325 mesh) we used is not easy to oxidize and created significant defects on rigid conjugated sp^2 structure. Therefore, a modified method by using graphite nanoparticles with high surface area was performed to increase the preparation yield.

The preparation procedure for N-GQDs was modified from the published method.[42,66] Graphite nanoparticles (15 g**,** SkySping Nanomaterials) were gradually added into 90 mL concentrated H_2SO_4 mingled with 12.5 g $K_2S_2O_8$ and 12.5 g P_2O_5 at 80 ^{0}C with gently stirring. The mixture was stirred at 80 ^{0}C for 4.5 h and then diluted with 500 mL 18MΩ pure water at 0 ^{0}C. After stirring overnight at room temperature, the diluted solution was centrifuged at 13000 rpm for 8 min to obtain a black pellet. The black pellet was suspended in 300 mL concentrated H_2SO_4 at 0 ^{0}C and 24 g $KMnO_4$ was slowly added into the mixture with vigorous stirring. The solution was heated up to 35 ^{0}C for 2 h and then poured into 700 mL DI water at 0 ^{0}C with 2 h stirring. 30% H_2O_2 was slowly dropped into the acidic solution

until bubble ceased and 10 % (v/v) HCl (1L) was well mixed with the solution. After centrifugation at 8000 rpm for 30 min, the gray yellowish pellet was collected. The pellet was washed with DI water three times and then dried under vacuum. The oxidized carbon pellet was re-dispersed into 80 mL dimethylformamide (DMF) and the suspension was sonicated for 2 h at least. The post-sonicated solution was transferred to a Teflon-lined autoclave and heated to 200 ^{0}C for 10 h. After naturally cooling down the temperature of solution, the DMF solution was centrifuged at 8000 rpm for 30 min to collect yellow solution. The black pellet was re-suspended into clean DMF and sonicated for 4 h. The pale yellowish solution was obtained with the same centrifugation condition. High quantity of N-GQDs can be extracted from the black pellet through by least 10 times of DMF extraction. The solution was dried by rotary evaporator and dissolved into DI water. The as-prepared N-doped GQDs aqueous solution was dialyzed with a 200 MWCO dialysis bag against 18 MΩ pure water for 3 days to remove DMF residues, which display blue fluorescence. The pure N-doped GQDs was used for further characterization.

H-2-1 Morphological Analysis

Since size influences the optical property of quantum dots[67], the morphology of N-GQDs was studied by transmission electron microscopy and atomic force microscopy (AFM). Regarding the contrast issue of TEM imaging between the graphene-like particles and support films on cupper grids, the TEM grids I used were coated with ultrathin carbon films. According to the TEM image, most of N-GQDs are circular shape (**Figure II-H-6**) and size distribution is between 2 and 7 nm (**Figure II-H-7**). The average size of N-GQDs is 4.04 nm, which is similar to the literature report.[42] Additionally, an AFM scan was performed on

a mica substrate by using an Agilent 5500 AFM instrument in tapping. Figure II-H-8 shows several N-GQDs were placed on the mica sheet, and Figure II-H-9 is the associated 3D image to exhibit height dimension of each N-GQD. The thickness of N-GQDs is between 0.8 and 3.3 nm. Considering that one layer of graphene is ca. 0.75 nm[58,68], N-GQDs have one to six layers and the average is three layers (1.48 nm). (**Figure II-H-10**)

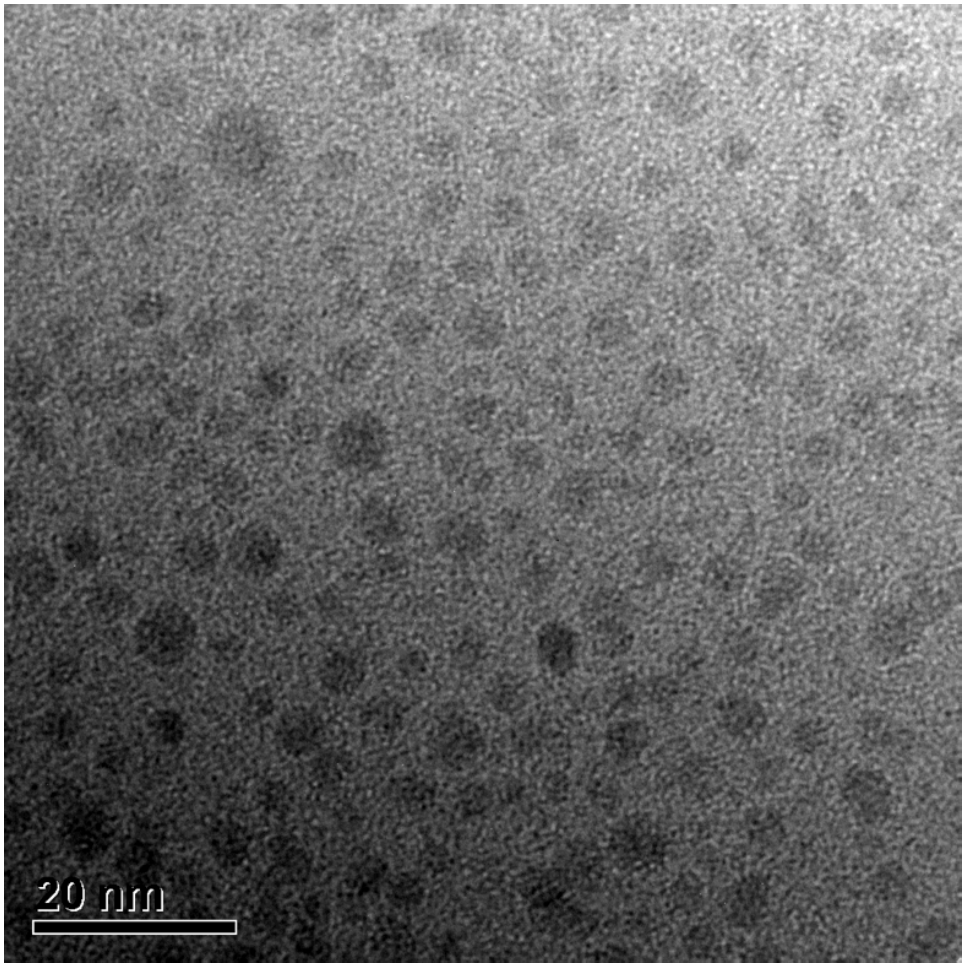

Figure II-H-6. The TEM image of N-GQDs on a copper grid supported with an ultrathin carbon film.

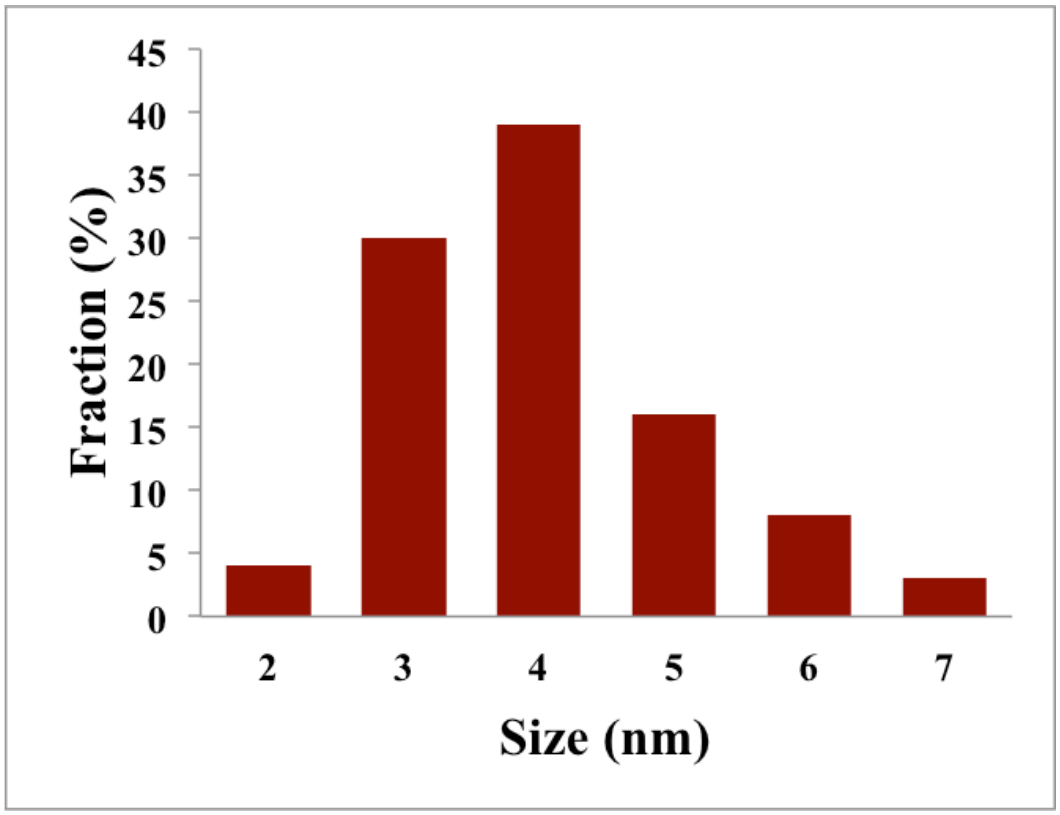

Figure II-H-7. The size distribution of N-GQDs.

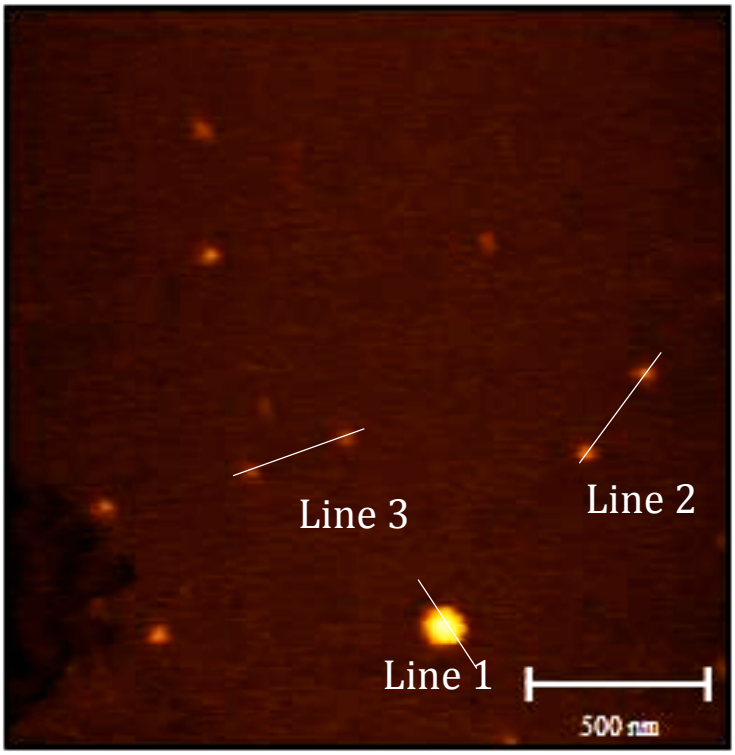

Figure II-H-8. The 2D AFM topographic image of N-GQDs on a mica sheet.

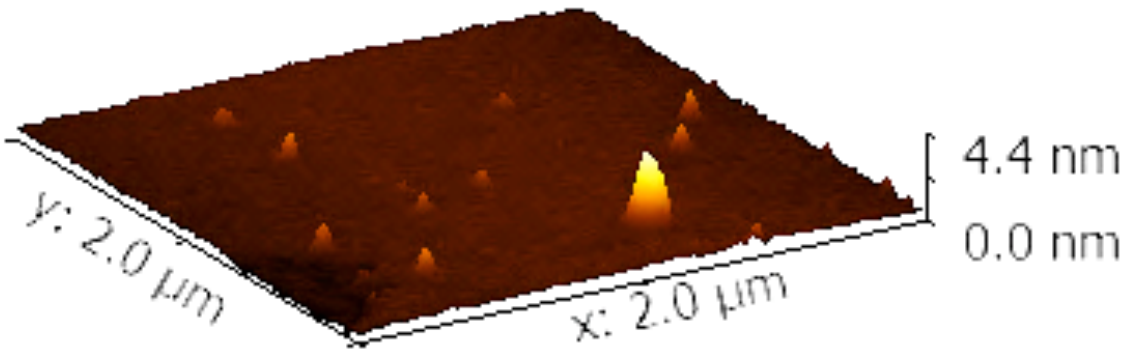

Figure II-H-9. The 3D AFM topographic image of N-GQDs on a mica sheet.

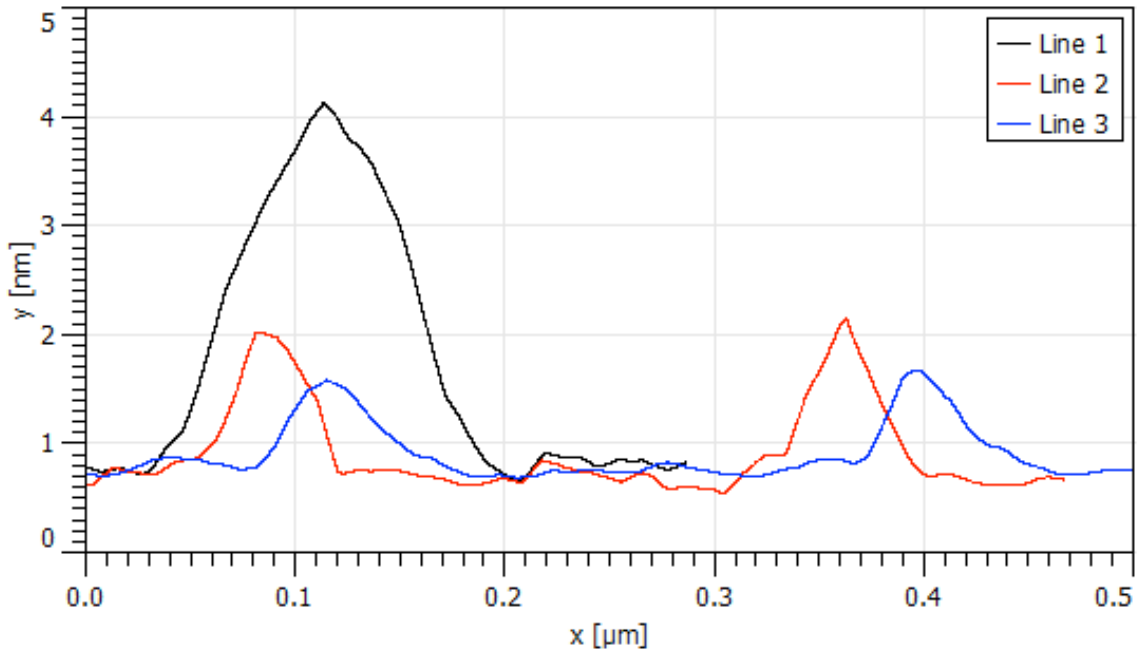

Figure II-H-10. The line-scan height profile of N-GQDs on a mica sheet.

H-2-2 Matrix-assisted Laser Desorption/Ionization - Time-of-flight Mass Spectrometry (MALDI-TOF-MS)

In order to study mass change in the top-down strategy for GQDs preparation, matrix-assisted laser desorption/ionization-time of flight mass spectrometry (MALDI-TOF MS) was applied to this experiment. The MALDI-TOF experiment shows the mass-to-charge ratio of N-doped GQDs (740-3250 m/z) is greatly smaller than their starting materials, graphite nanoparticles (2000-5000 m/z). (**Figure II-H-11**) According to the literature[69], a 1 nm of square of graphene has around 38 carbons, which is equal to a molecular weight of 456. Assuming that as-prepared N-GQDs are only one layer thick and square, their size distribution would be between 2-7 nm based on the MALDI-TOF result and matches the TEM result (**Figure II-H-7**). This method can help us quickly predict the particle sizes without utilizing expensive electron microscopy.

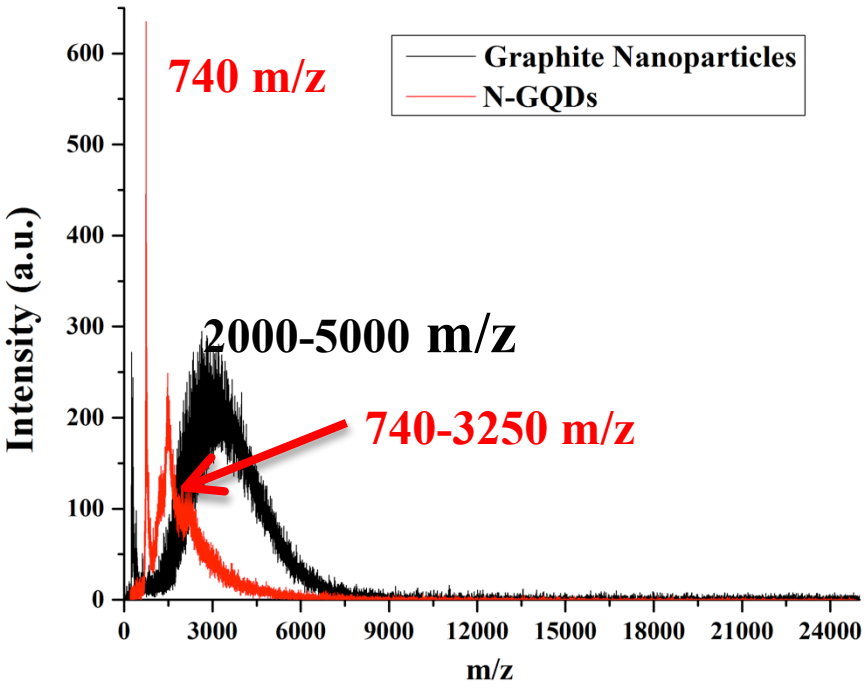

Figure II-H-11. The MALDI-TOF mass spectra of graphite nanoparticles and N-GQDs.

H-2-3 Fourier-transform Infrared (FT-IR) Spectroscopy

N-GQDs ethanol solution was dropped on a calcium fluoride (CaF_2) window and gradually evaporated the ethanol. The solid-state FT-IR spectrum shows N-GQDs have a broad peak at 3268 cm^{-1} that represents O-H stretching of carboxylic acid. (**Figure II-H-12**) The peak of 1712 cm^{-1} in the spectrum is associated with the C=O stretching mode of a carboxylic acid. These two evidences prove N-GQDs have the carboxyl functional group. IR peaks at 2944, 2925 and 2852 cm^{-1} reveal N-GQDs also have sp^3 C-H bonds while the peak at 1620 cm^{-1} indicates that they have C=C bonds in the structure. Additionally, the multiple peaks between 1432 and 1463 cm^{-1} represent the aromatic C=C bending modes and indicate this carbon nanomaterial still maintains aromaticity.

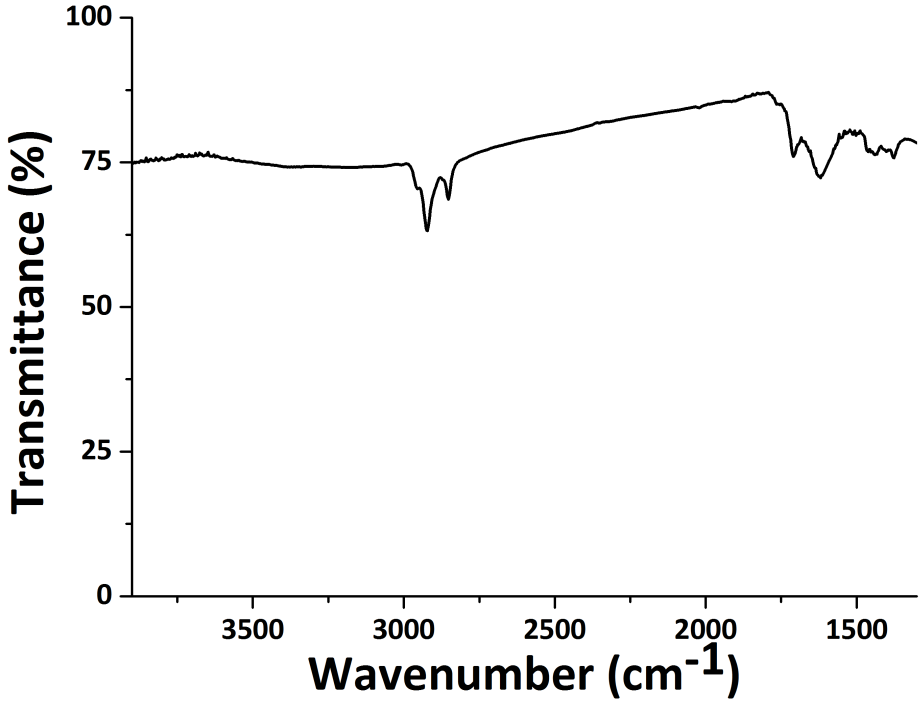

Figure II-H-12. The solid state IR spectrum of N-GQDs on a CaF_2 window.

H-2-4 X-ray Photoelectron Spectroscopy (XPS)

In addition to FT-IR spectroscopy, x-ray photoelectron spectroscopy (XPS) was applied to investigate possible functional groups on the surface of N-GQDs. In comparison to the XPS survey spectrum of graphite nanoparticles, N-GQDs have tremendously higher intensity of N 1s peak (399.5 eV). (**Figure II-H-13**) The reason could be that dimethyl amine decomposed from DMF under high temperature reacts with some functional groups such as epoxide on the surface of GQDs under ring-opening mechanism.[42] Additionally, according to the deconvoluted XPS spectrum of N-GQDs for the C 1s peak (**Figure II-H-14**), these carbon nanoparticles have a peak at 285.1 eV representing C-N bonds.[70] The peak at 283.9 eV is attributed to the abundant C=C bonds in the π- conjugated network after

Hummers' oxidation and solvothermal decomposition.[42] Especially, the O-C=O bond (287.8 eV) is introduced to N-GQDs and can be assigned to carboxyl group based on its FT-IR spectrum.[70]

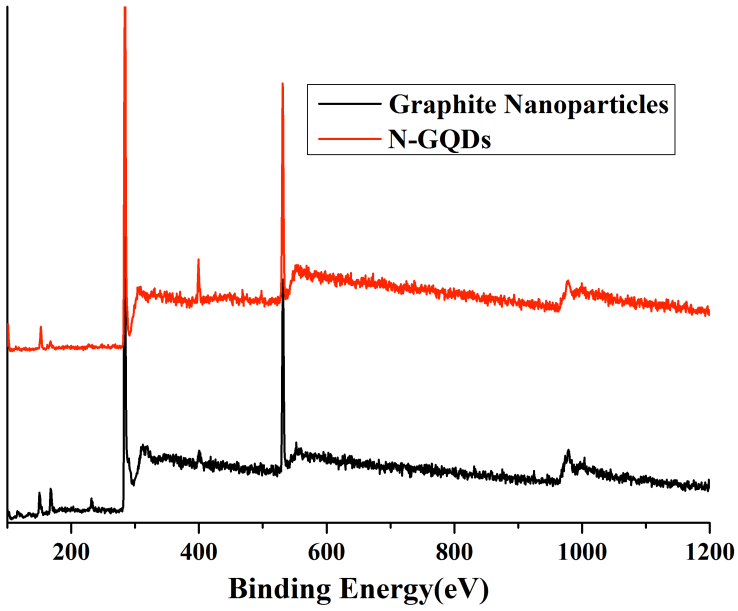

Figure II-H-13. XPS survey scan spectrum of graphite nanoparticles and N-GQDs.

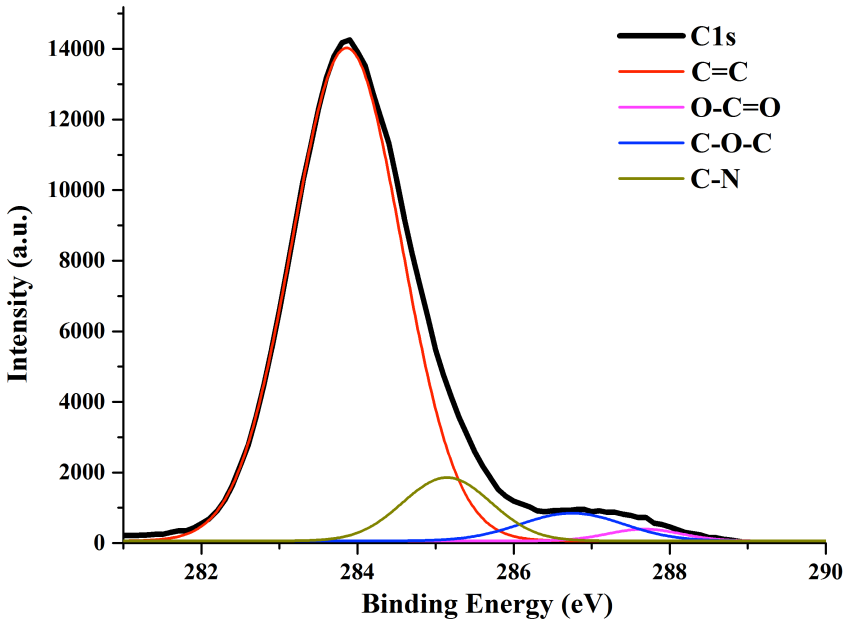

Figure II-H-14. C 1s high resolution XPS spectrum of N-GQDs.

H-2-5 UV-vis Spectroscopy and Photoluminescence Spectroscopy

The aqueous solution of N-GQDs is pale yellow and has strong green emission under 365 nm irradiation (**Figure II-H-15a**). The UV-vis absorption spectrum of N-GQDs dispersed in 18 MΩ water shows an peak at 227 nm that is attributed to the π - π* transition of C=C bond[42] and a peak at 322 nm, which is consistent with the literature data[44]. (**Figure II-H-15b**) The photoluminescence (PL) spectra present green emission under various wavelength excitations (**Figure II-H-15b**), and the fluorescent quantum yield (QY_f) was measured by following the literature.[58,71] Rhodamine B in ethanol (200 Proof) with 65% fluorescent quantum yield (Φ_R) acts as a reference. The QY_f (Φ_x) of N-GQDs was calculated according to the following equation:

$$\Phi_x = \Phi_R \left(\frac{Grad_x}{Grad_R}\right)\left(\frac{n_x^2}{n_R^2}\right)$$

$Grad_x$ and $Grad_R$ represent the gradient from the plot of integrated emission intensity vs absorbance at 365 nm. (**Figure II-H-16**) n_x and n_R are the refractive index of solvent I used for N-GQDs (water: 1.845) and rhodamine B (ethanol: 1.847). The subscript "x" refers to the N-GQDs while "R" refers to the reference. The QY_f of N-GQDs is 2.31% that is smaller than some of literature reports.[42,54,57,58] The possible reason is that N-GQDs have a significant amount of carboxylic acid and epoxide groups that serve as nonradiative electron-hole recombination centers to decrease the PL efficiency and increase the heat losses.[57] Therefore, these carbon nanomaterials may have photothermal effects that will be described in next section. (**H-2-6 Photothermal effect)**

Figure II-H-17 shows two-photon induced fluorescence spectrum of N-GQDs aqueous solution under 800 nm femtosecond laser excitation with 560 mW power, 80 MHz repetition rate and 140 fs pulse for 5 s exposure. The reference is fluorescein and the estimated two-photon cross section is 5 GM.

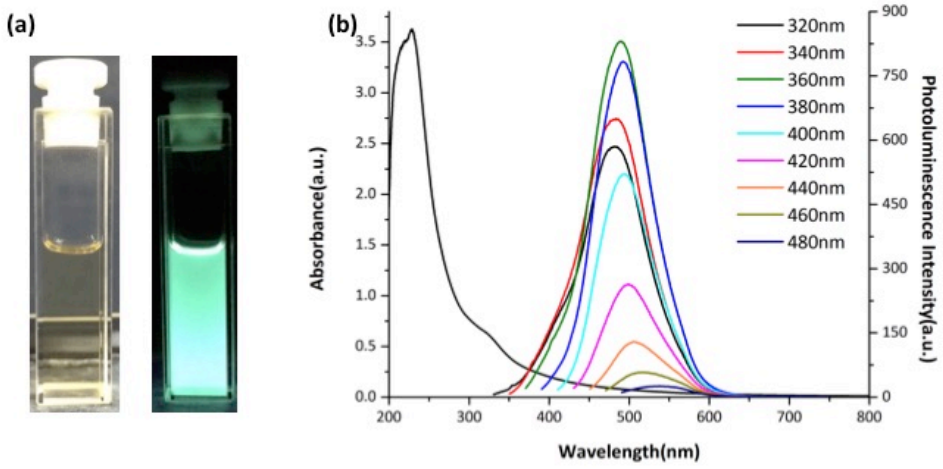

Figure II-H-15. (a) The photograph show N- GQDs aqueous solution without (left) and with (right) UV lamp (365nm) irradiation. (b) The absorption and emission spectra of N-GQDs aqueous solution.

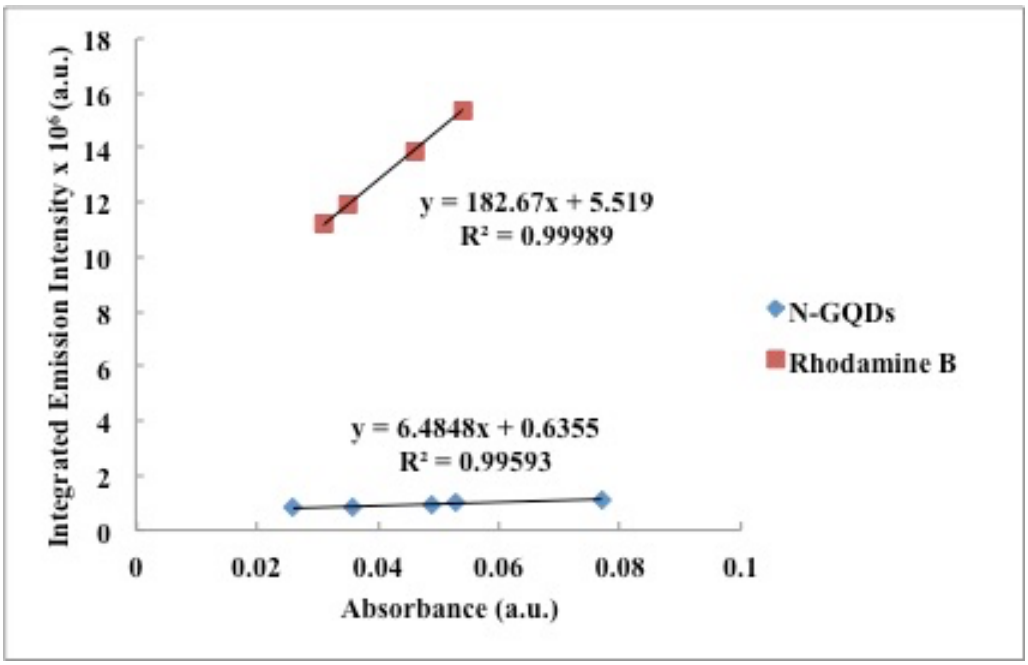

Figure II-H-16. A plot of integrated emission intensity vs absorbance at 365 nm.

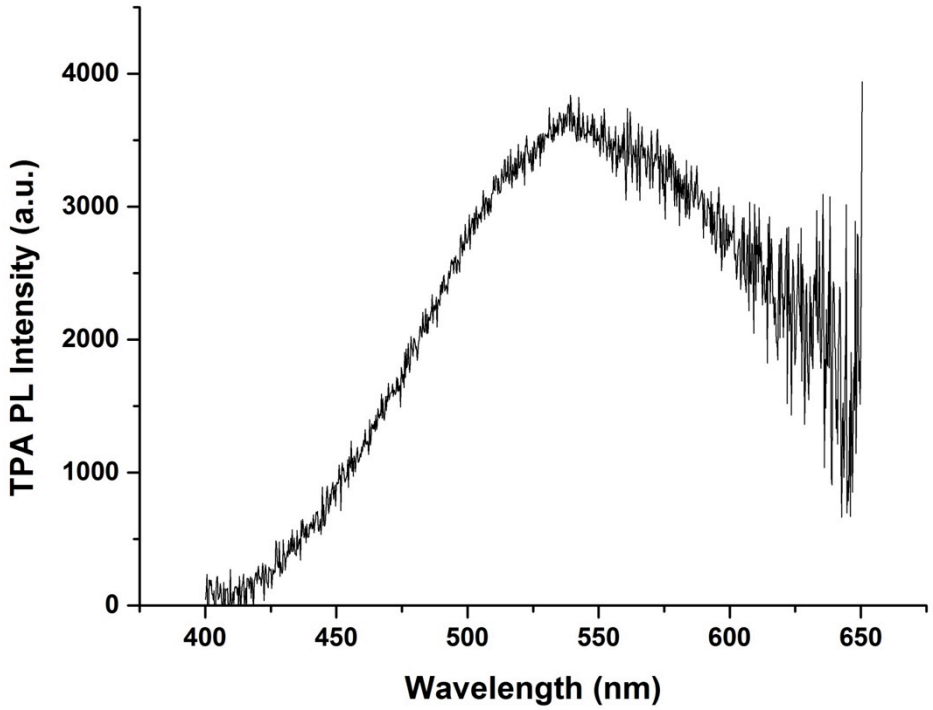

Figure II-H-17. Two-photon-induced fluorescence spectrum of N-GQD aqueous solution with concentration of 264 μg/mL under 800 nm femtosecond laser excitation.

H-2-6 Photothermal effect

Chen et al. have reported that graphene nanoparticles can convert NIR light to heat.[59] However, they didn't report how they set up the experiment and what the power density of laser they used. Therefore, in order to study the photothermal phenomenon, 2 mL aqueous solution of N-GQDs with concentration in 2 μg/mL was prepared and added into a designed cuvette with a magnetic stir bar. (**Figure II-H-18**) The whole system wasn't isolated from the environment and the solution was stirred during the measurement. The real-time temperature record was performed by using a temperature recorder with two K-type thermocouples. One thermocouple was inserted into the sample cell while another was inserted into the control cell that only contained pure water. The value of temperature increased is the subtraction between two cells. In comparison to 18 MΩ pure water, the temperature of N-GQDs(aq) increase 0.5 ^{0}C under 794 nm laser irradiation with a power density of 19.95 W/cm^2 for 30 min exposure. (**Figure II-H-19**)

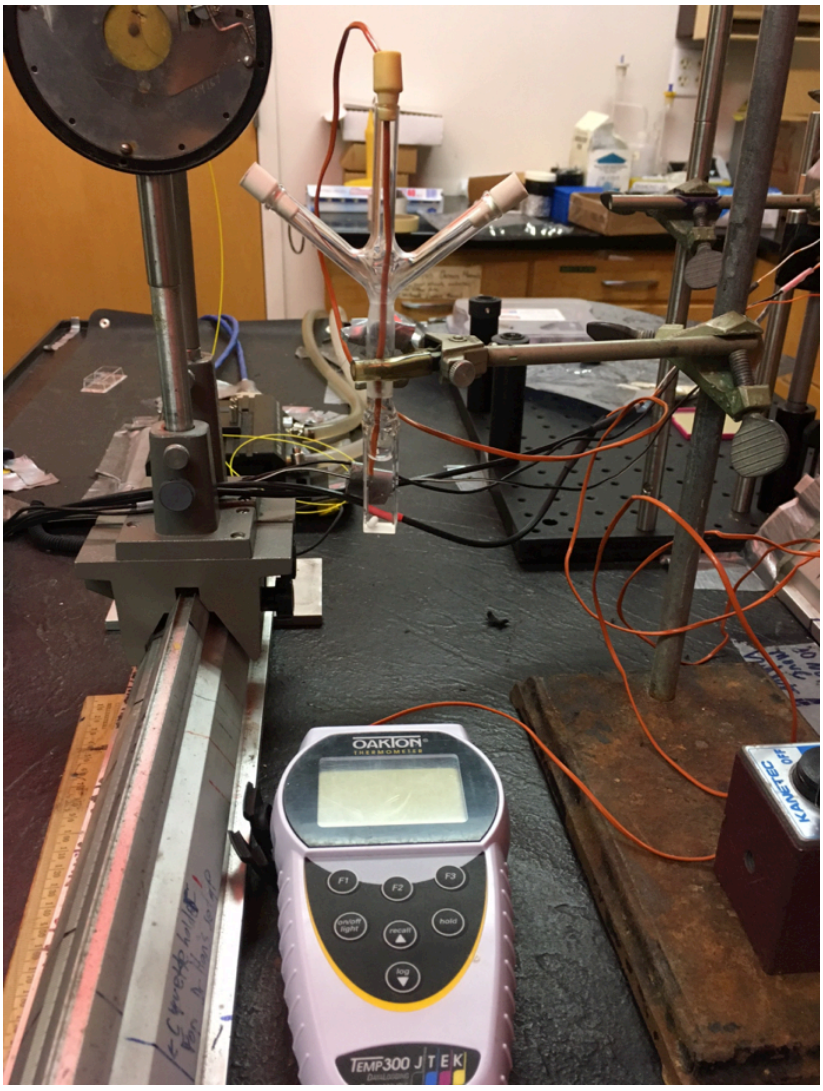

Figure II-H-18. The setup for a photothermal experiment with a designed cuvette.

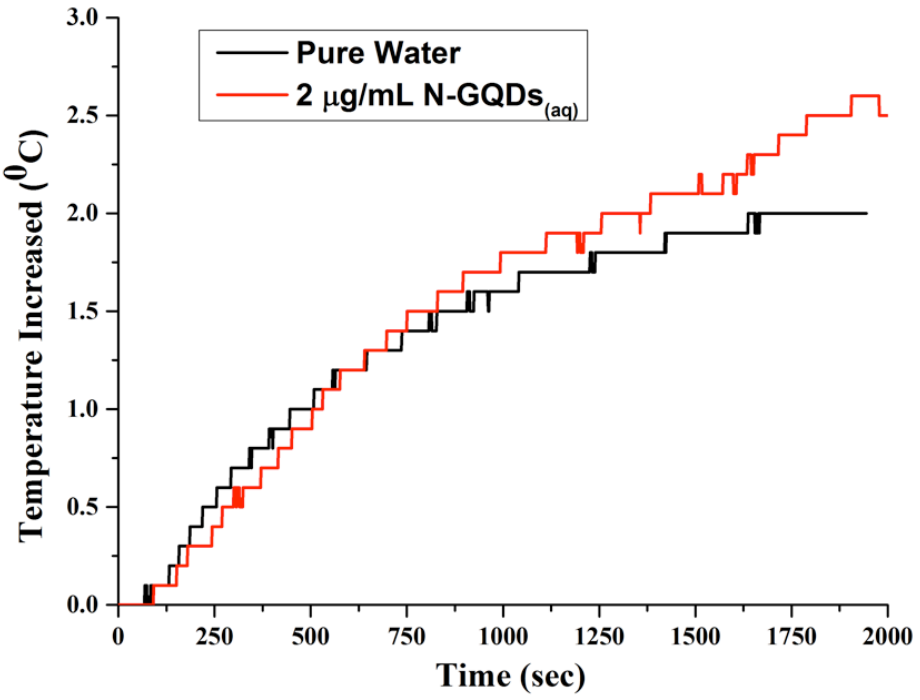

Figure II-H-19. The plot of temperature increased vs irradiation time. The sample solution (pure water or $GQDs_{(aq)}$) was added into a designed quartz cell and irradiated by a 794 nm diode laser for 30 min in an open system.

I. Reference

(1) Ford, P. C. Photochemical Delivery of Nitric Oxide. *Nitric Oxide* **2013**, *34*, 56–64.

(2) Hideg, K.; Lloyd, D. Reaction Products from Aβ-Unsaturated Ketones and Aliphatic Diamines or Dithiols. *J. Chem. Soc. C Org.* **1971**, No. 0, 3441–3445.

(3) Liang, X.; J. Sadler, P. Cyclam Complexes and Their Applications in Medicine. *Chem. Soc. Rev.* **2004**, *33* (4), 246–266.

(4) Curtis, N. F. 507. Some Cyclic Tetra-Amines and Their Metal-Ion Complexes. Part I. Two Isomeric Hexamethyltetra-Azacyclotetradecanes and Their copper(II) and nickel(II) Complexes. *J. Chem. Soc. Resumed* **1964**, No. 0, 2644–2650.

(5) Curtis, N. F.; Hay, R. W. A Novel Heterocycle Synthesis. Formation of 5,7,7,12,14,14-Hexamethyl-1,4,8,11-Tetra-Azacyclotetradeca-4,11-Diene Dihydroperchlorate by Reaction of Diaminoethane Monohydroperchlorate with Mesityl Oxide or Acetone. *Chem. Commun. Lond.* **1966**, No. 15, 524–525.

(6) Warner, L. G.; Rose, N. J.; Busch, D. H. Stereochemistry of a Macrocyclic Complex. Chelate Ring Conformations and Unusual Isomers. *J. Am. Chem. Soc.* **1967**, *89* (3), 703–704.

(7) Hay, R. W.; Pujari, M. P.; Hideg, K.; Hankovszky, O. H. Macrocyclic Ligands with Potential Axial Interactions. The Preparation of copper(II), nickel(II) and cobalt(III) Complexes of 7,14-O-Hydroxyphenyl-5,12-Dimethyl-1,4,8,11-Tetraazacyclotetradeca-4,11-Diene. *Transit. Met. Chem.* **1985**, *10* (5), 188–191.

(8) Belmessieri, D.; Morrill, L. C.; Simal, C.; Slawin, A. M. Z.; Smith, A. D. Organocatalytic Functionalization of Carboxylic Acids: Isothiourea-Catalyzed Asymmetric

Intra- and Intermolecular Michael Addition−Lactonizations. *J. Am. Chem. Soc.* **2011**, *133* (8), 2714–2720.

(9) Hay, R. W.; Gidney, P. M. Cobalt(III) and rhodium(III) Complexes of Mesa-5,12-Dimethyl-7,14-Di-Phenyl-1,4,8,11-Tetra-Azacyclotetradeca-4,11-Diene and Meso-Meso-5,12-Dimethyl-7,14-Diphenyl-1,4,8,11-Tetra-Azacyclotetradecane. *J. Chem. Soc. Dalton Trans.* **1976**, No. 11, 974–978.

(10) Cook, D. F.; Curtis, N. F.; Rickard, C. E. F.; Waters, J. M.; Weatherburn, D. C. Compounds of nickel(II) with 5RS,7RS,12SR,14SR-5,12-Dimethyl-7,14-Diphenyl-1,4,8,11-Tetraazacyclotetradecane, mmL2; the Structures of δ-[Ni(mmL2)](ClO4)2, Trans-β-[Ni(mmL2)(NO2-N)2] and Cis-α-[Ni(mmL2)(acac)]ClO4. *Inorganica Chim. Acta* **2003**, *355*, 1–14.

(11) Ostrowski, A. D.; Absalonson, R. O.; Leo, M. A. D.; Wu, G.; Pavlovich, J. G.; Adamson, J.; Azhar, B.; Iretskii, A. V.; Megson, I. L.; Ford, P. C. Photochemistry of Trans-Cr(cyclam)(ONO)2+, a Nitric Oxide Precursor. *Inorg. Chem.* **2011**, *50* (10), 4453–4462.

(12) Ferguson, J.; Tobe, M. L. Complexes of chromium(III) with a Cyclic Tetradentate Secondary Amine. *Inorganica Chim. Acta* **1970**, *4*, 109–112.

(13) Poon, C. K.; Pun, K. C. Improved Syntheses of Trans Isomers of chromium(III) Complexes with 1,4,8,11-Tetraazacyclotetradecane. *Inorg. Chem.* **1980**, *19* (2), 568–569.

(14) De Leo, M. A.; Bu, X.; Bentow, J.; Ford, P. C. The Synthesis, Characterization and Structures of the chromium(III) Dinitrito Complexes: Trans-[Cr(L)(ONO)2]+ (L=1,4,8,11-Tetraazacyclotetradecane or 5,7,7,12,14,14-Hexamethyl-1,4,8,11-Tetraazacyclotetradecane). *Inorganica Chim. Acta* **2000**, *300–302*, 944–950.

(15) Yamaji, M.; Hama, Y.; Miyazaki, Y.; Hoshino, M. Photochemical Formation of oxochromium(IV) Tetraphenylporphyrin from nitritochromium(III) Tetraphenylporphyrin in Benzene. *Inorg. Chem.* **1992**, *31* (5), 932–934.

(16) Yamaji, M. Photochemistry of chlorochromium(III) Tetraphenylporphyrinate in Acetone. Studies on Photodissociation of the Axial Acetone in the Temperature Range 180-295 K by Laser Photolysis. *Inorg. Chem.* **1991**, *30* (14), 2949–2952.

(17) Inamo, M.; Eba, K.; Nakano, K.; Itoh, N.; Hoshino, M. Laser Photolysis Studies of the Photochemical Reactions of Chromium(III) Octaethylporphyrin and Tetramesitylporphyrin Complexes in Toluene Solution. *Inorg. Chem.* **2003**, *42* (19), 6095–6105.

(18) Inamo, M.; Nakaba, H.; Nakajima, K.; Hoshino, M. Laser Photolysis of Chromium(III) Porphyrins with Axial Pyridines in Dichloromethane and Toluene Solutions. Novel Effects of a Hydrogen Bond in the Ligand Exchange Reaction. *Inorg. Chem.* **2000**, *39* (20), 4417–4423.

(19) De Leo, M.; Ford, P. C. Reversible Photolabilization of NO from Chromium(III)-Coordinated Nitrite. A New Strategy for Nitric Oxide Delivery. *J. Am. Chem. Soc.* **1999**, *121* (9), 1980–1981.

(20) DeRosa, F.; Bu, X.; Ford, P. C. Chromium(III) Complexes for Photochemical Nitric Oxide Generation from Coordinated Nitrite: Synthesis and Photochemistry of Macrocyclic Complexes with Pendant Chromophores, Trans-[Cr(L)(ONO)2]BF4. *Inorg. Chem.* **2005**, *44* (12), 4157–4165.

(21) Levy, E. S.; Tajon, C. A.; Bischof, T. S.; Iafrati, J.; Fernandez-Bravo, A.; Garfield, D. J.; Chamanzar, M.; Maharbiz, M. M.; Sohal, V. S.; Schuck, P. J.; Cohen, B. E.; Chan, E.

M. Energy-Looping Nanoparticles: Harnessing Excited-State Absorption for Deep-Tissue Imaging. *ACS Nano* **2016**, *10* (9), 8423–8433.

(22) Xie, X.; Gao, N.; Deng, R.; Sun, Q.; Xu, Q.-H.; Liu, X. Mechanistic Investigation of Photon Upconversion in Nd3+-Sensitized Core–Shell Nanoparticles. *J. Am. Chem. Soc.* **2013**, *135* (34), 12608–12611.

(23) Ostrowski, A. D.; Chan, E. M.; Gargas, D. J.; Katz, E. M.; Han, G.; Schuck, P. J.; Milliron, D. J.; Cohen, B. E. Controlled Synthesis and Single-Particle Imaging of Bright, Sub-10 Nm Lanthanide-Doped Upconverting Nanocrystals. *ACS Nano* **2012**, *6* (3), 2686–2692.

(24) Wang, F.; Han, Y.; Lim, C. S.; Lu, Y.; Wang, J.; Xu, J.; Chen, H.; Zhang, C.; Hong, M.; Liu, X. Simultaneous Phase and Size Control of Upconversion Nanocrystals through Lanthanide Doping. *Nature* **2010**, *463* (7284), 1061–1065.

(25) Yi, G. S.; Chow, G. M. Synthesis of Hexagonal-Phase NaYF4:Yb,Er and NaYF4:Yb,Tm Nanocrystals with Efficient Up-Conversion Fluorescence. *Adv. Funct. Mater.* **2006**, *16* (18), 2324–2329.

(26) Wang, Y.-F.; Liu, G.-Y.; Sun, L.-D.; Xiao, J.-W.; Zhou, J.-C.; Yan, C.-H. Nd3+-Sensitized Upconversion Nanophosphors: Efficient In Vivo Bioimaging Probes with Minimized Heating Effect. *ACS Nano* **2013**, *7* (8), 7200–7206.

(27) Zhao, Y.; Zhan, Q.; Liu, J.; He, S. Optically Investigating Nd3+-Yb3+ Cascade Sensitized Upconversion Nanoparticles for High Resolution, Rapid Scanning, Deep and Damage-Free Bio-Imaging. *Biomed. Opt. Express* **2015**, *6* (3), 838–848.

(28) Hitomi, Y.; Iwamoto, Y.; Kodera, M. Electronic Tuning of Nitric Oxide Release from Manganese Nitrosyl Complexes by Visible Light Irradiation: Enhancement of Nitric

Oxide Release Efficiency by the Nitro-Substituted Quinoline Ligand. *Dalton Trans.* **2013**, *43* (5), 2161–2167.

(29) Park, T. G.; Yong Lee, H.; Sung Nam, Y. A New Preparation Method for Protein Loaded Poly(d,l-Lactic-Co-Glycolic Acid) Microspheres and Protein Release Mechanism Study. *J. Controlled Release* **1998**, *55* (2–3), 181–191.

(30) Zambaux, M. F.; Bonneaux, F.; Gref, R.; Maincent, P.; Dellacherie, E.; Alonso, M. J.; Labrude, P.; Vigneron, C. Influence of Experimental Parameters on the Characteristics of Poly(lactic Acid) Nanoparticles Prepared by a Double Emulsion Method. *J. Controlled Release* **1998**, *50* (1–3), 31–40.

(31) Champion, J. A.; Katare, Y. K.; Mitragotri, S. Particle Shape: A New Design Parameter for Micro- and Nanoscale Drug Delivery Carriers. *J. Controlled Release* **2007**, *121* (1–2), 3–9.

(32) Jiang, K.; Sun, S.; Zhang, L.; Lu, Y.; Wu, A.; Cai, C.; Lin, H. Red, Green, and Blue Luminescence by Carbon Dots: Full-Color Emission Tuning and Multicolor Cellular Imaging. *Angew. Chem. Int. Ed.* **2015**, *54* (18), 5360–5363.

(33) Liu, H.; Ye, T.; Mao, C. Fluorescent Carbon Nanoparticles Derived from Candle Soot. *Angew. Chem. Int. Ed.* **2007**, *46* (34), 6473–6475.

(34) Souza, D. R. da S.; Mesquita, J. P. de; Lago, R. M.; Caminhas, L. D.; Pereira, F. V. Cellulose Nanocrystals: A Versatile Precursor for the Preparation of Different Carbon Structures and Luminescent Carbon Dots. *Ind. Crops Prod.* **2016**, *93*, 121–128.

(35) Briscoe, J.; Marinovic, A.; Sevilla, M.; Dunn, S.; Titirici, M. Biomass-Derived Carbon Quantum Dot Sensitizers for Solid-State Nanostructured Solar Cells. *Angew. Chem. Int. Ed.* **2015**, *54* (15), 4463–4468.

(36) Peng, H.; Li, Y.; Jiang, C.; Luo, C.; Qi, R.; Huang, R.; Duan, C.-G.; Travas-Sejdic, J. Tuning the Properties of Luminescent Nitrogen-Doped Carbon Dots by Reaction Precursors. *Carbon* **2016**, *100*, 386–394.

(37) Sun, S.; Zhang, L.; Jiang, K.; Wu, A.; Lin, H. Toward High-Efficient Red Emissive Carbon Dots: Facile Preparation, Unique Properties, and Applications as Multifunctional Theranostic Agents. *Chem. Mater.* **2016**, *28* (23), 8659–8668.

(38) Tetsuka, H.; Nagoya, A.; Asahi, R. Highly Luminescent Flexible Amino-Functionalized Graphene Quantum Dots@cellulose Nanofiber–clay Hybrids for White-Light Emitting Diodes. *J. Mater. Chem. C* **2015**, *3* (15), 3536–3541.

(39) Sun, H.; Gao, N.; Wu, L.; Ren, J.; Wei, W.; Qu, X. Highly Photoluminescent Amino-Functionalized Graphene Quantum Dots Used for Sensing Copper Ions. *Chem. – Eur. J.* **2013**, *19* (40), 13362–13368.

(40) Tetsuka, H.; Asahi, R.; Nagoya, A.; Okamoto, K.; Tajima, I.; Ohta, R.; Okamoto, A. Optically Tunable Amino-Functionalized Graphene Quantum Dots. *Adv. Mater.* **2012**, *24* (39), 5333–5338.

(41) Feng, L.; Liu, Y.-W.; Tang, X.-Y.; Piao, Y.; Chen, S.-F.; Deng, S.-L.; Xie, S.-Y.; Wang, Y.; Zheng, L.-S. Propagative Exfoliation of High Quality Graphene. *Chem. Mater.* **2013**, *25* (22), 4487–4496.

(42) Liu, Q.; Guo, B.; Rao, Z.; Zhang, B.; Gong, J. R. Strong Two-Photon-Induced Fluorescence from Photostable, Biocompatible Nitrogen-Doped Graphene Quantum Dots for Cellular and Deep-Tissue Imaging. *Nano Lett.* **2013**, *13* (6), 2436–2441.

(43) Lee, S.-H.; Seo, S.-D.; Jin, Y.-H.; Shim, H.-W.; Kim, D.-W. A Graphite Foil Electrode Covered with Electrochemically Exfoliated Graphene Nanosheets. *Electrochem. Commun.* **2010**, *12* (10), 1419–1422.

(44) Li, Y.; Hu, Y.; Zhao, Y.; Shi, G.; Deng, L.; Hou, Y.; Qu, L. An Electrochemical Avenue to Green-Luminescent Graphene Quantum Dots as Potential Electron-Acceptors for Photovoltaics. *Adv. Mater.* **2011**, *23* (6), 776–780.

(45) Bourelle, E.; Dougiade, J.; Metrot, A. Electrochemical Exfoliation of Graphite in Trifluoroacetic Media. *Mol. Cryst. Liq. Cryst. Sci. Technol. Sect. Mol. Cryst. Liq. Cryst.* **1994**, *244* (1), 227–232.

(46) Parvez, K.; Wu, Z.-S.; Li, R.; Liu, X.; Graf, R.; Feng, X.; Müllen, K. Exfoliation of Graphite into Graphene in Aqueous Solutions of Inorganic Salts. *J. Am. Chem. Soc.* **2014**, *136* (16), 6083–6091.

(47) Wei, D.; Grande, L.; Chundi, V.; White, R.; Bower, C.; Andrew, P.; Ryhänen, T. Graphene from Electrochemical Exfoliation and Its Direct Applications in Enhanced Energy Storage Devices. *Chem. Commun.* **2012**, *48* (9), 1239–1241.

(48) Su, C.-Y.; Lu, A.-Y.; Xu, Y.; Chen, F.-R.; Khlobystov, A. N.; Li, L.-J. High-Quality Thin Graphene Films from Fast Electrochemical Exfoliation. *ACS Nano* **2011**, *5* (3), 2332–2339.

(49) Wang, J.; Manga, K. K.; Bao, Q.; Loh, K. P. High-Yield Synthesis of Few-Layer Graphene Flakes through Electrochemical Expansion of Graphite in Propylene Carbonate Electrolyte. *J. Am. Chem. Soc.* **2011**, *133* (23), 8888–8891.

(50) Liu, J.; Poh, C. K.; Zhan, D.; Lai, L.; Lim, S. H.; Wang, L.; Liu, X.; Gopal Sahoo, N.; Li, C.; Shen, Z.; Lin, J. Improved Synthesis of Graphene Flakes from the Multiple Electrochemical Exfoliation of Graphite Rod. *Nano Energy* **2013**, *2* (3), 377–386.

(51) Lu, J.; Yang, J.; Wang, J.; Lim, A.; Wang, S.; Loh, K. P. One-Pot Synthesis of Fluorescent Carbon Nanoribbons, Nanoparticles, and Graphene by the Exfoliation of Graphite in Ionic Liquids. *ACS Nano* **2009**, *3* (8), 2367–2375.

(52) Hummers, W. S.; Offeman, R. E. Preparation of Graphitic Oxide. *J. Am. Chem. Soc.* **1958**, *80* (6), 1339–1339.

(53) Loh, K. P.; Bao, Q.; Eda, G.; Chhowalla, M. Graphene Oxide as a Chemically Tunable Platform for Optical Applications. *Nat. Chem.* **2010**, *2* (12), 1015–1024.

(54) Wang, L.; Zhu, S.-J.; Wang, H.-Y.; Qu, S.-N.; Zhang, Y.-L.; Zhang, J.-H.; Chen, Q.-D.; Xu, H.-L.; Han, W.; Yang, B.; Sun, H.-B. Common Origin of Green Luminescence in Carbon Nanodots and Graphene Quantum Dots. *ACS Nano* **2014**, *8* (3), 2541–2547.

(55) Liu, Y.; Wu, P. Graphene Quantum Dot Hybrids as Efficient Metal-Free Electrocatalyst for the Oxygen Reduction Reaction. *ACS Appl. Mater. Interfaces* **2013**, *5* (8), 3362–3369.

(56) Pan, D.; Zhang, J.; Li, Z.; Wu, M. Hydrothermal Route for Cutting Graphene Sheets into Blue-Luminescent Graphene Quantum Dots. *Adv. Mater.* **2010**, *22* (6), 734–738.

(57) Tetsuka, H.; Asahi, R.; Nagoya, A.; Okamoto, K.; Tajima, I.; Ohta, R.; Okamoto, A. Optically Tunable Amino-Functionalized Graphene Quantum Dots. *Adv. Mater.* **2012**, *24* (39), 5333–5338.

(58) Feng, L.; Tang, X.-Y.; Zhong, Y.-X.; Liu, Y.-W.; Song, X.-H.; Deng, S.-L.; Xie, S.-Y.; Yan, J.-W.; Zheng, L.-S. Ultra-Bright Alkylated Graphene Quantum Dots. *Nanoscale* **2014**, *6* (21), 12635–12643.

(59) He, Q.; Kiesewetter, D. O.; Qu, Y.; Fu, X.; Fan, J.; Huang, P.; Liu, Y.; Zhu, G.; Liu, Y.; Qian, Z.; Chen, X. NIR-Responsive On-Demand Release of CO from Metal Carbonyl-Caged Graphene Oxide Nanomedicine. *Adv. Mater.* **2015**, *27* (42), 6741–6746.

(60) Ming, H.; Ma, Z.; Liu, Y.; Pan, K.; Yu, H.; Wang, F.; Kang, Z. Large Scale Electrochemical Synthesis of High Quality Carbon Nanodots and Their Photocatalytic Property. *Dalton Trans.* **2012**, *41* (31), 9526–9531.

(61) Liu, J.; Yang, H.; Zhen, S. G.; Poh, C. K.; Chaurasia, A.; Luo, J.; Wu, X.; Yeow, E. K. L.; Sahoo, N. G.; Lin, J.; Shen, Z. A Green Approach to the Synthesis of High-Quality Graphene Oxide Flakes via Electrochemical Exfoliation of Pencil Core. *RSC Adv.* **2013**, *3* (29), 11745–11750.

(62) Parvez, K.; Li, R.; Puniredd, S. R.; Hernandez, Y.; Hinkel, F.; Wang, S.; Feng, X.; Müllen, K. Electrochemically Exfoliated Graphene as Solution-Processable, Highly Conductive Electrodes for Organic Electronics. *ACS Nano* **2013**, *7* (4), 3598–3606.

(63) Su, C.-Y.; Lu, A.-Y.; Xu, Y.; Chen, F.-R.; Khlobystov, A. N.; Li, L.-J. High-Quality Thin Graphene Films from Fast Electrochemical Exfoliation. *ACS Nano* **2011**, *5* (3), 2332–2339.

(64) Liu, F.; Jang, M.-H.; Ha, H. D.; Kim, J.-H.; Cho, Y.-H.; Seo, T. S. Facile Synthetic Method for Pristine Graphene Quantum Dots and Graphene Oxide Quantum Dots: Origin of Blue and Green Luminescence. *Adv. Mater.* **2013**, *25* (27), 3657–3662.

(65) Jang, M.-H.; Ha, H. D.; Lee, E.-S.; Liu, F.; Kim, Y.-H.; Seo, T. S.; Cho, Y.-H. Is the Chain of Oxidation and Reduction Process Reversible in Luminescent Graphene Quantum Dots? *Small* **2015**, *11* (31), 3773–3781.

(66) Xu, Y.; Bai, H.; Lu, G.; Li, C.; Shi, G. Flexible Graphene Films via the Filtration of Water-Soluble Noncovalent Functionalized Graphene Sheets. *J. Am. Chem. Soc.* **2008**, *130* (18), 5856–5857.

(67) Kim, S.; Hwang, S. W.; Kim, M.-K.; Shin, D. Y.; Shin, D. H.; Kim, C. O.; Yang, S. B.; Park, J. H.; Hwang, E.; Choi, S.-H.; Ko, G.; Sim, S.; Sone, C.; Choi, H. J.; Bae, S.; Hong, B. H. Anomalous Behaviors of Visible Luminescence from Graphene Quantum Dots: Interplay between Size and Shape. *ACS Nano* **2012**, *6* (9), 8203–8208.

(68) Luo, P.; Ji, Z.; Li, C.; Shi, G. Aryl-Modified Graphene Quantum Dots with Enhanced Photoluminescence and Improved pH Tolerance. *Nanoscale* **2013**, *5* (16), 7361–7367.

(69) Niyogi, S.; Bekyarova, E.; Itkis, M. E.; McWilliams, J. L.; Hamon, M. A.; Haddon, R. C. Solution Properties of Graphite and Graphene. *J. Am. Chem. Soc.* **2006**, *128* (24), 7720–7721.

(70) Zhu, X.; Zuo, X.; Hu, R.; Xiao, X.; Liang, Y.; Nan, J. Hydrothermal Synthesis of Two Photoluminescent Nitrogen-Doped Graphene Quantum Dots Emitted Green and Khaki Luminescence. *Mater. Chem. Phys.* **2014**, *147* (3), 963–967.

(71) Casey, K. G.; Quitevis, E. L. Effect of Solvent Polarity on Nonradiative Processes in Xanthene Dyes: Rhodamine B in Normal Alcohols. *J. Phys. Chem.* **1988**, *92* (23), 6590–6594.

III. Macrophage-Mediated Delivery of Light Activated Nitric Oxide Prodrugs for Cancer Therapy with Spatial, Temporal and Concentration Control

A. Abstract

Nitric oxide (NO) holds great promise as a treatment for cancer hypoxia; however, precise control over its dosage and localization is necessary to assure success. Often, these factors are difficult to control due to the short biological half-life of free NO and diffusion limitations of NO releasing molecules to areas of tumor hypoxia. Here, we describe a method to provide spatial, temporal, and concentration control over NO-based cancer therapies by utilizing bone marrow derived murine macrophages (BMMs) as carriers for biodegradable polymeric micro-particles containing the photoactivated NO releasing moiety, $[Mn(NO)dpaq^{NO}{}_2]BPh_4$, and Nd^{3+} doped upconverting nanoparticles (Nd-UCNP). Both components are activated by tissue penetrating near-infrared (NIR) light allowing for simultaneous therapeutic NO delivery and photoluminescence (PL) imaging capabilities with a single NIR laser source. The micro-particles were determined to be non-toxic to their macrophage hosts in the absence of light and to demonstrate the ability to generate intracellularly localized NO upon NIR excitation. Histological sectioning revealed that the macrophages penetrate deep into large NIH-3T3/4T1 cocultured tumor spheroids. NIR laser excitation of these macrophage treated spheroids led to the release of measurable amounts of NO that could be quantified in quasi real-time. Furthermore, the Nd-UCNP PL demonstrated macrophage infiltration into the spheroids. Most strikingly, by varying light source intensity, we were able to garner control over NO release rates reducing hypoxia inducible factor 1 alpha (HIF-1α) levels with low doses of NO while demonstrating direct cytoxicity to

spheroids with high doses of NO. The use of macrophages as “Trojan Horses” to carry micro-particles with a theranostic payload represents a novel approach that overcomes challenges often faced with therapeutic administration of NO and offers the potential of multiple treatment strategies with a single system.

B. Introduction

In many solid tumors, the rapid rate of tumor cell growth leads to hypoxic areas with poor blood supply and low oxygen concentration.[1] Such hypoxia serves as a signal to begin the wound healing process through the production of prosurvival and proliferative factors such as hypoxia-inducible factor 1-α (HIF-1α) and vascular endothelial growth factor (VEGF).[2,3] While this response to hypoxia is crucial for efficient wound healing, its implementation in areas of tumor hypoxia is the cause of problems such as resistance to chemotherapy and radiation leading to poor prognosis and reduced survival.[3,4]

Nitric oxide (NO) has exhibited significant potential as a cancer therapy; however, its effects are highly dosage- and location-dependent.[5] Previous reports have indicated that high NO concentrations can induce p53 (~300 nM) or nitrosative stress mediated apoptosis (>1000 nM).[5–7] Low concentrations (hundreds of pM and tens of nM) have been shown to produce beneficial shifts in the composition of the tumor microenvironment through the reduction of factors such as p-glycoprotein and HIF-1α that have been implicated in providing cancer cells with increased resistance to traditional chemotherapeutics like doxorubicin as well radiation therapy.[8–11] In contrast, intermediate concentrations of NO have tumor protective effects through apoptosis resistance caused by the stabilization of proteins such as HIF-1α and protein kinase B (Akt-P).[5]

Its relatively short lifetime in physiological media and significant systemic side effects have made NO difficult to implement as a therapy for cancer without an effective targeting strategy.[6] One such approach is to use photo-activated NO releasing moieties (photoNORMs), since triggering with light provides precise spatial and temporal control of

delivery.[12,13] However, this methodology is limited by the strong wavelength dependence of light transmission through tissue.[14] Ultraviolet and shorter visible wavelengths have much less tissue penetration than do longer red or (ideally) near-infrared (NIR) wavelengths. The ability of NIR light to penetrate deeper into tissue has inspired various approaches to designing photoNORM systems including the engineering of molecular compounds that are photoactive at longer wavelengths[15,16] and the use of antennas for multi-photon sensitization of NO release with NIR light.[12,17] However, delivering these conjugates to the desired physiological targets continues to be challenging. For example, it is difficult to make such delivery to hypoxic areas of tumors, where the vascular structures are poorly developed,[18] via simple diffusion from the blood stream.

It is well established that tumor hypoxia generates inflammatory signals. These signals recruit monocytes from the blood via chemotaxis, and once at the site, these cells differentiate into macrophages that are inactivated from their normal roles as immune cells. As a result, macrophages can make up 50-70% of a tumor mass in some cases.[1,18] With this in mind, several recent studies have utilized macrophages as drug carriers[19,20] and demonstrated the ability to localize drugs in areas of hypoxia at levels difficult to attain with conventional delivery methods.[18,21–23] While these payloads may be tumorcidal, recent research has indicated the importance of being able to control the tumor microenvironment to assure long term therapeutic success.[24]

Figure III-B-1 shows the present study demonstrates the utility of macrophages as carriers of micron-sized, immunoglobulin G (IgG) coated, poly(lactic-co-glycolic acid) (PLGA) micro-particles in which one can incorporate different payloads. The encapsulated payload here included a photoNORM that can be triggered for NO release by NIR light,[15] as

well as Nd^{3+} doped upconverting nanoparticles (Nd-UCNPs) to provide imaging capabilities under NIR light.[25] BALB/c bone marrow derived macrophages (BMMs) were shown to phagocytose large numbers of these micro-particle carriers. The use of macrophages allowed for far deeper penetration of drug into large NIH-3T3/4T1 cocultured tumor spheroids than the micro-particles alone. It is shown that, once carried inside the spheroid by the BMM, the photoNORM in the micro-particles can be activated with NIR light. Furthermore, at high light intensity, NO concentrations sufficient to cause direct tumor cytotoxicity were generated, while at low light intensity, the NO released led to striking changes in the tumor microenvironment as evidenced by a significant drop in HIF-1α expression.

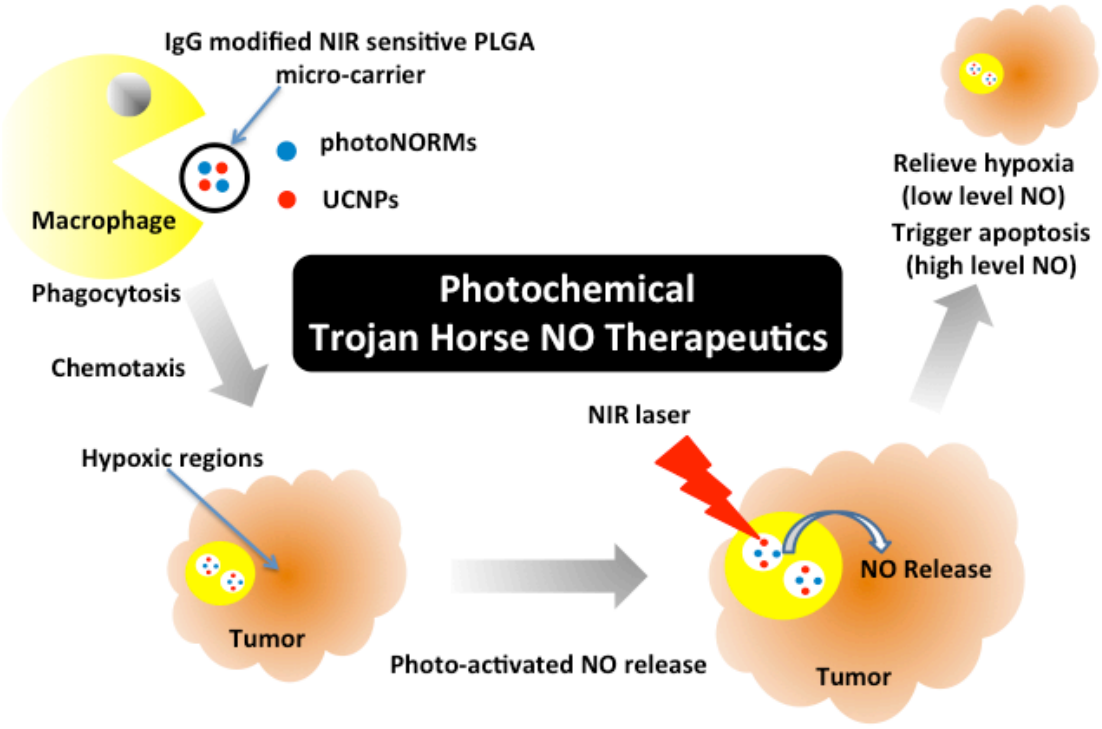

Figure III-B-1. Macrophage-mediated delivery of micro-particles containing a photoNORM and UCNPs for NIR light triggered NO release.

C. NIR active photoNORM and bioimaging Nd-UCNPs

The cell-mediated delivery platform described here consisted of murine bone marrow macrophages (BMMs) loaded with polymer-based micro-carriers in which were incorporated an NIR sensitive photoNORM and NIR active bioimaging Nd-UCNPs. The photoNORM was prepared by metathesis of the water-soluble $[Mn(dpaq^{NO_2})(NO)]ClO_4$ ($dpaq^{NO_2}$ = 2-[*N*,*N*-bis(pyridin-2-ylmethyl)]-amino-*N*′-5-nitro-quinolin-8-yl-acetamido) with sodium tetraphenylborate to give the corresponding, hydrophobic photoNORM $[Mn(dpaq^{NO_2})(NO)]BPh_4$ (**I**). The hydrophobicity was needed to minimize leakage of **I** from the micro-carrier to the medium. This BPh_4^- salt was further purified by recrystallization to obtain black needle crystals. Figure III-C-1 shows the spectrum of **I** in acetonitrile. Although λ_{max} of the longest wavelength band is ~ 650 nm, this absorbance extends to the NIR region s (ε: 20.2 $M^{-1}cm^{-1}$ at 794 nm) and overlaps with the 794 nm diode laser used as the excitation source in the present study. (**Figure III-C-1 Inset**) Direct 794 nm photolysis of I in acetonitrile solution does indeed lead to NO release as measured using the Sievers Nitric Oxide Analyzer (NOA) with a quantum yield of 0.18. (**Figure III-C-2** and **Figure III-C-3**).

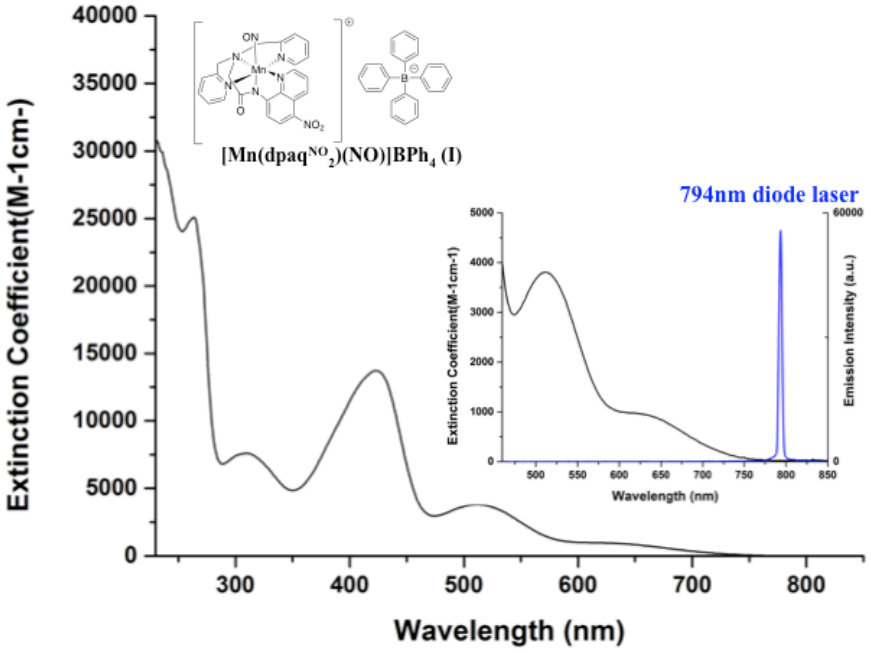

Figure III-C-1. Absorption spectrum of [Mn(dpaq$^{NO}_{2}$)(NO)]BPh$_4$ in acetonitrile and the emission spectrum of 794 nm diode laser (Inset).

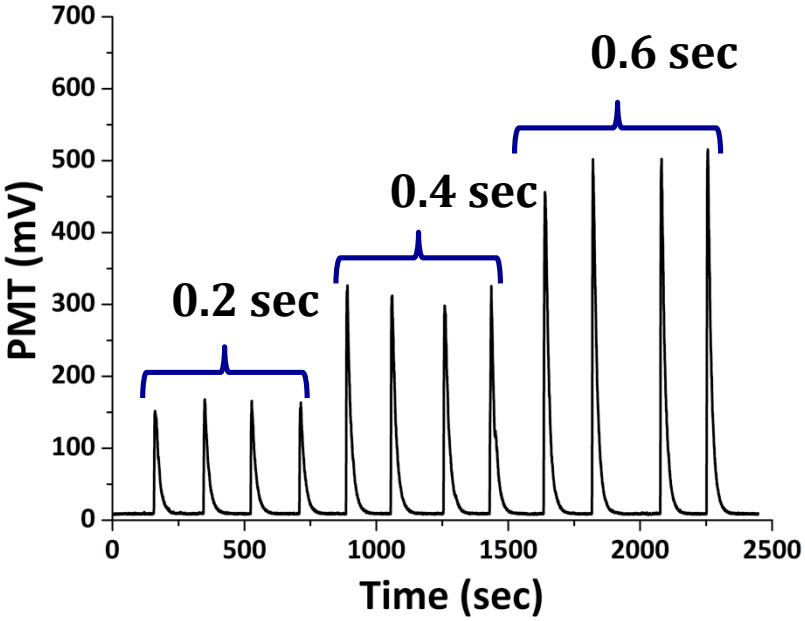

Figure III-C-2. NOA signals from the 794 laser photolysis of $[Mn(dpaq^{NO_2})(NO)]BPh_4$ in acetonitrile at 1.9 W/cm^2 power density with different irradiation time (0.2, 0.4 and 0.6 sec).

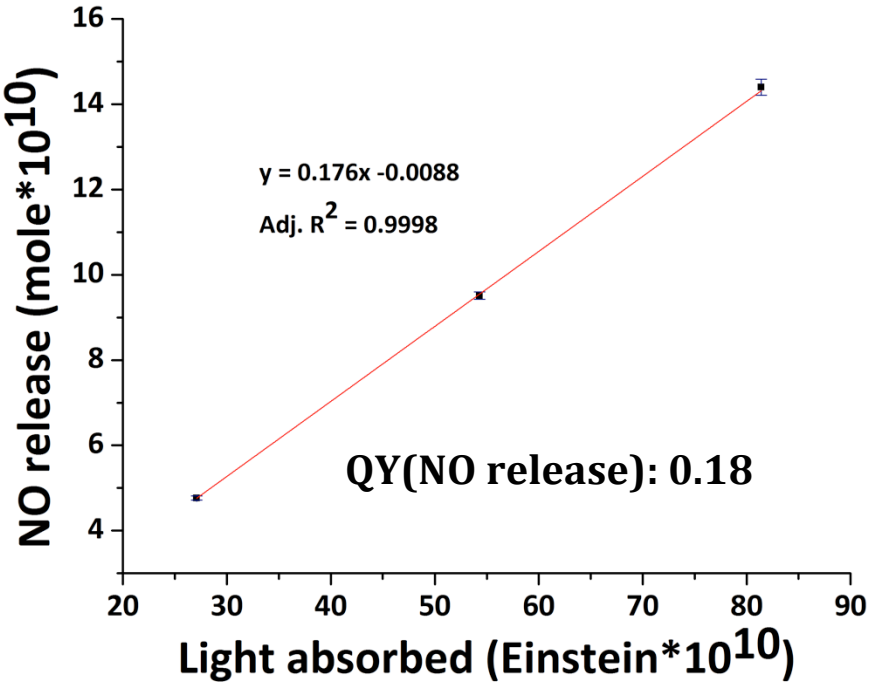

Figure III-C-3. Plot of NO detected vs light absorbed.

The Nd-UCNPs were high quality core/shell upconverting nanoparticles (Figure 1, bottom) synthesized using the robotic Workstation for Automated Nanocrystal Discovery and Analysis (WANDA) of the Molecular Foundry at Lawrence Berkeley National Laboratory.[26–28] The core host material with 10 nm size was $NaYF_4$ with 20% Gd^{3+} to give a hexagonal structure to give higher upconversion efficiency,[29,30] and this was doped with the lanthanide ions Yb^{3+} (30%), Nd (1.0%) and Tm (0.5%). The shell with 2 nm thickness was $NaGdF_4$ doped with Nd^{3+} (20%). The shell minimizes surface quenching effects and improves the luminescence efficiency of UCNPs. The Nd^{3+} dopant in these

$NaYF_4$:Yb/Gd/Nd/Tm(30/20/1/0.5%)@$NaGdF_4$:Nd(20%) core-shell nanoparticles (Nd-UCNPs) has an absorption band at ca. 800 nm allowing these materials to be excited at wavelengths (ca. 775-825 nm, better absorption: 785-800 nm) where the absorption of water is minimal.[25] Energy transfer from the excited Nd^{3+} to Yb^{3+} in the core,[31] followed by energy migration from Yb^{3+} to emitter Tm^{3+} from which various photoluminescence (PL) bands in the UV and visible range are observed. The transmission electron microcopy (TEM) and PL spectra of these Nd-UCNPs are shown in Figure III-C-4.

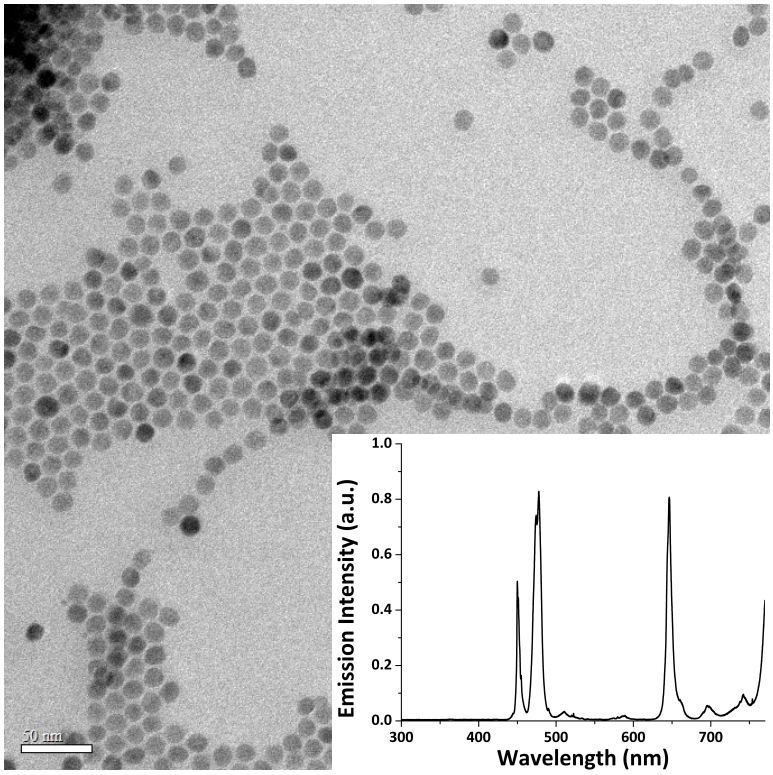

Figure III-C-4. TEM image of $NaYF_4$:Yb/Gd/Nd/Tm(30/20/1/0.5%)@$NaGdF_4$:Nd(20%) core-shell nanoparticles. *Inset*: The upconversion emission spectrum of Nd-UCNPs under excitation by an 800 nm continuous-wave (CW) laser.

D. Polymer Microencapuslaton

We encapsulated BPh_4 salt of the Mn photoNORM and Nd-UCNPs into PLGA microparticles with ca. 1-micron size and spherical shape via micro-emulsion technique (Figure III-D-1).[32,33] The average loading of the manganese photoNORM is 4.36 ± 0.66 wt% determined by inductively coupled plasma atomic emission spectroscopy (ICP-AES). Initially, a beaker was utilized during the emulsion process, however; low yields of particles were obtained. This was replaced by a half-spherical glass bottle to increase the preparation yield of micro-carriers. In a beaker vibration from the homogenizer is unable to reach the corners of the vessel allowing PLGA to settle lowering the yield. In a round vessel, there are no corners and sonic energy is distributed equally preventing settling and allowing more of the PLGA to form particles of the correct size. The spherical particles have the optimal shape for phagocytosis (Figure III-D-2).[34] Particles range in size between 350 nm and 2 μm. (Figure III-D-3 and Figure III-D-4) The PLGA utilized to produce these microcarriers is acid terminated. This provides free carboxylates on the surface of micro-carriers that were modified with immunoglobulin G (IgG) by amide coupling in 0.1 M pH 5.5 MES buffer solution to greatly increase the efficiency of phagocytosis. A bicinchoninic acid (BCA) protein assay indicates there is ca. 44 μg of IgG per mg of PLGA microparticles.

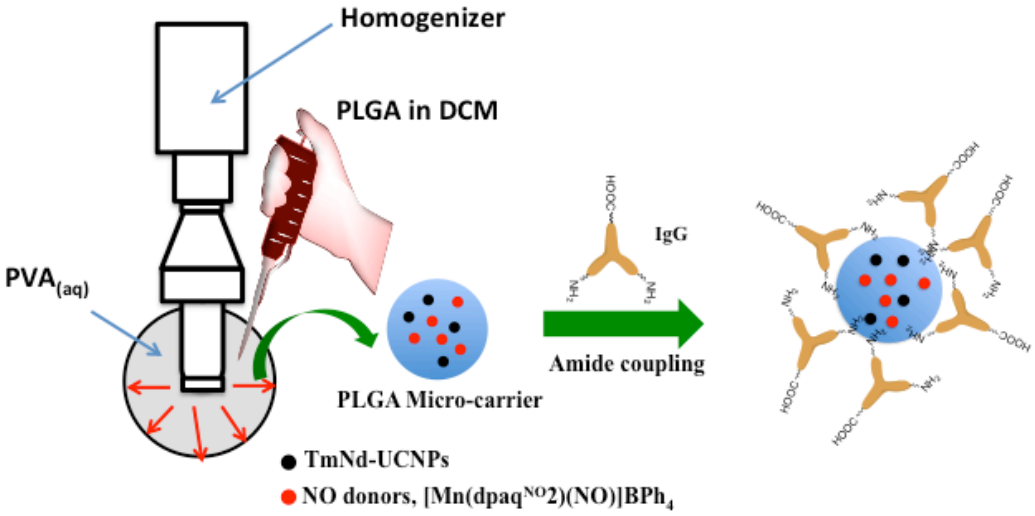

Figure III-D-1. The preparation of PLGA micro-particles and their surface modification with IgG antibody.

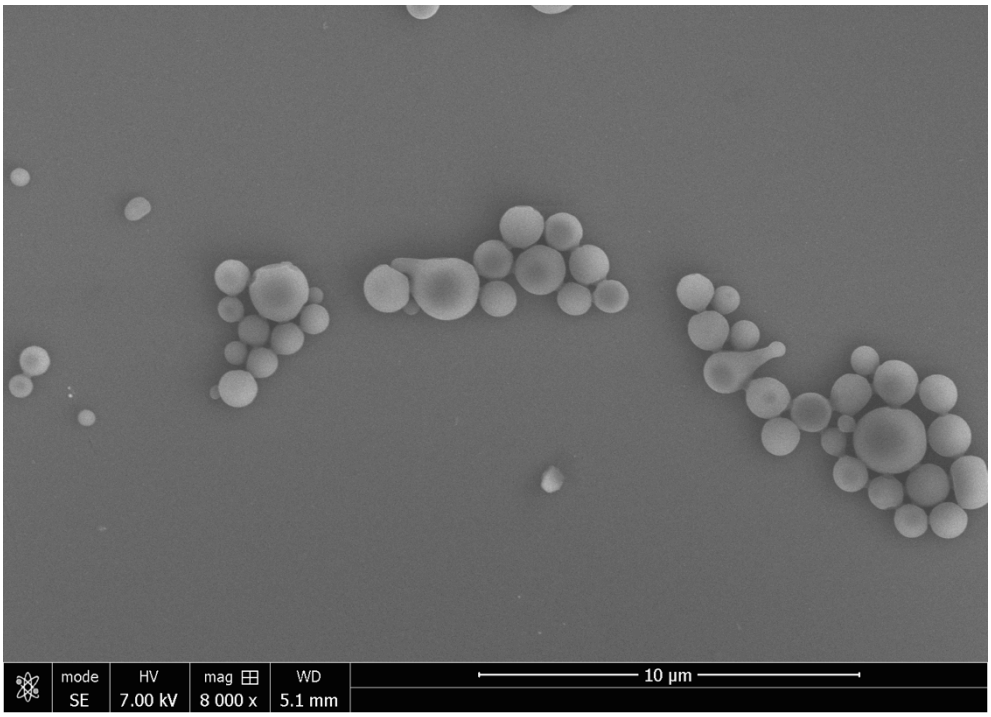

Figure III-D-2. The SEM image of PLGA microparticles loaded with $[Mn(dpaq^{NO}{}_2)(NO)]BPh_4$ (**I**) and Nd-UCNPs (scale bar = 10 µm).

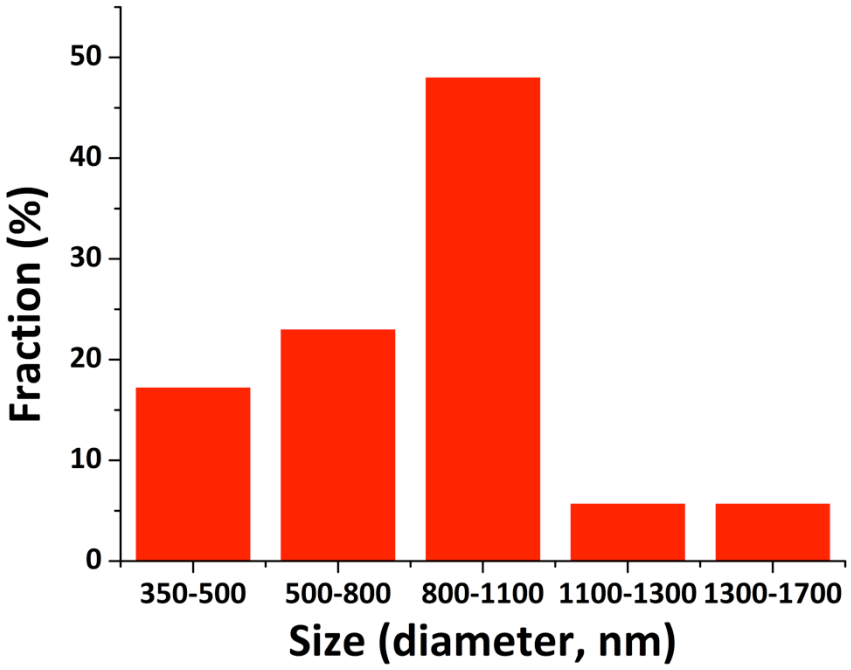

Figure III-D-3. Size distribution of the microparticles determined using ImageJ.

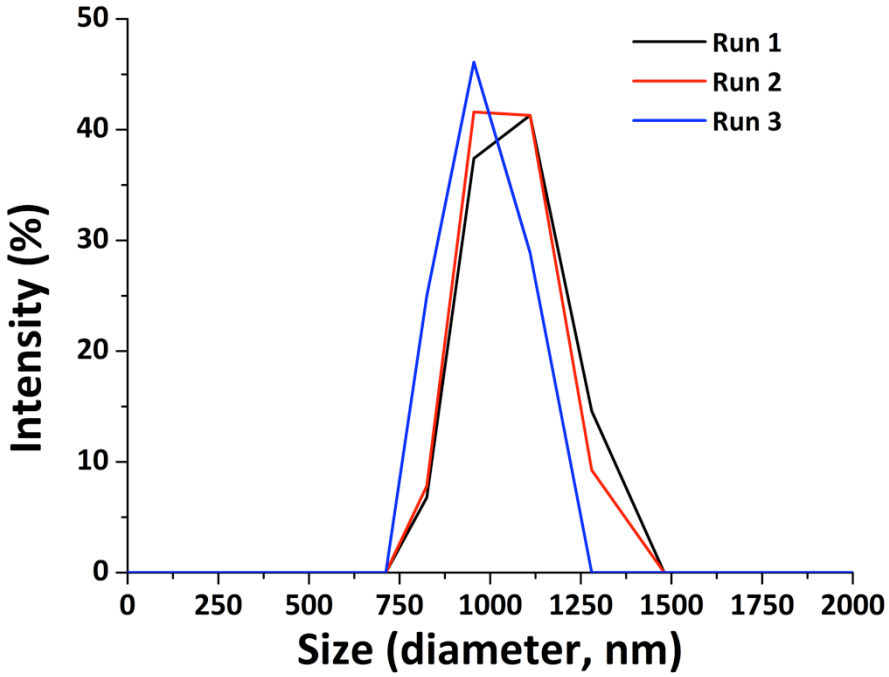

Figure III-D-4. Size distribution of the microparticles determined using dynamic light scattering.

E. NO release from photoNORM loaded polymer micro-particles

Previous studies in these laboratories[35–37] have shown that UCNPs can serve as photosensitizers that absorb NIR photons and emit visible light to trigger NO release from non-NIR sensitive photoNORMs. However, this process requires relatively high power irradiation owing to the relatively inefficient multi-photon upconversion mechanism of UCNPs and energy transfer from UCNPs to photoNORMs. However, the Mn photoNORM **I** is photosensitive to release NO via direct single-photon excitation at 794 nm, and this allows one to overcome the scattering constraints that may be problematic for multiphoton excitation in deeper tissue. However, since the extinction coefficient for I at this wavelength is low (20.2 $M^{-1}cm^{-1}$), it was of interest to see whether the visible light generated by that upconversion from the Nd-UCNP would enhance NO release owing to the significantly higher extinction coefficients of **I** in this spectral region. In order to test this possibility, micro-particle of two different compositions were prepared. One containing both **I** and Nd-UCNPs (PLGA-1), the other containing only the manganese photoNORM I (PLGA-2). Data obtained from dynamic light scattering (DLS) showed these two particle groups to be similar in average size (~1 micron, **Figure III-E-1**), while ICP-AES showed the former to have somewhat higher loading of I (4.76 wt% vs 3.79 wt% respectively). Particles of both types (0.5 mg) were separately suspended in 2.5 mL pH 7.4 phosphate buffered saline (PBS) solution and were irradiated with a 794 nm diode laser (at different power settings) while stirring and purging with medical grade air. The purge gas was analyzed for NO using the NOA for 1.0 second irradiation times at different power densities (in W/cm^2). The NOA signals recorded are shown in Figure III-E-2 while Figure III-E-3 plots the quantity of NO released from these micro-carriers in response to the different excitation laser power densities. (**Figure III-E-4**) Notably, both plots appear linear, which is consistent with a

single photon excitation mechanism for NO release. Additionally, the efficiencies of NO release for PLGA-1 and PLGA-2 are 1.63 pmole W^{-1} cm2 s^{-1} and 2.06 pmole W^{-1} cm2 s^{-1} respectively. When differences in loading are taken into account, this corresponds to a 37% lower NO release from the Nd-UCNP loaded micro-particles. Clearly, the Nd-UCNPs are not improving the efficiency of NO release in this case, thus have value primarily for imaging purposes.

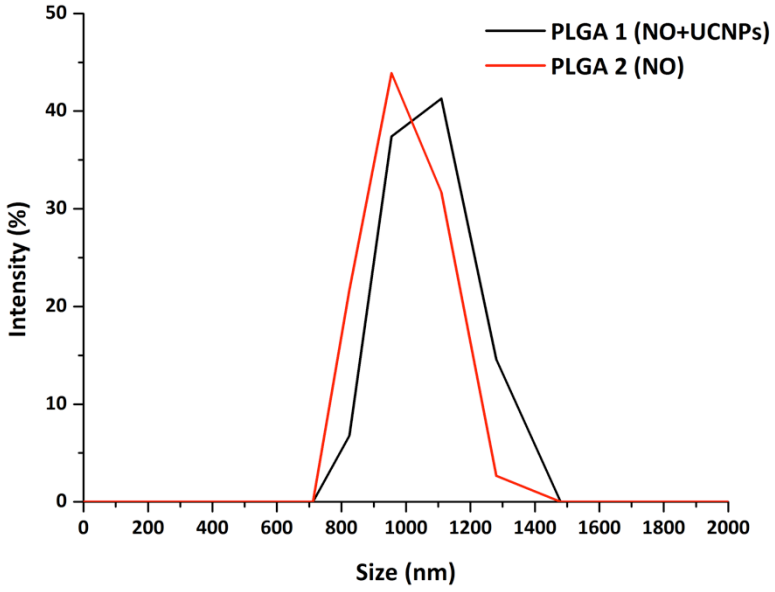

Figure III-E-1. Size distribution of the micro-carriers PLGA-1 and PLGA-2 as determined using dynamic light scattering.

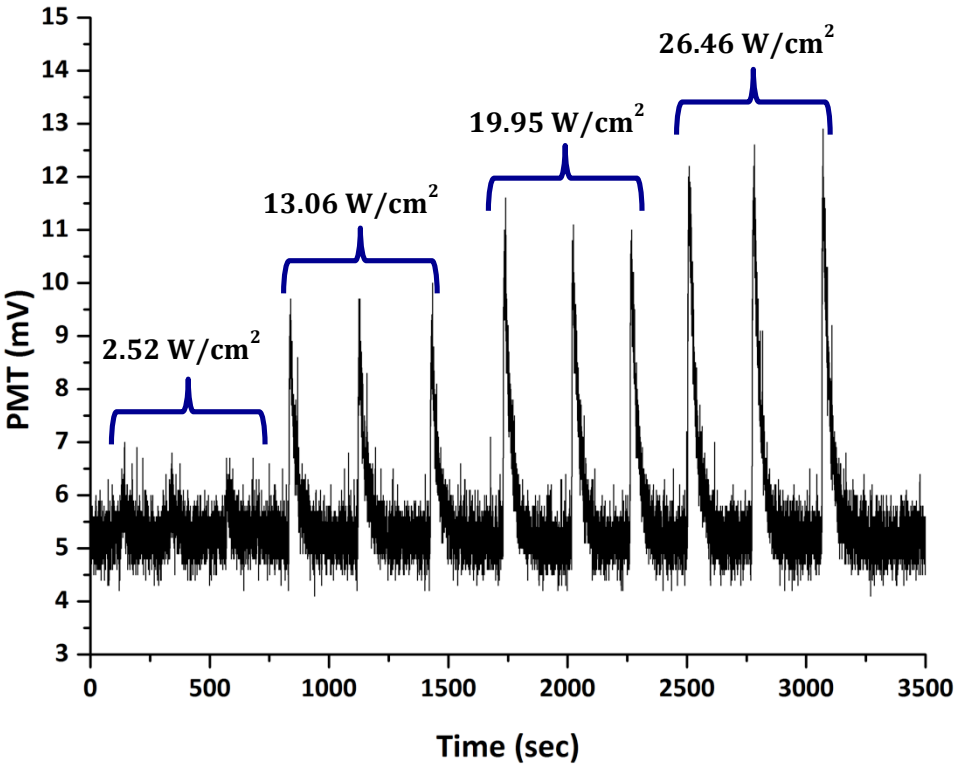

Figure III-E-2. NOA signals from the 794 laser photolysis of suspensions of PLGA-1 at different power densities in W/cm^2.

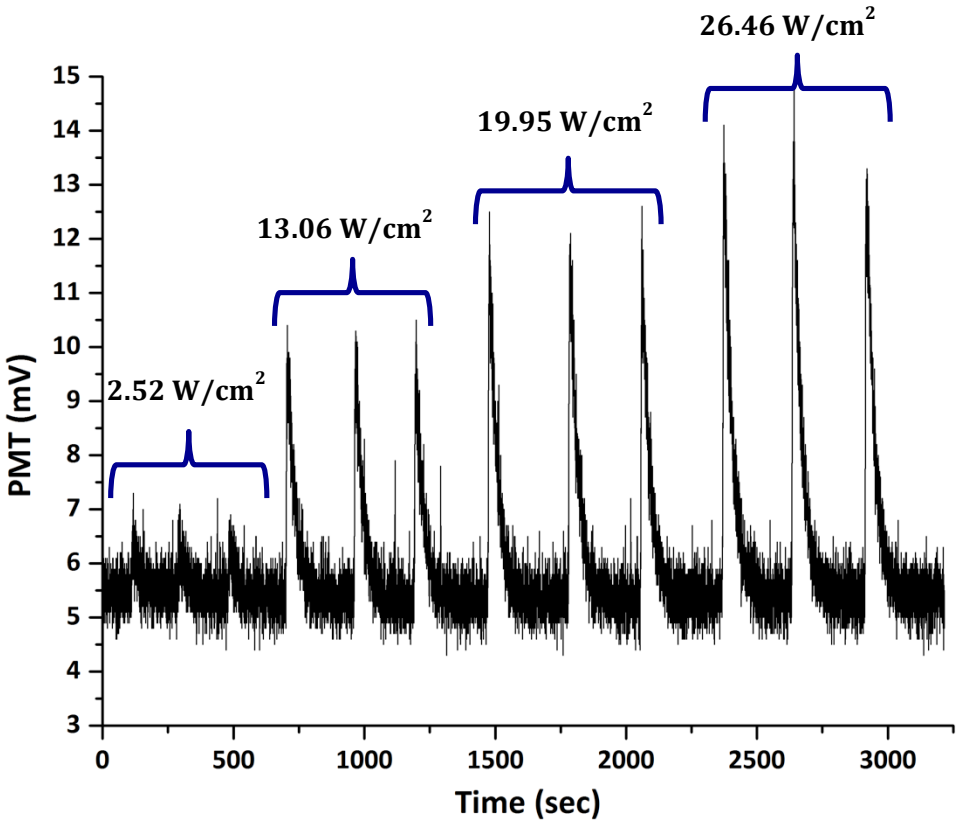

Figure III-E-3. NOA signals from the 794 laser photolysis of suspensions of PLGA-2 at different power densities in W/cm^2.

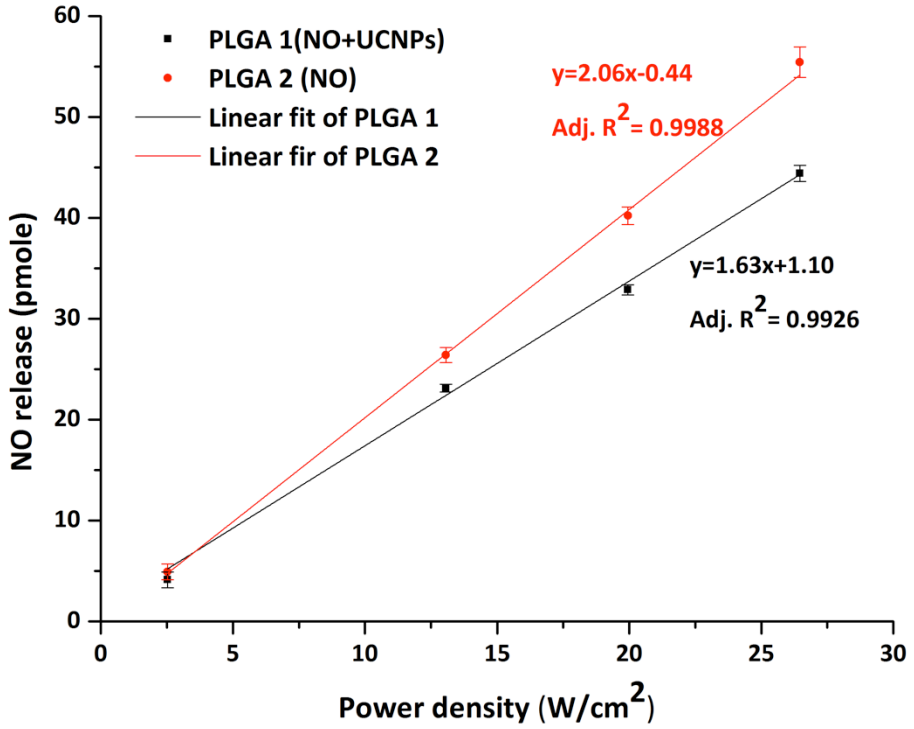

Figure III-E-4. Plots of the NOA detected NO released vs laser power density for the 794 nm photolysis of PBS suspensions of the micro-carriers PLGA-1 (black) and PLGA-2 (red).

F. Particle uptake and compatibility

The goal of these experiments was to determine the number of loaded PLGA micro-particles that can be phagocytosed into each macrophage. It has been previously shown that rigid spheres, about one micron diameter, are readily taken up by this mechanism.[38,39] As noted above, the micro-particles were also surface modified with a covalently bound layer of immunoglobulin G (IgG) to enhanced uptake. Based on the An alamarBlue® cell viability assay was used to determine the compatibility of the micro-particles with the cells. Figure III-F-1 shows that these particles displayed no significant toxicity for concentrations as high

as 100 μg/mL for incubation periods of 24 and 48 h with BMMs. Moderate toxicity was observed at higher concentrations. From these results, the incubation concentration of 100 μg/mL was selected for all further experiments. Analysis of BMMs containing NO-donor loaded particles with ICP-AES determined an uptake of 0.667 μg manganese per 1 x 106 cells. This translates into 263 μg particles or 12.14 nanomole of NO as the photoNORM **I**.

BMMs loaded with particles containing NO-donor and UCNPs (BMMp+) were then tested to verify internal release of NO using the NO sensor 4-amino-5-methylamino-2',7'-difluorofluorescein diacetate (DAF-FM),[40] which reacts to form a fluorescent compound when exposed to intracellular NO. DAF-FM was incubated with macrophages both containing and not containing photoNORM loaded micro-particles. Prior to DAF-FM incubation, these cells were treated with L-N-nitroarginine methyl ester (L-NAME), a nitric oxide synthase (NOS) inhibitor, to reduce any background from biologic production of NO.[41] Upon 794 nm laser exposure at a power of 13.02 W/cm^2 for 90 s, BMMp+ produced a visible fluorescence response while macrophages without particles did not. (**Figure III-F-2**).

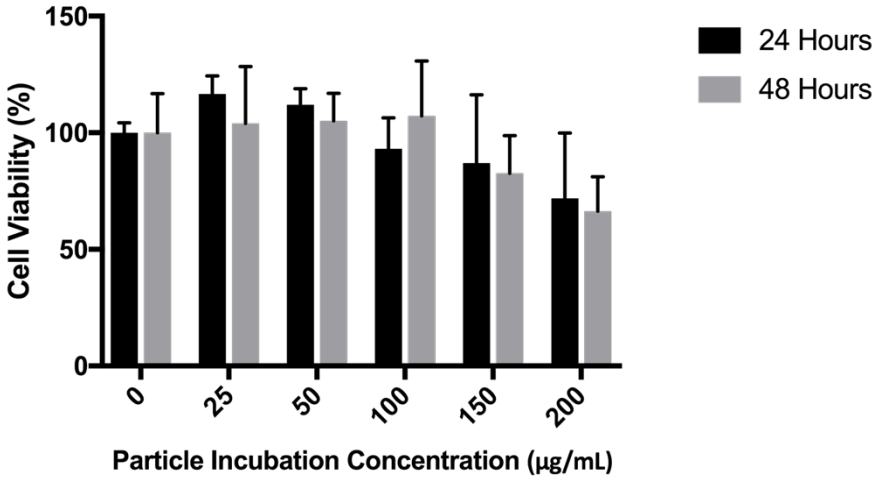

Figure III-F-1. Viability of BMMs with various particle incubation concentrations after 24 and 48 h.

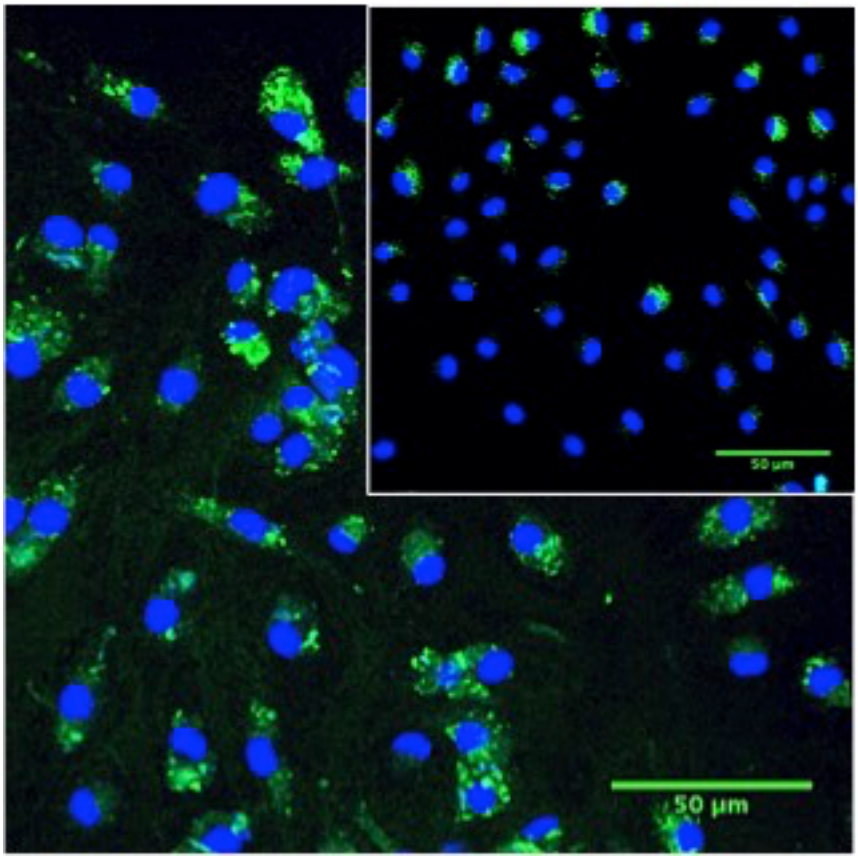

Figure III-F-2. $BMMp^{+}$ irradiated with a 794 nm laser for 90 s. The inset figure is the control experiment with BMMs only. NO was detected using 4-amino-5-methylamino-2',7'-difluorofluorescein diacetate (DAF-FM-2DA) fluorescent reporter (green color). (both samples were incubated with L-N^{G}-nitroarginine methyl ester (L-NAME) to inhibit endogenous NO generation.) Blue color is 4',6-diamidino-2-phenylindole (DAPI) stain.

G. Micro-particle effects on macrophage chemotaxis

The ability of macrophages to target tissue such as tumors is governed by their ability to undergo chemotaxis towards sights of inflammation.[1] Thus, it is crucial that the macrophage "Trojan Horses" retain this function after drug loading. This question was probed using a transendothelial assay (**Figure III-G-1**).

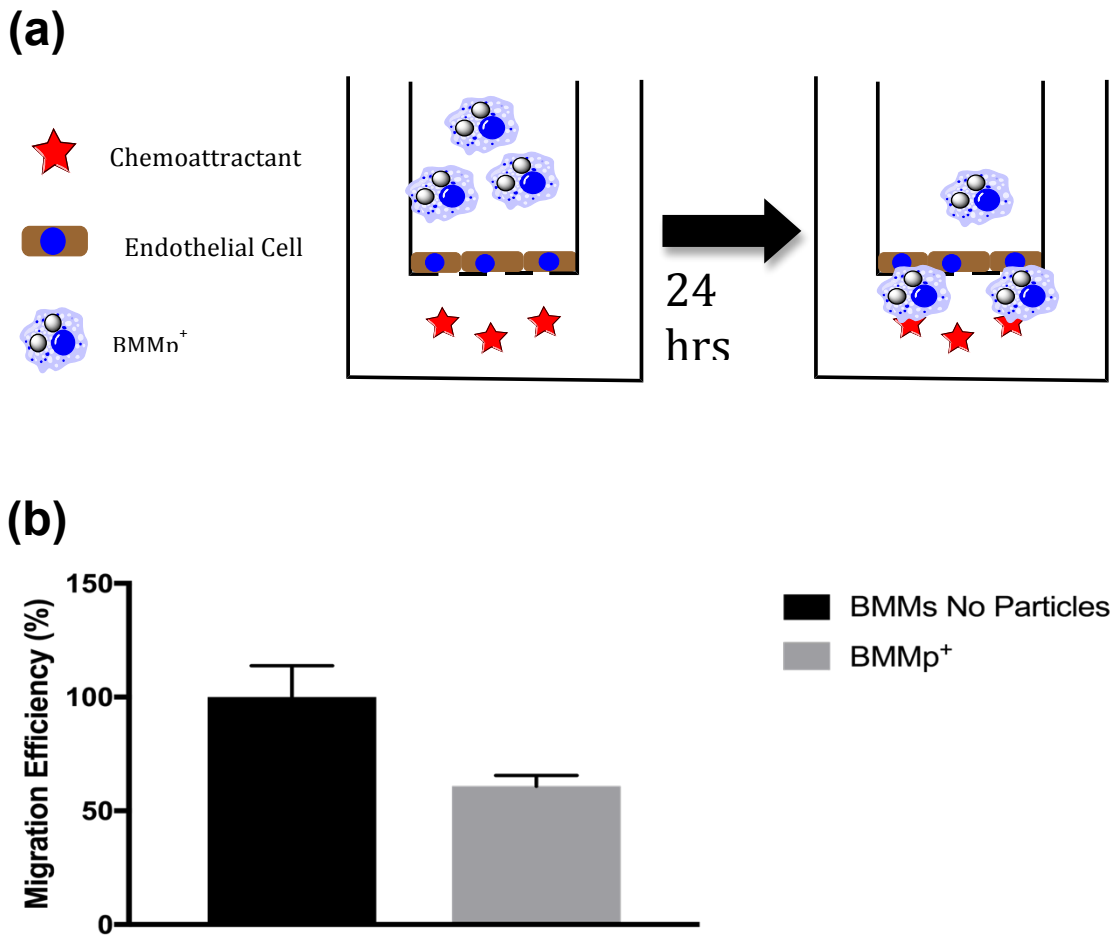

Figure III-G-1. *Top:* An illustration of macrophage chemotaxis in a transendothelial assay. Macrophages are placed on top of the endothelial layer and MCP-1 on the other as a chemotaxic agent. Macrophages are attracted to the chemoattractant and traverse the endothelial monolayer. These cells are quantified by adding NucBlue® to stain the nuclei of

cells that have crossed so they can be analyzed by counting cell nuclei with a fluorescent microscope. *Bottom*: A Graph comparing the migration efficiency of macrophages with and without particles

First, monolayers of bEnd.3 blood brain barrier (BBB) endothelial cells were grown on FluoroBlokTM transwell inserts inside of the wells of a 24-well plate and used as model endothelium barriers, since such monolayers are very tight thereby making migration very challenging.[42] After monolayer confluency, media containing 1 x 10^5 BMMp+, media containing a comparable number of BMMs without particles, and media alone were added to the top of separate transwells while monocyte chemoattractant protein-1 (MCP-1) was added below. After 24 h, the inserts were stained with NucBlue® allowing for quantification of chemotaxis by counting the number of nuclei of cells that had migrated to the bottom of the insert and subtracting it from wells that had a confluent bEnd.3 monolayer with no added BMMs. Results indicated that (10.4 ± 0.8) x 10^3 macrophages containing particles vs. (17.1 ± 2.4) x 10^3 cells without particles had migrated across the endothelium layers. Thus, phagocytosis of such micro-particles causes a 39% reduction in chemotaxis in agreement with a previous report,[23] although in the latter case an even sharper drop in chemotaxis was observed without the inclusion of an endothelial monolayer.[23] The more efficient barrier crossing in the present case may be attributed to using micron-sized rather than nano-sized particles. Phagocytosis of particles smaller than 500 nm leads to significant drops in vector migration rates due to the lack of asymmetric actin polarization.[43] Additionally, exposing tumors to ionizing radiation causes increases in inflammation and the release chemotactic factors. As shown previously, such treatment may be utilized to enhance overall macrophage recruitment and improve therapeutic efficacy if needed.[23,44]

H. Tumor spheroid penetration and NO release

After traversing the endothelium, macrophages need to be able to follow chemotactic gradients arising deep from within the tumor tissue. Tumor spheroids were utilized to mimic the 3D tumor environment. Cocultured murine NIH/3T3 fibroblast : 4T1 breast cancer cell spheroids with a 5:1 cell seeding ratio similar to those developed previously were employed here.[45] The incorporation of fibroblasts into tumor spheroids has been reported to induce the formation of a tumor stroma which enhances spheroid compactness, helps resist nanoparticle penetration and increases the expression of pro-inflammatory cytokines used in leukocyte chemotaxis.[45,46] Use of this seeding ratio in a hanging drop technique was able to produce large spheroids with an average diameter of 962 ± 60 μm ((1.35 ± 0.05) x 10^5 cells/spheroid) after 10 days of incubation with introduction of macrophages on day 7 making them considerably larger than spheroids produced with 4T1 cells alone (**Figure III-H-1**). Pimonidazole (PIMO) staining of spheroids revealed a high level of hypoxia throughout the spheroid interior. Considering that hypoxia normally occurs 100-150 μm into a tumor,[47] this is not surprising. It is important to note that spheroids without the fibroblast cells were significantly smaller than those with them likely due to macrophage supported tumor growth[48] (**Figure III-H-2**).

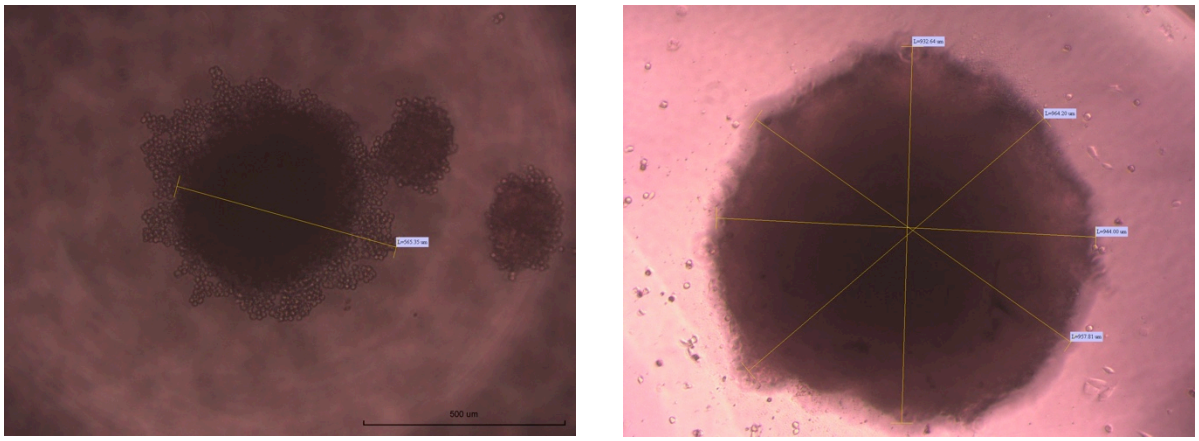

Figure III-H-1. Representative images of tumor spheroids produced with 4T1 cells alone (left) or a 5:1 3T3:4T1 coculture method (right) after infiltration with particle loaded macrophages. Due to the density of the spheroids, particles cannot be seen in these images.

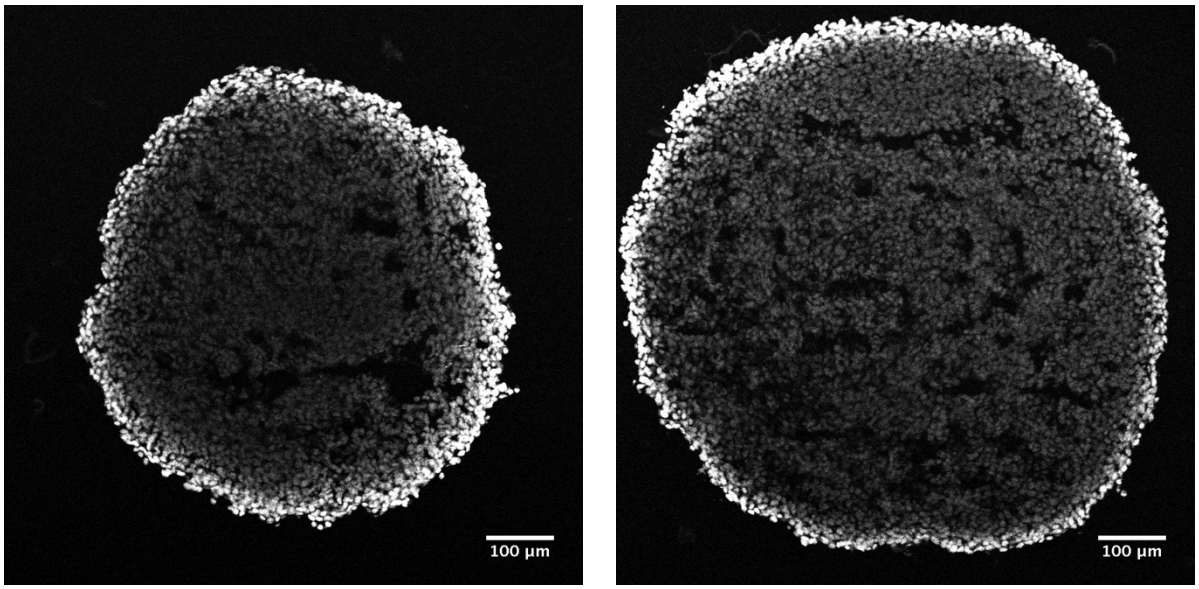

Figure III-H-2. Comparisons of NIH-3T3/4T1 coculture spheroid size after 10 days of growth with (right) and without (left) macrophages introduced on day 7. Images represent center slices of tumor spheroids stained with DAPI acquired with a confocal microscope.

Macrophages labeled with CellTracker™ deep red were used to track the chemotaxic penetration of BMMp+ into tumor spheroids. Images of tumor spheroid center slices indicated deep spheroid penetration (**Figure III-H-3**). For the spheroids examined, macrophages were unable to reach the center of the spheroid and instead formed a visible ring around a center section. Oxygen is required for macrophage chemotaxis, and these spheroids are sufficiently large it is likely that the center is a necrotic region where oxygen is too low. Flow cytometry of spheroids dissociated with Accumax™ demonstrated a macrophage composition of 0.53 ± 0.4% cell number or 715 ± 540 macrophages per spheroid (**Figure III-H-4**). Assuming macrophages were loaded with particles at a rate as shown by ICP, these macrophages brought an estimated 8.7 ± 6.6 picomole of the photoNORM into the spheroid. The value of the macrophages as carrier for these micro-particles was demonstrated using particles labeled with fluorescent IgG. Spheroid slices (**Figure III-H-5**) demonstrated that macrophages with internalized fluorescent particles carried their payload into the spheroids but that the micro-particles alone when incubated with spheroids were unable to penetrate more than a few cell lengths (**Figure III-H-6**).

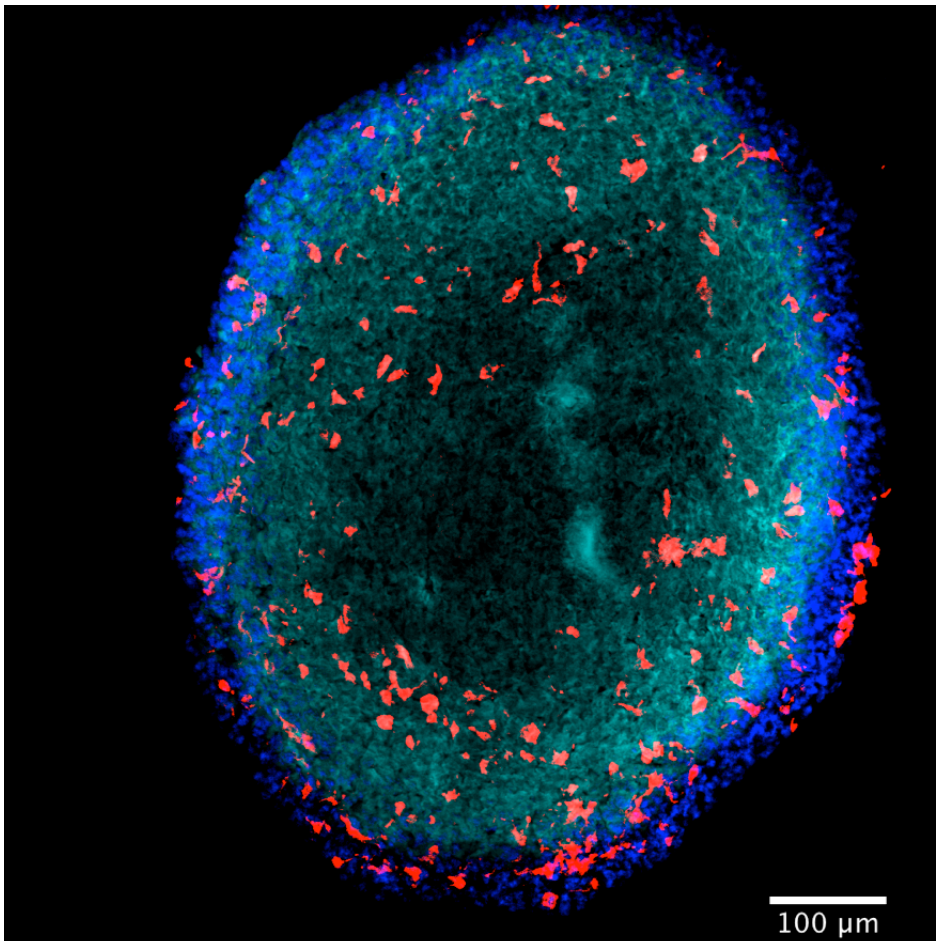

Figure III-H-3. The slice of 4T1/NIH-3T3 cocultured breast tumor spheroids incubated with BMMs only. Blue is 4',6-diamidino-2-phenylindole (DAPI) and red represents macrophages stained with CellTracker™ deep red. Spheroids was stained with a Hypoxyprobe™ Red549 to label hypoxia (cyan).

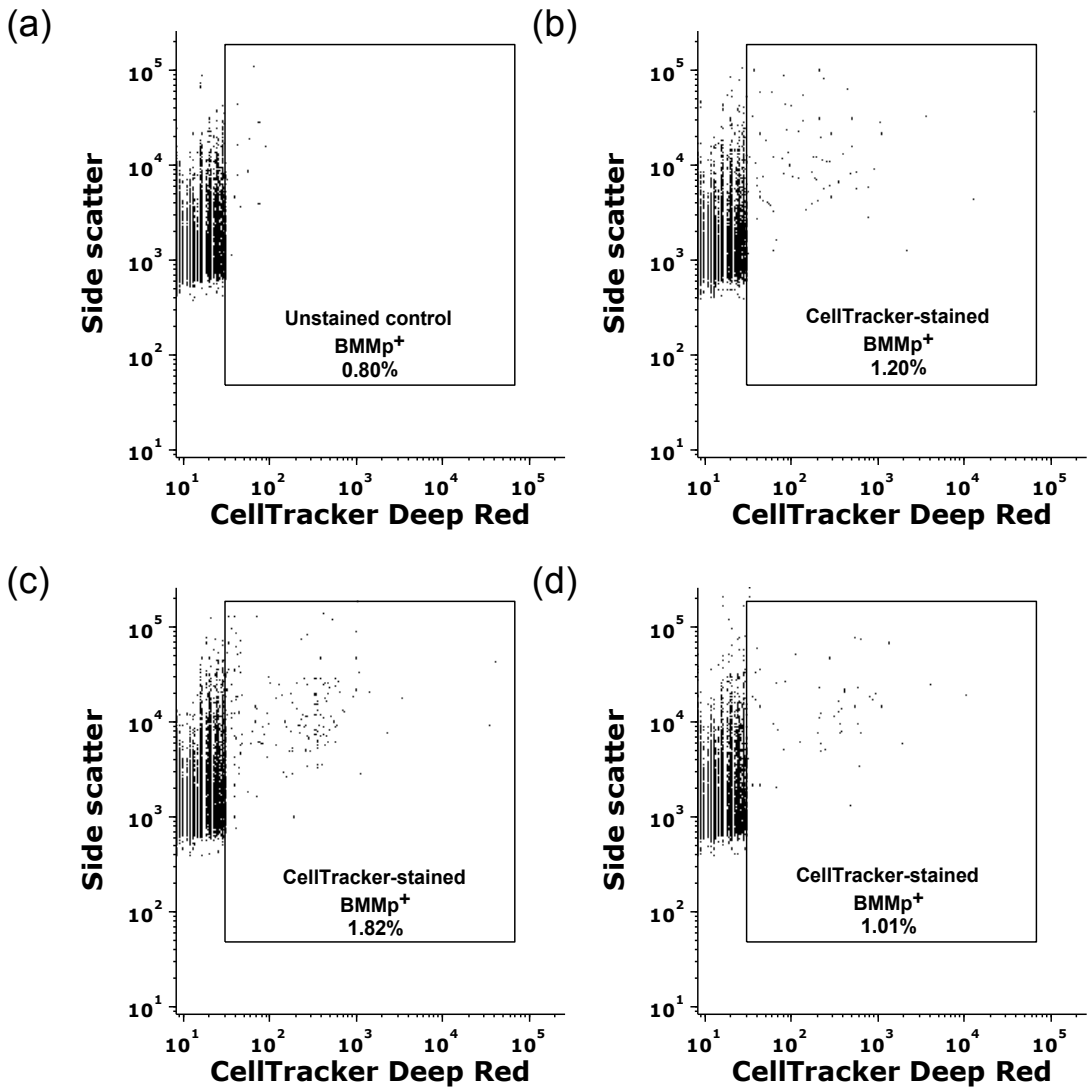

Figure III-H-4. Flow Cytometry analysis of macrophage infiltration into tumor spheroids (b-d). Macrophages were labeled with Celltracker^{TM} deep red to allow for their identification. Results were subtracted from the proportion of gated cells in the control (a).

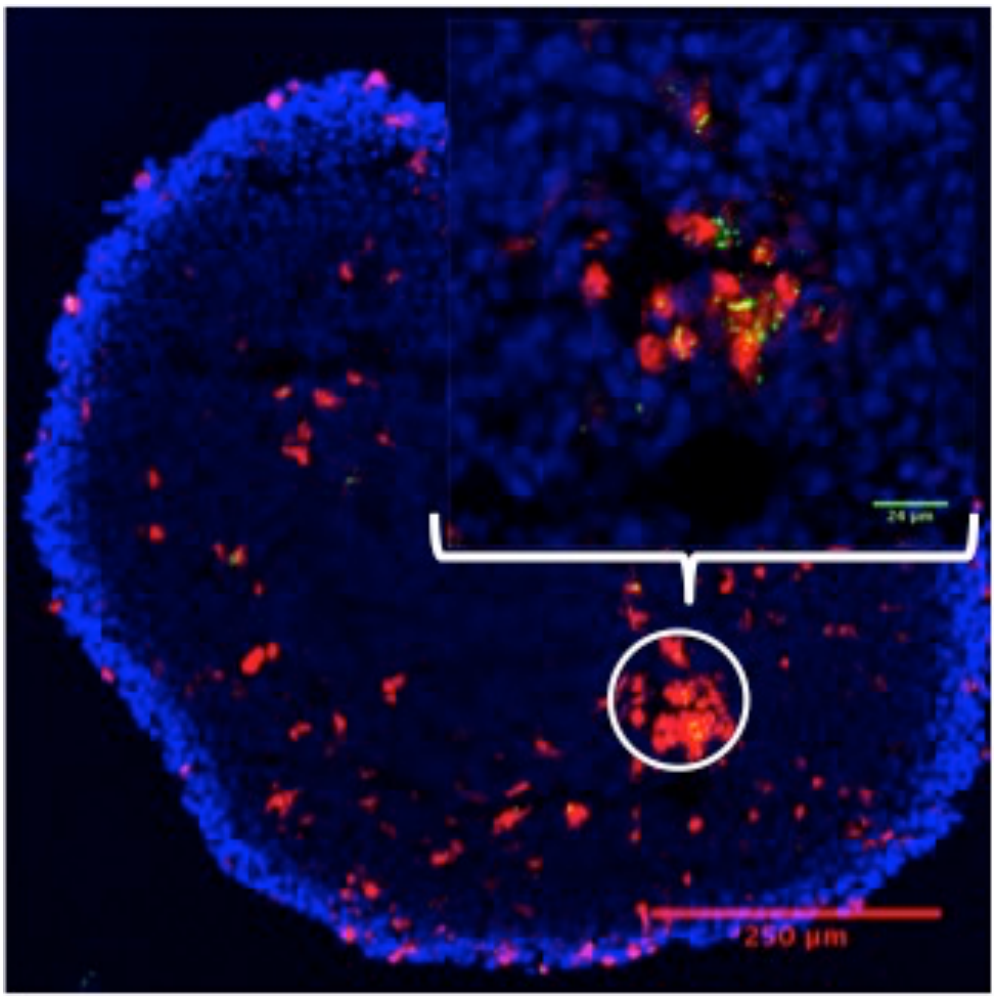

Figure III-H-5. The slice of 4T1/NIH-3T3 cocultured breast tumor spheroids incubated with cy-3-IgG labeled $BMMp^{+}$ (green spots). Blue is 4',6-diamidino-2-phenylindole (DAPI) and red represents macrophages stained with CellTracker^{TM} deep red.

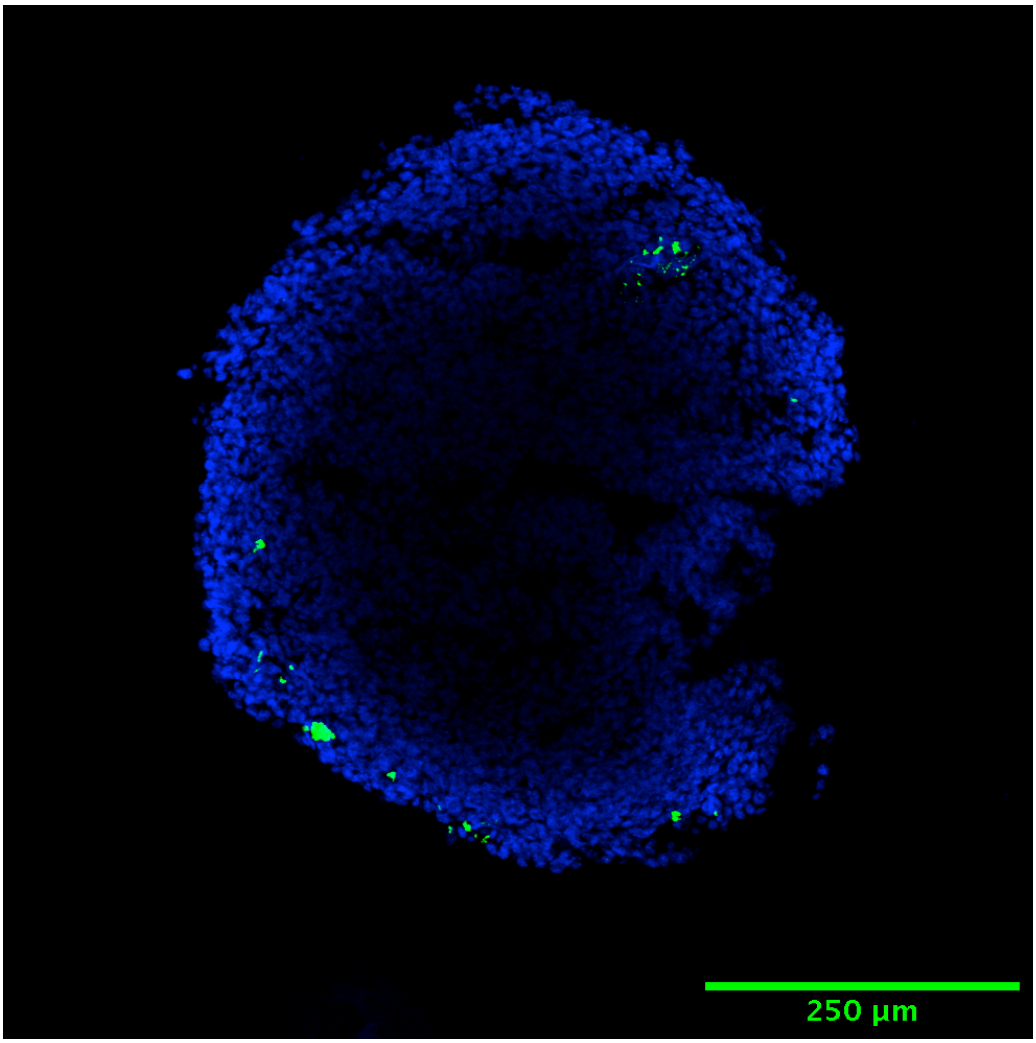

Figure III-H-6. The slice of 4T1/NIH-3T3 cocultured breast tumor spheroids incubated with cy-3-IgG labeled micro-particles (green spots). Blue is 4',6-diamidino-2-phenylindole (DAPI).

The next question was whether the NO photo-generated within these spheroids can be detected externally. To the best of our knowledge, the use of a NOA to measure NO diffusion form tumor spheroids has not been reported previously. Five spheroids incubated with BMMp+ or BMMs with PLGA-only particles (BMMp-) were put in the corner of a custom designed cuvette (**Figure III-H-7**) with 1 mL Hank's Balanced Salt Solution

(HBSS) solution and excited with the 794 nm diode laser operating at a power density of 13.1 W/cm^2. In typical NOA measurements, the solution is bubbled with the carrier gas and stirred allowing the NO generated to swept from the solution to the detector. However, such conditions would likely cause spheroid disassembly and cell lysis. To avoid this, the spheroids were blanketed with unstirred HBSS solution and irradiated with the laser for specified time periods (**Figure III-H-8**). Subsequent gentle bubbling with medical-grade air above the spheroids released most of the NO in solution without disturbing the spheroids. This allowed the procedure to be repeated several times on the same sample (**Figure III-H-9** & **Figure III-H-10**). The NO released from the 6 min (total) photolysis of five spheroids invaded by BMMp+ was 13.6 pmol (or 2.72(avg) pmole per spheroid) (**Figure III-H-9a**), while spheroids treated with BMMp- gave no measurable response (**Figure III-H-9b**). Based on spheroid volumes of ~1 μL, NO steady state concentrations in excess of 1 μM are being generated, and these are in excess of that needed to induce p53 and nitrosative stress mediated apoptosis.[5]

Figure III-H-7. The custom designed cuvette for the experiment of NO photo-release from spheroids

Figure III-H-8. The NIH/3T3:4T1 tumor spheroids in 1 mL Hank's buffered salt solution (HBSS) under 794 nm laser irradiation. *Inset:* the scheme represents that the spheroids can be placed at the corner of the cuvette and exposed to NIR laser excitation.

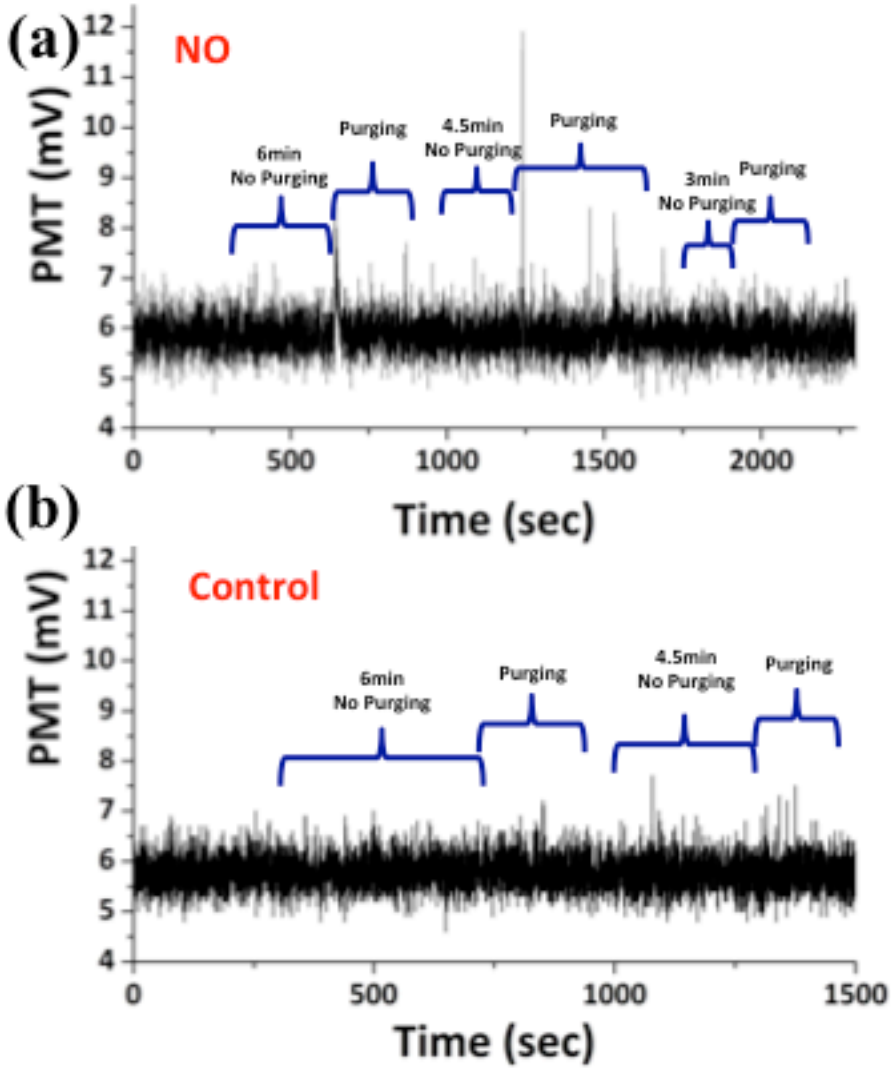

Figure III-H-9. (a): NO released from five spheroids infiltrated with BMMp+ in 1 mL HBSS solution under 794 nm laser irradiation with 13.1 W/cm^2. Down: The control experiment of six spheroids loaded with BMMp-.

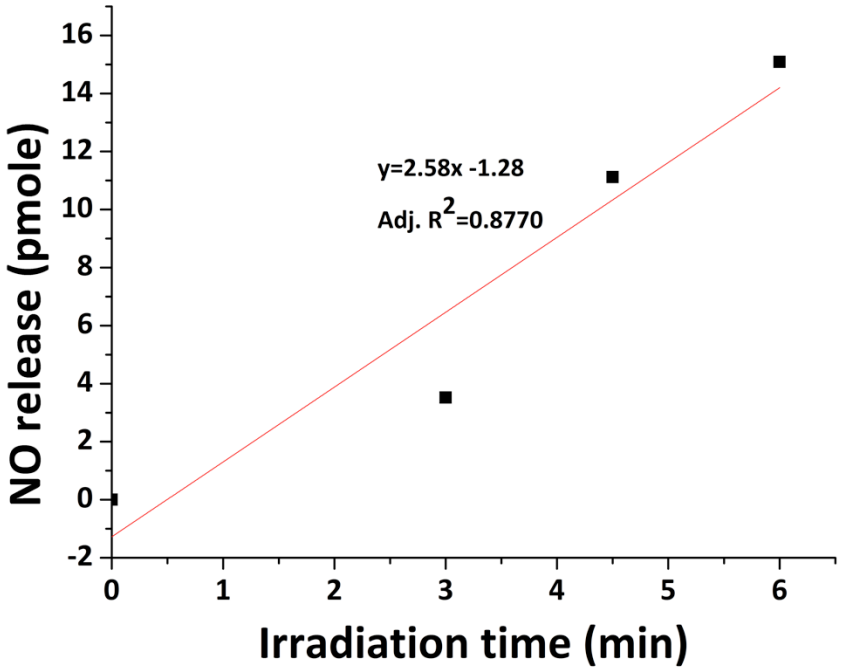

Figure III-H-10. Plot of NO detected vs irradiation time.

I. Testing therapeutic efficacy in coculture tumor spheroids

As mentioned previously, the key to unlocking the full therapeutic potential of nitric oxide is garnering spatial, temporal and concentration control of delivery. Spatial and temporal control are gained using light as the triggering mechanism, while spatial control is strongly enhanced by a localization mechanism such as offered by the use of macrophages. Concentration control (dosage) should be achievable by simply changing the amount of light delivered to the target.

For example, Figure III-I-1 illustrates the results of irradiating spheroids containing BMMp+ or BMMp- with 794 nm light. The irradiation times were for 1 to 3 six-minute periods with a power density of 13.1 W/cm^2. Cell viability was probed after 24 h using a p-nitrophenyl phosphate (PNPP) assay.[49] Irradiation of spheroids containing photoNORM loaded macrophages led to 25.7% reduction in tumor viability after 12 min while spheroids with macrophages and blank micro-particles demonstrated only a 6.6% drop in cell viability. While this reduction in viability from a single round of therapy is somewhat modest, such treatment is likely done in several applications. Additionally, the spheroids used in this study were based 4T1 breast cancer cells, which are reported to be p53 deficient, so most of the damage can be attributed to nitrositive stress. About 50% of cancers have p53 pathways that are induced by NO to trigger apoptosis; in such cells, this treatment will likely be much more effective.[50]

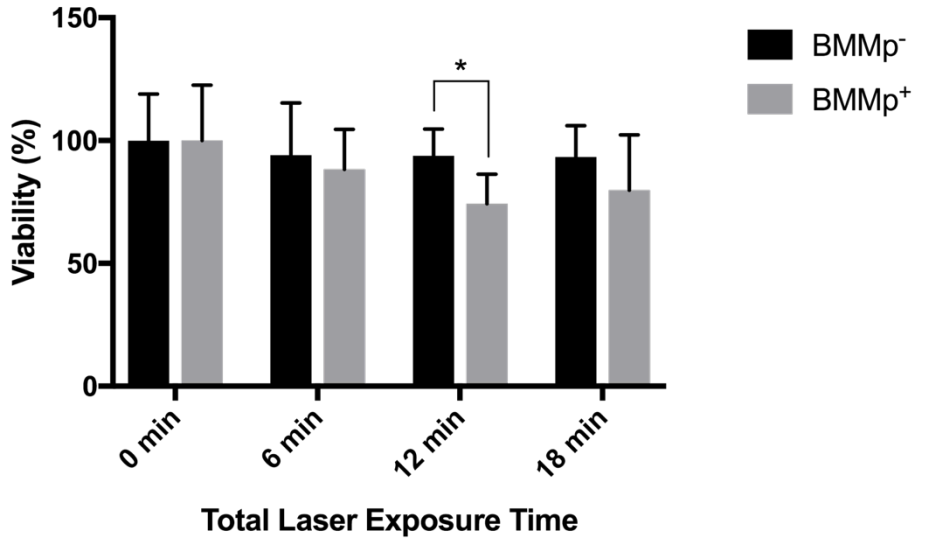

Figure III-I-1. The viability of spheroids after 6, 12, or 18 min of laser exposure in 6-min increments. Viability was measured using a PNPP assay 24 h after spheroid treatment. * = $p \leq 0.05$ (students t-test)

Experiments utilizing a 735 nm LED with a much lower power density of 0.58 mW/cm^2 for 8.5 h were conducted to assess the effects of low-level NO generation on the levels of HIF-1α in tumor spheroids. This factor is upregulated in hypoxia and is correlated with tumor cell survival, metastasis, and angiogenesis as well as poor patient prognosis.[51] After exposure, spheroids were dissociated into a single cell suspension. Cells were then fixed and labeled with anti-HIF-1α followed by a fluorescent secondary antibody. Analysis with flow cytometry revealed that low level NO treatment resulted in a significant reduction in the number of cells expressing HIF-1α from 96.7 ± 0.5 % to 77.7 ± 8.7 % in samples containing BMMp+ with and without light exposure respectively (Figure III-I-2). Spheroids with BMMp- failed to show a change in HIF-1α expression with or without light. These data agree with previous studies which demonstrated that low levels of NO in hypoxia leads to

destabilization of HIF-1α in hypoxia due to its inhibition of cytochrome C oxidase,[9,52] a critical component of mitochondrial respiration. When cytochrome C oxidase is inactivated by NO, oxygen that was going to be used for cellular respiration finds use in nonrespiratory oxygen dependent cellular processes including includes the activation of the prolyl hydroxylases responsible for the degradation of HIF-1α.[52] In a second trial, spheroids containing BMMp- and BMMp+ exposed to an LED source for a shorter period of time (7 h). Unfortunately, the production of a small number of spheroids during this experiment limited the number of different conditions that could be tested leading to the exclusion of samples without LED exposure. However, it is worth nothing that an even greater reduction in the expression of HIF-1α from 90.3 ± 5.1% to 62.2 ± 2.5% in Samples with BMMp- and BMMp+ respectively (SI Figure S10). We hypothesize that this reduction in HIF-1α with a smaller exposure time likely indicates that the supply of NO was exhausted between 7 and 8.5h. Future optimization to identify the precise time required for maximal effect will be necessary in order to fully realize the potential of this therapy.

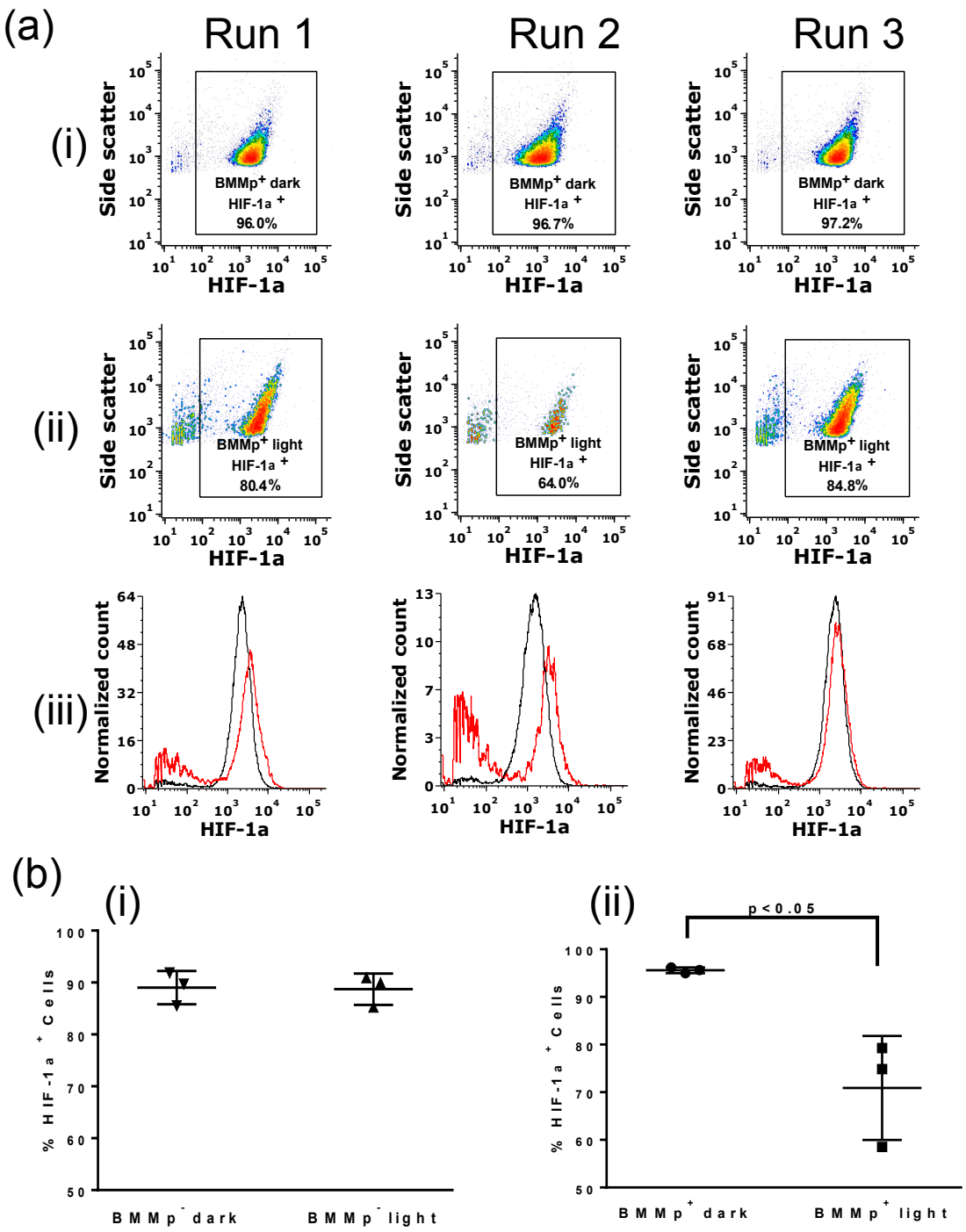

Figure III-I-2. (a) Flow cytometry analysis of dissociated tumor spheroids stained for HIF-1α under different treatments. Gated cells correlate with a positive signal from staining. (i) and (ii) three runs of analysis for spheroids loaded with BMMp+ with and without 735

nm LED exposure at 0.58 mW/cm^2 for 8.5 h. (iii) The comparison of (i) black and (ii) red for each run. Red and black lines represent particles with and without light exposure respectively. (b) The summary of flow cytometry analysis for the control (i) and the NO release study (ii). (i) represents spheroids with $BMMp^-$ with and without 735nm LED irradiation.

J. Testing UCNPs for imaging

Incorporation of an imaging agent has many advantages, most importantly, providing information on the location and concentration of the prodrug in the tumor, and this was one reason that the Nd-UCNPs were incorporated. Furthermore, the chemotaxic capacities of macrophages allow them to hone in inflammation and may provide a mechanism to detect hidden metastasis sites an ability which may allow for treatment of these sites in their early stages. The Nd-UCNPs are photoactivated by NIR light of the same wavelength as I allowing for theranostic capabilities with a single laser source. In order to test this, we incubated spheroids with BMMp+ or BMMp-. Spheroids were first labeled with calcein AM to provide visualization of their periphery. Figure III-J-1 shows 3D images of these spheroids taken with an 810nm laser source from a two-photon confocal microscope. Weak signals were noted on the surface of spheroids after treatment with $BMMp^{+}$ while those treated with $BMMp^{-}$ failed to produce a signal. However, it is clear that emission from the Nd-UCNPs is relatively inefficient with the 3W confocal microscope laser and that there is room to improve this by optimizing imaging conditions.

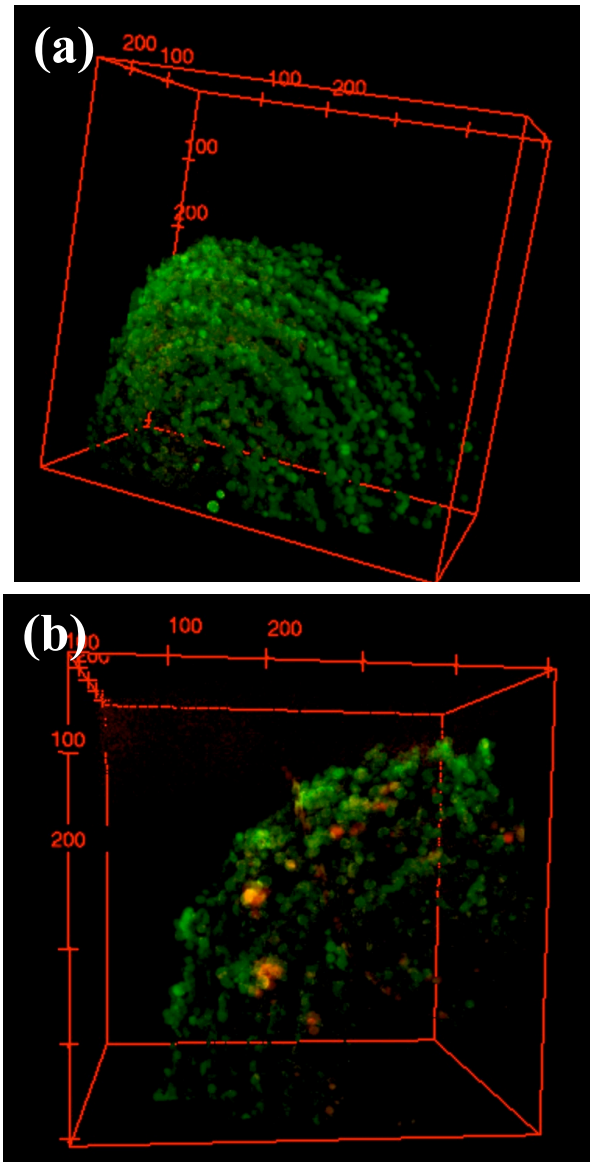

Figure III-J-1. Z-stack two-photon confocal images (dimensions = 508.4 µm x 508.4 µm) of live spheroids containing BMMs (a) with blank particles and (b) with UCNPs and NO-donor loaded particles. Spheroids were stained with calcein AM (green). Particles were identified via two-photon emission (red) from embedded UCNPs with laser excitation at 810 nm with a pulse energy of 37.5 nJ. Detected signal from UCNPs emission is between 420 – 460 nm.

K. Summary

We have successfully demonstrated the use of bone marrow derived macrophages as carriers for polymer-based micro-carriers in which a photoNORM I and UCNP have been incorporated for therapeutic and imaging applications. These carrier cells were able to load large quantities of therapeutics without significant effects on viability. Loaded BMMp+ cells maintained most of their chemotaxic ability allowing them to traverse an in vitro BBB transendothelial model. These macrophages also demonstrated the ability to deeply penetrate large tumor spheroids bringing their cargo with them, a feat which proved impossible for the micro-particles alone. Once inside the spheroids, the Nd-UCNPs could be used to visualize infiltrated macrophages in live spheroids using the 808 nm laser source of a confocal microscope. Photoactivation with a NIR laser at 794 nm released large quantities of NO from I as indicated by NOA. The steady state concentration of this NO could be controlled by simply changing the intensity of the light. With this in mind, we were able to induce therapeutically beneficial effects from two different areas of the NO spectrum. By utilizing a laser source over a several minutes of exposure direct cytotoxicity was induced by the high levels of NO generated. Lower power excitation over several hours with a LED induced changes in the tumor microenvironment as evidenced by the destabilization of HIF-1α with the lower levels of NO generated. Although not explored in the current study, it should be noted that targeted NO release in the hypoxic regions of tumors should serve to enhance the effectiveness of cancer radiotherapy.[53,54] Taken together, macrophage-mediated delivery of photoNORMs represents a fresh approach to overcome the hurdles traditionally associated with the use of nitric oxide in cancer treatments.

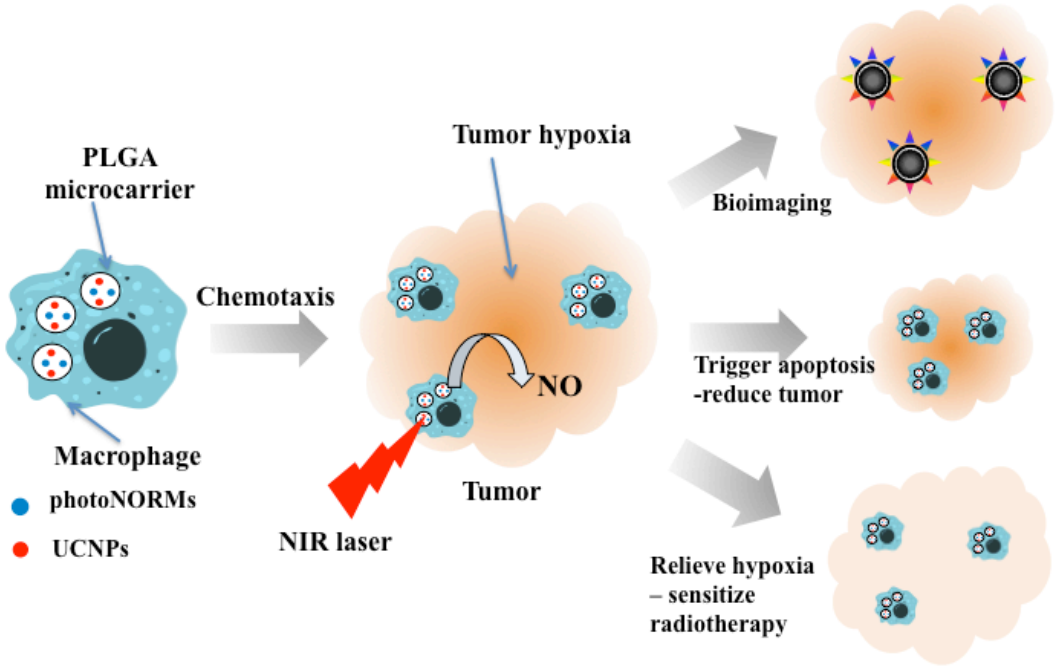

Figure III-K-1. The schematic figure summarize the therapeutic functionality of photochemical Trojan horse therapy and its potential applications.

L. Materials

All cell lines were purchased from ATCC (4T1, NIH-3T3, and bEnd.3). All BALB/C mice (6-8 weeks old) were purchased from Charles River. Sodium tetraphenylborate, sodium trifluoroacetate, sodium oleate, ammonium fluoride, lanthanide chlorides (99.9+%), oleic acid (OA) (90%), 1-octadecene (ODE) (90%), poly(vinyl) alcohol (PVA, Mw: 13000-23000), 4-morpholineethanesulfonic acid (MES, low moisture content, 99+%), immunoglobulin G (IgG from mouse serum), N-(3-Dimethylaminopropyl)-N′-ethylcarbodiimide hydrochloride (EDC•HCl, commercial grade), TritonTM X-100 (BioXtra), Tween® 20 (BioXtra), agarose (BioReagent), sodium hydroxide (NaOH, ACS

reagent grade), sodium acetate (RegentPlus®), purified human plasma fibronectin (1 mg/mL), and Perfecta3D® 96-well hanging drop plates were purchased from Sigma-Aldrich. 10X PBS (OmniPur® liquid concentrate) was purchased from EMD Millipore. poly(lactic-co-glycolic acid) (5050 DLG 8A, acid terminated) was purchased from Lakeshore Biomaterials. 4-Amino-5-methylamino-2',7'-difluorofluorescein diacetate (DAF-FM-2DA, Molecular Probes®) was purchased from Life Technologies. N-hydroxysuccinimide (NHS), fetal bovine serum (FBS), Dulbecco's Modified Eagle Medium high glucose (DMEM), Dulbecco's Modified Eagle Medium: Nutrient mixture F12 GlutaMAXTM and high glucose (DMEM/F12), sodium pyruvate solution (100 mM), penicillin streptomycin 10,000 U/mL (P/S), trypsin/EDTA (0.25%), Hank's Balanced Salt Solution without calcium and magnesium (HBSS) Dulbecco's Phosphate Buffered Saline without calcium and magnesium (DPBS) NucBlue®, CellTrackerTM Deep Red, goat serum, FITC labeled Goat-anti-rabbit, Rabbit anti-HIF-1α, p-nitrophenyl phosphate (PNPP) substrate tablets, calcein AM, micro bicinchoninic acid assay kit, and alamarBlue® was purchased from Thermo Fisher Scientific. All TC and Non-TC treated plasticware for cell culture, and FluoroblokTM transwell inserts were purchased from Corning. BambankerTM cell freezing media was purchased from Bulldog Bio. AccumaxTM was purchased from Innovative Cell Technologies. L-N-nitroarginine methyl ester hydrochloride salt (L-NAME) was purchased from Caymen Chemical. Murine monocyte colony stimulating factor 1 (MCSF-1) and murine monocyte chemoattractant protein 1 (MCP-1) were purchased from Peprotech. Hypoxyprobe-Red549 Kit containing pimonidazole HCl and mouse DylightTM 549-Mab was purchased from Hypoxyprobe. Immunoglobulin G labeled with Cyanine 3.5 (Cy3.5-IgG) was purchased from Jackson Immuno.

M. Analytical Instrumentation

Absorbance spectra were taken on a Shimadzu UV-2401PC. Nitric oxide was measured using a General Electric Sievers Nitric Oxide Analyzer NOA 280i. Samples were photolyzed with a 3 watt 798 nm SheauPac fiber coupled laser module (actual excitation wavelength: 794 nm). XRD spectra were obtained on a Bruker AXS D8 Discover GADDS X-Ray diffractometer (XRD). Upconversion emission spectra were obtained on a Horiba Jobin Yvon LabRAM ARAMIS automated scanning confocal Raman microscope. DLS data were obtained on a Malvern NANO-ZS. TEM images were obtained on a FEI Titan 300 kV FEG Transmission electron microscope. SEM images were obtained on a FEI Nova Nano 650 FEG scanning electron microscope. Confocal images were obtained on a Olympus Flowview 1000 Spectral Confocal. Tumor sectioning were performed on a Leica Cryostat Microtome. Flow cytometry data were obtained on a FACS Aria high-speed cell sorter.

N. Reference

(1) Murdoch, C.; Giannoudis, A.; Lewis, C. E. Mechanisms Regulating the Recruitment of Macrophages into Hypoxic Areas of Tumors and Other Ischemic Tissues. *Blood* **2004**, *104* (8), 2224–2234.

(2) Burke, B.; Giannoudis, A.; Corke, K. P.; Gill, D.; Wells, M.; Ziegler-Heitbrock, L.; Lewis, C. E. Hypoxia-Induced Gene Expression in Human Macrophages: Implications for Ischemic Tissues and Hypoxia-Regulated Gene Therapy. *Am. J. Pathol.* **2003**, *163* (4), 1233–1243.

(3) Harris, A. L. Hypoxia — a Key Regulatory Factor in Tumour Growth. *Nat. Rev. Cancer* **2002**, *2* (1), 38–47.

(4) Begg, A. C.; Stewart, F. A.; Vens, C. Strategies to Improve Radiotherapy with Targeted Drugs. *Nat. Rev. Cancer* **2011**, *11* (4), 239–253.

(5) Ridnour, L. A.; Thomas, D. D.; Switzer, C.; Flores-Santana, W.; Isenberg, J. S.; Ambs, S.; Roberts, D. D.; Wink, D. A. Molecular Mechanisms for Discrete Nitric Oxide Levels in Cancer. *Nitric Oxide* **2008**, *19* (2), 73–76.

(6) Mocellin, S.; Bronte, V.; Nitti, D. Nitric Oxide, a Double Edged Sword in Cancer Biology: Searching for Therapeutic Opportunities. *Med. Res. Rev.* **2007**, *27* (3), 317–352.

(7) Thomas, D. D.; Espey, M. G.; Ridnour, L. A.; Hofseth, L. J.; Mancardi, D.; Harris, C. C.; Wink, D. A. Hypoxic Inducible Factor 1α, Extracellular Signal-Regulated Kinase, and p53 Are Regulated by Distinct Threshold Concentrations of Nitric Oxide. *Proc. Natl. Acad. Sci. U. S. A.* **2004**, *101* (24), 8894–8899.

(8) Tan, L.; Huang, R.; Li, X.; Liu, S.; Shen, Y.-M. Controllable Release of Nitric Oxide and Doxorubicin from Engineered Nanospheres for Synergistic Tumor Therapy. *Acta Biomater.* **2017**, *57* (Supplement C), 498–510.

(9) Mateo, J.; García-Lecea, M.; Cadenas, S.; Hernández, C.; Moncada, S. Regulation of Hypoxia-Inducible Factor-1α by Nitric Oxide through Mitochondria-Dependent and -Independent Pathways. *Biochem. J.* **2003**, *376* (2), 537–544.

(10) Bonavida, B.; Garban, H. Nitric Oxide-Mediated Sensitization of Resistant Tumor Cells to Apoptosis by Chemo-Immunotherapeutics. *Redox Biol.* **2015**, *6*, 486–494.

(11) Yasuda, H. Solid Tumor Physiology and Hypoxia-Induced Chemo/Radio-Resistance: Novel Strategy for Cancer Therapy: Nitric Oxide Donor as a Therapeutic Enhancer. *Nitric Oxide* **2008**, *19* (2), 205–216.

(12) Weissleder, R. A Clearer Vision for in Vivo Imaging. *Nat. Biotechnol.* **2001**, *19* (4), 316–317.

(13) Ford, P. C. Photochemical Delivery of Nitric Oxide. *Nitric Oxide* **2013**, *34*, 56–64.

(14) König, K. Multiphoton Microscopy in Life Sciences. *J. Microsc.* **2000**, *200* (2), 83–104.

(15) Hitomi, Y.; Iwamoto, Y.; Kodera, M. Electronic Tuning of Nitric Oxide Release from Manganese Nitrosyl Complexes by Visible Light Irradiation: Enhancement of Nitric Oxide Release Efficiency by the Nitro-Substituted Quinoline Ligand. *Dalton Trans.* **2013**, *43* (5), 2161–2167.

(16) Eroy-Reveles, A. A.; Leung, Y.; Beavers, C. M.; Olmstead, M. M.; Mascharak, P. K. Near-Infrared Light Activated Release of Nitric Oxide from Designed Photoactive Manganese Nitrosyls: Strategy, Design, and Potential as NO Donors. *J. Am. Chem. Soc.* **2008**, *130* (13), 4447–4458.

(17) Ford, P. C. Polychromophoric Metal Complexes for Generating the Bioregulatory Agent Nitric Oxide by Single- and Two-Photon Excitation. *Acc. Chem. Res.* **2008**, *41* (2), 190–200.

(18) Choi, M.-R.; Stanton-Maxey, K. J.; Stanley, J. K.; Levin, C. S.; Bardhan, R.; Akin, D.; Badve, S.; Sturgis, J.; Robinson, J. P.; Bashir, R.; Halas, N. J.; Clare, S. E. A Cellular Trojan Horse for Delivery of Therapeutic Nanoparticles into Tumors. *Nano Lett.* **2007**, *7* (12), 3759–3765.

(19) Doshi, N.; Swiston, A. J.; Gilbert, J. B.; Alcaraz, M. L.; Cohen, R. E.; Rubner, M. F.; Mitragotri, S. Cell-Based Drug Delivery Devices Using Phagocytosis-Resistant Backpacks. *Adv. Mater.* **2011**, *23* (12), H105–H109.

(20) Anselmo, A. C.; Mitragotri, S. Cell-Mediated Delivery of Nanoparticles: Taking Advantage of Circulatory Cells to Target Nanoparticles. *J. Controlled Release* **2014**, *190*, 531–541.

(21) Choi, J.; Kim, H.-Y.; Ju, E. J.; Jung, J.; Park, J.; Chung, H.-K.; Lee, J. S.; Lee, J. S.; Park, H. J.; Song, S. Y.; Jeong, S.-Y.; Choi, E. K. Use of Macrophages to Deliver Therapeutic and Imaging Contrast Agents to Tumors. *Biomaterials* **2012**, *33* (16), 4195–4203.

(22) Huang, W.-C.; Shen, M.-Y.; Chen, H.-H.; Lin, S.-C.; Chiang, W.-H.; Wu, P.-H.; Chang, C.-W.; Chiang, C.-S.; Chiu, H.-C. Monocytic Delivery of Therapeutic Oxygen Bubbles for Dual-Modality Treatment of Tumor Hypoxia. *J. Controlled Release* **2015**, *220* (Part B), 738–750.

(23) Huang, W.-C.; Chiang, W.-H.; Cheng, Y.-H.; Lin, W.-C.; Yu, C.-F.; Yen, C.-Y.; Yeh, C.-K.; Chern, C.-S.; Chiang, C.-S.; Chiu, H.-C. Tumortropic Monocyte-Mediated

Delivery of Echogenic Polymer Bubbles and Therapeutic Vesicles for Chemotherapy of Tumor Hypoxia. *Biomaterials* **2015**, *71* (Supplement C), 71–83.

(24) Junttila, M. R.; de Sauvage, F. J. Influence of Tumour Micro-Environment Heterogeneity on Therapeutic Response. *Nature* **2013**, *501* (7467), 346–354.

(25) Wang, Y.-F.; Liu, G.-Y.; Sun, L.-D.; Xiao, J.-W.; Zhou, J.-C.; Yan, C.-H. Nd3+-Sensitized Upconversion Nanophosphors: Efficient In Vivo Bioimaging Probes with Minimized Heating Effect. *ACS Nano* **2013**, *7* (8), 7200–7206.

(26) Levy, E. S.; Tajon, C. A.; Bischof, T. S.; Iafrati, J.; Fernandez-Bravo, A.; Garfield, D. J.; Chamanzar, M.; Maharbiz, M. M.; Sohal, V. S.; Schuck, P. J.; Cohen, B. E.; Chan, E. M. Energy-Looping Nanoparticles: Harnessing Excited-State Absorption for Deep-Tissue Imaging. *ACS Nano* **2016**, *10* (9), 8423–8433.

(27) Xie, X.; Gao, N.; Deng, R.; Sun, Q.; Xu, Q.-H.; Liu, X. Mechanistic Investigation of Photon Upconversion in Nd3+-Sensitized Core–Shell Nanoparticles. *J. Am. Chem. Soc.* **2013**, *135* (34), 12608–12611.

(28) Ostrowski, A. D.; Chan, E. M.; Gargas, D. J.; Katz, E. M.; Han, G.; Schuck, P. J.; Milliron, D. J.; Cohen, B. E. Controlled Synthesis and Single-Particle Imaging of Bright, Sub-10 Nm Lanthanide-Doped Upconverting Nanocrystals. *ACS Nano* **2012**, *6* (3), 2686–2692.

(29) Wang, F.; Han, Y.; Lim, C. S.; Lu, Y.; Wang, J.; Xu, J.; Chen, H.; Zhang, C.; Hong, M.; Liu, X. Simultaneous Phase and Size Control of Upconversion Nanocrystals through Lanthanide Doping. *Nature* **2010**, *463* (7284), 1061–1065.

(30) Yi, G. S.; Chow, G. M. Synthesis of Hexagonal-Phase NaYF4:Yb,Er and NaYF4:Yb,Tm Nanocrystals with Efficient Up-Conversion Fluorescence. *Adv. Funct. Mater.* **2006**, *16* (18), 2324–2329.

(31) Zhao, Y.; Zhan, Q.; Liu, J.; He, S. Optically Investigating Nd3+-Yb3+ Cascade Sensitized Upconversion Nanoparticles for High Resolution, Rapid Scanning, Deep and Damage-Free Bio-Imaging. *Biomed. Opt. Express* **2015**, *6* (3), 838–848.

(32) Park, T. G.; Yong Lee, H.; Sung Nam, Y. A New Preparation Method for Protein Loaded Poly(d,l-Lactic-Co-Glycolic Acid) Microspheres and Protein Release Mechanism Study. *J. Controlled Release* **1998**, *55* (2–3), 181–191.

(33) Zambaux, M. F.; Bonneaux, F.; Gref, R.; Maincent, P.; Dellacherie, E.; Alonso, M. J.; Labrude, P.; Vigneron, C. Influence of Experimental Parameters on the Characteristics of Poly(lactic Acid) Nanoparticles Prepared by a Double Emulsion Method. *J. Controlled Release* **1998**, *50* (1–3), 31–40.

(34) Champion, J. A.; Katare, Y. K.; Mitragotri, S. Particle Shape: A New Design Parameter for Micro- and Nanoscale Drug Delivery Carriers. *J. Controlled Release* **2007**, *121* (1–2), 3–9.

(35) Garcia, J. V.; Yang, J.; Shen, D.; Yao, C.; Li, X.; Wang, R.; Stucky, G. D.; Zhao, D.; Ford, P. C.; Zhang, F. NIR-Triggered Release of Caged Nitric Oxide Using Upconverting Nanostructured Materials. *Small* **2012**, *8* (24), 3800–3805.

(36) Burks, P. T.; Garcia, J. V.; GonzalezIrias, R.; Tillman, J. T.; Niu, M.; Mikhailovsky, A. A.; Zhang, J.; Zhang, F.; Ford, P. C. Nitric Oxide Releasing Materials Triggered by Near-Infrared Excitation Through Tissue Filters. *J. Am. Chem. Soc.* **2013**, *135* (48), 18145–18152.

(37) Pierri, A. E.; Huang, P.-J.; Garcia, J. V.; Stanfill, J. G.; Chui, M.; Wu, G.; Zheng, N.; Ford, P. C. A photoCORM Nanocarrier for CO Release Using NIR Light. *Chem. Commun.* **2015**, *51* (11), 2072–2075.

(38) Champion, J. A.; Mitragotri, S. Role of Target Geometry in Phagocytosis. *Proc. Natl. Acad. Sci. U. S. A.* **2006**, *103* (13), 4930–4934.

(39) Beningo, K. A.; Wang, Y. Fc-Receptor-Mediated Phagocytosis Is Regulated by Mechanical Properties of the Target. *J. Cell Sci.* **2002**, *115* (4), 849–856.

(40) Levy, E. S.; Morales, D. P.; Garcia, J. V.; Reich, N. O.; Ford, P. C. Near-IR Mediated Intracellular Uncaging of NO from Cell Targeted Hollow Gold Nanoparticles. *Chem. Commun.* **2015**, *51* (100), 17692–17695.

(41) Pfeiffer, S.; Leopold, E.; Schmidt, K.; Brunner, F.; Mayer, B. Inhibition of Nitric Oxide Synthesis by NG-Nitro-L-Arginine Methyl Ester (L-NAME): Requirement for Bioactivation to the Free Acid, NG-Nitro-L-Arginine. *Br. J. Pharmacol.* **1996**, *118* (6), 1433–1440.

(42) Chen, Y.; Liu, L. Modern Methods for Delivery of Drugs across the Blood–brain Barrier. *Adv. Drug Deliv. Rev.* **2012**, *64* (7), 640–665.

(43) Chang, Y.-N.; Guo, H.; Li, J.; Song, Y.; Zhang, M.; Jin, J.; Xing, G.; Zhao, Y. Adjusting the Balance between Effective Loading and Vector Migration of Macrophage Vehicles to Deliver Nanoparticles. *PLOS ONE* **2013**, *8* (10), e76024.

(44) Jiang, P.-S.; Yu, C.-F.; Yen, C.-Y.; Woo, C. W.; Lo, S.-H.; Huang, Y.-K.; Hong, J.-H.; Chiang, C.-S. Irradiation Enhances the Ability of Monocytes as Nanoparticle Carrier for Cancer Therapy. *PLOS ONE* **2015**, *10* (9), e0139043.

(45) Priwitaningrum, D. L.; Blondé, J.-B. G.; Sridhar, A.; van Baarlen, J.; Hennink, W. E.; Storm, G.; Le Gac, S.; Prakash, J. Tumor Stroma-Containing 3D Spheroid Arrays: A Tool to Study Nanoparticle Penetration. *J. Controlled Release* **2016**, *244* (Part B), 257–268.

(46) Silzle, T.; Kreutz, M.; Dobler, M. A.; Brockhoff, G.; Knuechel, R.; Kunz-Schughart, L. A. Tumor-Associated Fibroblasts Recruit Blood Monocytes into Tumor Tissue. *Eur. J. Immunol.* **2003**, *33* (5), 1311–1320.

(47) Brown, J. M. Tumor Hypoxia in Cancer Therapy. *Methods Enzymol.* **2007**, *435*, 295–321.

(48) Sica, A.; Schioppa, T.; Mantovani, A.; Allavena, P. Tumour-Associated Macrophages Are a Distinct M2 Polarised Population Promoting Tumour Progression: Potential Targets of Anti-Cancer Therapy. *Eur. J. Cancer* **2006**, *42* (6), 717–727.

(49) Friedrich, J.; Eder, W.; Castaneda, J.; Doss, M.; Huber, E.; Ebner, R.; Kunz-Schughart, L. A. A Reliable Tool to Determine Cell Viability in Complex 3-D Culture: The Acid Phosphatase Assay. *J. Biomol. Screen.* **2007**, *12* (7), 925–937.

(50) Yerlikaya, A.; Okur, E.; Ulukaya, E. The p53-Independent Induction of Apoptosis in Breast Cancer Cells in Response to Proteasome Inhibitor Bortezomib. *Tumor Biol.* **2012**, *33* (5), 1385–1392.

(51) Masoud, G. N.; Li, W. HIF-1α Pathway: Role, Regulation and Intervention for Cancer Therapy. *Acta Pharm. Sin. B* **2015**, *5* (5), 378–389.

(52) Hagen, T.; Taylor, C. T.; Lam, F.; Moncada, S. Redistribution of Intracellular Oxygen in Hypoxia by Nitric Oxide: Effect on HIF1α. *Science* **2003**, *302* (5652), 1975–1978.

(53) Mitchell, J. B.; Wink, D. A.; DeGraff, W.; Gamson, J.; Keefer, L. K.; Krishna, M. C. Hypoxic Mammalian Cell Radiosensitization by Nitric Oxide. *Cancer Res.* **1993**, *53* (24), 5845–5848.

(54) Bourassa, J.; DeGraff, W.; Kudo, S.; Wink, D. A.; Mitchell, J. B.; Ford, P. C. Photochemistry of Roussin's Red Salt, Na2[Fe2S2(NO)4], and of Roussin's Black Salt,

NH4[Fe4S3(NO)7]. In Situ Nitric Oxide Generation To Sensitize γ-Radiation Induced Cell Death1. *J. Am. Chem. Soc.* **1997**, *119* (12), 2853–2860.

IV. The Application of Graphene Quantum dots (GQDs) in NIR Light-triggered Release of Small Molecule Bioregulators

A. Abstract

The new nano-carriers with nitrogen doped graphene quantum dots (N-GQDs) as photo-active cores was developed for photo-triggered nitric oxide (NO) delivery. N-GQDs with carboxyl groups (~4 nm) was prepared from graphite nanoparticles (~50 nm) treated with Hummers' oxidation method and solvothermal decomposition process (see Chapter II). Through amide coupling with oleylamine, C18-GQDs were synthesized and these were assembled with an amphiphilic biotinylated DSPE-PEG. The result was the formation of hydrophilic nano-carriers with lipophilic domains for loading with the hydrophobic NO precursor, trans-[PetACr(ONO)$_2$]BPh$_4$.This PetACrONO is UV-visible light sensitive and stable in acetonitrile at physiologically relevant temperature (37 ^{0}C). Notably, the GQDs-based nano-carriers loaded with PetACrONO release NO upon 794 nm laser exposure. Additionally, the surface of nano-carriers can be modified with cell penetrating peptides (CPPs) via biotin-streptavidin-biotin assembly strategy. The preliminary cell study shows CPPs-modified GQDs@DSPE-PEG containing PetACrONO can be delivered into HeLa cells and NO can be intracellularly uncaged under 794 nm laser irradiation.

B. Introduction

Nitric oxide (NO), a small molecule bioregulator (SMB), has attracted considerable attention due to its promising applications in cardiovascular disease[1,2], cancer treatment[3,4], antibacterial activity[5–8] and wound healing[9]. The therapeutic effect of NO pro-drugs greatly depends on the concentration, duration and the specific site of NO delivery.[10] Nanomolar concentrations of NO is a vasodilator and is cytoprotective in cells while micromolar concentrations of NO can suppress tumor growth and, when administered in tandem with γ-radiation, is a radiation sensitizer.[3,11–16] Photochemical delivery allows for control over the timing, dosage and location of NO release by precisely controlling the intensity and location of light irradiation.[10] However, there are key challenges associated with using such photo-activated NO releasing moieties ("photoNORMs").[17] One is to activate these precursors with tissue penetrating near infrared (NIR) light (700-900 nm), while another is to deliver these precursors directly to the target sites such as tumors.

In order to address the first challenge, several photo-active nanomaterials such as upconverting nanoparticles (UCNPs)[18–21], carbon quantum dots (CQDs)[22–24] and gold nanoparticles[25] have already been applied to NIR light-triggered SMB delivery system. In particular, CQDs possesses unique NIR-responsive photophysical properties such as high two-photon cross-section (48000 Göppert-Mayer unit)[26,27] and photothermal effect[22,24]. Therefore, compared with UCNPs and gold nanoparticles, this metal-free carbon nanomaterial has potential to serve as an alternative NIR photosensitizer. Even though several papers discuss CQDs-based applications in NIR-activated SMB release, they still have several puzzles left behind their work. Callan and Sortino at el. claimed NO can be

uncaged from their carbon quantum dot–NO photoreleaser nanohybrids via an energy transfer mechanism under 800 nm two-photon excitation. But, they didn't have any direct evidence to prove it.[23] Chen and his co-workers argued that their metal carbonyl-caged graphene oxide nanomedicine is able to release carbon monoxide (CO) upon 808 nm continuous wavelength (CW) laser irradiation.[22] Even though they tried to prove the mechanism of CO release is photocatalytic and not photothermal decomposition, they didn't consider that the local heating on graphene oxide nanomaterials (one type of CQDs) may have very high temperature to directly decompose Mn-carbonyl molecules. Recently, Liu et. al declared ruthenium nitrosyl functionalized graphene quantum dots (GQDs, one type of CQDs) have impressive photothermal effect to trigger NO release from ruthenium nitrosyl (RuNO) under 808 nm laser exposure.[24] This is the first literature to clearly show RuNO functionalized GQDs has significant strong photothermal effect in comparison with naked GQDs. Unfortunately, the GQDs they prepared may not be graphene-like nanomaterials based on their TEM and AFM results, and could be graphite nanoparticles due to their same dimension on diameter (~3 nm) and thickness (~3 nm).

Therefore, in order to understand if PetACrONO, the new photoNORM we synthesized (Described in Chapter II), can generate NO in GQDs-based nano-composites under photothermal decomposition process, we designed two different carriers: PetACrONO functionalized GQDs (PetACrONO-GQDs, **Figure IV-B-1**) and PetACrONO-loaded GQDs@DSPE-PEG (**Figure IV-B-2**). Trans-$[AminoPetACr(ONO)_2]^+$ was designed to covalently bond with carboxyl groups on the surface of GQDs in the PetACrONO-GQDs system which mimics Liu's work. In contrast to PetACrONO-GQDs, polymeric nano-carriers GQDs@DSPE-PEG can encapsulate PetACrONO non-covalently into their

lipophilic domains. The latter design may prevent photocatalytic mechanism described in Chen's work due to the long distance between PetACrONO and GQD cores.

Moreover, to address the second challenge for photochemical SMB delivery, cell-penetrating peptide, biotinylated TAT peptide, was applied to overcome the barrier of cellular membranes and efficiently deliver our nano-carriers inside HeLa cancer cells.[28–32]

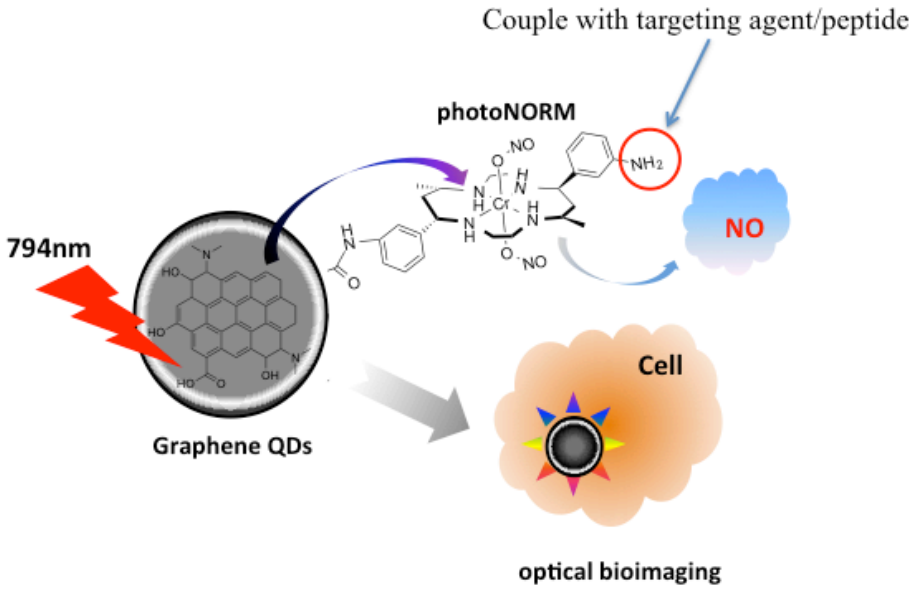

Figure IV-B-1. The scheme presents PetACrONO covalently bonded on the graphene QDs (PetACrONO-GQDs) can release NO under 794 nm laser irradiation.

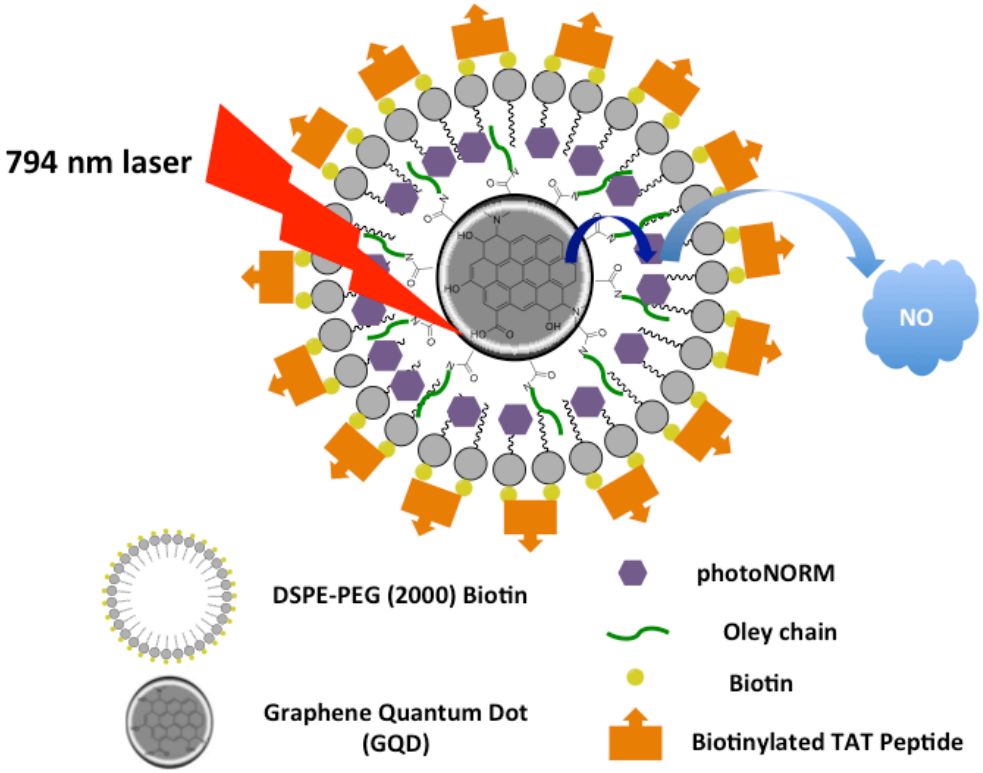

Figure IV-B-2. The scheme presents PetACrONO can be loaded into the lipophilic domains of the nano-carrier GQDs@DSPE-PEG and the surface of nano-carrier can assemble with biotinlyated TAT peptide to enhance the internalization of cancer cells.

C. Preparation of GQDs-based Nanocarriers, GQDs@DSPE-PEG

Our previous research demonstrated that the hydrophobic UCNPs with oleic acid as a surfactant can assemble with the amphiphilic phospholipid-functionalized poly(ethylene glycol) (DSPE-PEG 2000 Carboxylic acid) via van der Waals forces to form water-soluble nanocarriers with lipid domains for a hydrophobic CO prodrug loading.[33] In order to prepare this kind of nanocarriers by using the same strategy, the surface of N-GQDs have to be modified with oleyl chain to further assemble with a DSPE-PEG. As described previously in Chapter II, the surface of N-GQDs possesses carboxylic acid (C=O: 1712 cm^{-1}), which can covalently bond with oleylamine. The FT-IR spectra (**Figure IV-C-1**) proved that the carboxylic acid on the N-GQDs was converted to amide (C=O: 1641 cm^{-1}) via amide coupling reaction. The following information is the preparation procedure of GQDs-based nanocarriers.

N-GQDs (1.322 mg, assuming 0.11 mmole) was dissolved in 200 proof ethanol by 1-hour sonication. 21.1 mg N-(3-Dimethylaminopropyl)-N'-ethylcarbodiimide hydrochloride (EDC•HCl) and 12.7 mg N-hydroxysuccinimide (NHS) were added into N-GQDs solution and stirred for one hour at room temperature. Oleylamine (36 μL) was injected into the mixture and stirred for at least 8 hours at room temperature. The solution was dried by a rotary evaporator and then dissolved into dichloromethane (DCM) by 1-hour sonication. Water-soluble impurities and unreacted N-GQDs were removed via solvent extraction from the DCM solution. After removed DCM, the oil-like residue was dissolved into hexane and dialyzed by using a 1000 MWCO dialysis tube against hexane for at least 3 days. The purified oleyl N-GQDs was stored in hexane before using it.

Purified Oleyl N-GQDs (24 mg) was dissolved in 2 mL DCM and 21 mg biotinylated DSPE-PEG 2000 was added into the DCM solution. The mixture was sonicated for 1 hour and dried under vacuum for overnight to form white powder. The white powder was suspended in water and dialyzed by using a 5000MWCO dialysis tube for one day to remove excess polymer. The nanocarriers, N-GQDs@DSPE-PEG, was dried under vacuum and keep in a freezer before using it.

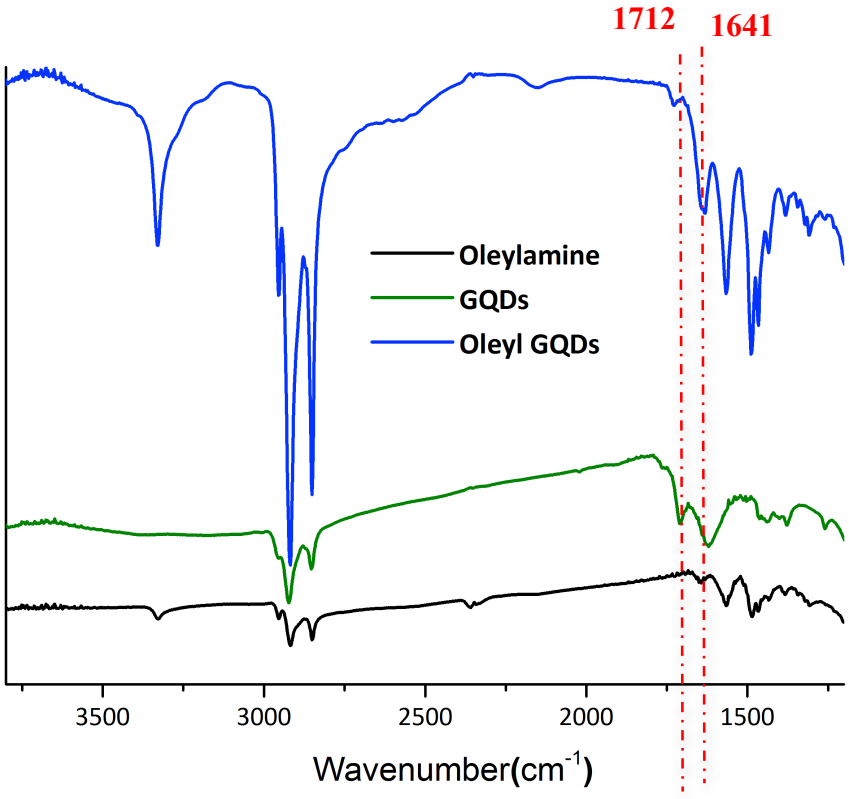

Figure IV-C-1. The FT-IR spectra of oleylamine, N-GQDs, oleyl N-GQDs.

D. PetACrONOBPh$_4$ loading

In order to infuse the hydrophobic PetACrONOBPh$_4$ into lipid domain of the nanocarriers, the modified procedure was applied.[33]

PetACrONOBPh$_4$ (10 mg) was marginally dissolved in 1 mL solution of 40% acetonitrile in water and 17 mg N-GQDs@DSPE-PEG was added into the solution. The mixture was stirred under dark for 20 hours at room temperature. The particles were collected by centrifugation and washed with 50% acetonitrile aqueous solution. The morphological study was performed by transmission electron microscopy (**Figure IV-D-1**). The distribution of particle size was measured by ImageJ (**Figure IV-D-2**) and most of particles are between 20 and 70 nm.

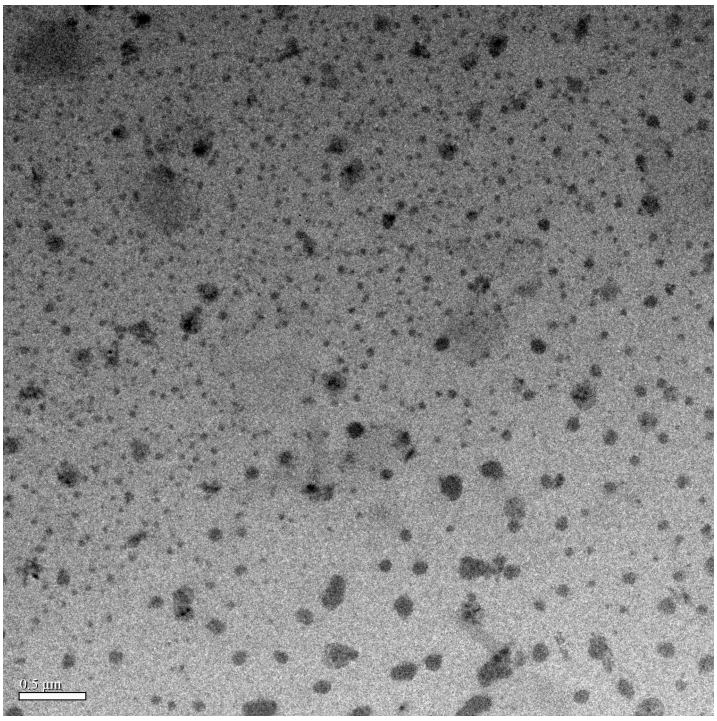

Figure IV-D-1. The TEM image of PetACrONOBPh$_4$ – loaded N-GQDs@DSPE-PEG.

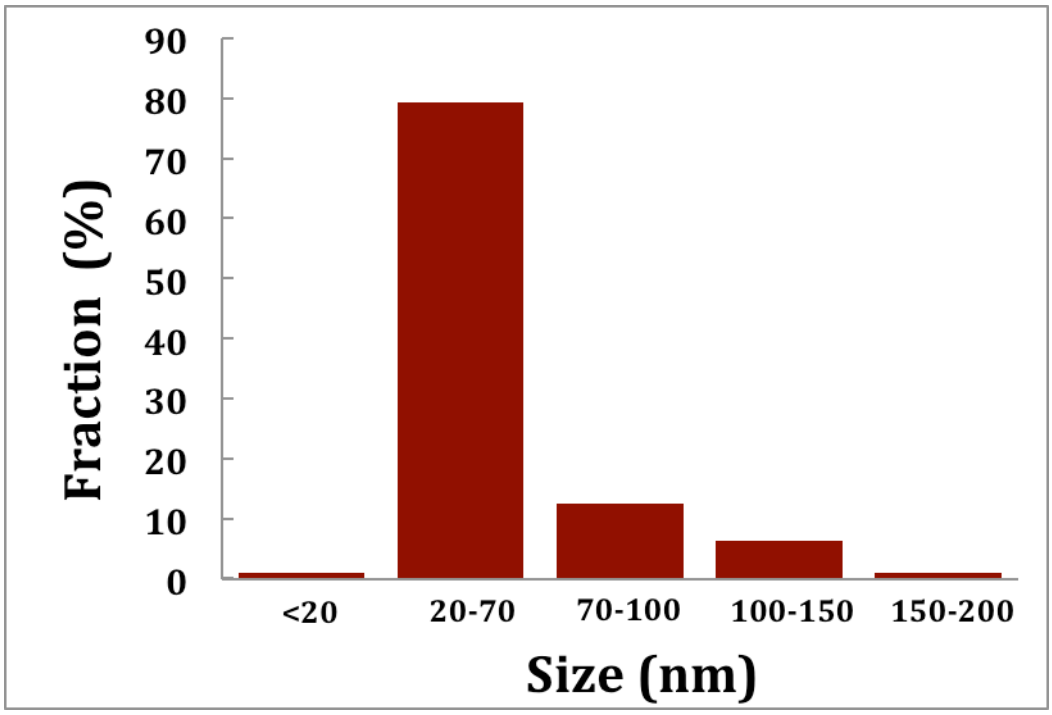

Figure IV-D-2. The size distribution of PetACrONOBPh$_4$ – loaded N-GQDs@DSPE-PEG.

E. NO Release Efficiency

NO release efficiency of PetACrONOBPh$_4$ - loaded N-GQDs@DSPE-PEG was investigated by using the Sievers Nitric Oxide Analyzer (NOA). The nanocarrier was suspended in 2 mL pH 7.4 phosphate buffered saline (PBS) solution in a designed cuvette. The suspension was stirred during the irradiation with a 794 nm diode laser and NO generated from the particles was carried to NOA by using medical air purging. Each peak in Figure IV E-1 and Figure IV-E-3 represents NO release under 794 nm laser irradiation. Figure IV-E-2 shows that NO release linearly responds to different power density of laser with 90-second exposure time. Additionally, under the same power density of irradiation (13.02 W/cm^2) and different exposure time, NO release efficiency of the nanocarriers is 0.21 pmole per second irradiation. (**Figure IV-E-4**) According to a literature report by Chen et.

al.[22], CO release from the MnCO-GO nanomedicine occurs via a photocatalytic mechanism. The graphene oxide nanoparticles absorb energy of NIR light and "transforms" NIR photon into an active electron that can reduce the manganese CO donor bonded on the surface of nanoparticles. They also claimed there is no CO release when the temperature of MnCO-GO suspension was increased with 5^0C by direct heating for 25 min. However, they didn't consider the local heating in the core of the nanomedicine could cause over a temperature increase >5 ^{o}C. Therefore, for the NIR induced release of NO from GQDs-based nanocarriers, photothermal decomposition mechanism should be considered.

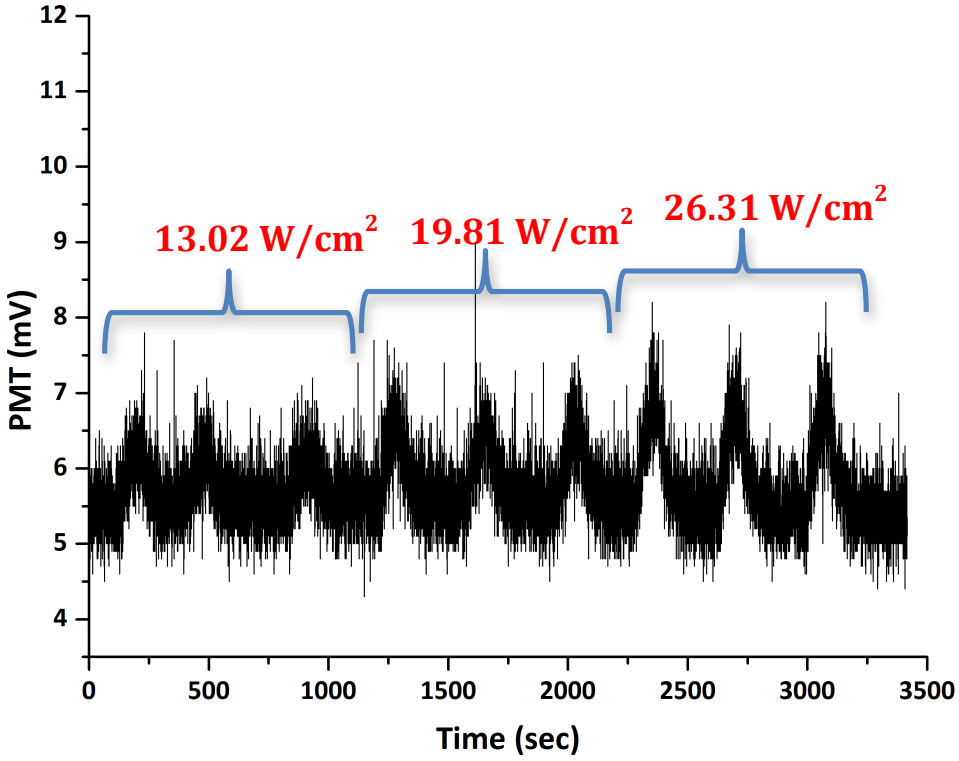

Figure IV-E-1. Photo-triggered NO released from PetACrONOBPh$_4$ – loaded N-GQDs@DSPE-PEG suspended in a 2 mL pH 7.4 PBS solution under 794 nm laser irradiation with different power density for 90 sec.

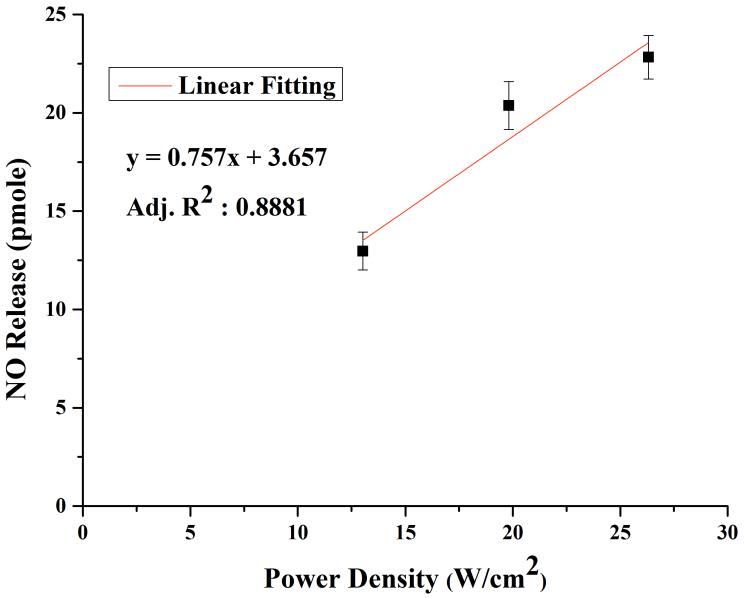

Figure IV-E-2. The plot of the amount of NO release vs power density of irradiation.

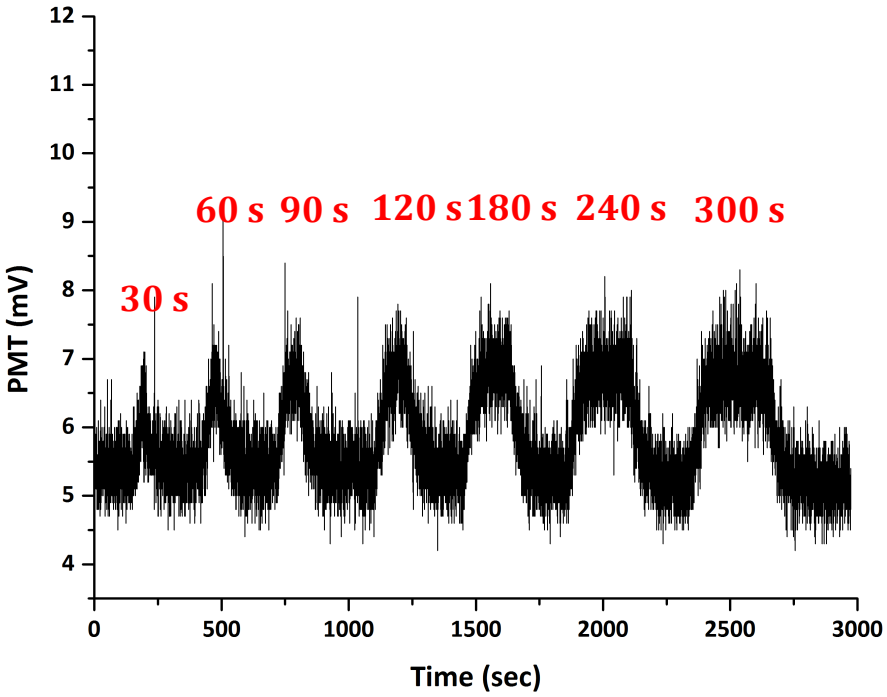

Figure IV-E-3. Photo-triggered NO released from PetACrONOBPh$_4$ – loaded N-GQDs@DSPE-PEG suspended in a 2 mL pH 7.4 PBS solution under 794 nm laser irradiation with power density of 13.02 W/cm^2 for 30, 60, 90, 120 180, 240 and 300 sec exposure.

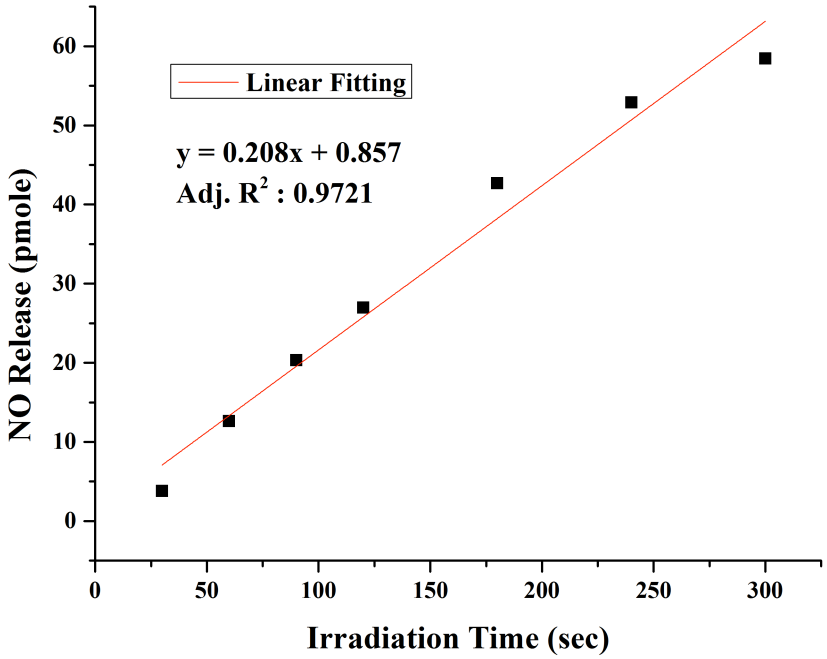

Figure IV-E-4. The plot of the amount of NO release vs irradiation time.

F. Biological Study

HIV-1-Trans-Activator of Transcription (TAT) peptide is a well-known cell-penetrating peptide (CPP) that can enter cells in seemingly energy-independent manner.[34] It also can efficiently deliver cargo with various sizes up to submicron into primary cells under receptor-independent process.[35] All biological studies were done by Demosthenes Morales and Erin Morgan in Professor Reich's group. In this preliminary study, we demonstrated the biotinlyated TAT peptide can be attached on the surface of biotinlyated N-GQDs@DSPE-PEG via biotin-streptavidin-biotin assembly method.[30] Additionally, HeLa cancer cell line was applied to study the cell internalization and in vitro NO visualization. According to the TEM image (**Figure IV-D-1** & **Figure IV-D-2**), the size of nanocarriers is between 20 and

200 nm and shouldn't be clearly observed by confocal microscopy. Compared with Figure IV-F-1a and b, Figure IV-F-1c apparently shows some big particles are inside of cells due to particles aggregation. In order to investigate the visualization of intracellular NO release from the nanocarriers, four different conditions of cell incubation was operated. All cells were treated with a nitric oxide synthase (NOS) inhibitor, L-N-nitroarginine methyl ester (L-NANE), to inhibit NO generated from cells.[36] Figure IV-F-2a and b represent the background images without the NO-nanocarriers loading. Most excitingly, after 794 nm laser irradiation of cells loaded with NO-nanocarriers with power density of 13.02 W/cm^2 for 2 min, NO was uncaged intracullarly and reacted with the nonfluorescent NO reporter, 4-amino-5-methylamino-2',7'-difluorofluorescein diacetate (DAF-FM-2DA), to form fluorescent benzotriazole which has green emission.[25] (**Figure IV-F-1c**) Meanwhile, there is negligible fluorescence in the control experiments under dark to show NO only release upon laser irradiation. (**Figure IV-F-1d**)

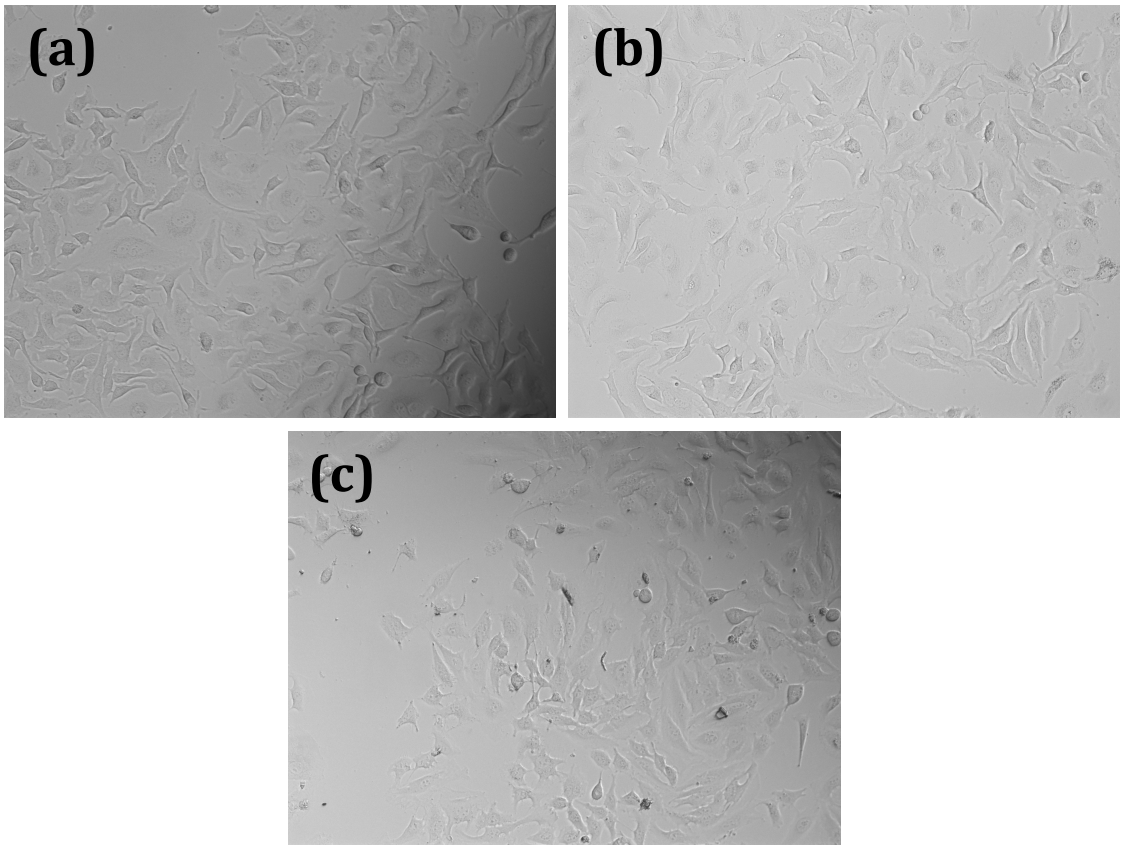

Figure IV-F-1. The bight-filed confocal images of HeLa cells only (a), HeLa cells incubated with DAF-FM-2DA (b) and HeLa cells incubated with the NO sensor 4-amino-5-methylamino-2',7'-difluorofluorescein diacetate (DAF-FM-2DA) and PetACrONOBPh$_4$-loaded N-GQDs@TAT-DSPE-PEG (c). All trials were treated with a nitric oxide synthase (NOS) inhibitor L-N-nitroarginine methyl ester (L-NANE).

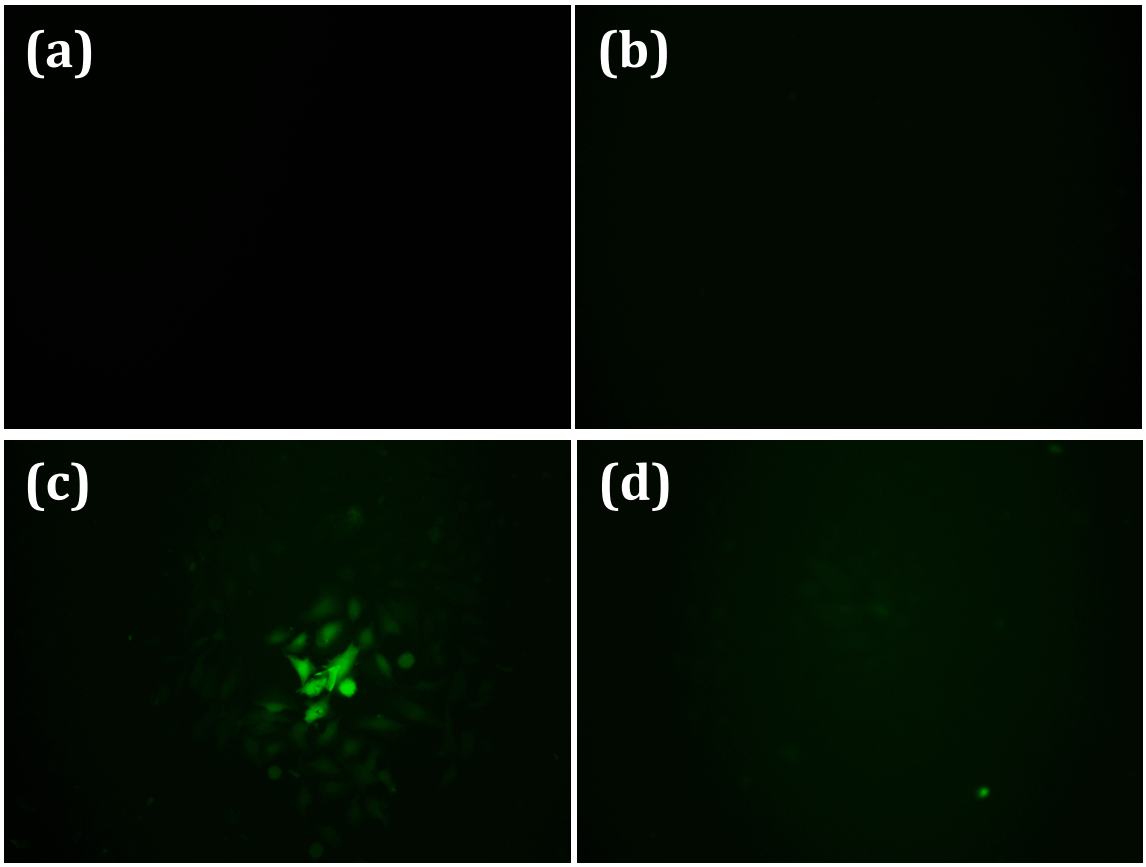

Figure IV-F-2. The dark-field confocal images of HeLa cells only (a), HeLa cells incubated with DAF-FM-2DA (b), HeLa cells incubated with DAF-FM-2DA and PetACrONOBPh$_4$-loaded N-GQDs@TAT-DSPE-PEG under 794 nm laser irradiation with power density of 13.02 W/cm^2 for 2 min (c), and HeLa cells incubated with DAF-FM-2DA and PetACrONOBPh$_4$-loaded N-GQDs@TAT-DSPE-PEG under dark (d).

G. Summary

We have already successfully synthesized carboxyl modified nitrogen-doped graphene quantum dots (N-GQDs). Based on morphological tests (Chapter II Section H), the as-synthesized N-GQDs are 4 nm in diameter and have 1.4 nm of thickness. Additionally, this carbon nanomaterials possess abundant nitrogen in the composition and carboxyl groups on the surface. Carboxyl N-GQDs can be coupled with oleylamine to form C18-GQDs and further assembled with biotinylated DSPE-PED (2000) to afford hydrophilic GQDs@DSPE-PEG nano-carriers. This nano-carriers have lipophilic domains that can be loaded with hydrophobic trans-[PetACr$(ONO)_2$]BPh_4. Our NIR photolysis indicates the amount of NO uncaged from PetACrONO-loaded GQDs@DSPE-PEG can linearly respond to 794 nm laser excitation with different exposure time and power density. Moreover, the preliminary biological study shows the TAT peptide modified nano-carriers containing PetACrONO can be delivered into HeLa cancer cells and intracellular NO release triggered by 794 nm laser irradiation can be visualized by a NO reporter, DAF-FM-2DA. Since PetACrONO wasn't covalently bonded on the surface of GQDs in this case, photocatalytic process for NO uncaging can be ignored but photothermal process may become dominated.

A novel trans-[AminoPetACrCl_2]Cl have been successfully synthesized and also been converted to trans-[AminoPetACr$(ONO)_2$]$^+$ proved by ESI-MS. However, we need more time to work on the purification method (Chapter II Section D). Once this AminoPetACrONO is prepared, it can be covalently bonded with carboxyl groups on the surface of GQDs to further study its NO release efficiency under 794 nm exposure.

H. Future Work and Possible Improvement

Although TAT-modified GQDs@DSPE-PEG containing PetACrONO was successfully prepared and its preliminary biological exam shows NO can be released inside cells under 794 nm laser irradiation, the carriers easily aggregate together to form micron size particles to greatly lower the production yield of nano size particles. Therefore, it is better to optimize the preparation method to avoid this issue.

In addition to the nano-carrier preparation, we still have to do more biological tests to investigate the functionality of TAT peptide to HeLa cancer cells in our nano-carrier system. The quantity of the PetACrONO-loaded nano-carrers delivered into cells with or without TAT assistance can be determined by ICP-AES. Moreover, one more control experiment should be done to show that HeLa cells incubated with L-NAME and DAF-FM-2DA don't have significant green emission after NIR photolysis. The toxicity test for nano-carriers with or without PetACrONO have to be performed in the future.

I. Materials

N-(3-Dimethylaminopropyl)-N′-ethylcarbodiimide hydrochloride (EDC•HCl, commercial grade) and oleylamine were purchased from 10X PBS (OmniPur® liquid concentrate) was purchased from EMD Millipore. N-hydroxysuccinimide (NHS) was purchased from Pierce. 4-Amino-5-methylamino-2',7'-difluorofluorescein diacetate (DAF-FM-2DA, Molecular Probes®) was purchased from Life Technologies. L-N-nitroarginine methyl ester hydrochloride salt (L-NAME) was purchased from Caymen Chemical. 1,2-

distearoyl-sn-glycero-3-phosphoethanolamine-N-[biotinyl(polyethylene glycol)-2000] (ammonium salt) (DSPE-PEG(2000) Biotin) was purchased from Avanti Polar Lipids.

J. Analytical Instrumentation

Nitric oxide was measured using a General Electric Sievers Nitric Oxide Analyzer NOA 280i. Samples were photolyzed with a 3 watt 798 nm SheauPac fiber coupled laser module (actual excitation wavelength: 794 nm). TEM images were obtained on a FEI Titan 300 kV FEG Transmission electron microscope. Confocal images were obtained on a Olympus Flowview 1000 Spectral Confocal. Infrared spectra were taken using a Mattson Research Series FTIR.

K. Reference

(1) Yetik-Anacak, G.; Catravas, J. D. Nitric Oxide and the Endothelium: History and Impact on Cardiovascular Disease. *Vascul. Pharmacol.* **2006**, *45* (5), 268–276.

(2) Cannon, R. O. Role of Nitric Oxide in Cardiovascular Disease: Focus on the Endothelium. *Clin. Chem.* **1998**, *44* (8), 1809–1819.

(3) Wink, D. A.; Vodovotz, Y.; Laval, J.; Laval, F.; Dewhirst, M. W.; Mitchell, J. B. The Multifaceted Roles of Nitric Oxide in Cancer. *Carcinogenesis* **1998**, *19* (5), 711–721.

(4) Wink, D. A.; Mitchell, J. B. Nitric Oxide and Cancer: An Introduction. *Free Radic. Biol. Med.* **2003**, *34* (8), 951–954.

(5) Halpenny, G. M.; Heilman, B.; Mascharak, P. K. Nitric Oxide (NO)-Induced Death of Gram-Negative Bacteria from a Light-Controlled NO-Releasing Platform. *Chem. Biodivers.* **2012**, *9* (9), 1829–1839.

(6) Lu, Y.; Slomberg, D. L.; Schoenfisch, M. H. Nitric Oxide-Releasing Chitosan Oligosaccharides as Antibacterial Agents. *Biomaterials* **2014**, *35* (5), 1716–1724.

(7) Xu, L.-C.; Wo, Y.; Meyerhoff, M. E.; Siedlecki, C. A. Inhibition of Bacterial Adhesion and Biofilm Formation by Dual Functional Textured and Nitric Oxide Releasing Surfaces. *Acta Biomater.* **2017**, *51*, 53–65.

(8) Yin, M.; Li, Z.; Ju, E.; Wang, Z.; Dong, K.; Ren, J.; Qu, X. Multifunctional Upconverting Nanoparticles for near-Infrared Triggered and Synergistic Antibacterial Resistance Therapy. *Chem. Commun.* **2014**, *50* (72), 10488–10490.

(9) Lee, W. H.; Ren, H.; Wu, J.; Novak, O.; Brown, R. B.; Xi, C.; Meyerhoff, M. E. Electrochemically Modulated Nitric Oxide Release From Flexible Silicone Rubber Patch:

Antimicrobial Activity For Potential Wound Healing Applications. *ACS Biomater. Sci. Eng.* **2016**, *2* (9), 1432–1435.

(10) Ford, P. C. Photochemical Delivery of Nitric Oxide. *Nitric Oxide* **2013**, *34*, 56–64.

(11) Jenkins, D. C.; Charles, I. G.; Thomsen, L. L.; Moss, D. W.; Holmes, L. S.; Baylis, S. A.; Rhodes, P.; Westmore, K.; Emson, P. C.; Moncada, S. Roles of Nitric Oxide in Tumor Growth. *Proc. Natl. Acad. Sci.* **1995**, *92* (10), 4392–4396.

(12) Boyd, C. S.; Cadenas, E. Nitric Oxide and Cell Signaling Pathways in Mitochondrial-Dependent Apoptosis. *Biol. Chem.* **2002**, *383* (3–4), 411–423.

(13) Hofseth, L. J.; Hussain, S. P.; Wogan, G. N.; Harris, C. C. Nitric Oxide in Cancer and chemoprevention1. *Free Radic. Biol. Med.* **2003**, *34* (8), 955–968.

(14) Xie, K.; Huang, S. Contribution of Nitric Oxide-Mediated Apoptosis to Cancer Metastasis Inefficiency. *Free Radic. Biol. Med.* **2003**, *34* (8), 969–986.

(15) Fukumura, D.; Kashiwagi, S.; Jain, R. K. The Role of Nitric Oxide in Tumour Progression. *Nat. Rev. Cancer* **2006**, *6* (7), 521–534.

(16) Mocellin, S.; Bronte, V.; Nitti, D. Nitric Oxide, a Double Edged Sword in Cancer Biology: Searching for Therapeutic Opportunities. *Med. Res. Rev.* **2007**, *27* (3), 317–352.

(17) Ford, P. C. Polychromophoric Metal Complexes for Generating the Bioregulatory Agent Nitric Oxide by Single- and Two-Photon Excitation. *Acc. Chem. Res.* **2008**, *41* (2), 190–200.

(18) Pierri, A. E.; Huang, P.-J.; Garcia, J. V.; Stanfill, J. G.; Chui, M.; Wu, G.; Zheng, N.; Ford, P. C. A photoCORM Nanocarrier for CO Release Using NIR Light. *Chem. Commun.* **2015**, *51* (11), 2072–2075.

(19) Ford, P. C. From Curiosity to Applications. A Personal Perspective on Inorganic Photochemistry. *Chem. Sci.* **2016**, *7* (5), 2964–2986.

(20) Garcia, J. V.; Yang, J.; Shen, D.; Yao, C.; Li, X.; Wang, R.; Stucky, G. D.; Zhao, D.; Ford, P. C.; Zhang, F. NIR-Triggered Release of Caged Nitric Oxide Using Upconverting Nanostructured Materials. *Small* **2012**, *8* (24), 3800–3805.

(21) Burks, P. T.; Garcia, J. V.; GonzalezIrias, R.; Tillman, J. T.; Niu, M.; Mikhailovsky, A. A.; Zhang, J.; Zhang, F.; Ford, P. C. Nitric Oxide Releasing Materials Triggered by Near-Infrared Excitation Through Tissue Filters. *J. Am. Chem. Soc.* **2013**, *135* (48), 18145–18152.

(22) He, Q.; Kiesewetter, D. O.; Qu, Y.; Fu, X.; Fan, J.; Huang, P.; Liu, Y.; Zhu, G.; Liu, Y.; Qian, Z.; Chen, X. NIR-Responsive On-Demand Release of CO from Metal Carbonyl-Caged Graphene Oxide Nanomedicine. *Adv. Mater.* **2015**, *27* (42), 6741–6746.

(23) Fowley, C.; McHale, A. P.; McCaughan, B.; Fraix, A.; Sortino, S.; Callan, J. F. Carbon Quantum dot–NO Photoreleaser Nanohybrids for Two-Photon Phototherapy of Hypoxic Tumors. *Chem. Commun.* **2014**, *51* (1), 81–84.

(24) Guo, M.; Xiang, H.-J.; Wang, Y.; Zhang, Q.-L.; An, L.; Yang, S.-P.; Ma, Y.; Wang, Y.; Liu, J.-G. Ruthenium Nitrosyl Functionalized Graphene Quantum Dots as an Efficient Nanoplatform for NIR-Light-Controlled and Mitochondria-Targeted Delivery of Nitric Oxide Combined with Photothermal Therapy. *Chem. Commun.* **2017**, *53* (22), 3253–3256.

(25) Levy, E. S.; Morales, D. P.; Garcia, J. V.; Reich, N. O.; Ford, P. C. Near-IR Mediated Intracellular Uncaging of NO from Cell Targeted Hollow Gold Nanoparticles. *Chem. Commun.* **2015**, *51* (100), 17692–17695.

(26) Kuo, W.-S.; Chang, C.-Y.; Chen, H.-H.; Hsu, C.-L. L.; Wang, J.-Y.; Kao, H.-F.; Chou, L. C.-S.; Chen, Y.-C.; Chen, S.-J.; Chang, W.-T.; Tseng, S.-W.; Wu, P.-C.; Pu, Y.-C. Two-Photon Photoexcited Photodynamic Therapy and Contrast Agent with Antimicrobial Graphene Quantum Dots. *ACS Appl. Mater. Interfaces* **2016**, *8* (44), 30467–30474.

(27) Liu, Q.; Guo, B.; Rao, Z.; Zhang, B.; Gong, J. R. Strong Two-Photon-Induced Fluorescence from Photostable, Biocompatible Nitrogen-Doped Graphene Quantum Dots for Cellular and Deep-Tissue Imaging. *Nano Lett.* **2013**, *13* (6), 2436–2441.

(28) Mäe, M.; Langel, Ü. Cell-Penetrating Peptides as Vectors for Peptide, Protein and Oligonucleotide Delivery. *Curr. Opin. Pharmacol.* **2006**, *6* (5), 509–514.

(29) Koren, E.; Torchilin, V. P. Cell-Penetrating Peptides: Breaking through to the Other Side. *Trends Mol. Med.* **2012**, *18* (7), 385–393.

(30) Braun, G. B.; Friman, T.; Pang, H.-B.; Pallaoro, A.; de Mendoza, T. H.; Willmore, A.-M. A.; Kotamraju, V. R.; Mann, A. P.; She, Z.-G.; Sugahara, K. N.; Reich, N. O.; Teesalu, T.; Ruoslahti, E. Etchable Plasmonic Nanoparticle Probes to Image and Quantify Cellular Internalization. *Nat. Mater.* **2014**, *13* (9), 904–911.

(31) Huang, X.; Hu, Q.; Braun, G. B.; Pallaoro, A.; Morales, D. P.; Zasadzinski, J.; Clegg, D. O.; Reich, N. O. Light-Activated RNA Interference in Human Embryonic Stem Cells. *Biomaterials* **2015**, *63*, 70–79.

(32) Mao, Z.; Wan, L.; Hu, L.; Ma, L.; Gao, C. Tat Peptide Mediated Cellular Uptake of SiO2 Submicron Particles. *Colloids Surf. B Biointerfaces* **2010**, *75* (2), 432–440.

(33) Pierri, A. E.; Huang, P.-J.; Garcia, J. V.; Stanfill, J. G.; Chui, M.; Wu, G.; Zheng, N.; Ford, P. C. A photoCORM Nanocarrier for CO Release Using NIR Light. *Chem. Commun.* **2015**, *51* (11), 2072–2075.

(34) Lundberg, P.; Langel, Ü. A Brief Introduction to Cell-Penetrating Peptides. *J. Mol. Recognit.* **2003**, *16* (5), 227–233.

(35) Mohammed, Y.; Teixidó, M.; Namjoshi, S.; Giralt, E.; Benson, H. Cyclic Dipeptide Shuttles as a Novel Skin Penetration Enhancement Approach: Preliminary Evaluation with Diclofenac. *PLOS ONE* **2016**, *11* (8), e0160973.

(36) Pfeiffer, S.; Leopold, E.; Schmidt, K.; Brunner, F.; Mayer, B. Inhibition of Nitric Oxide Synthesis by NG-Nitro-L-Arginine Methyl Ester (L-NAME): Requirement for Bioactivation to the Free Acid, NG-Nitro-L-Arginine. *Br. J. Pharmacol.* **1996**, *118* (6), 1433–1440.

Appendix

1. Crystal Information of *trans*-[Cr(PetA)(Cl)$_2$]Cl (4)

Table 1. Crystal data and structure refinement for *trans*-[Cr(PetA)(Cl)$_2$]Cl (**4**).

Identification code	09112014_new_0m	
Empirical formula	C26 H44 Cl3 Cr N4 O2	
Formula weight	603.00	
Temperature	100(2) K	
Wavelength	0.71073 Å	
Crystal system	Monoclinic	
Space group	C2/c	
Unit cell dimensions	a = 27.500(2) Å	a= 90°.
	b = 6.4888(5) Å	b= 116.871(4)°.
	c = 18.2253(13) Å	g = 90°.
Volume	2901.0(4) Å^3	
Z	4	
Density (calculated)	1.381 Mg/m^3	
Absorption coefficient	0.701 mm^{-1}	
F(000)	1276	
Crystal size	0.200 x 0.150 x 0.050 mm^3	
Theta range for data collection	1.660 to 27.135°.	
Index ranges	-25<=h<=35, -5<=k<=8, -23<=l<=15	
Reflections collected	9594	
Independent reflections	3205 [R(int) = 0.0316]	
Completeness to theta = 25.242°	99.9 %	
Absorption correction	Semi-empirical from equivalents	
Max. and min. transmission	0.7455 and 0.6414	
Refinement method	Full-matrix least-squares on F^2	
Data / restraints / parameters	3205 / 15 / 190	
Goodness-of-fit on F^2	1.147	
Final R indices [I>2sigma(I)]	R1 = 0.0639, wR2 = 0.1361	
R indices (all data)	R1 = 0.0775, wR2 = 0.1425	
Extinction coefficient	n/a	

Largest diff. peak and hole	0.810 and -0.863 e.Å^{-3}

Table 2. Atomic coordinates (x 10^4) and equivalent isotropic displacement parameters ($Å^2$x 10^3) for *trans*-[Cr(PetA)$(Cl)_2$]Cl (**4**). U(eq) is defined as one third of the trace of the orthogonalized U^{ij} tensor.

	x	y	z	U(eq)
C(1)	815(1)	3802(8)	1731(2)	41(1)
C(2)	1143(1)	5716(8)	1748(2)	42(1)
C(3)	1215(1)	6138(7)	970(2)	33(1)
C(4)	1667(1)	7698(7)	1136(2)	32(1)
C(5)	1713(2)	9481(8)	1579(2)	40(1)
C(6)	2124(2)	10898(8)	1725(2)	44(1)
C(7)	2497(2)	10531(8)	1421(2)	44(1)
C(8)	2464(2)	8734(9)	992(2)	46(1)
C(9)	2052(1)	7305(8)	848(2)	38(1)
C(10)	-139(1)	2536(7)	1205(2)	31(1)
C(11)	947(2)	3088(10)	2603(2)	55(2)
C(12)	714(1)	7074(7)	-525(2)	29(1)
C(13)	1584(2)	8291(9)	4280(3)	62(2)
Cl(1)	-449(1)	7884(2)	139(1)	35(1)
Cl(2)	0	7478(2)	2500	55(1)
Cr(1)	0	5000	0	29(1)
N(1)	218(1)	4279(6)	1224(2)	31(1)
N(2)	683(1)	6836(6)	272(2)	29(1)
O(1)	1169(3)	8749(12)	3512(4)	54(1)
O(2)	1347(2)	7102(10)	3648(4)	54(1)

Table 3. Bond lengths [Å] and angles [°] for *trans*-[Cr(PetA)$(Cl)_2$]Cl (**4**).

C(1)-N(1)	1.507(4)
C(1)-C(2)	1.527(6)
C(1)-C(11)	1.534(5)
C(1)-H(1)	1.0000
C(2)-C(3)	1.543(5)
C(2)-H(2A)	0.9900
C(2)-H(2B)	0.9900
C(3)-N(2)	1.511(4)
C(3)-C(4)	1.522(5)
C(3)-H(3)	1.0000
C(4)-C(5)	1.383(6)
C(4)-C(9)	1.402(5)
C(5)-C(6)	1.387(6)
C(5)-H(5)	0.9500
C(6)-C(7)	1.390(6)
C(6)-H(6)	0.9500
C(7)-C(8)	1.384(7)
C(7)-H(7)	0.9500
C(8)-C(9)	1.394(6)
C(8)-H(8)	0.9500
C(9)-H(9)	0.9500
C(10)-N(1)	1.488(5)
C(10)-C(12)#1	1.526(5)
C(10)-H(10A)	0.9900
C(10)-H(10B)	0.9900
C(11)-H(11A)	0.9800
C(11)-H(11B)	0.9800
C(11)-H(11C)	0.9800
C(12)-N(2)	1.500(4)
C(12)-C(10)#1	1.526(5)
C(12)-H(12A)	0.9900
C(12)-H(12B)	0.9900
C(13)-O(2)	1.291(6)

C(13)-O(1)	1.380(7)
C(13)-H(13A)	1.011(9)
C(13)-H(13B)	1.018(9)
C(13)-H(13C)	1.005(9)
Cl(1)-Cr(1)	2.3176(11)
Cr(1)-N(1)#1	2.085(3)
Cr(1)-N(1)	2.085(3)
Cr(1)-N(2)	2.086(3)
Cr(1)-N(2)#1	2.086(3)
Cr(1)-Cl(1)#1	2.3176(11)
N(1)-H(1N)	0.997(10)
N(2)-H(2N)	0.993(10)
O(1)-H(2)	1.017(10)
O(2)-H(2)	1.028(9)
N(1)-C(1)-C(2)	108.3(4)
N(1)-C(1)-C(11)	112.3(3)
C(2)-C(1)-C(11)	111.4(3)
N(1)-C(1)-H(1)	108.3
C(2)-C(1)-H(1)	108.3
C(11)-C(1)-H(1)	108.3
C(1)-C(2)-C(3)	116.5(4)
C(1)-C(2)-H(2A)	108.2
C(3)-C(2)-H(2A)	108.2
C(1)-C(2)-H(2B)	108.2
C(3)-C(2)-H(2B)	108.2
H(2A)-C(2)-H(2B)	107.3
N(2)-C(3)-C(4)	111.2(3)
N(2)-C(3)-C(2)	110.4(3)
C(4)-C(3)-C(2)	111.6(3)
N(2)-C(3)-H(3)	107.8
C(4)-C(3)-H(3)	107.8
C(2)-C(3)-H(3)	107.8
C(5)-C(4)-C(9)	119.0(4)
C(5)-C(4)-C(3)	121.6(3)
C(9)-C(4)-C(3)	119.4(4)

C(4)-C(5)-C(6)	121.2(4)
C(4)-C(5)-H(5)	119.4
C(6)-C(5)-H(5)	119.4
C(5)-C(6)-C(7)	119.7(5)
C(5)-C(6)-H(6)	120.2
C(7)-C(6)-H(6)	120.2
C(8)-C(7)-C(6)	119.8(4)
C(8)-C(7)-H(7)	120.1
C(6)-C(7)-H(7)	120.1
C(7)-C(8)-C(9)	120.5(4)
C(7)-C(8)-H(8)	119.7
C(9)-C(8)-H(8)	119.7
C(8)-C(9)-C(4)	119.7(5)
C(8)-C(9)-H(9)	120.1
C(4)-C(9)-H(9)	120.1
N(1)-C(10)-C(12)#1	108.9(3)
N(1)-C(10)-H(10A)	109.9
C(12)#1-C(10)-H(10A)	109.9
N(1)-C(10)-H(10B)	109.9
C(12)#1-C(10)-H(10B)	109.9
H(10A)-C(10)-H(10B)	108.3
C(1)-C(11)-H(11A)	109.5
C(1)-C(11)-H(11B)	109.5
H(11A)-C(11)-H(11B)	109.5
C(1)-C(11)-H(11C)	109.5
H(11A)-C(11)-H(11C)	109.5
H(11B)-C(11)-H(11C)	109.5
N(2)-C(12)-C(10)#1	108.2(3)
N(2)-C(12)-H(12A)	110.1
C(10)#1-C(12)-H(12A)	110.1
N(2)-C(12)-H(12B)	110.1
C(10)#1-C(12)-H(12B)	110.1
H(12A)-C(12)-H(12B)	108.4
O(2)-C(13)-O(1)	51.1(4)
O(2)-C(13)-H(13A)	122(2)

O(1)-C(13)-H(13A)	122(2)
O(2)-C(13)-H(13B)	144.4(17)
O(1)-C(13)-H(13B)	99.8(13)
H(13A)-C(13)-H(13B)	89.5(10)
O(2)-C(13)-H(13C)	104.6(14)
O(1)-C(13)-H(13C)	145.6(18)
H(13A)-C(13)-H(13C)	90.9(10)
H(13B)-C(13)-H(13C)	89.9(10)
N(1)#1-Cr(1)-N(1)	180.0
N(1)#1-Cr(1)-N(2)	85.35(11)
N(1)-Cr(1)-N(2)	94.65(11)
N(1)#1-Cr(1)-N(2)#1	94.65(11)
N(1)-Cr(1)-N(2)#1	85.35(11)
N(2)-Cr(1)-N(2)#1	180.00(10)
N(1)#1-Cr(1)-Cl(1)	91.48(11)
N(1)-Cr(1)-Cl(1)	88.52(11)
N(2)-Cr(1)-Cl(1)	88.85(10)
N(2)#1-Cr(1)-Cl(1)	91.15(10)
N(1)#1-Cr(1)-Cl(1)#1	88.52(11)
N(1)-Cr(1)-Cl(1)#1	91.48(11)
N(2)-Cr(1)-Cl(1)#1	91.15(10)
N(2)#1-Cr(1)-Cl(1)#1	88.85(10)
Cl(1)-Cr(1)-Cl(1)#1	180.00(4)
C(10)-N(1)-C(1)	112.5(3)
C(10)-N(1)-Cr(1)	106.1(2)
C(1)-N(1)-Cr(1)	114.1(2)
C(10)-N(1)-H(1N)	109(3)
C(1)-N(1)-H(1N)	111(3)
Cr(1)-N(1)-H(1N)	104(3)
C(12)-N(2)-C(3)	112.9(3)
C(12)-N(2)-Cr(1)	105.5(2)
C(3)-N(2)-Cr(1)	117.0(2)
C(12)-N(2)-H(2N)	108(2)
C(3)-N(2)-H(2N)	110(2)
Cr(1)-N(2)-H(2N)	103(2)

C(13)-O(1)-H(2)	116.5(9)
C(13)-O(2)-H(2)	123.6(9)

Symmetry transformations used to generate equivalent atoms: #1 -x,-y+1,-z

Table 4. Anisotropic displacement parameters ($Å^2 x\ 10^3$) for *trans*-[Cr(PetA)$(Cl)_2$]Cl (**4**). The anisotropic displacement factor exponent takes the form: $-2p^2[\ h^2\ a^{*2}U^{11} + ...\ + 2\ h\ k\ a^*\ b^*\ U^{12}\ ]$

	U^{11}	U^{22}	U^{33}	U^{23}	U^{13}	U^{12}
C(1)	15(2)	81(3)	19(2)	16(2)	1(1)	-15(2)
C(2)	15(2)	85(4)	15(2)	11(2)	-1(1)	-19(2)
C(3)	12(2)	64(3)	16(2)	10(2)	0(1)	-10(2)
C(4)	11(2)	63(3)	15(2)	10(2)	0(1)	-7(2)
C(5)	16(2)	70(3)	26(2)	5(2)	3(1)	-8(2)
C(6)	22(2)	67(3)	27(2)	5(2)	-2(2)	-8(2)
C(7)	21(2)	77(4)	23(2)	13(2)	-2(2)	-21(2)
C(8)	18(2)	92(4)	24(2)	12(2)	7(2)	-11(2)
C(9)	18(2)	73(3)	20(2)	7(2)	5(1)	-8(2)
C(10)	19(2)	56(3)	15(2)	8(2)	6(1)	-10(2)
C(11)	26(2)	108(5)	19(2)	20(2)	0(2)	-21(3)
C(12)	18(2)	55(3)	14(2)	7(2)	6(1)	-9(2)
C(13)	54(3)	98(5)	34(2)	0(3)	19(2)	40(3)
Cl(1)	18(1)	64(1)	22(1)	11(1)	7(1)	-7(1)
Cl(2)	89(1)	30(1)	19(1)	0	-1(1)	0
Cr(1)	11(1)	62(1)	11(1)	8(1)	2(1)	-10(1)
N(1)	15(1)	61(2)	13(1)	8(1)	2(1)	-12(2)
N(2)	13(1)	59(2)	12(1)	6(1)	3(1)	-8(1)
O(1)	45(3)	56(3)	51(3)	-23(3)	13(2)	-2(2)
O(2)	45(3)	56(3)	51(3)	-23(3)	13(2)	-2(2)

Table 5. Hydrogen coordinates (x 10^4) and isotropic displacement parameters ($Å^2$x 10^3) for *trans*-[Cr(PetA)$(Cl)_2$]Cl (**4**).

	x	y	z	U(eq)
H(1)	915	2669	1452	49
H(2A)	1509	5595	2221	50
H(2B)	964	6930	1849	50
H(3)	1322	4814	802	40
H(5)	1458	9740	1787	48
H(6)	2151	12113	2032	52
H(7)	2775	11512	1507	53
H(8)	2724	8472	794	55
H(9)	2033	6069	556	46
H(10A)	-146	2423	1742	37
H(10B)	4	1228	1100	37
H(11A)	835	4153	2877	82
H(11B)	1340	2847	2916	82
H(11C)	750	1807	2573	82
H(12A)	866	5807	-645	35
H(12B)	955	8244	-489	35
H(1N)	110(20)	5530(50)	1440(30)	65(17)
H(2N)	576(16)	8190(30)	410(20)	31(11)
H(13A)	1517(13)	8160(70)	4779(12)	100
H(13B)	1736(15)	9730(30)	4467(15)	100
H(13C)	1960(8)	7700(60)	4593(16)	100
H(2)	1031(16)	7570(30)	3101(13)	100

2. Crystal Information of *cis*-[Cr(PetA)(Cl)$_2$]Cl (5)

Table 1. Crystal data and structure refinement for *cis*-[Cr(PetA)(Cl)$_2$]Cl (**5**).

Identification code	b02272017_0m_a	
Empirical formula	C24 H36 Cl3 Cr N4	
Formula weight	538.92	
Temperature	100(2) K	
Wavelength	0.71073 Å	
Crystal system	Trigonal	
Space group	$P3_221$	
Unit cell dimensions	a = 12.8928(11) Å	a= 90°.
	b = 12.8928(11) Å	b= 90°.
	c = 13.1562(14) Å	g = 120°.
Volume	1893.9(4) Å^3	
Z	3	
Density (calculated)	1.418 Mg/m^3	
Absorption coefficient	0.791 mm^{-1}	
F(000)	849	
Crystal size	0.100 x 0.100 x 0.050 mm^3	
Theta range for data collection	1.824 to 26.423°.	
Index ranges	-5<=h<=16, -16<=k<=12, -16<=l<=16	
Reflections collected	8616	
Independent reflections	2600 [R(int) = 0.0426]	
Completeness to theta = 25.242°	100.0 %	
Absorption correction	Semi-empirical from equivalents	
Refinement method	Full-matrix least-squares on F^2	
Data / restraints / parameters	2600 / 0 / 147	
Goodness-of-fit on F^2	1.058	
Final R indices [I>2sigma(I)]	R1 = 0.0473, wR2 = 0.1190	
R indices (all data)	R1 = 0.0574, wR2 = 0.1250	
Absolute structure parameter	0.009(18)	
Extinction coefficient	n/a	
Largest diff. peak and hole	1.739 and -0.376 e.Å^{-3}	

Table 2. Atomic coordinates (x 10^4) and equivalent isotropic displacement parameters ($Å^2$x 10^3) for *cis*-[Cr(PetA)$(Cl)_2$]Cl (**5**). U(eq) is defined as one third of the trace of the orthogonalized U^{ij} tensor.

	x	y	z	U(eq)
C(1)	3258(5)	10497(5)	-267(4)	17(1)
C(2)	3850(5)	11653(5)	317(4)	17(1)
C(3)	1432(5)	8474(5)	-321(4)	20(1)
C(4)	1958(5)	7759(5)	159(4)	20(1)
C(5)	1729(5)	7492(5)	1291(4)	19(1)
C(6)	2078(5)	6567(5)	1652(4)	22(1)
C(7)	1266(7)	5579(5)	2215(4)	26(1)
C(8)	1598(7)	4765(6)	2581(5)	35(2)
C(9)	2696(7)	4902(7)	2372(5)	36(2)
C(10)	3486(6)	5882(6)	1790(5)	30(2)
C(11)	3183(6)	6711(6)	1447(5)	26(1)
C(12)	1543(6)	8482(6)	-1467(5)	26(1)
Cl(1)	1404(1)	11442(1)	1488(1)	22(1)
Cl(2)	5200(2)	10000	1667	30(1)
Cr(1)	1971(1)	10000	1667	14(1)
N(1)	1997(4)	9729(4)	101(3)	16(1)
N(2)	3761(4)	11375(4)	1425(3)	16(1)

Table 3. Bond lengths [Å] and angles [°] for *cis*-[Cr(PetA)$(Cl)_2$]Cl (**5**).

C(1)-N(1)	1.499(7)
C(1)-C(2)	1.501(7)
C(1)-H(1A)	0.9900
C(1)-H(1B)	0.9900
C(2)-N(2)	1.491(7)
C(2)-H(2A)	0.9900
C(2)-H(2B)	0.9900
C(3)-N(1)	1.510(7)
C(3)-C(12)	1.514(8)
C(3)-C(4)	1.528(8)
C(3)-H(3)	1.0000
C(4)-C(5)	1.523(8)
C(4)-H(4A)	0.9900
C(4)-H(4B)	0.9900
C(5)-N(2)#1	1.508(7)
C(5)-C(6)	1.545(8)
C(5)-H(5)	1.0000
C(6)-C(11)	1.369(9)
C(6)-C(7)	1.390(9)
C(7)-C(8)	1.402(9)
C(7)-H(7)	0.9500
C(8)-C(9)	1.364(11)
C(8)-H(8)	0.9500
C(9)-C(10)	1.390(10)
C(9)-H(9)	0.9500
C(10)-C(11)	1.383(9)
C(10)-H(10)	0.9500
C(11)-H(11)	0.9500
C(12)-H(12A)	0.9800
C(12)-H(12B)	0.9800
C(12)-H(12C)	0.9800
Cl(1)-Cr(1)	2.3251(16)

Cr(1)-N(1)	2.092(4)
Cr(1)-N(1)#1	2.092(4)
Cr(1)-N(2)#1	2.116(5)
Cr(1)-N(2)	2.116(5)
Cr(1)-Cl(1)#1	2.3251(16)
N(1)-H(1)	1.0000
N(2)-C(5)#1	1.508(7)
N(2)-H(2)	1.0000

N(1)-C(1)-C(2)	109.6(4)
N(1)-C(1)-H(1A)	109.7
C(2)-C(1)-H(1A)	109.7
N(1)-C(1)-H(1B)	109.7
C(2)-C(1)-H(1B)	109.7
H(1A)-C(1)-H(1B)	108.2
N(2)-C(2)-C(1)	108.8(4)
N(2)-C(2)-H(2A)	109.9
C(1)-C(2)-H(2A)	109.9
N(2)-C(2)-H(2B)	109.9
C(1)-C(2)-H(2B)	109.9
H(2A)-C(2)-H(2B)	108.3
N(1)-C(3)-C(12)	111.5(4)
N(1)-C(3)-C(4)	111.9(4)
C(12)-C(3)-C(4)	110.3(5)
N(1)-C(3)-H(3)	107.6
C(12)-C(3)-H(3)	107.6
C(4)-C(3)-H(3)	107.6
C(5)-C(4)-C(3)	116.5(5)
C(5)-C(4)-H(4A)	108.2
C(3)-C(4)-H(4A)	108.2
C(5)-C(4)-H(4B)	108.2
C(3)-C(4)-H(4B)	108.2
H(4A)-C(4)-H(4B)	107.3
N(2)#1-C(5)-C(4)	110.9(4)
N(2)#1-C(5)-C(6)	110.1(4)

C(4)-C(5)-C(6)	112.1(5)
N(2)#1-C(5)-H(5)	107.9
C(4)-C(5)-H(5)	107.9
C(6)-C(5)-H(5)	107.9
C(11)-C(6)-C(7)	119.0(6)
C(11)-C(6)-C(5)	121.4(6)
C(7)-C(6)-C(5)	119.6(5)
C(6)-C(7)-C(8)	119.8(7)
C(6)-C(7)-H(7)	120.1
C(8)-C(7)-H(7)	120.1
C(9)-C(8)-C(7)	121.2(7)
C(9)-C(8)-H(8)	119.4
C(7)-C(8)-H(8)	119.4
C(8)-C(9)-C(10)	118.0(6)
C(8)-C(9)-H(9)	121.0
C(10)-C(9)-H(9)	121.0
C(11)-C(10)-C(9)	121.4(7)
C(11)-C(10)-H(10)	119.3
C(9)-C(10)-H(10)	119.3
C(6)-C(11)-C(10)	120.5(6)
C(6)-C(11)-H(11)	119.7
C(10)-C(11)-H(11)	119.7
C(3)-C(12)-H(12A)	109.5
C(3)-C(12)-H(12B)	109.5
H(12A)-C(12)-H(12B)	109.5
C(3)-C(12)-H(12C)	109.5
H(12A)-C(12)-H(12C)	109.5
H(12B)-C(12)-H(12C)	109.5
N(1)-Cr(1)-N(1)#1	168.6(3)
N(1)-Cr(1)-N(2)#1	88.64(17)
N(1)#1-Cr(1)-N(2)#1	83.67(18)
N(1)-Cr(1)-N(2)	83.67(18)
N(1)#1-Cr(1)-N(2)	88.64(17)
N(2)#1-Cr(1)-N(2)	95.6(3)
N(1)-Cr(1)-Cl(1)#1	94.07(13)

N(1)#1-Cr(1)-Cl(1)#1	94.10(13)
N(2)#1-Cr(1)-Cl(1)#1	87.85(13)
N(2)-Cr(1)-Cl(1)#1	175.84(14)
N(1)-Cr(1)-Cl(1)	94.10(13)
N(1)#1-Cr(1)-Cl(1)	94.06(13)
N(2)#1-Cr(1)-Cl(1)	175.84(14)
N(2)-Cr(1)-Cl(1)	87.85(13)
Cl(1)#1-Cr(1)-Cl(1)	88.84(9)
C(1)-N(1)-C(3)	111.8(4)
C(1)-N(1)-Cr(1)	108.1(3)
C(3)-N(1)-Cr(1)	120.1(3)
C(1)-N(1)-H(1)	105.2
C(3)-N(1)-H(1)	105.2
Cr(1)-N(1)-H(1)	105.2
C(2)-N(2)-C(5)#1	110.4(4)
C(2)-N(2)-Cr(1)	105.6(3)
C(5)#1-N(2)-Cr(1)	118.4(3)
C(2)-N(2)-H(2)	107.3
C(5)#1-N(2)-H(2)	107.3
Cr(1)-N(2)-H(2)	107.3

Symmetry transformations used to generate equivalent atoms:

#1 x-y+1,-y+2,-z+1/3

Table 4. Anisotropic displacement parameters ($Å^2 x\ 10^3$) for *cis*-[Cr(PetA)$(Cl)_2$]Cl (**5**). The anisotropic displacement factor exponent takes the form: $-2p^2[\ h^2\ a^{*2}U^{11} + ...\ + 2\ h\ k\ a^*\ b^*\ U^{12}\ ]$

	U^{11}	U^{22}	U^{33}	U^{23}	U^{13}	U^{12}
C(1)	17(3)	20(3)	14(2)	3(2)	1(2)	9(2)
C(2)	16(3)	15(3)	17(3)	6(2)	6(2)	6(2)
C(3)	21(3)	13(3)	23(3)	2(2)	0(2)	6(2)
C(4)	25(3)	15(3)	20(3)	-5(2)	-1(2)	10(2)
C(5)	17(3)	14(3)	26(3)	1(2)	0(2)	6(2)
C(6)	27(4)	15(3)	20(3)	-5(2)	-4(2)	9(2)
C(7)	41(4)	16(3)	19(3)	-3(2)	-7(3)	13(3)
C(8)	52(4)	16(3)	29(3)	-1(3)	-6(3)	11(3)
C(9)	62(5)	26(3)	31(3)	-13(3)	-22(3)	30(4)
C(10)	39(4)	28(4)	33(3)	-15(3)	-19(3)	24(3)
C(11)	31(4)	21(3)	27(3)	-5(3)	-4(3)	14(3)
C(12)	33(4)	19(3)	28(3)	-3(3)	-2(3)	14(3)
Cl(1)	22(1)	24(1)	26(1)	2(1)	-1(1)	16(1)
Cl(2)	15(1)	23(1)	55(2)	7(1)	4(1)	11(1)
Cr(1)	12(1)	13(1)	16(1)	2(1)	1(1)	6(1)
N(1)	15(2)	12(2)	21(2)	1(2)	-2(2)	7(2)
N(2)	15(2)	16(2)	16(2)	2(2)	1(2)	8(2)

Table 5. Hydrogen coordinates (x 10^4) and isotropic displacement parameters ($Å^2$x 10^3) for *cis*-[Cr(PetA)$(Cl)_2$]Cl (**5**).

	x	y	z	U(eq)
H(1A)	3254	10665	-1001	21
H(1B)	3710	10071	-172	21
H(2A)	4702	12135	115	20
H(2B)	3451	12121	166	20
H(3)	560	8058	-152	24
H(4A)	1632	6987	-206	24
H(4B)	2835	8203	48	24
H(5)	852	7146	1414	23
H(7)	489	5456	2351	31
H(8)	1048	4105	2983	42
H(9)	2915	4345	2616	44
H(10)	4249	5985	1625	36
H(11)	3747	7384	1066	31
H(12A)	1262	8996	-1762	40
H(12B)	1057	7665	-1728	40
H(12C)	2384	8792	-1654	40
H(1)	1536	10084	-208	20
H(2)	4288	11027	1563	19

3. Crystal Information of *trans*-[Cr(PetA)(ONO)$_2$]BF$_4$ (6)

Table 1. : Crystal data and structure refinement for *trans*-[Cr(PetA)(ONO)$_2$]BF$_4$.

Identification code	06232014_1_0m	
Empirical formula	$C_{25}H_{38}BCl_2CrF_4N_6O_4$	
Formula weight	696.32	
Temperature	100(2) K	
Wavelength	0.71073 Å	
Crystal system	Triclinic	
Space group	P-1	
Unit cell dimensions	a = 9.1893(11) Å	a= 80.745(4)°.
	b = 11.7329(14) Å	b= 73.030(4)°.
	c = 15.259(2) Å	g = 79.087(4)°.
Volume	1535.3(3) Å^3	
Z	2	
Density (calculated)	1.506 Mg/m^3	
Absorption coefficient	0.613 mm^{-1}	
F(000)	722	
Crystal size	0.200 x 0.100 x 0.050 mm^3	
Theta range for data collection	1.779 to 27.301°.	
Index ranges	-10<=h<=11, -15<=k<=15, -9<=l<=19	
Reflections collected	11331	
Independent reflections	6835 [R(int) = 0.0247]	
Completeness to theta = 25.242°	99.9 %	
Absorption correction	Semi-empirical from equivalents	
Max. and min. transmission	0.7455 and 0.6737	
Refinement method	Full-matrix least-squares on F^2	
Data / restraints / parameters	6835 / 0 / 409	
Goodness-of-fit on F^2	1.043	
Final R indices [I>2sigma(I)]	R1 = 0.0495, wR2 = 0.1204	
R indices (all data)	R1 = 0.0762, wR2 = 0.1343	
Extinction coefficient	n/a	
Largest diff. peak and hole	1.069 and -0.974 e.Å^{-3}	

Table 2: Atomic coordinates (x 10^4) and equivalent isotropic displacement parameters ($Å^2$x 10^3) for *trans*-[Cr(PetA)$(ONO)_2$]BF_4. U(eq) is defined as one third of the trace of the orthogonalized U^{ij} tensor.

	x	y	z	U(eq)
B(1)	1933(4)	5551(3)	2719(2)	20(1)
C(1)	9220(4)	2444(3)	5043(2)	25(1)
C(2)	7602(3)	2924(3)	4948(2)	18(1)
C(3)	8251(3)	4937(3)	4404(2)	17(1)
C(4)	7590(3)	6212(3)	4481(2)	18(1)
C(5)	5157(3)	7619(3)	4533(2)	16(1)
C(6)	3573(3)	7766(3)	4360(2)	18(1)
C(7)	6062(3)	8593(3)	4022(2)	18(1)
C(8)	6072(4)	9031(3)	3120(2)	27(1)
C(9)	6901(5)	9918(3)	2667(3)	40(1)
C(10)	7728(5)	10387(3)	3106(3)	41(1)
C(11)	7742(4)	9955(3)	3995(3)	40(1)
C(12)	6902(4)	9068(3)	4455(2)	32(1)
C(13)	6769(3)	5092(3)	257(2)	16(1)
C(14)	7301(3)	6920(3)	680(2)	17(1)
C(15)	8397(3)	7386(3)	1082(2)	17(1)
C(16)	10013(3)	7429(2)	449(2)	16(1)
C(17)	5642(3)	7256(3)	1221(2)	23(1)
C(18)	12533(3)	6167(3)	-142(2)	15(1)
C(19)	10842(3)	8295(2)	687(2)	18(1)
C(20)	10733(4)	8430(3)	1594(2)	24(1)
C(21)	11536(4)	9212(3)	1781(3)	31(1)
C(22)	12460(4)	9856(3)	1066(3)	32(1)
C(23)	12575(4)	9726(3)	167(3)	30(1)
C(24)	11760(4)	8956(3)	-20(2)	24(1)
C(25)	3302(5)	2454(3)	2422(3)	41(1)
Cl(1)	4606(1)	2158(1)	1370(1)	38(1)

Cl(2)	2677(1)	1194(1)	3114(1)	44(1)
Cr(1)	5000	5000	5000	10(1)
Cr(2)	10000	5000	0	10(1)
F(1)	2521(2)	6452(2)	2927(1)	32(1)
F(2)	2821(2)	5194(2)	1874(1)	27(1)
F(3)	1933(2)	4630(2)	3424(1)	26(1)
F(4)	432(2)	5934(2)	2654(1)	31(1)
N(1)	7179(3)	4198(2)	5071(2)	15(1)
N(2)	6034(3)	6439(2)	4316(2)	15(1)
N(3)	7742(3)	5622(2)	664(2)	13(1)
N(4)	10917(3)	6216(2)	445(2)	13(1)
N(5)	5817(3)	4833(2)	3050(2)	22(1)
N(6)	9367(3)	4007(3)	1892(2)	29(1)
O(1)	5277(2)	4289(2)	3872(1)	17(1)
O(2)	5898(3)	4277(2)	2425(1)	26(1)
O(3)	10285(2)	3867(2)	1062(1)	17(1)
O(4)	9617(3)	3229(2)	2481(2)	34(1)

Table 3: Bond lengths [Å] and angles [°] for *trans*-[Cr(PetA)$(ONO)_2$]BF_4.

B(1)-F(1)	1.391(4)
B(1)-F(2)	1.391(4)
B(1)-F(4)	1.394(4)
B(1)-F(3)	1.396(4)
C(1)-C(2)	1.527(4)
C(1)-H(1A)	0.9800
C(1)-H(1B)	0.9800
C(1)-H(1C)	0.9800
C(2)-N(1)	1.500(4)
C(2)-C(6)#1	1.526(4)
C(2)-H(2A)	1.0000
C(3)-N(1)	1.487(4)
C(3)-C(4)	1.514(4)
C(3)-H(3A)	0.9900
C(3)-H(3B)	0.9900
C(4)-N(2)	1.491(4)
C(4)-H(4A)	0.9900
C(4)-H(4B)	0.9900
C(5)-N(2)	1.498(4)
C(5)-C(7)	1.517(4)
C(5)-C(6)	1.527(4)
C(5)-H(5)	1.0000
C(6)-C(2)#1	1.526(4)
C(6)-H(6A)	0.9900
C(6)-H(6B)	0.9900
C(7)-C(12)	1.386(4)
C(7)-C(8)	1.387(4)
C(8)-C(9)	1.380(5)
C(8)-H(8)	0.9500
C(9)-C(10)	1.379(6)
C(9)-H(9)	0.9500
C(10)-C(11)	1.373(6)
C(10)-H(10)	0.9500

C(11)-C(12)	1.387(5)
C(11)-H(11)	0.9500
C(12)-H(12)	0.9500
C(13)-N(3)	1.494(3)
C(13)-C(18)#2	1.512(4)
C(13)-H(13A)	0.9900
C(13)-H(13B)	0.9900
C(14)-N(3)	1.503(4)
C(14)-C(17)	1.518(4)
C(14)-C(15)	1.538(4)
C(14)-H(14)	1.0000
C(15)-C(16)	1.522(4)
C(15)-H(15A)	0.9900
C(15)-H(15B)	0.9900
C(16)-N(4)	1.506(4)
C(16)-C(19)	1.523(4)
C(16)-H(16)	1.0000
C(17)-H(17A)	0.9800
C(17)-H(17B)	0.9800
C(17)-H(17C)	0.9800
C(18)-N(4)	1.490(3)
C(18)-C(13)#2	1.512(4)
C(18)-H(18A)	0.9900
C(18)-H(18B)	0.9900
C(19)-C(24)	1.387(4)
C(19)-C(20)	1.392(4)
C(20)-C(21)	1.390(4)
C(20)-H(20)	0.9500
C(21)-C(22)	1.386(5)
C(21)-H(21)	0.9500
C(22)-C(23)	1.375(5)
C(22)-H(22)	0.9500
C(23)-C(24)	1.387(5)
C(23)-H(23)	0.9500
C(24)-H(24)	0.9500

C(25)-Cl(1)	1.741(4)
C(25)-Cl(2)	1.760(4)
C(25)-H(25A)	0.9900
C(25)-H(25B)	0.9900
Cr(1)-O(1)#1	1.9616(19)
Cr(1)-O(1)	1.9616(19)
Cr(1)-N(1)#1	2.071(2)
Cr(1)-N(1)	2.071(2)
Cr(1)-N(2)#1	2.075(2)
Cr(1)-N(2)	2.075(2)
Cr(2)-O(3)	1.9708(19)
Cr(2)-O(3)#2	1.9708(19)
Cr(2)-N(3)	2.074(2)
Cr(2)-N(3)#2	2.074(2)
Cr(2)-N(4)#2	2.076(2)
Cr(2)-N(4)	2.076(2)
N(1)-H(1)	0.72(4)
N(2)-H(2)	0.81(4)
N(3)-H(3)	0.81(3)
N(4)-H(4)	0.74(3)
N(5)-O(2)	1.218(3)
N(5)-O(1)	1.313(3)
N(6)-O(4)	1.214(3)
N(6)-O(3)	1.316(3)

F(1)-B(1)-F(2)	109.9(3)
F(1)-B(1)-F(4)	110.2(3)
F(2)-B(1)-F(4)	108.0(3)
F(1)-B(1)-F(3)	108.5(3)
F(2)-B(1)-F(3)	110.9(3)
F(4)-B(1)-F(3)	109.4(3)
C(2)-C(1)-H(1A)	109.5
C(2)-C(1)-H(1B)	109.5
H(1A)-C(1)-H(1B)	109.5
C(2)-C(1)-H(1C)	109.5

H(1A)-C(1)-H(1C)	109.5
H(1B)-C(1)-H(1C)	109.5
N(1)-C(2)-C(6)#1	110.1(2)
N(1)-C(2)-C(1)	111.7(2)
C(6)#1-C(2)-C(1)	110.4(3)
N(1)-C(2)-H(2A)	108.2
C(6)#1-C(2)-H(2A)	108.2
C(1)-C(2)-H(2A)	108.2
N(1)-C(3)-C(4)	109.3(2)
N(1)-C(3)-H(3A)	109.8
C(4)-C(3)-H(3A)	109.8
N(1)-C(3)-H(3B)	109.8
C(4)-C(3)-H(3B)	109.8
H(3A)-C(3)-H(3B)	108.3
N(2)-C(4)-C(3)	109.2(2)
N(2)-C(4)-H(4A)	109.8
C(3)-C(4)-H(4A)	109.8
N(2)-C(4)-H(4B)	109.8
C(3)-C(4)-H(4B)	109.8
H(4A)-C(4)-H(4B)	108.3
N(2)-C(5)-C(7)	111.9(2)
N(2)-C(5)-C(6)	110.2(2)
C(7)-C(5)-C(6)	112.8(2)
N(2)-C(5)-H(5)	107.2
C(7)-C(5)-H(5)	107.2
C(6)-C(5)-H(5)	107.2
C(2)#1-C(6)-C(5)	116.5(2)
C(2)#1-C(6)-H(6A)	108.2
C(5)-C(6)-H(6A)	108.2
C(2)#1-C(6)-H(6B)	108.2
C(5)-C(6)-H(6B)	108.2
H(6A)-C(6)-H(6B)	107.3
C(12)-C(7)-C(8)	118.4(3)
C(12)-C(7)-C(5)	120.2(3)
C(8)-C(7)-C(5)	121.4(3)

C(9)-C(8)-C(7)	120.6(3)
C(9)-C(8)-H(8)	119.7
C(7)-C(8)-H(8)	119.7
C(10)-C(9)-C(8)	120.4(4)
C(10)-C(9)-H(9)	119.8
C(8)-C(9)-H(9)	119.8
C(11)-C(10)-C(9)	119.6(3)
C(11)-C(10)-H(10)	120.2
C(9)-C(10)-H(10)	120.2
C(10)-C(11)-C(12)	120.1(4)
C(10)-C(11)-H(11)	120.0
C(12)-C(11)-H(11)	120.0
C(7)-C(12)-C(11)	120.8(3)
C(7)-C(12)-H(12)	119.6
C(11)-C(12)-H(12)	119.6
N(3)-C(13)-C(18)#2	108.6(2)
N(3)-C(13)-H(13A)	110.0
C(18)#2-C(13)-H(13A)	110.0
N(3)-C(13)-H(13B)	110.0
C(18)#2-C(13)-H(13B)	110.0
H(13A)-C(13)-H(13B)	108.3
N(3)-C(14)-C(17)	112.3(2)
N(3)-C(14)-C(15)	109.6(2)
C(17)-C(14)-C(15)	110.4(2)
N(3)-C(14)-H(14)	108.2
C(17)-C(14)-H(14)	108.2
C(15)-C(14)-H(14)	108.2
C(16)-C(15)-C(14)	115.1(2)
C(16)-C(15)-H(15A)	108.5
C(14)-C(15)-H(15A)	108.5
C(16)-C(15)-H(15B)	108.5
C(14)-C(15)-H(15B)	108.5
H(15A)-C(15)-H(15B)	107.5
N(4)-C(16)-C(15)	109.4(2)
N(4)-C(16)-C(19)	111.9(2)

C(15)-C(16)-C(19) 113.2(2)
N(4)-C(16)-H(16) 107.4
C(15)-C(16)-H(16) 107.4
C(19)-C(16)-H(16) 107.4
C(14)-C(17)-H(17A) 109.5
C(14)-C(17)-H(17B) 109.5
H(17A)-C(17)-H(17B) 109.5
C(14)-C(17)-H(17C) 109.5
H(17A)-C(17)-H(17C) 109.5
H(17B)-C(17)-H(17C) 109.5
N(4)-C(18)-C(13)#2 109.3(2)
N(4)-C(18)-H(18A) 109.8
C(13)#2-C(18)-H(18A) 109.8
N(4)-C(18)-H(18B) 109.8
C(13)#2-C(18)-H(18B) 109.8
H(18A)-C(18)-H(18B) 108.3
C(24)-C(19)-C(20) 118.7(3)
C(24)-C(19)-C(16) 119.3(3)
C(20)-C(19)-C(16) 122.0(3)
C(21)-C(20)-C(19) 120.2(3)
C(21)-C(20)-H(20) 119.9
C(19)-C(20)-H(20) 119.9
C(22)-C(21)-C(20) 120.3(3)
C(22)-C(21)-H(21) 119.9
C(20)-C(21)-H(21) 119.9
C(23)-C(22)-C(21) 119.8(3)
C(23)-C(22)-H(22) 120.1
C(21)-C(22)-H(22) 120.1
C(22)-C(23)-C(24) 119.9(3)
C(22)-C(23)-H(23) 120.0
C(24)-C(23)-H(23) 120.0
C(19)-C(24)-C(23) 121.1(3)
C(19)-C(24)-H(24) 119.5
C(23)-C(24)-H(24) 119.5
Cl(1)-C(25)-Cl(2) 113.2(2)

Cl(1)-C(25)-H(25A) 108.9
Cl(2)-C(25)-H(25A) 108.9
Cl(1)-C(25)-H(25B) 108.9
Cl(2)-C(25)-H(25B) 108.9
H(25A)-C(25)-H(25B) 107.8
O(1)#1-Cr(1)-O(1) 180.0
O(1)#1-Cr(1)-N(1)#1 90.06(9)
O(1)-Cr(1)-N(1)#1 89.94(9)
O(1)#1-Cr(1)-N(1) 89.94(9)
O(1)-Cr(1)-N(1) 90.07(9)
N(1)#1-Cr(1)-N(1) 180.0
O(1)#1-Cr(1)-N(2)#1 94.51(9)
O(1)-Cr(1)-N(2)#1 85.49(9)
N(1)#1-Cr(1)-N(2)#1 86.28(10)
N(1)-Cr(1)-N(2)#1 93.72(10)
O(1)#1-Cr(1)-N(2) 85.49(9)
O(1)-Cr(1)-N(2) 94.51(9)
N(1)#1-Cr(1)-N(2) 93.72(10)
N(1)-Cr(1)-N(2) 86.28(10)
N(2)#1-Cr(1)-N(2) 180.0
O(3)-Cr(2)-O(3)#2 180.00(8)
O(3)-Cr(2)-N(3) 93.41(9)
O(3)#2-Cr(2)-N(3) 86.59(9)
O(3)-Cr(2)-N(3)#2 86.59(9)
O(3)#2-Cr(2)-N(3)#2 93.41(9)
N(3)-Cr(2)-N(3)#2 180.0
O(3)-Cr(2)-N(4)#2 89.45(9)
O(3)#2-Cr(2)-N(4)#2 90.55(9)
N(3)-Cr(2)-N(4)#2 85.83(9)
N(3)#2-Cr(2)-N(4)#2 94.17(9)
O(3)-Cr(2)-N(4) 90.55(9)
O(3)#2-Cr(2)-N(4) 89.45(9)
N(3)-Cr(2)-N(4) 94.17(9)
N(3)#2-Cr(2)-N(4) 85.83(9)
N(4)#2-Cr(2)-N(4) 180.0

C(3)-N(1)-C(2)	113.4(2)
C(3)-N(1)-Cr(1)	105.17(17)
C(2)-N(1)-Cr(1)	117.48(18)
C(3)-N(1)-H(1)	108(3)
C(2)-N(1)-H(1)	110(3)
Cr(1)-N(1)-H(1)	102(3)
C(4)-N(2)-C(5)	113.8(2)
C(4)-N(2)-Cr(1)	105.01(17)
C(5)-N(2)-Cr(1)	117.02(17)
C(4)-N(2)-H(2)	103(2)
C(5)-N(2)-H(2)	108(2)
Cr(1)-N(2)-H(2)	109(2)
C(13)-N(3)-C(14)	113.5(2)
C(13)-N(3)-Cr(2)	105.55(17)
C(14)-N(3)-Cr(2)	117.49(17)
C(13)-N(3)-H(3)	107(2)
C(14)-N(3)-H(3)	107(2)
Cr(2)-N(3)-H(3)	106(2)
C(18)-N(4)-C(16)	113.6(2)
C(18)-N(4)-Cr(2)	105.28(17)
C(16)-N(4)-Cr(2)	115.15(17)
C(18)-N(4)-H(4)	108(2)
C(16)-N(4)-H(4)	103(2)
Cr(2)-N(4)-H(4)	112(2)
O(2)-N(5)-O(1)	113.3(2)
O(4)-N(6)-O(3)	114.0(3)
N(5)-O(1)-Cr(1)	121.69(18)
N(6)-O(3)-Cr(2)	120.13(18)

Symmetry transformations used to generate equivalent atoms:

#1 -x+1,-y+1,-z+1 #2 -x+2,-y+1,-z

Table 4: Anisotropic displacement parameters ($Å^2 x\ 10^3$) for *trans*-$[Cr(PetA)(ONO)_2]BF_4$. The anisotropic displacement factor exponent takes the form: $-2p^2[h^2 a^{*2} U^{11} + ... + 2 h k a^* b^* U^{12}]$

	U^{11}	U^{22}	U^{33}	U^{23}	U^{13}	U^{12}
B(1)	20(2)	27(2)	14(2)	-1(1)	-4(1)	-5(2)
C(1)	16(2)	26(2)	34(2)	-6(1)	-9(1)	1(1)
C(2)	14(1)	20(2)	21(2)	-5(1)	-5(1)	-1(1)
C(3)	10(1)	24(2)	17(1)	-1(1)	-2(1)	-4(1)
C(4)	14(1)	22(2)	20(2)	1(1)	-3(1)	-9(1)
C(5)	16(1)	19(2)	16(1)	-1(1)	-5(1)	-5(1)
C(6)	18(2)	19(2)	18(1)	0(1)	-6(1)	-4(1)
C(7)	20(2)	16(2)	17(1)	-5(1)	0(1)	-3(1)
C(8)	34(2)	27(2)	20(2)	1(1)	-4(1)	-10(2)
C(9)	47(2)	35(2)	32(2)	8(2)	-1(2)	-15(2)
C(10)	42(2)	20(2)	49(2)	-4(2)	10(2)	-15(2)
C(11)	36(2)	37(2)	50(2)	-19(2)	-1(2)	-19(2)
C(12)	37(2)	39(2)	27(2)	-7(2)	-7(2)	-17(2)
C(13)	11(1)	23(2)	15(1)	-4(1)	-5(1)	-4(1)
C(14)	15(1)	18(2)	20(1)	-3(1)	-7(1)	-3(1)
C(15)	15(1)	17(2)	22(2)	-8(1)	-5(1)	-2(1)
C(16)	17(1)	15(1)	20(1)	-2(1)	-8(1)	-2(1)
C(17)	15(2)	23(2)	31(2)	-6(1)	-5(1)	-2(1)
C(18)	11(1)	20(2)	15(1)	-3(1)	-3(1)	-6(1)
C(19)	17(1)	12(1)	27(2)	-2(1)	-10(1)	-1(1)
C(20)	28(2)	21(2)	26(2)	-4(1)	-12(1)	-7(1)
C(21)	34(2)	31(2)	37(2)	-11(2)	-15(2)	-10(2)
C(22)	30(2)	19(2)	54(2)	-10(2)	-18(2)	-5(1)
C(23)	27(2)	18(2)	42(2)	3(2)	-6(2)	-9(1)
C(24)	25(2)	20(2)	27(2)	0(1)	-7(1)	-6(1)
C(25)	36(2)	31(2)	51(2)	-11(2)	-2(2)	-6(2)
Cl(1)	36(1)	41(1)	38(1)	-2(1)	-7(1)	-12(1)

Cl(2)	49(1)	49(1)	31(1)	-6(1)	-4(1)	-5(1)
Cr(1)	9(1)	16(1)	6(1)	-1(1)	-2(1)	-4(1)
Cr(2)	9(1)	14(1)	9(1)	-1(1)	-4(1)	-4(1)
F(1)	41(1)	36(1)	25(1)	-7(1)	-14(1)	-13(1)
F(2)	33(1)	34(1)	14(1)	-6(1)	-3(1)	-5(1)
F(3)	24(1)	33(1)	17(1)	5(1)	-6(1)	-2(1)
F(4)	19(1)	40(1)	31(1)	12(1)	-9(1)	-6(1)
N(1)	13(1)	20(1)	12(1)	-1(1)	-4(1)	-3(1)
N(2)	14(1)	20(1)	10(1)	-3(1)	-2(1)	-3(1)
N(3)	13(1)	17(1)	10(1)	0(1)	-5(1)	-6(1)
N(4)	13(1)	17(1)	11(1)	-1(1)	-4(1)	-3(1)
N(5)	20(1)	31(2)	13(1)	-1(1)	-4(1)	-6(1)
N(6)	28(2)	40(2)	17(1)	1(1)	-6(1)	-1(1)
O(1)	18(1)	24(1)	9(1)	-1(1)	-3(1)	-6(1)
O(2)	28(1)	38(1)	13(1)	-7(1)	-4(1)	-7(1)
O(3)	17(1)	21(1)	12(1)	0(1)	-5(1)	-3(1)
O(4)	34(1)	45(2)	19(1)	9(1)	-9(1)	-6(1)

Table 5: Hydrogen coordinates (x 10^4) and isotropic displacement parameters ($Å^2$x 10^3) for *trans*-[Cr(PetA)$(ONO)_2$]BF_4.

	x	y	z	U(eq)
H(1A)	9969	2860	4568	38
H(1B)	9451	1609	4968	38
H(1C)	9279	2554	5654	38
H(2A)	7577	2828	4313	22
H(3A)	8397	4757	3769	21
H(3B)	9266	4770	4538	21
H(4A)	7512	6405	5103	22
H(4B)	8275	6710	4021	22
H(5)	4987	7649	5207	20
H(6A)	3136	8606	4348	22
H(6B)	3713	7539	3740	22
H(8)	5502	8717	2813	32
H(9)	6903	10207	2048	48
H(10)	8285	11006	2794	49
H(11)	8327	10264	4296	48
H(12)	6903	8783	5074	39
H(13A)	6723	5527	-349	19
H(13B)	5708	5133	667	19
H(14)	7423	7290	30	20
H(15A)	7936	8184	1244	21
H(15B)	8476	6888	1660	21
H(16)	9912	7691	-191	20
H(17A)	4957	6970	948	35
H(17B)	5399	8108	1202	35
H(17C)	5499	6906	1863	35
H(18A)	13141	6525	150	18
H(18B)	12549	6612	-753	18

H(20)	10107	7986	2088	28
H(21)	11451	9306	2402	37
H(22)	13014	10386	1196	38
H(23)	13211	10164	-325	36
H(24)	11831	8880	-642	29
H(25A)	2397	2998	2304	49
H(25B)	3791	2850	2762	49
H(1)	7170(40)	4290(30)	5530(30)	26(11)
H(2)	6230(40)	6420(30)	3770(30)	22(9)
H(3)	7610(40)	5330(30)	1200(20)	13(8)
H(4)	10940(30)	6060(30)	930(20)	5(8)

Table 6: Torsion angles [°] for *trans*-[Cr(PetA)$(ONO)_2$]BF_4.

N(1)-C(3)-C(4)-N(2)	-57.1(3)
N(2)-C(5)-C(6)-C(2)#1	72.7(3)
C(7)-C(5)-C(6)-C(2)#1	-161.4(2)
N(2)-C(5)-C(7)-C(12)	-96.6(3)
C(6)-C(5)-C(7)-C(12)	138.4(3)
N(2)-C(5)-C(7)-C(8)	83.5(3)
C(6)-C(5)-C(7)-C(8)	-41.4(4)
C(12)-C(7)-C(8)-C(9)	0.1(5)
C(5)-C(7)-C(8)-C(9)	180.0(3)
C(7)-C(8)-C(9)-C(10)	-0.4(6)
C(8)-C(9)-C(10)-C(11)	1.0(6)
C(9)-C(10)-C(11)-C(12)	-1.3(6)
C(8)-C(7)-C(12)-C(11)	-0.5(5)
C(5)-C(7)-C(12)-C(11)	179.7(3)
C(10)-C(11)-C(12)-C(7)	1.1(6)
N(3)-C(14)-C(15)-C(16)	73.3(3)
C(17)-C(14)-C(15)-C(16)	-162.6(3)
C(14)-C(15)-C(16)-N(4)	-76.9(3)
C(14)-C(15)-C(16)-C(19)	157.6(2)
N(4)-C(16)-C(19)-C(24)	94.7(3)
C(15)-C(16)-C(19)-C(24)	-141.2(3)
N(4)-C(16)-C(19)-C(20)	-84.1(3)
C(15)-C(16)-C(19)-C(20)	40.1(4)
C(24)-C(19)-C(20)-C(21)	-0.2(5)
C(16)-C(19)-C(20)-C(21)	178.6(3)
C(19)-C(20)-C(21)-C(22)	-0.5(5)
C(20)-C(21)-C(22)-C(23)	0.4(5)
C(21)-C(22)-C(23)-C(24)	0.3(5)
C(20)-C(19)-C(24)-C(23)	0.9(5)
C(16)-C(19)-C(24)-C(23)	-177.9(3)
C(22)-C(23)-C(24)-C(19)	-1.0(5)
C(4)-C(3)-N(1)-C(2)	170.9(2)
C(4)-C(3)-N(1)-Cr(1)	41.2(3)

C(6)#1-C(2)-N(1)-C(3)	-178.6(2)
C(1)-C(2)-N(1)-C(3)	58.4(3)
C(6)#1-C(2)-N(1)-Cr(1)	-55.4(3)
C(1)-C(2)-N(1)-Cr(1)	-178.4(2)
C(3)-C(4)-N(2)-C(5)	170.1(2)
C(3)-C(4)-N(2)-Cr(1)	40.8(2)
C(7)-C(5)-N(2)-C(4)	54.6(3)
C(6)-C(5)-N(2)-C(4)	-179.0(2)
C(7)-C(5)-N(2)-Cr(1)	177.46(18)
C(6)-C(5)-N(2)-Cr(1)	-56.1(3)
C(18)#2-C(13)-N(3)-C(14)	171.3(2)
C(18)#2-C(13)-N(3)-Cr(2)	41.2(2)
C(17)-C(14)-N(3)-C(13)	58.7(3)
C(15)-C(14)-N(3)-C(13)	-178.2(2)
C(17)-C(14)-N(3)-Cr(2)	-177.51(19)
C(15)-C(14)-N(3)-Cr(2)	-54.4(3)
C(13)#2-C(18)-N(4)-C(16)	-168.4(2)
C(13)#2-C(18)-N(4)-Cr(2)	-41.5(2)
C(15)-C(16)-N(4)-C(18)	-178.8(2)
C(19)-C(16)-N(4)-C(18)	-52.6(3)
C(15)-C(16)-N(4)-Cr(2)	59.7(3)
C(19)-C(16)-N(4)-Cr(2)	-174.04(19)
O(2)-N(5)-O(1)-Cr(1)	-179.08(19)
O(4)-N(6)-O(3)-Cr(2)	177.1(2)

4. Crystal Information of NitroPetA (3") Ligand

Table 1. Crystal data and structure refinement for NitroPetA (**3"**).

Identification code	hpj20150627-2-3	
Empirical formula	C24 H34 N6 O4	
Formula weight	470.57	
Temperature	100.01(10) K	
Wavelength	1.54184 Å	
Crystal system	Triclinic	
Space group	P-1	
Unit cell dimensions	a = 7.1135(5) Å	a= 104.275(6)°.
	b = 8.5554(6) Å	b= 99.129(6)°.
	c = 10.6673(6) Å	g = 101.428(6)°.
Volume	601.79(7) $Å^3$	
Z	1	
Density (calculated)	1.298 Mg/m^3	
Absorption coefficient	0.737 mm^{-1}	
F(000)	252	
Crystal size	0.15 x 0.08 x 0.05 mm^3	
Theta range for data collection	4.383 to 65.046°.	
Index ranges	-8<=h<=8, -10<=k<=10, -12<=l<=12	
Reflections collected	8603	
Independent reflections	2019 [R(int) = 0.0271]	
Completeness to theta = 67.684°	98.5 %	
Absorption correction	Semi-empirical from equivalents	
Max. and min. transmission	1.00000 and 0.88862	
Refinement method	Full-matrix least-squares on F^2	
Data / restraints / parameters	2019 / 0 / 163	
Goodness-of-fit on F^2	1.078	
Final R indices [I>2sigma(I)]	R1 = 0.0420, wR2 = 0.1088	
R indices (all data)	R1 = 0.0438, wR2 = 0.1106	
Extinction coefficient	n/a	
Largest diff. peak and hole	0.315 and -0.190 e.$Å^{-3}$	

Table 2. Atomic coordinates (x 10^4) and equivalent isotropic displacement parameters ($Å^2$x 10^3) for NitroPetA (**3"**). U(eq) is defined as one third of the trace of the orthogonalized U^{ij} tensor.

	x	y	z	U(eq)
O(1)	4332(2)	8356(2)	-1058(1)	37(1)
O(2)	1792(2)	8068(2)	-187(1)	39(1)
N(1)	3484(2)	7978(2)	-219(1)	27(1)
N(2)	323(2)	7337(2)	6277(1)	25(1)
N(3)	1883(2)	6156(2)	3868(1)	23(1)
C(2)	4528(2)	7356(2)	785(1)	22(1)
C(6)	4436(2)	6104(2)	2549(1)	22(1)
C(8)	3322(2)	5282(2)	3411(2)	23(1)
C(7)	3493(2)	6761(2)	1635(1)	22(1)
C(3)	6479(2)	7361(2)	818(2)	26(1)
C(4)	7409(2)	6710(2)	1736(2)	29(1)
C(10)	1237(2)	8400(2)	5536(2)	28(1)
C(9)	2786(2)	7696(2)	4934(2)	27(1)
C(5)	6398(2)	6086(2)	2582(2)	25(1)
C(11)	-1528(2)	7682(2)	6594(2)	27(1)
C(13)	-2372(2)	6528(2)	7364(2)	24(1)
C(12)	-1349(3)	9480(2)	7365(2)	33(1)

Table 3. Bond lengths [Å] and angles [°] for NitroPetA (**3"**).

O(1)-N(1)	1.2272(17)
O(2)-N(1)	1.2267(18)
N(1)-C(2)	1.471(2)
N(2)-C(10)	1.4694(19)
N(2)-C(11)	1.476(2)
N(2)-H(2)	0.89(2)
N(3)-C(8)	1.4581(19)
N(3)-C(9)	1.462(2)
N(3)-H(3)	0.90(2)
C(2)-C(7)	1.383(2)
C(2)-C(3)	1.383(2)
C(6)-C(8)	1.516(2)
C(6)-C(7)	1.390(2)
C(6)-C(5)	1.394(2)
C(8)-H(8)	1.0000
C(8)-C(13)#1	1.521(2)
C(7)-H(7)	0.9500
C(3)-H(3A)	0.9500
C(3)-C(4)	1.384(2)
C(4)-H(4)	0.9500
C(4)-C(5)	1.381(2)
C(10)-H(10A)	0.9900
C(10)-H(10B)	0.9900
C(10)-C(9)	1.512(2)
C(9)-H(9A)	0.9900
C(9)-H(9B)	0.9900
C(5)-H(5)	0.9500
C(11)-H(11)	1.0000
C(11)-C(13)	1.527(2)
C(11)-C(12)	1.525(2)
C(13)-C(8)#1	1.521(2)
C(13)-H(13A)	0.9900
C(13)-H(13B)	0.9900

C(12)-H(12A)	0.9800
C(12)-H(12B)	0.9800
C(12)-H(12C)	0.9800

O(1)-N(1)-C(2)	118.67(13)
O(2)-N(1)-O(1)	123.18(13)
O(2)-N(1)-C(2)	118.14(12)
C(10)-N(2)-C(11)	113.75(12)
C(10)-N(2)-H(2)	107.5(12)
C(11)-N(2)-H(2)	107.8(12)
C(8)-N(3)-C(9)	112.67(12)
C(8)-N(3)-H(3)	107.7(11)
C(9)-N(3)-H(3)	109.2(11)
C(7)-C(2)-N(1)	118.27(13)
C(3)-C(2)-N(1)	118.69(13)
C(3)-C(2)-C(7)	123.03(14)
C(7)-C(6)-C(8)	121.08(13)
C(7)-C(6)-C(5)	118.53(14)
C(5)-C(6)-C(8)	120.16(13)
N(3)-C(8)-C(6)	112.14(12)
N(3)-C(8)-H(8)	108.1
N(3)-C(8)-C(13)#1	111.86(12)
C(6)-C(8)-H(8)	108.1
C(6)-C(8)-C(13)#1	108.45(12)
C(13)#1-C(8)-H(8)	108.1
C(2)-C(7)-C(6)	118.89(13)
C(2)-C(7)-H(7)	120.6
C(6)-C(7)-H(7)	120.6
C(2)-C(3)-H(3A)	121.2
C(2)-C(3)-C(4)	117.67(14)
C(4)-C(3)-H(3A)	121.2
C(3)-C(4)-H(4)	119.8
C(5)-C(4)-C(3)	120.34(14)
C(5)-C(4)-H(4)	119.8
N(2)-C(10)-H(10A)	109.5

N(2)-C(10)-H(10B)	109.5
N(2)-C(10)-C(9)	110.73(13)
H(10A)-C(10)-H(10B)	108.1
C(9)-C(10)-H(10A)	109.5
C(9)-C(10)-H(10B)	109.5
N(3)-C(9)-C(10)	110.77(13)
N(3)-C(9)-H(9A)	109.5
N(3)-C(9)-H(9B)	109.5
C(10)-C(9)-H(9A)	109.5
C(10)-C(9)-H(9B)	109.5
H(9A)-C(9)-H(9B)	108.1
C(6)-C(5)-H(5)	119.2
C(4)-C(5)-C(6)	121.52(14)
C(4)-C(5)-H(5)	119.2
N(2)-C(11)-H(11)	107.6
N(2)-C(11)-C(13)	110.22(12)
N(2)-C(11)-C(12)	114.55(13)
C(13)-C(11)-H(11)	107.6
C(12)-C(11)-H(11)	107.6
C(12)-C(11)-C(13)	109.08(13)
C(8)#1-C(13)-C(11)	117.17(13)
C(8)#1-C(13)-H(13A)	108.0
C(8)#1-C(13)-H(13B)	108.0
C(11)-C(13)-H(13A)	108.0
C(11)-C(13)-H(13B)	108.0
H(13A)-C(13)-H(13B)	107.2
C(11)-C(12)-H(12A)	109.5
C(11)-C(12)-H(12B)	109.5
C(11)-C(12)-H(12C)	109.5
H(12A)-C(12)-H(12B)	109.5
H(12A)-C(12)-H(12C)	109.5
H(12B)-C(12)-H(12C)	109.5

Symmetry transformations used to generate equivalent atoms:
#1 -x,-y+1,-z+1

Table 4. Anisotropic displacement parameters ($Å^2 x\ 10^3$) for NitroPetA (**3"**). The anisotropic displacement factor exponent takes the form: $-2p^2[\ h^2\ a^{*2}U^{11} + ... + 2\ h\ k\ a^*\ b^*\ U^{12}\ ]$

	U^{11}	U^{22}	U^{33}	U^{23}	U^{13}	U^{12}
O(1)	56(1)	37(1)	27(1)	18(1)	19(1)	14(1)
O(2)	33(1)	56(1)	37(1)	24(1)	7(1)	17(1)
N(1)	35(1)	27(1)	22(1)	9(1)	8(1)	7(1)
N(2)	29(1)	25(1)	24(1)	10(1)	11(1)	8(1)
N(3)	24(1)	24(1)	24(1)	8(1)	11(1)	7(1)
C(2)	27(1)	21(1)	18(1)	6(1)	6(1)	6(1)
C(6)	26(1)	21(1)	18(1)	4(1)	7(1)	6(1)
C(8)	25(1)	28(1)	22(1)	11(1)	9(1)	10(1)
C(7)	20(1)	24(1)	22(1)	7(1)	9(1)	7(1)
C(3)	27(1)	25(1)	26(1)	5(1)	13(1)	2(1)
C(4)	20(1)	32(1)	34(1)	6(1)	9(1)	5(1)
C(10)	34(1)	23(1)	30(1)	9(1)	16(1)	7(1)
C(9)	31(1)	25(1)	28(1)	9(1)	14(1)	6(1)
C(5)	24(1)	27(1)	24(1)	5(1)	2(1)	8(1)
C(11)	33(1)	26(1)	27(1)	10(1)	14(1)	9(1)
C(13)	29(1)	26(1)	24(1)	9(1)	13(1)	10(1)
C(12)	40(1)	26(1)	38(1)	11(1)	20(1)	9(1)

Table 5. Hydrogen coordinates (x 10^4) and isotropic displacement parameters ($Å^2$x 10^3) for NitroPetA (**3"**).

	x	y	z	U(eq)
H(8)	4292	5302	4208	28
H(7)	2160	6800	1593	26
H(3A)	7159	7795	232	32
H(4)	8749	6692	1784	35
H(10A)	1846	9534	6139	33
H(10B)	217	8483	4824	33
H(9A)	3545	8522	4579	33
H(9B)	3707	7472	5628	33
H(5)	7056	5635	3201	31
H(11)	-2494	7428	5736	32
H(13A)	-1298	6550	8087	29
H(13B)	-3364	6994	7782	29
H(12A)	-454	9750	8230	50
H(12B)	-2646	9619	7493	50
H(12C)	-830	10226	6868	50
H(3)	1050(30)	5470(20)	4161(18)	27(5)
H(2)	1170(30)	7530(20)	7040(20)	30(5)

5. Crystal Information of *trans*-[Cr(NitroPetA)$(Cl)_2$]Cl (4")

Table 1. Crystal data and structure refinement for *trans*-[Cr(NitroPetA)$(Cl)_2$]Cl (**4"**).

Identification code	f07252014_3rd_0m	
Empirical formula	C24 H34 Cl3 Cr N6 O4	
Formula weight	628.92	
Temperature	107(2) K	
Wavelength	0.71073 Å	
Crystal system	Triclinic	
Space group	P-1	
Unit cell dimensions	a = 6.7988(8) Å	a= 69.310(4)°.
	b = 9.1567(12) Å	b= 84.726(4)°.
	c = 12.3814(15) Å	g = 80.948(4)°.
Volume	711.56(15) $Å^3$	
Z	1	
Density (calculated)	1.468 Mg/m^3	
Absorption coefficient	0.725 mm^{-1}	
F(000)	327	
Crystal size	0.250 x 0.100 x 0.050 mm^3	
Theta range for data collection	1.759 to 26.301°.	
Index ranges	-8<=h<=8, -6<=k<=11, -15<=l<=15	
Reflections collected	4806	
Independent reflections	2887 [R(int) = 0.0179]	
Completeness to theta = 25.242°	99.7 %	
Absorption correction	Multi scan	
Max. and min. transmission	0.7454 and 0.6619	
Refinement method	Full-matrix least-squares on F^2	
Data / restraints / parameters	2887 / 1 / 186	
Goodness-of-fit on F^2	1.041	
Final R indices [I>2sigma(I)]	R1 = 0.0662, wR2 = 0.1982	
R indices (all data)	R1 = 0.0778, wR2 = 0.2113	
Extinction coefficient	n/a	
Largest diff. peak and hole	2.544 and -0.549 $e.Å^{-3}$	

Table 2. Atomic coordinates (x 10^4) and equivalent isotropic displacement parameters ($Å^2$x 10^3) for *trans*-[Cr(NitroPetA)$(Cl)_2$]Cl (**4"**). U(eq) is defined as one third of the trace of the orthogonalized U^{ij} tensor.

	x	y	z	U(eq)
C(1)	5530(7)	6663(5)	5508(4)	21(1)
C(2)	5894(6)	7376(5)	4214(4)	19(1)
C(3)	6764(6)	9832(5)	2689(3)	19(1)
C(4)	7518(7)	11411(5)	2468(4)	21(1)
C(5)	6076(7)	12659(5)	2803(4)	22(1)
C(6)	6824(9)	14259(5)	2243(4)	35(1)
C(7)	8040(7)	8920(5)	2000(4)	23(1)
C(8)	7213(8)	8588(5)	1164(4)	27(1)
C(9)	8420(8)	7724(5)	552(4)	30(1)
C(10)	10399(8)	7210(6)	754(5)	35(1)
C(11)	11237(8)	7570(7)	1578(5)	40(1)
C(12)	10066(8)	8415(6)	2214(5)	34(1)
Cl(1)	7730(1)	9419(1)	6138(1)	21(1)
Cl(2A)	811(3)	6238(3)	4941(2)	15(1)
Cr(1)	5000	10000	5000	13(1)
N(1)	4114(5)	7805(4)	5910(3)	16(1)
N(2)	6683(5)	8897(4)	3945(3)	15(1)
N(3)	7481(8)	7333(5)	-308(4)	40(1)
O(1)	5643(8)	7743(6)	-427(4)	58(1)
O(2)	8509(7)	6572(5)	-834(3)	49(1)
Cl(2B)	624(13)	6691(11)	5231(8)	15(1)

Table 3. Bond lengths [Å] and angles [°] for *trans*-[Cr(NitroPetA)$(Cl)_2$]Cl (**4"**).

C(1)-N(1)	1.494(5)
C(1)-C(2)	1.514(6)
C(1)-H(1A)	0.9900
C(1)-H(1B)	0.9900
C(2)-N(2)	1.487(5)
C(2)-H(2A)	0.9900
C(2)-H(2B)	0.9900
C(3)-N(2)	1.488(5)
C(3)-C(7)	1.522(6)
C(3)-C(4)	1.536(6)
C(3)-H(3)	1.0000
C(4)-C(5)	1.531(6)
C(4)-H(4A)	0.9900
C(4)-H(4B)	0.9900
C(5)-N(1)#1	1.496(5)
C(5)-C(6)	1.529(6)
C(5)-H(5)	1.0000
C(6)-H(6A)	0.9800
C(6)-H(6B)	0.9800
C(6)-H(6C)	0.9800
C(7)-C(8)	1.365(7)
C(7)-C(12)	1.401(7)
C(8)-C(9)	1.407(7)
C(8)-H(8)	0.9500
C(9)-C(10)	1.369(8)
C(9)-N(3)	1.461(7)
C(10)-C(11)	1.371(8)
C(10)-H(10)	0.9500
C(11)-C(12)	1.404(7)
C(11)-H(11)	0.9500
C(12)-H(12)	0.9500
Cl(1)-Cr(1)	2.3136(10)

Cl(2A)-Cl(2B)	0.631(10)
Cr(1)-N(1)	2.080(3)
Cr(1)-N(1)#1	2.080(3)
Cr(1)-N(2)#1	2.080(3)
Cr(1)-N(2)	2.080(3)
Cr(1)-Cl(1)#1	2.3136(10)
N(1)-C(5)#1	1.496(5)
N(1)-H(1)	0.898(10)
N(2)-H(2)	0.83(6)
N(3)-O(2)	1.218(6)
N(3)-O(1)	1.254(7)

N(1)-C(1)-C(2)	109.0(3)
N(1)-C(1)-H(1A)	109.9
C(2)-C(1)-H(1A)	109.9
N(1)-C(1)-H(1B)	109.9
C(2)-C(1)-H(1B)	109.9
H(1A)-C(1)-H(1B)	108.3
N(2)-C(2)-C(1)	109.0(3)
N(2)-C(2)-H(2A)	109.9
C(1)-C(2)-H(2A)	109.9
N(2)-C(2)-H(2B)	109.9
C(1)-C(2)-H(2B)	109.9
H(2A)-C(2)-H(2B)	108.3
N(2)-C(3)-C(7)	111.8(3)
N(2)-C(3)-C(4)	111.1(3)
C(7)-C(3)-C(4)	110.5(3)
N(2)-C(3)-H(3)	107.8
C(7)-C(3)-H(3)	107.8
C(4)-C(3)-H(3)	107.8
C(5)-C(4)-C(3)	116.5(3)
C(5)-C(4)-H(4A)	108.2
C(3)-C(4)-H(4A)	108.2
C(5)-C(4)-H(4B)	108.2
C(3)-C(4)-H(4B)	108.2

H(4A)-C(4)-H(4B)	107.3
N(1)#1-C(5)-C(6)	111.7(4)
N(1)#1-C(5)-C(4)	109.8(3)
C(6)-C(5)-C(4)	109.2(4)
N(1)#1-C(5)-H(5)	108.7
C(6)-C(5)-H(5)	108.7
C(4)-C(5)-H(5)	108.7
C(5)-C(6)-H(6A)	109.5
C(5)-C(6)-H(6B)	109.5
H(6A)-C(6)-H(6B)	109.5
C(5)-C(6)-H(6C)	109.5
H(6A)-C(6)-H(6C)	109.5
H(6B)-C(6)-H(6C)	109.5
C(8)-C(7)-C(12)	119.3(4)
C(8)-C(7)-C(3)	120.0(4)
C(12)-C(7)-C(3)	120.6(4)
C(7)-C(8)-C(9)	118.8(5)
C(7)-C(8)-H(8)	120.6
C(9)-C(8)-H(8)	120.6
C(10)-C(9)-C(8)	122.7(5)
C(10)-C(9)-N(3)	119.6(4)
C(8)-C(9)-N(3)	117.7(5)
C(9)-C(10)-C(11)	118.4(5)
C(9)-C(10)-H(10)	120.8
C(11)-C(10)-H(10)	120.8
C(10)-C(11)-C(12)	120.3(5)
C(10)-C(11)-H(11)	119.9
C(12)-C(11)-H(11)	119.9
C(7)-C(12)-C(11)	120.4(5)
C(7)-C(12)-H(12)	119.8
C(11)-C(12)-H(12)	119.8
N(1)-Cr(1)-N(1)#1	180.0
N(1)-Cr(1)-N(2)#1	94.25(13)
N(1)#1-Cr(1)-N(2)#1	85.75(13)
N(1)-Cr(1)-N(2)	85.75(13)

N(1)#1-Cr(1)-N(2)	94.25(13)
N(2)#1-Cr(1)-N(2)	180.0
N(1)-Cr(1)-Cl(1)#1	88.85(10)
N(1)#1-Cr(1)-Cl(1)#1	91.15(10)
N(2)#1-Cr(1)-Cl(1)#1	88.81(10)
N(2)-Cr(1)-Cl(1)#1	91.18(10)
N(1)-Cr(1)-Cl(1)	91.15(10)
N(1)#1-Cr(1)-Cl(1)	88.85(10)
N(2)#1-Cr(1)-Cl(1)	91.19(10)
N(2)-Cr(1)-Cl(1)	88.81(10)
Cl(1)#1-Cr(1)-Cl(1)	180.0
C(1)-N(1)-C(5)#1	113.3(3)
C(1)-N(1)-Cr(1)	105.3(2)
C(5)#1-N(1)-Cr(1)	116.8(2)
C(1)-N(1)-H(1)	109(3)
C(5)#1-N(1)-H(1)	107(3)
Cr(1)-N(1)-H(1)	106(3)
C(2)-N(2)-C(3)	113.4(3)
C(2)-N(2)-Cr(1)	105.3(2)
C(3)-N(2)-Cr(1)	116.2(2)
C(2)-N(2)-H(2)	110(4)
C(3)-N(2)-H(2)	109(4)
Cr(1)-N(2)-H(2)	103(4)
O(2)-N(3)-O(1)	123.6(5)
O(2)-N(3)-C(9)	118.2(5)
O(1)-N(3)-C(9)	118.1(4)

Symmetry transformations used to generate equivalent atoms:

#1 -x+1,-y+2,-z+1

Table 4. Anisotropic displacement parameters ($Å^2 x\ 10^3$) for *trans*-[Cr(NitroPetA)$(Cl)_2$]Cl (**4"**). The anisotropic displacement factor exponent takes the form: $-2p^2[\ h^2\ a^{*2}U^{11} + ... + 2\ h\ k\ a^*\ b^*\ U^{12}\ ]$

	U^{11}	U^{22}	U^{33}	U^{23}	U^{13}	U^{12}
C(1)	27(2)	15(2)	22(2)	-8(2)	5(2)	-4(2)
C(2)	23(2)	14(2)	22(2)	-10(2)	3(2)	-4(2)
C(3)	22(2)	20(2)	16(2)	-8(2)	4(2)	-3(2)
C(4)	27(2)	17(2)	19(2)	-7(2)	7(2)	-4(2)
C(5)	33(2)	14(2)	16(2)	-4(2)	5(2)	-2(2)
C(6)	58(3)	20(2)	24(2)	-7(2)	12(2)	-10(2)
C(7)	32(2)	16(2)	21(2)	-7(2)	10(2)	-7(2)
C(8)	40(3)	20(2)	21(2)	-7(2)	6(2)	-5(2)
C(9)	54(3)	19(2)	15(2)	-4(2)	3(2)	-9(2)
C(10)	43(3)	27(2)	34(3)	-12(2)	16(2)	-5(2)
C(11)	31(3)	41(3)	53(3)	-27(3)	12(2)	-2(2)
C(12)	32(3)	33(3)	40(3)	-21(2)	7(2)	-3(2)
Cl(1)	18(1)	24(1)	23(1)	-11(1)	-4(1)	-2(1)
Cr(1)	14(1)	12(1)	15(1)	-6(1)	1(1)	-3(1)
N(1)	18(2)	12(2)	17(2)	-7(1)	3(1)	-3(1)
N(2)	15(2)	15(2)	18(2)	-7(1)	1(1)	-3(1)
N(3)	66(3)	30(2)	23(2)	-12(2)	-3(2)	3(2)
O(1)	71(3)	63(3)	50(3)	-36(2)	-27(2)	18(2)
O(2)	79(3)	42(2)	33(2)	-25(2)	5(2)	0(2)

Table 5. Hydrogen coordinates (x 10^4) and isotropic displacement parameters ($Å^2$x 10^3) for *trans*-[Cr(NitroPetA)$(Cl)_2$]Cl (**4"**).

	x	y	z	U(eq)
H(1A)	4962	5666	5698	25
H(1B)	6805	6427	5902	25
H(2A)	6865	6647	3938	23
H(2B)	4633	7556	3817	23
H(3)	5376	10064	2410	23
H(4A)	8751	11200	2897	26
H(4B)	7883	11862	1635	26
H(5)	4737	12723	2503	26
H(6A)	5915	15059	2463	52
H(6B)	6876	14545	1401	52
H(6C)	8161	14198	2506	52
H(8)	5847	8936	997	33
H(10)	11174	6619	332	42
H(11)	12615	7246	1721	48
H(12)	10653	8647	2792	40
H(2)	7820(80)	8730(60)	4190(40)	20(12)
H(1)	2890(30)	7850(60)	5670(40)	19(12)

6. Crystal Information of *trans*-[Cr(AminoPetA)(Cl)$_2$]BF$_4$ (5")

Table 1. Crystal data and structure refinement for *trans*-[Cr(AminoPetA)(Cl)$_2$]BF$_4$ (**5"**).

Identification code	b10102014_0m	
Empirical formula	C28 H44 B Cl2 Cr F4 N8	
Formula weight	702.42	
Temperature	107(2) K	
Wavelength	0.71073 Å	
Crystal system	Monoclinic	
Space group	C2/c	
Unit cell dimensions	a = 31.812(4) Å	a= 90°.
	b = 6.4411(9) Å	b= 125.256(6)°.
	c = 19.781(3) Å	g = 90°.
Volume	3309.9(8) Å^3	
Z	4	
Density (calculated)	1.410 Mg/m^3	
Absorption coefficient	0.563 mm^{-1}	
F(000)	1468	
Crystal size	0.250 x 0.200 x 0.100 mm^3	
Theta range for data collection	2.062 to 27.411°.	
Index ranges	-39<=h<=39, -8<=k<=6, -13<=l<=25	
Reflections collected	6333	
Independent reflections	3680 [R(int) = 0.0280]	
Completeness to theta = 25.242°	99.0 %	
Absorption correction	Semi-empirical from equivalents	
Max. and min. transmission	0.7455 and 0.6590	
Refinement method	Full-matrix least-squares on F^2	
Data / restraints / parameters	3680 / 2 / 215	
Goodness-of-fit on F^2	0.989	
Final R indices [I>2sigma(I)]	R1 = 0.0427, wR2 = 0.0959	
R indices (all data)	R1 = 0.0607, wR2 = 0.1051	
Extinction coefficient	n/a	
Largest diff. peak and hole	0.493 and -0.387 e.Å^{-3}	

Table 2. Atomic coordinates (x 10^4) and equivalent isotropic displacement parameters ($Å^2$x 10^3) for *trans*-[Cr(AminoPetA)$(Cl)_2$]BF_4 (**5"**). U(eq) is defined as one third of the trace of the orthogonalized U^{ij} tensor.

	x	y	z	U(eq)
B(1)	0	7064(7)	7500	42(1)
C(1)	635(1)	1953(4)	-392(1)	20(1)
C(2)	1102(1)	912(4)	1841(1)	23(1)
C(3)	799(1)	-933(4)	1822(1)	21(1)
C(4)	-91(1)	-2285(4)	1140(1)	20(1)
C(5)	928(1)	-1345(4)	2675(2)	28(1)
C(6)	1139(1)	1135(4)	1111(1)	20(1)
C(7)	1567(1)	2593(4)	1298(2)	26(1)
C(8)	1894(1)	1980(5)	1094(2)	32(1)
C(9)	2279(1)	3309(5)	1215(2)	43(1)
C(10)	2324(1)	5248(5)	1544(2)	47(1)
C(11)	2007(1)	5839(5)	1760(2)	45(1)
C(12)	1625(1)	4532(4)	1638(2)	36(1)
C(13)	1728(1)	7690(6)	9479(2)	49(1)
C(14)	1411(1)	5944(6)	9333(2)	70(1)
Cl(1)	415(1)	-2939(1)	3(1)	19(1)
Cr(1)	0	0	0	13(1)
F(1)	395(1)	6436(5)	7342(2)	38(1)
F(2)	265(1)	5359(5)	7653(2)	38(1)
F(3)	271(1)	8272(3)	8188(1)	55(1)
N(1)	634(1)	1790(3)	354(1)	16(1)
N(2)	238(1)	-571(3)	1197(1)	16(1)
N(3)	2606(1)	2642(6)	1014(2)	62(1)
N(4)	1971(1)	9117(6)	9618(2)	75(1)

Table 3. Bond lengths [Å] and angles [°] for *trans*-[Cr(AminoPetA)$(Cl)_2$]BF_4 (**5"**).

B(1)-F(2)#1	1.309(5)
B(1)-F(2)	1.309(5)
B(1)-F(3)	1.359(3)
B(1)-F(3)#1	1.359(3)
B(1)-F(1)#1	1.516(3)
B(1)-F(1)	1.516(3)
C(1)-N(1)	1.479(3)
C(1)-C(4)#2	1.507(3)
C(1)-H(1A)	0.9900
C(1)-H(1B)	0.9900
C(2)-C(3)	1.519(3)
C(2)-C(6)	1.522(3)
C(2)-H(2A)	0.9900
C(2)-H(2B)	0.9900
C(3)-N(2)	1.490(3)
C(3)-C(5)	1.510(3)
C(3)-H(3)	1.0000
C(4)-N(2)	1.480(3)
C(4)-C(1)#2	1.507(3)
C(4)-H(4A)	0.9900
C(4)-H(4B)	0.9900
C(5)-H(5A)	0.9800
C(5)-H(5B)	0.9800
C(5)-H(5C)	0.9800
C(6)-N(1)	1.493(3)
C(6)-C(7)	1.513(3)
C(6)-H(6)	1.0000
C(7)-C(8)	1.374(4)
C(7)-C(12)	1.380(4)
C(8)-C(9)	1.397(4)
C(8)-H(8)	0.9500
C(9)-C(10)	1.378(5)

C(9)-N(3)	1.379(4)
C(10)-C(11)	1.355(5)
C(10)-H(10)	0.9500
C(11)-C(12)	1.383(4)
C(11)-H(11)	0.9500
C(12)-H(12)	0.9500
C(13)-N(4)	1.128(5)
C(13)-C(14)	1.425(5)
C(14)-H(14A)	0.9800
C(14)-H(14B)	0.9800
C(14)-H(14C)	0.9800
Cl(1)-Cr(1)	2.3056(6)
Cr(1)-N(2)#2	2.0602(19)
Cr(1)-N(2)	2.0603(19)
Cr(1)-N(1)	2.0628(18)
Cr(1)-N(1)#2	2.0629(18)
Cr(1)-Cl(1)#2	2.3055(6)
F(2)-F(2)#1	1.424(7)
N(1)-H(5)	0.81(3)
N(2)-H(2)	0.84(3)
N(3)-H(3A)	0.8800
N(3)-H(3B)	0.8800

F(2)#1-B(1)-F(2)	65.9(4)
F(2)#1-B(1)-F(3)	131.5(2)
F(2)-B(1)-F(3)	107.34(19)
F(2)#1-B(1)-F(3)#1	107.35(19)
F(2)-B(1)-F(3)#1	131.5(2)
F(3)-B(1)-F(3)#1	110.1(4)
F(2)#1-B(1)-F(1)#1	47.4(2)
F(2)-B(1)-F(1)#1	103.2(3)
F(3)-B(1)-F(1)#1	93.86(16)
F(3)#1-B(1)-F(1)#1	103.78(15)
F(2)#1-B(1)-F(1)	103.2(3)
F(2)-B(1)-F(1)	47.4(2)

F(3)-B(1)-F(1)	103.78(15)
F(3)#1-B(1)-F(1)	93.85(16)
F(1)#1-B(1)-F(1)	149.1(4)
N(1)-C(1)-C(4)#2	109.20(18)
N(1)-C(1)-H(1A)	109.8
C(4)#2-C(1)-H(1A)	109.8
N(1)-C(1)-H(1B)	109.8
C(4)#2-C(1)-H(1B)	109.8
H(1A)-C(1)-H(1B)	108.3
C(3)-C(2)-C(6)	116.6(2)
C(3)-C(2)-H(2A)	108.1
C(6)-C(2)-H(2A)	108.1
C(3)-C(2)-H(2B)	108.1
C(6)-C(2)-H(2B)	108.1
H(2A)-C(2)-H(2B)	107.3
N(2)-C(3)-C(5)	112.30(19)
N(2)-C(3)-C(2)	109.73(18)
C(5)-C(3)-C(2)	110.5(2)
N(2)-C(3)-H(3)	108.1
C(5)-C(3)-H(3)	108.1
C(2)-C(3)-H(3)	108.1
N(2)-C(4)-C(1)#2	109.12(18)
N(2)-C(4)-H(4A)	109.9
C(1)#2-C(4)-H(4A)	109.9
N(2)-C(4)-H(4B)	109.9
C(1)#2-C(4)-H(4B)	109.9
H(4A)-C(4)-H(4B)	108.3
C(3)-C(5)-H(5A)	109.5
C(3)-C(5)-H(5B)	109.5
H(5A)-C(5)-H(5B)	109.5
C(3)-C(5)-H(5C)	109.5
H(5A)-C(5)-H(5C)	109.5
H(5B)-C(5)-H(5C)	109.5
N(1)-C(6)-C(7)	111.46(19)
N(1)-C(6)-C(2)	110.51(18)

C(7)-C(6)-C(2)	112.20(19)
N(1)-C(6)-H(6)	107.5
C(7)-C(6)-H(6)	107.5
C(2)-C(6)-H(6)	107.5
C(8)-C(7)-C(12)	119.6(2)
C(8)-C(7)-C(6)	118.5(2)
C(12)-C(7)-C(6)	121.9(2)
C(7)-C(8)-C(9)	120.8(3)
C(7)-C(8)-H(8)	119.6
C(9)-C(8)-H(8)	119.6
C(10)-C(9)-N(3)	122.0(3)
C(10)-C(9)-C(8)	118.5(3)
N(3)-C(9)-C(8)	119.5(3)
C(11)-C(10)-C(9)	120.7(3)
C(11)-C(10)-H(10)	119.6
C(9)-C(10)-H(10)	119.6
C(10)-C(11)-C(12)	121.0(3)
C(10)-C(11)-H(11)	119.5
C(12)-C(11)-H(11)	119.5
C(11)-C(12)-C(7)	119.4(3)
C(11)-C(12)-H(12)	120.3
C(7)-C(12)-H(12)	120.3
N(4)-C(13)-C(14)	176.3(5)
C(13)-C(14)-H(14A)	109.5
C(13)-C(14)-H(14B)	109.5
H(14A)-C(14)-H(14B)	109.5
C(13)-C(14)-H(14C)	109.5
H(14A)-C(14)-H(14C)	109.5
H(14B)-C(14)-H(14C)	109.5
N(2)#2-Cr(1)-N(2)	180.0
N(2)#2-Cr(1)-N(1)	85.90(7)
N(2)-Cr(1)-N(1)	94.10(7)
N(2)#2-Cr(1)-N(1)#2	94.10(7)
N(2)-Cr(1)-N(1)#2	85.90(7)
N(1)-Cr(1)-N(1)#2	180.0

N(2)#2-Cr(1)-Cl(1)#2	91.17(6)
N(2)-Cr(1)-Cl(1)#2	88.82(6)
N(1)-Cr(1)-Cl(1)#2	89.29(6)
N(1)#2-Cr(1)-Cl(1)#2	90.71(6)
N(2)#2-Cr(1)-Cl(1)	88.82(6)
N(2)-Cr(1)-Cl(1)	91.18(6)
N(1)-Cr(1)-Cl(1)	90.71(6)
N(1)#2-Cr(1)-Cl(1)	89.29(6)
Cl(1)#2-Cr(1)-Cl(1)	180.0
B(1)-F(2)-F(2)#1	57.04(19)
C(1)-N(1)-C(6)	113.56(18)
C(1)-N(1)-Cr(1)	105.37(13)
C(6)-N(1)-Cr(1)	117.27(14)
C(1)-N(1)-H(5)	105.7(18)
C(6)-N(1)-H(5)	107.6(17)
Cr(1)-N(1)-H(5)	106.6(18)
C(4)-N(2)-C(3)	113.63(18)
C(4)-N(2)-Cr(1)	105.79(13)
C(3)-N(2)-Cr(1)	116.84(14)
C(4)-N(2)-H(2)	108.5(16)
C(3)-N(2)-H(2)	106.6(16)
Cr(1)-N(2)-H(2)	104.9(16)
C(9)-N(3)-H(3A)	120.0
C(9)-N(3)-H(3B)	120.0
H(3A)-N(3)-H(3B)	120.0

Symmetry transformations used to generate equivalent atoms:

#1 -x,y,-z+3/2 #2 -x,-y,-z

Table 4. Anisotropic displacement parameters ($Å^2 x\ 10^3$) for *trans*-[Cr(AminoPetA)$(Cl)_2$]BF_4 (**5"**). The anisotropic displacement factor exponent takes the form: $-2p^2[\ h^2\ a^{*2}U^{11} + ...\ + 2\ h\ k\ a^*\ b^*\ U^{12}\ ]$

	U^{11}	U^{22}	U^{33}	U^{23}	U^{13}	U^{12}
B(1)	34(2)	23(2)	51(3)	0	14(2)	0
C(1)	19(1)	22(1)	24(1)	2(1)	14(1)	-2(1)
C(2)	16(1)	26(1)	20(1)	-2(1)	6(1)	-3(1)
C(3)	18(1)	24(1)	17(1)	1(1)	8(1)	2(1)
C(4)	22(1)	20(1)	19(1)	1(1)	13(1)	-4(1)
C(5)	25(1)	37(2)	19(1)	3(1)	10(1)	1(1)
C(6)	13(1)	20(1)	22(1)	2(1)	7(1)	-1(1)
C(7)	15(1)	26(1)	24(1)	6(1)	4(1)	-4(1)
C(8)	20(1)	38(2)	33(1)	10(1)	12(1)	-3(1)
C(9)	18(1)	61(2)	36(2)	20(2)	8(1)	-6(1)
C(10)	24(1)	48(2)	39(2)	17(1)	1(1)	-18(1)
C(11)	30(1)	31(2)	38(2)	6(1)	-1(1)	-11(1)
C(12)	24(1)	27(1)	35(2)	1(1)	5(1)	-5(1)
C(13)	39(2)	61(2)	43(2)	18(2)	21(1)	-2(2)
C(14)	55(2)	61(2)	54(2)	12(2)	8(2)	-18(2)
Cl(1)	20(1)	16(1)	23(1)	-1(1)	13(1)	0(1)
Cr(1)	13(1)	13(1)	15(1)	-1(1)	8(1)	-1(1)
F(1)	42(1)	37(1)	41(1)	-11(1)	27(1)	4(1)
F(2)	42(1)	37(1)	41(1)	-11(1)	27(1)	4(1)
F(3)	62(1)	71(1)	46(1)	-14(1)	40(1)	4(1)
N(1)	16(1)	15(1)	18(1)	-1(1)	9(1)	-1(1)
N(2)	16(1)	16(1)	17(1)	-1(1)	10(1)	0(1)
N(3)	32(1)	88(2)	73(2)	14(2)	34(1)	-13(2)
N(4)	64(2)	77(2)	89(3)	18(2)	48(2)	-19(2)

Table 5. Hydrogen coordinates (x 10^4) and isotropic displacement parameters ($Å^2$x 10^3) for *trans*-[Cr(AminoPetA)$(Cl)_2$]BF_4 (**5"**).

	x	y	z	U(eq)
H(1A)	776	665	-460	24
H(1B)	854	3130	-330	24
H(2A)	1456	824	2353	28
H(2B)	944	2193	1878	28
H(3)	900	-2182	1648	25
H(4A)	-85	-2319	1647	24
H(4B)	41	-3629	1093	24
H(5A)	844	-118	2868	42
H(5B)	1297	-1647	3059	42
H(5C)	729	-2536	2652	42
H(6)	1222	-266	998	24
H(8)	1859	637	869	38
H(10)	2580	6180	1622	56
H(11)	2049	7170	1998	54
H(12)	1403	4966	1788	43
H(14A)	1311	5982	9717	106
H(14B)	1603	4662	9420	106
H(14C)	1102	5985	8762	106
H(2)	163(9)	510(40)	1343(15)	11(6)
H(5)	573(9)	2950(40)	436(15)	16(7)
H(3A)	2852	3464	1095	74
H(3B)	2568	1395	804	74